

MASTER OF SCIENCE THESIS

---

# Wake Bursting Effects of a Drooped Spoiler Panel in a Wing-Flap Configuration

An Experimental Investigation

C. Kounenis

---

November 2012



# **Wake Bursting Effects of a Drooped Spoiler Panel in a Wing-Flap Configuration**

**An Experimental Investigation**

MASTER OF SCIENCE THESIS

For obtaining the degree of Master of Science in Aerospace Engineering at Delft University of Technology

C. Kounenis

November 2012

Faculty of Aerospace Engineering · Delft University of Technology



Copyright © Aerospace Engineering, Delft University of Technology  
All rights reserved.

DELFT UNIVERSITY OF TECHNOLOGY  
FACULTY OF AEROSPACE ENGINEERING  
DEPARTMENT OF AERODYNAMICS

**DECLARATION**

The undersigned hereby certify that they have read and recommend to the Faculty of Aerospace Engineering for acceptance a thesis entitled "**Wake Bursting Effects of a Drooped Spoiler Panel in a Wing-Flap Configuration**" by **C.Kounenis** in partial fulfilment of the requirements for the degree of **Master of Science**.



Dated: November 2012

Committee Members:

---

Prof.dr.ir. G. (Georg) Eitelberg

---

dr. ir. L. (Leo) Veldhuis (Supervisor)

---

dr.M.(Marios) Kotsonis

---

dr.D.(Daniele) Ragni



# Preface

In April 2010, I received an offer to come and study at Delft University of Technology. This was a very important day for me, as this meant the end of a long "journey", my bachelor studies at Queen Mary, University of London, and a fresh start in a different country, university and educational system.

The main reason for choosing TU Delft was the wide range of its Aerodynamics master structure, covering all aspects, from theoretical, experimental to computational. This was exactly what I was looking for my postgraduate studies. Moreover, the already known reputation of the university in combination with my passion of exploring new possibilities made this decision even easier.

In August 2010, I enthusiastically arrived in Delft in order to begin my postgraduate degree in Aerodynamics at the Aerospace Engineering Faculty of Delft University of Technology after four wonderful years in London. Soon, I realised that my choice was the right one, meeting very dedicated professors and colleagues, with great passion about what they were doing. The master degree in Aerodynamics, was very demanding and it included a lot of sacrifices, mainly personal life ones. However, everything in life comes with an expense, and during these twenty-seven months at TU Delft, I learned a lot about Aerodynamics, I matured as a person and scientist, but also made strong friendships with very interesting people all around the world, which hopefully will be continued in the future.

My master thesis was one of the most fascinating periods of my time in Delft and I learned valuable things, which will surely help me in my future career. The topic was chosen because of the great interest I have in flow control techniques and high lift devices. In addition, my desire to work in the experimental side of Aerodynamics, made this decision much easier, especially because of the great experience in the department with experimental techniques and mainly Particle Image Velocimetry.

These two years passed by very quickly and my next step will be to continue my studies by undertaking a Phd degree back in the UK, at Durham University, on road vehicle aerodynamics in collaboration with Jaguar Land Rover. Delft University of Technology and especially my professors helped me significantly to take this decision and I will always be grateful about that.

---

C. Kounenis

Delft, November 2012

# Abstract

Nowadays, the evolution of multi-element airfoils presents a change of route, towards a "circular arch", in order to achieve the ultimate lift force [9]. Particularly, for wing-flap configurations, the enhancement of high lift performance, is of great interest and growing research at Delft University of Technology. Typically, the main approach with respect to delivering higher lift forces is by deflecting the flap to higher angles of attack. However, the higher this angle is, the larger the curvature of the flow. As a result, separated flow dominates most of the flap's contour and significant part of the lift force might be lost. This problem is known to engineers for years and in order to overcome this lift loss, additional flow control techniques seem to be essential. Thus, with the goal of lift improvement in mind, the effect of drooped spoiler application was investigated experimentally, for a wing- Fowler flap model, at critical flight conditions i.e. high flap deflection angle of  $50^\circ$  and  $Re = 1.6 \cdot 10^6$  (40 m/s).

The first wind-tunnel experiments were carried out at the Low-Speed Low-Turbulence Wind-tunnel (LTT). Flow visualisation techniques showed that for a drooped spoiler panel angle of  $15^\circ$ , the model's flap surface stayed fully attached in contrast to the clean wing configuration, which "suffered" from partially separated flow on this region. In order to comprehend the drooped spoiler panel concept and possibly delay flow separation, the effects of different types of drooped spoiler panels were investigated. The difference between these panels was the panel's deflection angle. The idea behind this concept is the creation of a convergent nozzle on the top of the suction surface of the Fowler flap, causing an increase in local velocities which would be large enough, to keep the flap flow attached. However, as the deflection angle of the panel was decreased, this effect was reduced significantly, causing insufficient velocity magnitudes, to overcome the strong three-dimensional separated flow. However, in contrast to the flow visualisation results, pressure measurements showed an overall decrease of lift coefficients, caused by wake bursting or also called off-the-surface separation. Then, it was decided to focus on the understanding of wake bursting phenomenon, due to limited work done up to date in this field.

The research on the wake bursting phenomenon consisted of experiments on the actual wing-flap combination and on a fundamental test set-up, including a flat plate in a diverging diffuser, in order to simulate the effect of adverse pressure gradient, which was realised to be the cause of the wake bursting phenomenon. For both experiments the main experimental technique used was Particle Image Velocimetry (PIV). The results, showed that wake bursting was initiated at larger angles of the whole configuration, where the flow had to follow a greater curvature. Moreover, it was also shown that wake bursting could possibly be the reason behind the attached flow on the surface of the Fowler flap, as part of the reversed flow in the wake region, seemed to move towards the boundary layer. In addition, it could be concluded that displacement thickness in combination with the pressure coefficient distribution on the wake, are the main factors which could warn about the possibility of it occurring. On the other hand, the boundary layer thick-

ness, could be of significant influence at lower angles of attack, however, at larger angles, where wake bursting phenomena were already apparent, it's effect did not seem of great importance.

Additionally, a short computational effort was tried using MSES code, without having a successful output. As realised, it would be nearly impossible to simulate the drooped panel and the flow around it, particularly at high flap angles, without facing convergence problems. Nevertheless, it could be suggested that further work should be carried out for clean wing configuration lift or wake bursting estimates and implementation in the design process, but for further control refinements, would need a lot of attention with respect to their accuracy.

Concluding, the selected configuration tested for flow separation delay was partially successful. The relatively large model, high Fowler flap deflection and large Reynolds number appeared not to be a huge obstacle in order to achieve flow separation elimination on the Fowler flap of the configuration. At low angles of attack and up to  $4^\circ$ , using drooped spoiler panel, the lift coefficients were higher and drag coefficients lower than for the clean wing configuration, proving that this flow control device could deliver interesting results with respect to high lift performance. However, the potential of lift improvement was strongly limited due to wake bursting effects. A better understanding of the wake bursting phenomenon is necessary. Literature was limited and the tests done for this work has shown that there are very important factors which could lead to the cause of this unwanted phenomenon and explanations on how it could be avoided in the design process of multi-element airfoils at large flap angles. For multi-element airfoils, this phenomenon could be the cause of great loss of performance and as a result, it would be very helpful to continue this research in order to further understand it and possibly find solutions to deal with it.

# Acknowledgements

I would like to take this opportunity to firstly thank the Faculty of Aerospace Engineering and Aerodynamics Department at Delft University of Technology, first of all for the valuable knowledge that I gained during these two years of my postgraduate studies, but also for giving me the opportunity of performing high class research, while showing my engineering skills. However, there is a list of people I would like to express my deep respect and gratitude for their willingness, guidance, attitude and support through this enjoyable time.

The first person is my supervisor dr. ir. L.L.M (Leo) Veldhuis, who was always there in order to help and motivate me, with loads of enthusiasm, kindness and persistence. Special thanks to my friends, Dr. Marios Kotsonis and Dr. Daniele Ragni for their priceless support, but also PhD candidates, Mr. Daniele Violato, Mr. Sina Ghaemi, Mr. Andrea Sciacchitano and Mr. Guiseppe Correale for their valuable help on many occasions during my thesis. Finally, I feel to say a big thank you to the technical staff in the faculty including Mr. Stefan Bernardy, Mr. Eric de Keizer and Mr. Leo Molewijk for the great collaboration we had all this time. Without their professionalism, excellent skills and technical support I would be unable to complete my thesis work.

Finally, I would like to express my appreciation and love to my family and friends for their priceless help, encouragement and trust to me through these two years of my education in Delft. You have all been a blessing to me and once more thank you very much.

---

C. Kounenis

Delft, November 2012

# Contents

<b>Preface</b>	<b>vi</b>
<b>Abstract</b>	<b>vii</b>
<b>Acknowledgements</b>	<b>ix</b>
<b>List of Figures</b>	<b>xiii</b>
<b>List of Tables</b>	<b>xx</b>
<b>Nomenclature</b>	<b>xxi</b>
<b>1 Introduction</b>	<b>1</b>
<b>2 Background Theory</b>	<b>6</b>
2.1 Boundary Layer . . . . .	6
2.2 High Lift Aerodynamics & Flow Control . . . . .	12
2.3 Wake Flows & Flow Reversal . . . . .	27
<b>3 Wind Tunnel Testing Campaign I</b>	<b>39</b>
3.1 Experimental Apparatus . . . . .	39
3.1.1 Experimental Facility: Low Turbulence Tunnel (LTT) . . . . .	39
3.1.2 X-400 Wing-Flap Configuration . . . . .	41
3.1.3 Drooped Spoiler Panel (DSP) . . . . .	43
3.2 Pressure Measurements & PIV Set-up . . . . .	45
3.3 Experimental Procedure . . . . .	48
3.3.1 Flow Visualisation Techniques . . . . .	48
3.3.2 Pressure Measurement Techniques . . . . .	49
3.3.3 Particle Image Velocimetry (PIV) . . . . .	55
3.4 Presentation & Discussion of Results . . . . .	56
3.4.1 Flow Visualisation Techniques . . . . .	56
3.4.2 Pressure Measurement Techniques . . . . .	59
3.4.3 Particle Image Velocimetry (PIV) . . . . .	73
3.5 Experimental Campaign I Conclusions . . . . .	85
<b>4 Wind Tunnel Testing Campaign II</b>	<b>88</b>
4.1 Experimental Apparatus . . . . .	88
4.1.1 Experimental Facility: M-Tunnel . . . . .	88
4.1.2 Plexiglass Flat Plate . . . . .	88

4.1.3	Diffuser Walls . . . . .	91
4.1.4	Wind-Tunnel Screen, Supporting Table & Top Walls . . . . .	92
4.2	PIV & Pressure Measurements Set-Up . . . . .	94
4.2.1	Pressure measurements set-up . . . . .	94
4.2.2	PIV set-up . . . . .	97
4.3	Experimental Procedure . . . . .	99
4.3.1	Flow Visualisation . . . . .	99
4.3.2	Surface Static Pressure Measurements . . . . .	100
4.3.3	Boundary Layer Total Pressure Measurements . . . . .	100
4.3.4	Wake Total Pressure Measurements . . . . .	101
4.3.5	PIV . . . . .	104
4.4	Presentation & Discussion of Results . . . . .	106
4.4.1	Flow Visualisation . . . . .	106
4.4.2	Pressure Measurements . . . . .	107
4.4.3	Particle Image Velocimetry (PIV) . . . . .	113
4.4.4	Gartshore's Wake Behaviour Relation . . . . .	121
4.5	Experimental Campaign II Conclusions . . . . .	124
<b>5</b>	<b>MSES Code For Maximum Lift Prediction</b>	<b>126</b>
5.1	Introduction to MSES Version 3.07 . . . . .	126
5.1.1	Theory . . . . .	126
5.1.2	User Interface . . . . .	129
5.2	Validation of <b>MSES</b> Linux Version . . . . .	130
5.3	X-400 Wing-Flap Model Configuration . . . . .	136
5.4	Presentation and Discussion of Results . . . . .	137
5.4.1	Case (A): $\delta_f = 40^\circ$ . . . . .	137
5.4.2	Case (B): $\delta_f = 50^\circ$ . . . . .	141
5.5	MSES Conclusions . . . . .	142
<b>6</b>	<b>Final Conclusions</b>	<b>143</b>
<b>7</b>	<b>Future Work &amp; Recommendations</b>	<b>146</b>
	<b>References</b>	<b>148</b>
	<b>Appendix A</b>	<b>151</b>
<b>A</b>	<b>Wind-Tunnel Campaign I</b>	<b>151</b>
A.1	X-400 wing-flap model and drooped spoiler panel (DSP) . . . . .	152
A.2	Pressure measurements set-up . . . . .	153
A.3	Particle Image Velocimetry (PIV) . . . . .	154
A.3.1	PIV Theoretical Background . . . . .	154
A.3.2	PIV instrumentation . . . . .	160
A.3.3	PIV set-up . . . . .	162
A.3.4	Tufts and Oil-Flow Visualisation Pictures for DSP1 . . . . .	165
A.3.5	Proof for Total Pressure Loss in the Boundary Layer . . . . .	167
A.3.6	PIV Additional Results . . . . .	169
	<b>Appendix B</b>	<b>171</b>

<b>B</b>	<b>Wind-Tunnel Campaign II</b>	<b>172</b>
B.1	Experimental apparatus and final set-up . . . . .	173
B.2	Pressure measurements and PIV set-up . . . . .	174
B.3	Pressure measurements additional information . . . . .	175
B.3.1	Boundary layer measurements . . . . .	175
B.3.2	Wake measurements . . . . .	176
B.3.3	PIV measurements . . . . .	176
B.4	PIV Additional Results . . . . .	177
B.4.1	Test Case 4: FOV 2- $V_t = 5.1\text{m/s}$ . . . . .	177
B.4.2	Test Case 5: FOV 2- $V_t = 14.1\text{m/s}$ . . . . .	178
B.4.3	Test Case 6: FOV 2- $V_t = 21.0\text{m/s}$ . . . . .	179
B.4.4	Test Case 7: FOV 3- $V_t = 5.1\text{m/s}$ . . . . .	180
B.4.5	Test Case 8: FOV 3- $V_t = 14.1\text{m/s}$ . . . . .	181
B.4.6	Test Case 9: FOV 3- $V_t = 21.0\text{m/s}$ . . . . .	182
<b>Appendix C</b>		<b>182</b>
<b>C</b>	<b>MSES Additional Information</b>	<b>183</b>
C.1	Standard input format . . . . .	184
C.2	Input file mses.x400 . . . . .	185
C.3	Validation of MSES Linux version . . . . .	185
C.4	Further results from X-400 model simulations . . . . .	189

# List of Figures

1.1	Future aircraft design that generates dramatic reductions in noise, emissions and fuel consumption could look like this hybrid wing body [19] . . . . .	2
1.2	Drooped Spoiler Panel (DSP) working principal at (a) cruise and (b) high lift phase [26] . . . . .	3
2.1	Potential free-stream flow and viscous boundary layer formed around a NACA 0012 airfoil, at moderate angle of attack [41] . . . . .	6
2.2	Boundary layer development on a flat plate [32] . . . . .	7
2.3	Possible velocity profiles depending on pressure gradient, $\frac{dp}{dx}$ : (a) convex profile, (b) concave profile and (c) straight profile . . . . .	8
2.4	Displacement thickness, $\delta^*$ , schematic . . . . .	9
2.5	Transition process from laminar to turbulent boundary layer [20] . . . . .	10
2.6	Flow development with flow separation taking on a flat plate [11] . . . . .	10
2.7	Lift coefficient variation with respect to angle of attack for a 2D airfoil [4] . . . .	12
2.8	Effects of (a) high lift devices and (b) trailing edge flaps on $C_L$ vs. $\alpha$ [9] . . . . .	13
2.9	Ludwig Prandtl: The pioneer of boundary layer and flow control [23] . . . . .	14
2.10	Schematics of (a) Advanced Trailing Edge Control Surfaces and (b) Smart High lift device concepts [26] . . . . .	15
2.11	Schematic of drooped spoiler panel concept [36] . . . . .	16
2.12	Pop-up secondary wing concept studied by Melin et al. [17] for HELIX project .	17
2.13	Gap and overlap variations (a), wind-tunnel results for ADHF and (b) Advanced Drooped Hinge Flap concept schematic [31] . . . . .	18
2.14	$C_L$ (a) and $C_D$ (b) vs. $\alpha$ for the unexcited case [13] . . . . .	19
2.15	$L/D$ vs. $\alpha$ with (excited) and without flow control (unexcited) [13] . . . . .	20
2.16	$C_l$ vs. angle of attack (a) for clean wing and AVG configurations and (b) Comparison of WT and CFD results [17] . . . . .	21
2.17	Illustration of the geometry and dimensions (a) of vortex generator and (b) Mesh of the vortex generator [3] . . . . .	22
2.18	$C_L$ vs. $\alpha$ (a) comparison and (b) $C_p$ -distribution comparison with and without VG's [3] . . . . .	22
2.19	$C_p$ -distribution (a) for various momentum coefficients and (b) Velocity field at the trailing edge region [24] . . . . .	23
2.20	Illustration of wake break-up above the flap as computed for a HELIX baseline three element airfoil in take-off configuration at $M_\infty = 0.20$ , $\alpha = 32^\circ$ and $Re = 21.0 \cdot 10^6$ [34] . . . . .	24
2.21	Schematic of the FFDA flow control device, mounted on top of the leading edge of the flap (a) bottom view (b) top view [34] . . . . .	25

2.22	Comparison of stream patterns in the centre plane for the HELIX 2D baseline landing configuration with (b) and without (a) FFDA at $M_\infty = 0.18$ , $\alpha = 18^\circ$ and $Re = 19.0 \cdot 10^6$ [34] . . . . .	25
2.23	Estimated effect of the FFDA device on the drag polars of the HELIX baseline aircraft for landing configuration at ( $\delta_{slat} = 27^\circ$ , $\delta_{flap} = 35^\circ$ ), $M = 0.20$ and $Re = 4.66 \cdot 10^6$ [34] . . . . .	26
2.24	Flap shroud used on F/A-18 (a) [very similar to drooped spoiler panel case] and (b) $C_p$ -distribution for drooped spoiler panel and cove tab [27] . . . . .	27
2.25	Flow of a wake into a pressure rise region [29] . . . . .	28
2.26	Flow phenomena over a 2D high lift airfoil configuration [15] . . . . .	29
2.27	Flat plate-diffuser wind tunnel set-up used to create adverse pressure gradient [15] . . . . .	29
2.28	Schematic of the 2D wind-tunnel test section geometry used by Driver et al. [8], including geometrical information on the set-up and the expected wake reversal region behind the flat plate . . . . .	30
2.29	Reynolds shear stress evolution for the small separation case (expansion ratio = 2.25) as presented by Driver et al. [8] . . . . .	31
2.30	Mean streamwise velocity in the curved wake case as presented by Starke et.al. [30] . . . . .	32
2.31	Wind tunnel set-up used for the investigation of the wake in adverse pressure gradient by Tummars et.al. Note that the origin of measurements is at the trailing edge of the plate [33] . . . . .	33
2.32	Measured and calculated mean velocity (a) and (b) kinetic energy along the centreline of the wake [33] . . . . .	33
2.33	NLR 7702 airfoil 2D schematic [1] . . . . .	34
2.34	Measurement grid (a) and (b) Distributions of mean streamwise velocity in the wake [1] . . . . .	35
2.35	Installation of airfoil in the Ames 7- by 10-Foot wind-tunnel used for the experiments presented by D. Adair et al. [2] . . . . .	36
2.36	Surface pressure distribution for the whole configuration (wing & flap) [2] . . . . .	37
2.37	Downward deflection of the spoiler according to X. Wang et al. [37] . . . . .	37
2.38	Lift coefficient (a) and lift-to-drag ratio (b) under the conditions of different angles of deflection of the spoiler [37] . . . . .	38
3.1	Schematic layout of the Low-Speed Low-Turbulence Wind-tunnel [9] . . . . .	40
3.2	Low-Speed Low-Turbulence Wind-tunnel test section area overview [9] . . . . .	40
3.3	2D schematic of the X-400 wing-flap configuration with retracted Fowler flap [9] . . . . .	41
3.4	Model set-up and geometrical information with respect to the wind-tunnel section [9] . . . . .	42
3.5	Gap and overlap definitions of the X-400 wing-flap configuration [9] . . . . .	42
3.6	Suction orifices at the Low-Speed Low-Turbulence Wind-tunnel wall [9] . . . . .	42
3.7	Drooped Spoiler Panel (DSP) concept schematic, including geometrical definitions . . . . .	43
3.8	DSP holding structure (a) 3D actual component and (b) 3D drawing . . . . .	44
3.9	Upper surface plate attached on the X-400 wing-flap scale model . . . . .	44
3.10	Transparent quadrant window on the lower circular disc of the LTT's test section (a) for visibility purposes and (b) Upper circular disc covered with duct tape and black painted configuration to avoid reflections . . . . .	46
3.11	2D lenses placement schematic in front of the laser head positioned from left to right . . . . .	46
3.12	2D schematic overview of the PIV set-up in top view, including geometrical information . . . . .	47
3.13	Camera placement below the wind tunnel test section . . . . .	48

3.14	Woollen tufts placed on the upper surface of the X-400 wing-flap configuration . . . . .	49
3.15	Paraffin oil applied on the Fowler flap of the X-400 configuration . . . . .	49
3.16	2D schematic of the probe set-up and measurement points location for total pressure probe measurements at $\alpha = 0^\circ$ , $\delta_f = 50^\circ$ and DSP1 (at $15^\circ$ ) attached . . . . .	51
3.17	2D schematic of the probe set-up and measurement points location for total pressure probe measurements at $\alpha = 6^\circ - 8^\circ$ , $\delta_f = 50^\circ$ and DSP1 (at $15^\circ$ ) attached . . . . .	52
3.18	Vortex generators schematic and picture, used on the main wing of the X-400 wing-flap model configuration . . . . .	53
3.19	Vortex generators placement on the X-400 wing-flap model configuration with respect to the drooped spoiler panel (DSP1) . . . . .	54
3.20	Schematic of DSP1, with 2 and 4 mm holes on it's inclined panel, including geometrical information . . . . .	54
3.21	X-400 with carborundum roughness placed at the bottom side of the main wing . . . . .	55
3.22	Flow visualisation using tufts (a) at $\alpha = 15^\circ$ for CWC and (b) Attached flow observed at $\alpha = 8^\circ$ with DSP1 attached on . . . . .	57
3.23	Flow features at $\alpha = 2^\circ$ without DSP (a) and with DSP (b) at $\alpha = 5^\circ$ . . . . .	58
3.24	Flow features at $\alpha = 10^\circ$ with DSP attached on the main wing of the X-400 model . . . . .	58
3.25	Wake rake placed behind the X-400 configuration in the LTT test section . . . . .	59
3.26	Wing (left) and flap (right) $C_p$ -distribution plots for CWC at $Re = 1.6 \cdot 10^6$ with $\delta_f = 50^\circ$ , $x_{overlap} = 0\%$ and $y_{gap} = 3.7\%$ . . . . .	61
3.27	Wing (left) and flap (right) $C_p$ -distribution plots for DSP1 at $Re = 1.6 \cdot 10^6$ with $\delta_f = 50^\circ$ , $x_{overlap} = 0\%$ and $y_{gap} = 3.7\%$ . . . . .	62
3.28	Wing (left) and flap (right) $C_p$ -distribution plots for DSP2 at $Re = 1.6 \cdot 10^6$ with $\delta_f = 50^\circ$ , $x_{overlap} = 0\%$ and $y_{gap} = 3.7\%$ . . . . .	63
3.29	Wing (left) and flap (right) $C_p$ -distribution plots for DSP4 at $Re = 1.6 \cdot 10^6$ with $\delta_f = 50^\circ$ , $x_{overlap} = 0\%$ and $y_{gap} = 3.7\%$ . . . . .	64
3.30	$C_L$ (a) and $C_D$ (b) vs. Angle of Attack (AoA) with (CWC) and without (DSP's) flow control at $Re = 1.6 \cdot 10^6$ with $\delta_f = 50^\circ$ , $x_{overlap} = 0\%$ and $y_{gap} = 3.7\%$ . . . . .	65
3.31	$C_L$ (left) and $C_D$ (right) vs. Angle of Attack (AoA) for CWC (upper) and DSP1 (lower) cases, for different Reynolds numbers (Re) with $\delta_f = 50^\circ$ , $x_{overlap} = 0\%$ and $y_{gap} = 3.7\%$ . . . . .	67
3.32	Wing (left) and flap (right) $C_p$ -distribution plots for CWC for different Reynolds numbers (Re) at $\alpha = 6^\circ$ with $\delta_f = 50^\circ$ , $x_{overlap} = 0\%$ and $y_{gap} = 3.7\%$ . . . . .	68
3.33	Phenomena that affect the flow around a multi-element airfoil. Note the reversed flow region above the Fowler flap surface [33] . . . . .	68
3.34	Total pressure measurements at different stations across the X-400 model at $\alpha = 0^\circ$ , $Re = 1.6 \cdot 10^6$ with $\delta_f = 50^\circ$ , $x_{overlap} = 0\%$ and $y_{gap} = 3.7\%$ . . . . .	70
3.35	Total pressure measurements at different stations across the X-400 model at $\alpha = 6^\circ$ and $8^\circ$ , $Re = 1.6 \cdot 10^6$ with $\delta_f = 50^\circ$ , $x_{overlap} = 0\%$ and $y_{gap} = 3.7\%$ . . . . .	71
3.36	$C_l$ (a) and $C_d$ (b) vs. Angle of Attack (AoA) and Fowler flap $C_p$ -distribution plots at $\alpha = 4^\circ$ (c) and $\alpha = 6^\circ$ (d) for DSP1, DSP1(VG1) and DSP1(VG2) with $\delta_f = 50^\circ$ , $x_{overlap} = 0\%$ and $y_{gap} = 3.7\%$ . . . . .	72
3.37	$C_l$ (a) and $C_d$ (b) vs. Angle of Attack (AoA) for DSP1, DSP1(h1), DSP1(h2) and DSP1(VG2) with $\delta_f = 50^\circ$ , $x_{overlap} = 0\%$ and $y_{gap} = 3.7\%$ . . . . .	73
3.38	Post-processed image of the wing-flap configuration (a), showing the reflection due to the laser beam and (b) Mask out-layer as applied using Davis software 8.1 for clean wing configuration (CWC) . . . . .	74
3.39	Field of View (FOV) including the lines (in white) for the positions of the velocity profiles . . . . .	75

3.40	Total velocity field with streamlines for CWC at $\alpha = 0^\circ$ and $V_t = 40\text{m/s}$ . . . . .	76
3.41	Explanatory schematic, showing the Fowler flap region flow field as well as the interaction and merging of main wing wake, slot flow and flap's boundary layer . . . . .	76
3.42	Displacement, $\delta^*$ , and momentum, $\theta$ , thickness (a) plot and Wake velocity profiles (b) at 4 different stations for CWC at $\alpha = 0^\circ$ and $V_t = 40\text{m/s}$ . . . . .	77
3.43	Total velocity field with streamlines for CWC at $\alpha = 8^\circ$ and $V_t = 40\text{m/s}$ . . . . .	78
3.44	Displacement, $\delta^*$ , and momentum, $\theta$ , thickness (a) plot and Wake velocity profiles (b) at 4 different stations for CWC at $\alpha = 8^\circ$ and $V_t = 40\text{m/s}$ . . . . .	78
3.45	Post-processed image of the wing-flap configuration (a), showing the reflection due to the laser beam and (b) Mask out-layer as applied using Davis software 8.1 for drooped spoiler panel (DSP1) . . . . .	79
3.46	Total velocity field with streamlines for DSP1 at $\alpha = 0^\circ$ and $V_t = 40\text{m/s}$ . . . . .	80
3.47	Displacement, $\delta^*$ , and momentum, $\theta$ , thickness plot (a) and Wake velocity profiles (b) at 4 different stations for DSP1 at $\alpha = 0^\circ$ and $V_t = 40\text{m/s}$ . . . . .	81
3.48	Total velocity field with streamlines for DSP1 at $\alpha = 8^\circ$ and $V_t = 40\text{m/s}$ . . . . .	81
3.49	Displacement, $\delta^*$ , and momentum, $\theta$ , thickness (a) plot and Wake velocity profiles (b) at 4 different stations for DSP1 at $\alpha = 8^\circ$ and $V_t = 40\text{m/s}$ . . . . .	82
3.50	Total velocity field with streamlines for DSP1 with upper and lower surface roughness on the main wing, at $\alpha = 0^\circ$ and $V_t = 40\text{m/s}$ . . . . .	83
3.51	Displacement, $\delta^*$ , and momentum, $\theta$ , thickness (a) plot and Wake velocity profiles (b) at 4 different stations for DSP1 with upper and lower surface roughness on the main wing, at $\alpha = 0^\circ$ and $V_t = 40\text{m/s}$ . . . . .	84
3.52	Total velocity field with streamlines for DSP1 with upper and lower surface roughness on the main wing, at $\alpha = 8^\circ$ and $V_t = 40\text{m/s}$ . . . . .	84
3.53	Displacement, $\delta^*$ , and momentum, $\theta$ , thickness (a) plot and Wake velocity profiles (b) at 4 different stations for DSP1 with upper and lower surface roughness on the main wing, at $\alpha = 8^\circ$ and $V_t = 40\text{m/s}$ . . . . .	85
4.1	Schematic overview of the M-tunnel, used for the second experimental campaign [22]	89
4.2	3D wind-tunnel set-up schematic, including test section of the M-tunnel, diffuser walls and support table . . . . .	89
4.3	Final plexiglass flat plate drawing with rounded leading edge and tapered trailing edge including geometrical information . . . . .	90
4.4	Carborundum grains applied on the flat plate's surface, close to the rounded leading edge region . . . . .	91
4.5	Schematic of the diffuser diverging and straight wall sections with pressure taps on blocks No. 2, 4, 6 and 8 measuring from left to right, including geometrical information . . . . .	92
4.6	Diffuser diverging wall with woollen tufts attached on it's surface . . . . .	93
4.7	Schematic of the screen placed at the end of the diffuser section including geometrical information . . . . .	93
4.8	Schematic of the screen placed at the end of the diffuser section including geometrical information . . . . .	94
4.9	Schematic diagram of pressure tap tube connections . . . . .	95
4.10	Scanning valve rear view with total pressure tubes connected, including explanations of individual parts . . . . .	96
4.11	Probe traverse system picture, including explanations of individual parts . . . . .	96
4.12	Final camera placement for PIV tests, including explanations of individual parts . . . . .	97

4.13	Schematic of the PIV set-up in top view including geometrical information and explanations of individual parts . . . . .	98
4.14	Laser holding structure (a) with laser attached on it and the lenses placed in front of it's head and (b) Alignment process of the laser beam through the screen slot . . . . .	99
4.15	Coordinate system used for boundary layer measurements . . . . .	100
4.16	Schematic of the flat plate positions where boundary layer total pressure measurements carried out, including geometrical information . . . . .	101
4.17	Schematic of the positions where wake total pressure measurements carried out with respect to the flat plate, including geometrical information . . . . .	103
4.18	PIV measurement positions schematic . . . . .	105
4.19	Woolen tuft behind flat plate at 12 m/s (a) showing no wake reversal and (b) at 22 m/s showing wake reversal . . . . .	106
4.20	Gauge pressure vs.streamwise distance (mm) in the diffuser, based on surface pressure tap measurements . . . . .	108
4.21	Flat plate total pressure boundary layer plots at points (a) Point 1 (-495 mm), (b) Point 2 (-412 mm), (c) Point 3 (-297 mm), (d) Point 4 (-193 mm), (e) Point 5 (-102 mm) and (f) Point 6 (-25 mm) . . . . .	109
4.22	Wake total pressure plots at points (a) Point 0 (30 mm), (b) Point 1 (100 mm), (c) Point 2 (132 mm) and (d) Point 3 (222 mm) . . . . .	110
4.22	Wake total pressure plots at points (e) Point 4 (265 mm), (f) Point 5 (320 mm), (g) Point 6 (425 mm), (h) Point 7 (520 mm) and (i) Point 8 (639 mm) . . . . .	111
4.23	Wake reversal width vs. downstream distance from trailing edge . . . . .	112
4.24	Total velocity (a) field with streamlines, (b) U-component velocity field, (c) V-component velocity field and (d) Displacement and Momentum loss thickness for FOV 1 and $V_t = 5.1\text{m/s}$ . . . . .	115
4.24	Wake velocity profiles (e) and Velocity deficit study (f) for FOV 1 and $V_t = 5.1\text{m/s}$	116
4.25	Displacement and momentum thickness for flat plate and wake . . . . .	117
4.26	Total velocity (a) field with streamlines, (b) U-component velocity field, (c) V-component velocity field and (d) Displacement and Momentum loss thickness for FOV 1 and $V_t = 14.1\text{m/s}$ . . . . .	118
4.26	Wake velocity profiles (e) and Velocity deficit study (f) for FOV 1 and $V_t = 14.1\text{m/s}$	119
4.27	Total velocity field with streamlines (a) and U-component velocity field (b) for FOV 1 and $V_t = 21.0\text{m/s}$ . . . . .	120
4.27	V-component velocity field (c), Displacement and Momentum loss thickness (d), Wake velocity profiles (e) and Velocity deficit study (f) for FOV 1 and $V_t = 21.0\text{m/s}$	121
4.28	Flow moving to a region of increasing pressure . . . . .	122
4.29	$\delta^*$ , (a) $C_p$ (b) vs. streamwise distance (mm) plots for FOV 1 and $V_t = 21.0\text{m/s}$ . . . . .	123
4.29	$\frac{dC_p}{dx}$ vs. streamwise distance (mm) plot (c) for FOV 1 and $V_t = 21.0\text{m/s}$ . . . . .	124
5.1	NACA 0012 study plots where (a) NACA 0012 shape, (b) $C_l$ vs. $\alpha$ , (c) $C_d$ vs. $\alpha$ , (d) $C_p$ -distribution plot at $\alpha = 4^\circ$ , (e) $C_p$ -distribution plot at $\alpha = 10^\circ$ , (f) $C_p$ -distribution plot at $\alpha = 15^\circ$ . . . . .	133
5.2	NACA 4412 study plots where (a) NACA 4412 shape, (b) $C_l$ vs. $\alpha$ , (c) $C_d$ vs. $\alpha$ , (d) $C_p$ -distribution plot at $\alpha = 3^\circ$ , (e) $C_p$ -distribution plot at $\alpha = 7^\circ$ , (f) $C_p$ -distribution plot at $\alpha = 10^\circ$ . . . . .	134
5.3	NACA 64 <sub>2</sub> 10 study plots where (a) NACA 64 <sub>2</sub> 10 shape, (b) $C_l$ vs. $\alpha$ , $C_d$ vs. $\alpha$ , (d) $C_p$ -distribution plot at $\alpha = 3^\circ$ , (e) $C_p$ -distribution plot at $\alpha = 7^\circ$ , (f) $C_p$ -distribution plot at $\alpha = 11^\circ$ . . . . .	135
5.4	2D X-400 wing-flap model configuration at (a) $\delta_f = 0^\circ$ and (b) $\delta_f = 50^\circ$ . . . . .	136

5.5	(a) $C_l$ vs. $\alpha$ , (b) $C_d$ vs. $\alpha$ , (c) $C_m$ vs. $\alpha$ , (d) $C_l$ vs. $C_d$ , (e) $C_p$ -distribution plot at $\alpha = 10^\circ$ for <b>Case 1</b> , (f) $C_p$ -distribution plot at $\alpha = 3^\circ$ for <b>Case 2</b> for X-400 wing-flap configuration at $\delta_f = 40^\circ$ . . . . .	140
5.6	MSES simulation results at flap angle of $\delta_f = 50^\circ$ . . . . .	141
A.1	The X-400 wing-flap configuration model positioned in the LTT. The model was set-up vertically to allow for angle of attack, $\alpha$ , adjustments. On the left (a), the side view is shown which corresponds to the upper surface (suction side) of the airfoil i.e. the main element and the deflected flap. On the right (b), the front view of the airfoil is shown. . . . .	152
A.2	The X-400 wing-flap configuration model positioned in the LTT with DSP attached. On the left (a), the upper surface plate is attached on the trailing edge of the X-400 main wing model. Geometrical details are explained in text. On the right (b), the drooped spoiler panel (DSP) device is attached on the wing-flap model configuration. . . . .	152
A.3	Marked lines on the bottom wall disc of the LTT test section, used to set-up the Fowler flap angle, $\delta_f$ . . . . .	153
A.4	Pressure scanner connected with tubes from surface pressure taps on the X-400 wing-flap configuration model . . . . .	154
A.5	Schematic overview of a 2C-PIV set-up [25] . . . . .	155
A.6	Image windowing and discrete cross-correlation map [28] . . . . .	155
A.7	Relative particle motion [18] . . . . .	156
A.8	Distribution of the light intensity scattered by a $1 \mu\text{m}$ oil droplet particle in air [25] . . . . .	157
A.9	Effect of particle image diameter for windowing. (a) Pixel locking and (b) too large particle diameter images [28] . . . . .	159
A.10	Droplet size distribution (left) [taken from the SAFEX fog generator users guide]. Seeding knob position (right) [28] . . . . .	160
A.11	Actual (3D) seeding generator image and it's position with respect to wind-tunnel test section . . . . .	160
A.12	Quantel Evergreen laser head [28] . . . . .	161
A.13	LaVision Imager Intense CCD camera [28] . . . . .	162
A.14	Laser structure with laser attached on it (a) Back view and (b) Side view . . . . .	163
A.15	Calibration image showing millimetre paper above Fowler flap (a) and Post-processed image from Davis software (b) for CWC . . . . .	164
A.16	Tufts flow visualisation with DSP1 at an angle of attack of (a) $0^\circ$ , (b) $2^\circ$ , (c) $5^\circ$ , (d) $8^\circ$ , (e) $10^\circ$ and (f) $15^\circ$ at $Re = 1.6 \cdot 10^6$ with $\delta_f = 50^\circ$ , $x_{overlap} = 0\%$ and $y_{gap} = 3.7\%$ . . . . .	165
A.17	Oil flow visualisation with DSP1 at an angle of attack of (a) $0^\circ$ , (b) $2^\circ$ , (c) $5^\circ$ , (d) $8^\circ$ , (e) $10^\circ$ and (f) $15^\circ$ at $Re = 1.6 \cdot 10^6$ with $\delta_f = 50^\circ$ , $x_{overlap} = 0\%$ and $y_{gap} = 3.7\%$ . . . . .	166
A.18	Boundary layer formation across a flat plate, where <b>Point 0</b> is on the surface of the flat plate and <b>Point 1</b> on the edge of the boundary layer . . . . .	167
A.19	(a) Total velocity field, (b) Total velocity field with streamlines, (c) Displacement, $\delta^*$ , and momentum, $\theta$ , thickness plot and (d) Wake velocity profiles at 4 different stations for CWC at $\alpha = 6^\circ$ and $V_t = 40\text{m/s}$ . . . . .	169
A.20	(a) Total velocity field, (b) Total velocity field with streamlines, (c) Displacement, $\delta^*$ , and momentum, $\theta$ , thickness plot and (d) Wake velocity profiles at 4 different stations for DSP1 at $\alpha = 6^\circ$ and $V_t = 40\text{m/s}$ . . . . .	170

A.21	(a) Total velocity field, (b) Total velocity field with streamlines, (c) Displacement, $\delta^*$ , and momentum, $\theta$ , thickness plot and (d) Wake velocity profiles at 4 different stations for DSP1 with upper and lower surface roughness on the main wing at $\alpha = 6^\circ$ and $V_t = 40\text{m/s}$ . . . . .	171
B.1	Plexiglass flat plate (a) during manufacturing process and (b) Plexiglass flat plate's placement in the wind-tunnel-diffuser set-up, including explanations of key features	173
B.2	Diffuser side-view (a) including explanations of various parts and (b) Final diffuser set-up prior to M-tunnel wind-tunnel testing . . . . .	173
B.3	Total pressure probe with flat nose (a) used for boundary layer measurements on the flat plate's surface and (b) Total pressure probe used for wake measurements behind the trailing edge of the flat plate . . . . .	174
B.4	CCD camera (a) position and holding structure and (b) Laser position with lenses placed in front of it's head as used during PIV experiments . . . . .	174
B.5	(a) Total velocity field with streamlines, (b) U-component velocity field, (c) Displacement and momentum loss thickness and (d) Wake velocity profiles for FOV 2 and $V_t = 5.1\text{m/s}$ . . . . .	177
B.6	(a) Total velocity field with streamlines, (b) U-component velocity field, (c) Displacement and Momentum loss thickness and (d) Wake velocity profiles for FOV 2 and $V_t = 14.1\text{m/s}$ . . . . .	178
B.7	(a) Total velocity field with streamlines, (b) U-component velocity field, (c) Displacement and Momentum loss thickness and (d) Wake velocity profiles for FOV 2 and $V_t = 21.0\text{m/s}$ . . . . .	179
B.8	(a) Total velocity field with streamlines, (b) U-component velocity field, (c) Displacement and Momentum loss thickness and (d) Wake velocity profiles for FOV 3 and $V_t = 5.1\text{m/s}$ . . . . .	180
B.9	(a) Total velocity field with streamlines, (b) U-component velocity field, (c) Displacement and Momentum loss thickness and (d) Wake velocity profiles for FOV 3 and $V_t = 14.1\text{m/s}$ . . . . .	181
B.10	(a) Total velocity field with streamlines, (b) U-component velocity field, (c) Displacement and Momentum loss thickness and (d) Wake velocity profiles for FOV 3 and $V_t = 21.0\text{m/s}$ . . . . .	182
C.1	NACA 0012 $C_p$ -distribution plots at (a) $\alpha = 0^\circ$ , (b) $\alpha = 2^\circ$ , (c) $\alpha = 6^\circ$ , (d) $\alpha = 9^\circ$ , (e) $\alpha = 12^\circ$ , (f) $\alpha = 16^\circ$ . . . . .	186
C.2	NACA 4412 $C_p$ -distribution plots at (a) $\alpha = 0^\circ$ , (b) $\alpha = 1^\circ$ , (c) $\alpha = 3^\circ$ , (d) $\alpha = 6^\circ$ , (e) $\alpha = 9^\circ$ , (f) $\alpha = 12^\circ$ . . . . .	187
C.3	NACA 64210 $C_p$ -distribution plots at (a) $\alpha = 0^\circ$ , (b) $\alpha = 2^\circ$ , (c) $\alpha = 4^\circ$ , (d) $\alpha = 6^\circ$ , (e) $\alpha = 8^\circ$ , (f) $\alpha = 11^\circ$ . . . . .	188
C.4	X-400 wing-flap configuration at <b>Case 1</b> $C_p$ -distribution plots at (a) $\alpha = 0^\circ$ , (b) $\alpha = 2^\circ$ , (c) $\alpha = 4^\circ$ , (d) $\alpha = 6^\circ$ , (e) $\alpha = 7^\circ$ , (f) $\alpha = 10^\circ$ . . . . .	189
C.5	X-400 wing-flap configuration at <b>Case 2</b> $C_p$ -distribution plots at (a) $\alpha = 0^\circ$ , (b) $\alpha = 1^\circ$ , (c) $\alpha = 3^\circ$ , (d) $\alpha = 4^\circ$ , (e) $\alpha = 5^\circ$ , (f) $\alpha = 6^\circ$ . . . . .	190
C.6	X-400 wing-flap configuration at <b>Case 3</b> $C_p$ -distribution plots at (a) $\alpha = 0^\circ$ , (b) $\alpha = 2^\circ$ , (c) $\alpha = 3^\circ$ , (d) $\alpha = 5^\circ$ , (e) $\alpha = 6^\circ$ , (f) $\alpha = 9^\circ$ . . . . .	191

# List of Tables

2.1	Widely used types of leading edge and trailing edge high lift devices . . . . .	13
3.1	Drooped Spoiler Panel (DSP) geometrical definitions . . . . .	43
3.2	X-400 Wing-Flap Model Settings as set for pressure measurement and PIV experiments . . . . .	45
3.3	Test matrix for flow visualisation tests (woollen tufts and oil flow) . . . . .	50
3.4	Test matrix for surface pressure tap measurements . . . . .	50
3.5	Test matrix (1) for pressure measurements at $\alpha = 0^\circ$ , $\delta_f = 50^\circ$ and DSP1 (at $15^\circ$ ) attached . . . . .	52
3.6	Test matrix (2) for pressure measurements at $\alpha = 6^\circ - 8^\circ$ , $\delta_f = 50^\circ$ and DSP1 (at $15^\circ$ ) attached . . . . .	53
3.7	Test Matrix for PIV experiments . . . . .	56
4.1	Plexiglass flat plate geometrical definitions . . . . .	89
4.2	Woollen tufts flow visualisation test matrix . . . . .	99
4.3	Diffuser surface static pressure measurements test matrix . . . . .	100
4.4	Boundary layer total pressure measurements test matrix . . . . .	101
4.5	Wake total pressure measurements test matrix . . . . .	102
4.6	PIV Test Matrix . . . . .	104
4.7	Surface static pressure measurements . . . . .	107
4.8	Statistical data with respect to wake reversal size . . . . .	112
5.1	MSES validation study matrix for Linux version . . . . .	131
5.2	X-400 wing-flap model setting parameters used for MSES calculations . . . . .	136
5.3	Simulation matrix using X-400 wing-flap configuration at $\delta_f = 40^\circ$ , including settings used and the results of these computations . . . . .	138
5.4	X-400 wing-flap configuration MSES simulation result at $\delta_f = 50^\circ$ . . . . .	141
A.1	PIV Davis settings used for acquisition and post-processing procedures . . . . .	164
B.1	Boundary layer total pressure measurement data for all points . . . . .	175
B.2	Wake total pressure measurement data for all points . . . . .	176
B.3	PIV Davis settings used for acquisition and post-processing procedures . . . . .	176

# Nomenclature

## Greek Letters

Symbol	Description	Units
$\alpha$	Geometric angle of attack	[°]
$\gamma$	Ratio of specific heats	[-]
$\delta$	Boundary Layer thickness	[mm]
$\delta^*$	Displacement thickness	[mm]
$\delta_f$	Flap deflection angle	[°]
$\Delta$	Difference	[-]
$\Delta_t$	Time difference	[s]
$\theta$	Momentum loss thickness	[mm]
$\theta_{\text{DSP}}$	Drooped spoiler panel deflection angle	[°]
$\lambda$	Wavelength	[mm]
$\mu$	Dynamic viscosity	[kg/ms]
$\nu$	Kinematic viscosity	[m <sup>2</sup> /s]
$\xi$	Length coordinate	[mm]
$\pi$	Mathematical constant	[-]
$\rho$	Density	[kg/m <sup>3</sup> ]

## Latin Symbols

Symbol	Description	Units
A	Area	[m <sup>2</sup> ]
c	Chord	[mm]
$C_d$	2D Drag coefficient	[-]
$C_f$	Skin friction coefficient	[-]
$C_l$	2D Lift coefficient	[-]
$C_{l_{\text{design}}}$	2D Design lift coefficient	[-]
$C_{l_{\text{max}}}$	2D Maximum lift coefficient	[-]
$C_L$	3D Lift coefficient	[-]
$C_D$	3D Drag coefficient	[-]
$C_\mu$	Momentum coefficient	[-]
$\frac{C_p}{C_p}$	Pressure coefficient	[-]
$\frac{C_p}{C_p}$	Canonical pressure coefficient	[-]

$d$	Diameter	[mm]
$d_{\text{diff}}$	Diffraction diameter	[mm]
$d_i$	Image distance	[mm]
$d_o$	Object distance	[mm]
$d_p$	Particle diameter	[mm]
$d_z$	Depth of field	[mm]
$D$	Drag force	[N]
$D$	Aperture diameter	[mm]
$f$	Focal length	[mm]
$f_{\#}$	Aperture number	[-]
$h$	Height	[mm]
$h_o$	Total enthalpy	[J]
$H$	Shape factor	[-]
$k$	Critical roughness height	[mm]
$l$	length	[mm]
$l_s$	Slot length	[mm]
$L$	Lift force	[N]
$\dot{m}$	Mass flow	[kg/s]
$M$	Image magnification	[mm]
$Ma$	Mach number	[-]
$N$	Number of samples	[-]
$N$	Number of pictures	[-]
$\hat{n}$	Unit normal	[-]
$p$	Pressure	[N/m <sup>2</sup> ]
$P_t$	Total pressure	[N/m <sup>2</sup> ]
$P_s$	Static pressure	[N/m <sup>2</sup> ]
$Pr$	Prandtl number	[-]
$Q$	Volumetric flow rate	[m <sup>3</sup> /s]
$q$	Dynamic pressure	[N/m <sup>2</sup> ]
$Re$	Reynolds number	[-]
$t$	Time	[s]
$t_s$	Slot thickness	[mm]
$T$	Temperature	[K]
$u$	X-component velocity	[m/s]
$U_e$	Free-stream velocity	[m/s]
$U_f$	Fluid velocity vector	[m/s]
$U_p$	Particle velocity	[m/s]
$U_s$	Slipping velocity	[m/s]
$U_f$	Fluid velocity vector	[m/s]
$v$	Y-component velocity	[m/s]
$V_t$	Wind tunnel velocity	[m/s]
$w$	Width	[mm]
$x$	Length coordinate	[mm]
$x_{\text{overlap}}$	Overlap length	[%]
$y$	Length coordinate	[mm]
$z$	Length coordinate	[mm]

## Subscripts

Symbol	Description
d	Design
e	Free-stream
f	Friction
f	Fluid
g	Gap
i	Image
k	Critical roughness height
l	Lift
max	Maximum
n	Normal
o	Object
p	Particle
p	Pressure
s	Static
s	Slot
t	Time
t	Total
t	Tunnel
z	Coordinate length
$\mu$	Momentum
$\infty$	Free-stream

## Abbreviations

Symbol	Description
AoA	Angle of Attack
AVG	Active Vortex Generator
CAD	Computer Aided Design
CCD	Charge Couple Device
CFD	Computational Fluid Dynamics
CMOS	Complementary Metal Oxide Semiconductor
CNC	Computer Numerical Control
CWC	Clean Wing Configuration
DC	Direct Current
DNS	Direct Numerical Simulation
DNW	German-Dutch Wind Tunnels
DSP	Drooped Spoiler Panel
DSP(VG)	Drooped Spoiler Panel with Vortex Generators
DSP(h)	Drooped Spoiler Panel with Holes
ETW	European Transonic Wind Tunnel
FFDA	Free Flying Delta Array
FOV	Field of View
HSL	High Speed Laboratory

HWA	Hot Wire Anemometry
IBL	Integral Boundary Layer
LDA	Laser Doppler Anemometry
LDV	Laser Doppler Velocimetry
LE	Leading Edge
LHS	Left Hand Side
LTT	Low Turbulence Tunnel
NACA	National Advisory Committee for Aeronautics
NASA	National Aeronautics and Space Administration
NLF	Natural Laminar Flow
NLR	National Aerospace Laboratory
PIV	Particle Image Velocimetry
PT	Pressure tap
RANS	Reynolds Averaged Navier Stokes
SESF	Segmented Extension Slotted Flap
RANS	Reynolds Averaged Navier Stokes
RHS	Right Hand Side
TC	Test Case
TE	Trailing Edge
VG	Vortex Generator
WT	Wind Tunnel
WTT	Wind Tunnel Testing
$\mu$ PIV	Macroscopic Particle Image Velocimetry

# Chapter 1

## Introduction

People around the world are taking to the skies in increasing numbers. Accommodating such growth in passengers, required new and more technologically advanced aircraft. As a result, over the last decades, the field of aviation has grown significantly. This is very clear by looking the evolution of the aircraft for the last forty years. Most of us could notice important changes on the external shape, size and design of the aircrafts, which are used daily by airliners to travel around the globe. Nevertheless, the key matter, is not that aircrafts are changing and keep evolving as the time passes by, but the reason of such a great research and development in this field.

Nowadays, most people are referring to sustainability, friendly-environment products and services. In brief, a huge effort is carried out by international companies, research centres and universities working closely to eliminate the emissions and contribute to a "green" environment. The reason behind this initiative is very simple and clear; a "greener" future would be the only solution to ensure a healthy and safe living for future generations of human kind. This is why aviation technology is continuously progressing and developing in various sections as advanced composite materials, efficient propulsion units and flight controls, in order to achieve this common goal and consequently minimise the impact flying has on the global environment. One of the most growing fields in this sector is also aerodynamics. Aerodynamics, is a field that while the problems are far from being solved, our capabilities have advanced tremendously. Therefore, efforts are taken in order to investigate how aircrafts could fly efficiently, but also with great performance figures. With this in mind, aerodynamicists are working for years, in order to come up with innovative ways to quiet airplanes, reduce air pollution and burn fuel more efficiently, by the use of lightweight composite structures, ultra-high bypass turbofans and the increase of laminar flow over aircraft surfaces, which could all be implemented on the next generation aircrafts. For more information on future solutions for green aviation, the reader is referred to [19].

The term lift should be familiar to most of the readers, and describes the force that keeps an aircraft flying, of course with the aid of the engines. However, the engines are responsible for emissions and hence environmental pollution. As a result, by taking aerodynamics into serious consideration, the use of the large engines, could be eliminated and consequently it's pollutant emissions too. This applies mainly for the "short" phases of flight envelope, namely, the take-off and landing procedures. That is why nowadays, aircrafts are using high lift devices, in order to increase their high lift capabilities, which are necessary during these two flight phases.

According to A. Smith, original flap development was motivated by three desired benefits [29]:

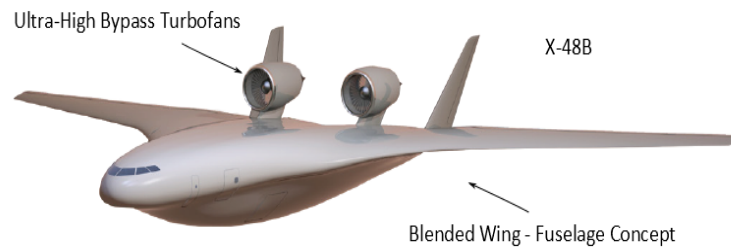


Figure 1.1: Future aircraft design that generates dramatic reductions in noise, emissions and fuel consumption could look like this hybrid wing body [19]

1. Slower flying speeds, hence shorter take-off and landing runs
2. Reduction of angle of attack near minimum flying speed
3. Reduction of the flap drag, in order to reduce thrust requirements and thus the noise

It should be understood that high lift systems are very important for the performance of modern aircrafts. The goal to fly efficiently made necessary the creation of more effective high lift devices. Each type of aircraft is designed and optimized for its own flight regime e.g. a low-speed commercial aircraft requires a different wing design with respect to the ones designed for a high-speed military aircraft. Nevertheless, the basic aerodynamic principles for generating high lift remain the same. Nowadays, the progression of multi-element airfoils has shown to develop towards a circular arc when the flaps and slats are maximum deflected. More lift could be created this way, resolving part of the problem, but still a significant part of the potential lift is lost, as the air flow can hardly follow the strong curvature dictated by the slat and flap deflections; eventually, the flow will separate at some point from the surface [9].

As the high lift systems keep evolving and pushed to their limits during the years, the importance of flow control methods became more vital and explored even more, in order to deal with flow separation situations. This is described by G.El Hak as well as in section 2.2 of this report. The types of flow control could be classified to passive and active. Each category has its own pros and cons and both were progressed during the last decades. Very interesting ideas came up through the years, with some of them used widely on high lift devices today. On the other hand, different ideas were tested but did never implemented for different reasons [12].

A growing interest in the past decade was realised in the field of passive flow control. The main reason is that requires no auxiliary power and no control loop. In the past, this resulted in the development of high lift systems which improved the lift performance by using slotted flaps. This enabled an aircraft to fly steeper during take-off and landing phases which directly reduced the area encountering air-traffic noise but also the time spent during this fuel consuming flight procedure. Moreover, during other critical flight conditions e.g. maximum and sustained turn rates, the benefits of such high lift systems were also numerous [9]. Furthermore, passive flow control is used due to the advantages it could offer. First of all, the cost of such devices would mostly be affordable for aircraft manufacturers. In addition, the lack of power mechanisms and

control loops, would reduce the weight of the devices, which is something that all the manufacturers would wish for. Relative to that, is the fact of a cheaper maintenance procedure, which of course would be preferred as it would also cost less for airliners choosing that. Of course, a lot more reasons could be presented, but these should be thought as the most important ones.

One of the ideas getting a lot of attention the last years with respect to passive flow control devices, was the Drooped Spoiler Panel concept [26, 27, 31, 36]. To improve the high lift characteristics, new spoiler and flap kinematics are currently investigated in various research programs like Clean-Sky [36]. In order to increase the low speed aerodynamic performance and reduce the complex flap kinematics and weight, the drooped spoiler panel, which is directly positioned in front of the flap, is allowed to have a downward deflection for particular high flap deflections. It's main purpose is the relieve of the large positive pressure gradient after the flap nose suction peak to prevent premature flow separation at large flap deflection angles up to  $50^\circ$ . As a result, the drag could be reduced and the lift of the whole configuration (wing-flap) could be increased significantly. Of course, this would result to lower speeds at landing phase of the flight and even shorter at take-off. A schematic of the drooped spoiler panel, is presented in Figure 1.2.

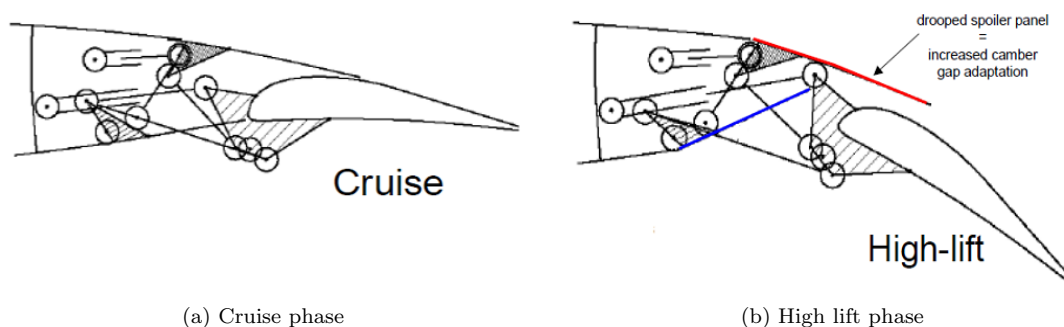


Figure 1.2: Drooped Spoiler Panel (DSP) working principal at (a) cruise and (b) high lift phase [26]

For this thesis work, the main objective was to determine the potential of a drooped spoiler panel as a passive high lift system to enhance the lift performance of a wing-Fowler flap configuration. The main focus was on separation control for the Fowler flap of a two-element airfoil, thus a relatively large flap deflection angle was selected for possible improvement. An experimental study of the drooped spoiler panel (DSP) was initiated and it's expected effect, was an increased effective camber of the airfoil with an associated increase in the lift coefficient. To perform this experimental research, the X-400 wing-flap configuration model investigated at a flap angle of  $\delta_f = 50^\circ$ , since the main objective of it's application was to reattach the flow in the area of a large adverse pressure gradient.

Several flow measurement techniques used through these tests, including detailed flow visualisation techniques on the surface flow over the model using the fluorescent oil technique and woolen tufts. Moreover, pressure measurement techniques including surface taps and probe measurements used, in order to get a more qualitative idea of the flow behaviour. Finally, particle image velocimetry (PIV) was carried out, to further validate the initial measurements and get an even clear view of flow phenomena in the area of interest. The first conclusions, after these tests were very positive, as the use of a drooped spoiler panel, lead to a fully attached flow. This

was a significant improvement over other techniques that used at Delft University of Technology in the past, which only led to a limited delay of flap stall. However, a disappointing effect was noticed during the pressure measurements showing that the overall lift value dropped considerably below the baseline case result. Despite the fact that the flow was fully attached over the full angle of attack range and the flap introduced a stronger downwash directly behind its trailing edge, the adverse pressure gradient was very strong that "wake bursting" or also called in literature "off-the-surface" separation occurred. This phenomenon, received limited attention in literature, is not very well understood until today. The overall circulation around the wing-flap model was considerably reduced due to the wide wake in which flow reversal takes place. For more information based on the results obtained, the reader is referred to section 3.4 of this report.

After careful consideration, it was decided to link the research objective to wake bursting and move back to literature study, but this time in order to find valuable information on wake flows and off-the-surface flow reversal. After extensive research in literature including some books but mainly published papers and reports [2, 6, 8, 12, 15, 29, 30, 33], the author realised that this field was much narrower than high lift aerodynamics and flow control. In terms of wake flows, the literature available was enough in order to give to the reader the knowledge available. However, most of the researchers asked for further study and results validation.

With respect to wake bursting, the literature was very limited. The published work found on the topic unfortunately was inadequate and even if this phenomenon was mentioned by some researchers in their works, the discussion on it or the experimental or computational work concentrated specifically on that was far from detailed. Most of the literature found included some very basic experimental work tried to obtain very accurate results for computational validation purposes. In addition, all of the papers were underlining the disagreement of experimental and computational results [8, 15, 29, 30, 33]. Hence, it was very clear that the amount of work on this field was not enough and this was a big boost as this work could be a big contribution to the field but on the other hand it was very difficult to proceed having very few information or knowledge of the phenomenon specifically. That is why in the last chapter of the literature study part of the report, there are not many results about wake bursting but mainly about wakes and experiments that other researchers have done which could be used in order to examine this phenomenon which even if it was noticed from 70's there was no-one so far trying to give some very deep insight to it and link it to the real practical case of high lift devices.

Thus, in this thesis work was tried to use most of this theoretical/fundamental work, found in literature and try to combine it with the practical case of wake bursting on high lift devices. Therefore, the plan was to proceed with simple configuration tests, as done in literature, and try to simulate this phenomenon in a much simpler configuration. This included flat plate-diffuser tests in a small open-return wind tunnel getting a significant amount of pressure, velocity and wake data using different measurement techniques including particle image velocimetry (PIV). All these data, then used in order to compare with the real configuration test cases, with the aim of giving some explanations and limits about this hardly detectable phenomenon.

Moreover, a computational study using MSES code was performed, in order to determine the possible agreement of experimental data with the ones obtained from computer simulations. The reason for choosing the MSES code, instead of any other CFD commercial package, was its user-friendly features but most importantly, the limited time needed to carry out multiple simulations, in order to get flow-field data for multi-element airfoils. A general overview of MSES code and the results of this computational study are presented in chapter 5.

Concluding, the structure of the remaining report will be presented. The next part in this report will be the background theory in chapter 2, including part of the literature study, performed during the beginning of this thesis work and used in order to present anything included in this report. After that, the experimental testing campaigns carried out, are presented, including information on the experimental apparatuses, set-up used, experimental procedures and finally the results obtained are discussed in chapters 3 and 4. Following that, the computational studies done using MSES code are presented in chapter 5. Then, the final conclusions, of all the findings will be presented with future work and recommendations in chapters 6 and 7 following this part. Finally, the bibliography and appendices with very useful data, could be found at the end of this report.

## Chapter 2

# Background Theory

In this chapter, the background theory as well as useful literature cases will be presented. Therefore, the chapter starts with a brief introduction on boundary layers. Then flow control and high lift aerodynamics are discussed and several literature cases are presented. Finally, relevant literature based on wake flows and wake flow reversal is introduced to the reader.

### 2.1 Boundary Layer

The boundary layer topic is very much known to anyone who has involved in aerodynamics, and as a result, only the very key points related to this work will be presented. Nowadays, most of the aerodynamicists are interested into the higher speed range flows or also called high-Reynolds number flows. For this particular case the flow has to be separated into two different regions. The first and most interesting one is the so-called boundary or viscous layer. The second one is the non-viscous or free-stream flow region. These are shown in Figure 2.1, the boundary layers and the external "frictionless" flow, schematically.

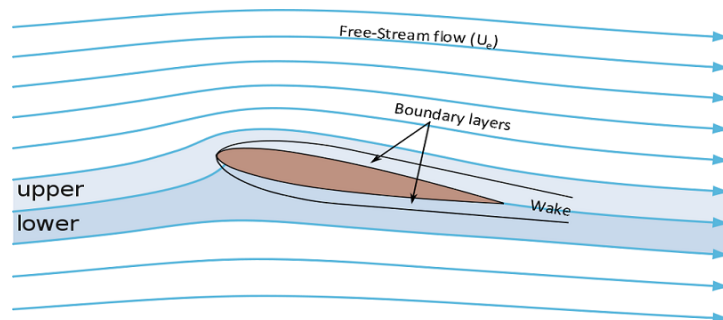


Figure 2.1: Potential free-stream flow and viscous boundary layer formed around a NACA 0012 airfoil, at moderate angle of attack [41]

Starting with the viscous boundary layer, where the velocity of the fluid particles is adjacent to the surface of the wall (where this layer is formed), it increases from a zero value on the wall to the value of the velocity in the outside region of the layer, usually called free-stream velocity,  $U_e$ . Again this is shown in Figure 2.2.

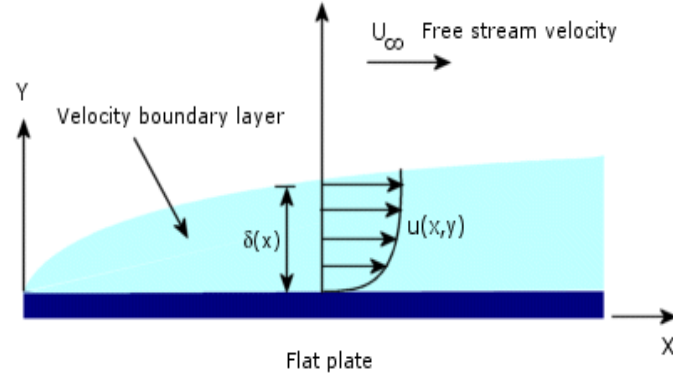


Figure 2.2: Boundary layer development on a flat plate [32]

Due to the resultant velocity gradients, inside the viscous boundary layer, the shear forces are quite large. However, outside the boundary layer, the velocity gradients become so small and as a result the shear stresses acting on a fluid element there, could be assumed as negligible. To get a deeper understanding of the boundary layer concept, it would be useful to present the equations for a two-dimensional incompressible flow in a Cartesian coordinate system. Note, that these equations are the ones solved by MSES code to perform computational simulations. The first equation to present is the differential form of the **continuity** equation.

$$\frac{du}{dx} + \frac{dv}{dy} = 0 \quad (2.1)$$

Then, the **momentum** equations are shown for the x and y axis respectively, where the x-coordinate is measured parallel to an airfoil's surface and the y-coordinate is measured perpendicular to it. Note that body forces are neglected.

$$\frac{du}{dt} + u \frac{du}{dx} + v \frac{du}{dy} = -\frac{1}{\rho} \frac{dp}{dx} + \nu \left( \frac{d^2u}{dx^2} + \frac{d^2u}{dy^2} \right) \quad (2.2)$$

$$\frac{dv}{dt} + u \frac{dv}{dx} + v \frac{dv}{dy} = -\frac{1}{\rho} \frac{dp}{dy} + \nu \left( \frac{d^2v}{dx^2} + \frac{d^2v}{dy^2} \right) \quad (2.3)$$

Where, u and v are the velocity components along x and y axis respectively.

Solving for the pressure gradients, using the momentum equations 2.2 and 2.3, one gets:

$$-\frac{dp}{dx} = \rho \frac{du}{dt} + \rho u \frac{du}{dx} + \rho v \frac{du}{dy} - \nu \left( \frac{d^2u}{dx^2} + \frac{d^2u}{dy^2} \right) \quad (2.4)$$

$$-\frac{dp}{dy} = \rho \frac{dv}{dt} + \rho u \frac{dv}{dx} + \rho v \frac{dv}{dy} - \nu \left( \frac{d^2v}{dx^2} + \frac{d^2v}{dy^2} \right) \quad (2.5)$$

From relation 2.4, the effect of pressure gradient on the velocity profile is apparent. When the pressure gradient decreases ( $\frac{dp}{dx} < 0$ ), the velocity profile is convex, as the velocity gradient is increasing ( $\frac{dU}{dx} > 0$ ). On the other hand, when the pressure gradient is increasing ( $\frac{dp}{dx} > 0$ ), the velocity profile is concave. This is due to the reduction of the velocity gradient ( $\frac{dU}{dx} < 0$ ). Finally, at the location of minimum pressure ( $\frac{dp}{dx} = 0$ ), the velocity profile is straight near the

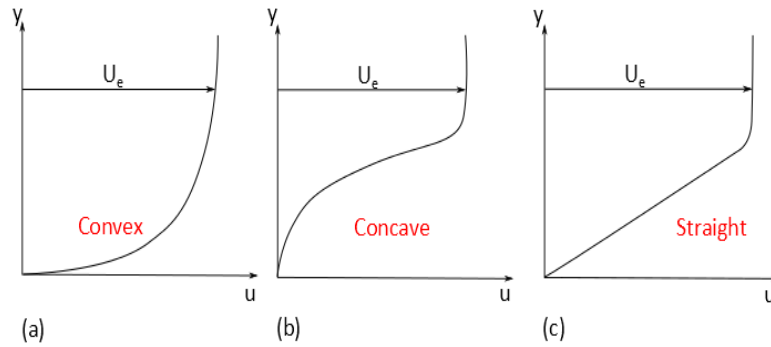


Figure 2.3: Possible velocity profiles depending on pressure gradient,  $\frac{dp}{dx}$  : (a) convex profile, (b) concave profile and (c) straight profile

wall, as the velocity gradient is also zero ( $\frac{dU}{dx} = 0$ ) [35]. This is shown with diagrams in Figure 2.3 .

Moreover, at the surface ( $y = 0$ ), velocity components,  $u$  and  $v$  are zero. Hence:

$$\frac{dp}{dx} = \mu \left( \frac{d^2u}{dy^2} \right)_{y=0} \quad (2.6)$$

Thus, a negative pressure gradient is more favourable than a positive pressure gradient. This has led to laminar flow airfoils. A favourable pressure gradient region is the zone where the flow moves from a region of higher pressure to a region of lower pressure. It's advantages are that prevents separation, slows down the rate of the boundary layer growth and delays the transition from laminar to turbulent flow. However, the last one is not always an advantage as will be seen later in this chapter. On the other hand, for the adverse pressure gradient region, the air flows from a region of lower pressure to a region of higher pressure. Briefly, one could say that when adverse pressure gradient exists flow separation is likely to follow. The reader might notice that the energy equation is missing. By limiting ourselves to incompressible flows, it is not necessary to include or to discuss about the energy equation [38]. Close to the wall, the normal component of the velocity vector is more or less compared to the streamwise component of velocity. Hence, one could state that ( $v \ll u$ ) and consequently, it could be deduced that:

$$\frac{dp}{dy} < \frac{dp}{dx} \quad (2.7)$$

As a result, the pressure gradient normal to the wall is thought as negligible.

$$\frac{dp}{dy} \approx 0 \quad (2.8)$$

From relation 2.8, since the pressure variation on the  $y$ -axis of the boundary layer is so small, the pressure distribution around an airfoil is principally that of the non-viscous flow, taking into account the displacement effect of the boundary layer. The boundary layer velocity distribution show asymptotic behaviour, therefore the boundary layer thickness is rather arbitrary. Two definitions are used frequently. The one is for the displacement thickness,  $\delta^*$  and momentum loss thickness,  $\theta$ . Both of these quantities used in the analysis of the results in both chapters 3 and 4. Displacement thickness is a measure of boundary layer thickness and is defined as the distance by which the boundary layer should be displaced to compensate for the reduction

in flow rate on account of boundary layer formation [4]. An improved pressure distribution may be obtained from the addition of the displacement thickness and the body contour. The displacement thickness,  $\delta^*$  is given by:

$$\delta^* = \int_0^{\infty} \left(1 - \frac{u}{U_e}\right) dy \quad (2.9)$$

Where  $U_e$ , is the free-stream velocity.

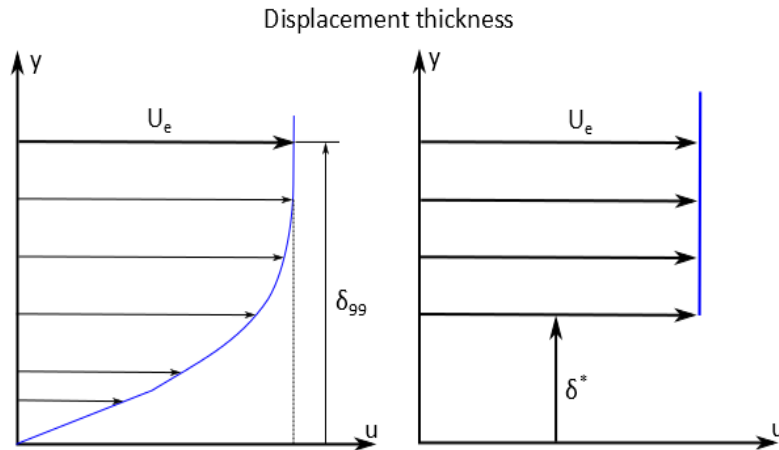


Figure 2.4: Displacement thickness,  $\delta^*$ , schematic

On the other hand, momentum thickness is a measure of the boundary layer thickness and is defined as the distance by which the boundary should be displaced to compensate for the reduction in momentum of the flowing fluid on account of boundary layer formation [4]. The momentum loss thickness, is directly related to the drag of the airfoil. The momentum loss thickness,  $\theta$ , is given by:

$$\theta = \int_0^{\infty} \frac{u}{U_e} \left(1 - \frac{u}{U_e}\right) dy \quad (2.10)$$

At this point, it would be very useful to discuss about the differences between the laminar and turbulent boundary layer and briefly discuss the transition process. To begin with the laminar boundary layer, the transverse exchange of momentum, takes place on a molecular scale. Due to this molecular movement, slower moving fluid particles from the lower layer of the fluid close to the wall are moving upwards to the upper layer slowing the particles there. On the other hand, when fast moving particles are moving downwards from the upper layer of the fluid to the lower one, they tend to accelerate the fluid particles there.

For the turbulent boundary layer, the transport of the fluid particles is not microscopic as for the laminar case, but macroscopic. Thus, in addition to the laminar shear stress, there is also a turbulent shear stress due to the momentum transport which is fairly large. The turbulent boundary layer is relatively thicker compared to the laminar boundary layer, but its velocity is also greater. This is explained by the faster-moving particles transported toward the wall and they produce higher velocities for the fluid particles closer to the surface. As a result, shear stresses are greater compared to the laminar case. What usually happens in practice, is the

transition of the laminar boundary layer to turbulent. The transition process in reality is not happening at a point, but takes place over a distance which sometimes can be as long as the laminar region [5]. This is shown schematically in Figure 2.5.

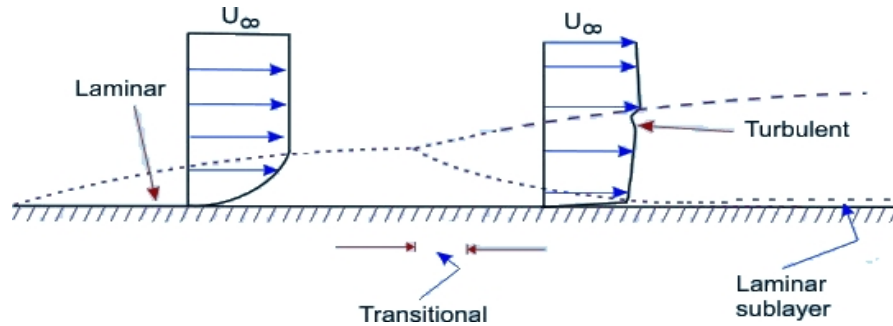


Figure 2.5: Transition process from laminar to turbulent boundary layer [20]

The last thing to discuss will be about flow separation which is closely linked to boundary layers and is vital for most practical applications. Using the simple example of the flat plate flow a viscous boundary layer will be formed around it and as the fluid's molecules contact the plate's wall or surface, the kinetic energy of the flow decays due to the wall friction also known as skin friction,  $C_f$ . Consequently the flow will decelerate. Additionally, as the flow "moves" downstream the pressure also increases. If this pressure increase will be large, then the mixing process will become too slow to keep the lower part of the layer moving. When this happens, the boundary layer will stop "following" the plate's surface and will eventually separate. At this point, the wall shear stresses become zero and air particles downstream of the separated region tend to move towards the lower pressure in the reverse direction to the main flow. This is presented schematically in Figure 2.6.

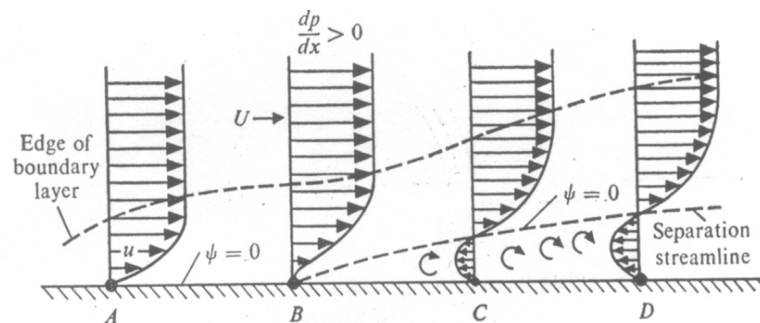


Figure 2.6: Flow development with flow separation taking on a flat plate [11]

In general, the boundary layer separation is linked to the thickening of the rotational flow region and ejection of vorticity. After the separation point, the shear layer either will pass over the region of the recirculating fluid and will re-attach to the body surface or will form a wake and will never re-attach to the body again. Separated flows could be classified into two different categories on the basis of the size of the separated region with respect to the body's dimension [6].

- If the size of separated region is reasonably small in comparison to the body and is bounded by a separation streamline connecting the points of separation and re-attachment, then this type of flow could be defined as simple separated flow.

- However, if the separated region has a long streamwise dimension in comparison to the body and extends to an infinitely long distance downstream, then this type of flow separation is called wake flow.

For this reason, in practical cases as flow over airfoils or bluff bodies, due to the large energy losses associated with boundary layer separation and formation of vortical flow, pressure drag is produced, which is the main form of drag [12]. Concluding about boundary layers, it should be noted that laminar boundary layer, can only withstand minor adverse pressure gradients without flow separation. On the other hand, the turbulent boundary layer, being excellent momentum conductor, is capable of overcoming much larger adverse pressure gradients without flow separation occurring. For further insight to boundary layer, the reader is referred to [4, 12].

## 2.2 High Lift Aerodynamics & Flow Control

In this section of the background theory, the key topics of this thesis work will be presented. The first one will be about high lift aerodynamics and the other one about flow control techniques. High lift is mainly used during the phases of take-off and landing phases of the flight. For transonic transports, the high lift system is crucial part of the whole configuration. In order to manage a realistic field performance while also obtaining efficient transonic performance, the high lift system should be incorporated into the design and it has to be fairly sophisticated as well.

The typical lift-coefficient variation with angle of attack for a single element airfoil is presented in Figure 2.7. The value of  $C_L$  varies linearly with  $\alpha$  for low-to-moderate angles of attack. This part is characterized by a smooth and mostly attached flow over the airfoil. However, angle of attack is increased, the flow tends to separate from the top surface of the airfoil, creating large wakes downstream. Consequently, when reaching a certain angle this leads to an abrupt decrease in lift and a large increase in drag. Prior to stall the maximum value of  $C_L$ , i.e.  $C_{L_{max}}$ , is reached which is one of the most important aspects of airfoil's performance. Relative to  $C_{L_{max}}$  is the stalling speed: the higher the  $C_{L_{max}}$  the lower the stalling speed [4].

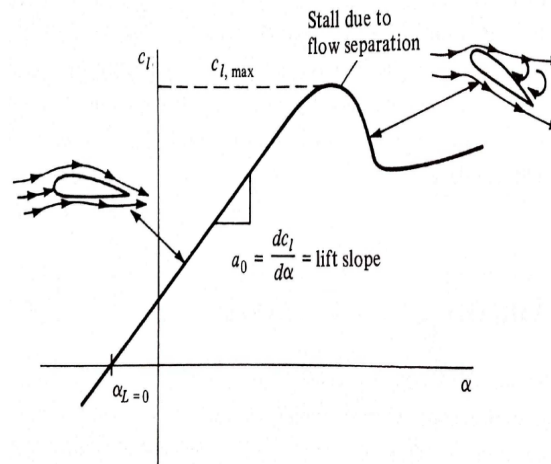
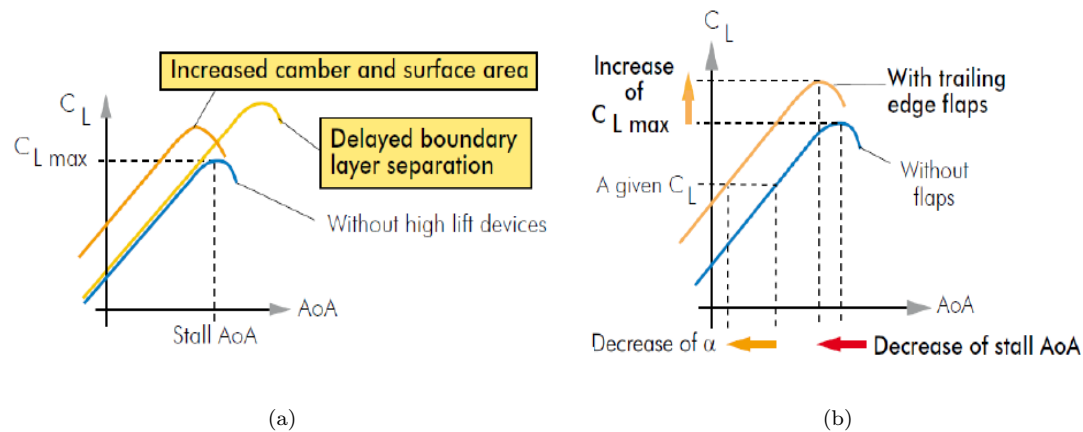


Figure 2.7: Lift coefficient variation with respect to angle of attack for a 2D airfoil [4]

To improve the lift performance of an airfoil, flaps are generally applied for lift enhancement in the aerospace industry. On current technology wings, as high lift devices, we mean the slats and the flaps. The idea behind the use of flaps is to increase the camber and the surface area of an airfoil, to improve its lift characteristics.

Deflection of a flap results in an increased lift and drag force at a given angle of attack but also increases  $C_{L_{max}}$  with respect to a clean airfoil with no flap deflection. Translated into the lift curve, a downwards deflection of the flap causes the curve to shift upwards and to the left of the lift values. In general, wings with deflected flaps stall at a lower angle of attack than wings without any flaps. This is due to the fact that the pressure gradients at  $C_{L_{max}}$  for both cases are roughly equal. Flaps also increase the downwash and the circulation relative to the airfoil, but also move the center of pressure ( $C_p$ ) rearwards creating a nose-down moment [9]. In Table 2.1, the most known leading and trailing edge devices are presented.

Figure 2.8: Effects of (a) high lift devices and (b) trailing edge flaps on  $C_L$  vs.  $\alpha$  [9]

Leading Edge Devices [LE]	Trailing Edge Devices [TE]
Increased leading edge radius	Plain flap
Centre hinged nose flap	Split flap
Surface hinged nose flap	Slotted flap
Krueger flap	<b>Fowler flap</b> (Thesis configuration)
Slotted Krueger	Double slotted flap (many variations)
Slat	Triple slotted flap(many variations)

Table 2.1: Widely used types of leading edge and trailing edge high lift devices

The advantages of a carefully designed high lift system are multiple. The most important, is the reduced fuel burn and consequently emissions. This was achieved by light systems and structures which enhanced the high lift performance of aircraft by reducing the number of moveable parts needed. In addition, due to the high lift devices, the lift values increased making the contribution of the engines considerably less during the phases of take-off and landing. Hence, the limited use of engine means less fuel burnt and of course less pollution to the environment. Moreover, the noise emissions were also reduced significantly, especially close to airport regions. Furthermore, increased maximum lift performance directly translates in enhanced safety and higher performance. For example an increase in  $L/D$  during take-off, could be used to allow for an increased climb rate. During the landing process it could lead to a reduced landing speed and consequently an increase in aircraft safety. To conclude, all these lead to the economic benefit of high lift contribution, with reduced costs and time for the passengers and airports operation [16].

The definition of flow control given by Flatt in 1961 states that: "Boundary layer control includes any mechanism or process through which the viscous boundary layer of a fluid flow is caused to behave differently than it normally would where the flow developing naturally along a smooth straight surface". Then L.Prandtl (1904) used active flow control of the boundary layer, in order to show the influence such a control method exerted on the flow pattern. He used suction to delay flow separation on the surface of a cylinder [12].

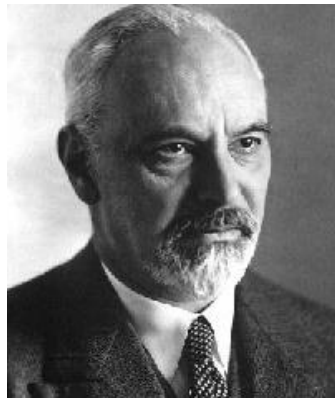


Figure 2.9: Ludwig Prandtl: The pioneer of boundary layer and flow control [23]

Flow control is very related to high lift aerodynamics and the potential benefits of efficient flow control range from saving money in fuel cost to achieving economically and environmentally competitive industrial processes involving fluid flows. Thus, the main gains of using flow control are namely:

1. Transition delay
2. Separation prevention
3. Drag reduction
4. Lift augmentation
5. Turbulence suppression
6. Noise abatement
7. Heat-mass transfer

Flow control could be applied passively or actively. Specifically, a control device could be passive, requiring no auxiliary power and no control loop. This category includes devices such as vortex generators, fences, strikes, etc. which are mounted to the main body but are not operated by an external energy source [12]. On the other hand, active flow control requires a control loop and is further divided into predetermined or reactive categories. The two most known types of active control will be briefly discussed.

**-Blowing:** Additive energy may be supplied to the surface fluid by injecting a foreign fluid in the neighbourhood of the wall. If the fluid is injecting parallel to the wall, the momentum of the shear layer is augmented whereas if it is injected normal to the wall the mixing rate is increased.

**-Suction:** This type of active flow control removes the decelerating flow particles in the neighbourhood of the wall and so prevents flow separation. For the prevention, it appears to be more effective to provide suction mainly in the region of adverse pressure gradient, where this phenomenon is more pronounced.

At this point part of the literature review of these two topics will be presented. To begin with Daniel Reckzeh, and his presentation at the KATnet II Conference in 2009, with title "*The Role of High-lift Aerodynamics; Design concepts and solutions for the future*" [26] is presented. The key points were the significant evolution of classical configurations, including new leading and trailing edge concepts, new passive flow control techniques and a lot of research on airframe source noise optimisation and wake vortex design. One remarkable example was the advanced trailing edge control surfaces. Something that should also be mentioned is the coupling of "smart configurations with flow control features". According to D.Reckzeh, this coupling could result in highly advanced high-lift systems, which would improve the overall aircraft configuration. Examples of this category are the laminar flow control wing, which could be accomplished either using passive or active flow control. In addition, the optimised interaction between engines and high lift systems, with ultimate target the best possible compromise between extreme high lift capabilities and system consequences. Finally smart high lift devices as the adaptive droop nose, blown super fowler flap and unslotted smart trailing edge including flow control were presented and are shown in Figure 2.10.

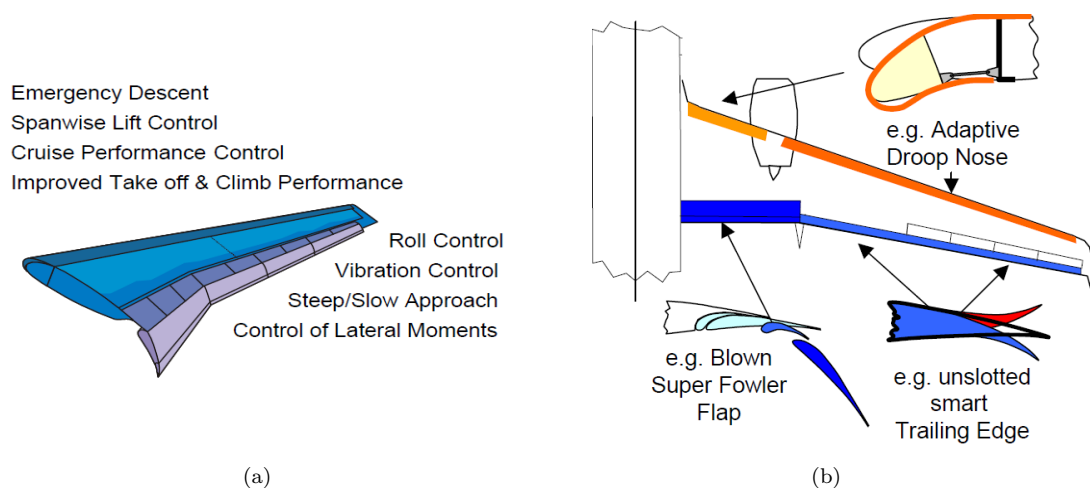


Figure 2.10: Schematics of (a) Advanced Trailing Edge Control Surfaces and (b) Smart High lift device concepts [26]

Moreover, in this presentation there were very remarkable ideas about novel low-noise high lift concepts and advanced high lift-systems using in particular active flow control on the main wing and high lift device. Furthermore, the variable camber trailing edge devices and drooped spoiler panel are discussed, in order to increase the low speed aerodynamic performance, and reduce the complex flap kinematics and weight. The last two projects were designed for implementation mainly on Fowler flap configurations and will be soon incorporated to the next generation aircraft according to the author [26].

The drooped spoiler panel concept is very similar to the thesis configuration used. However, in this case, it is used as a passive flow control, in order to delay or prevent flow separation of the Fowler flap at very high angles of attack. This will be discussed in chapter 3 in detail.

Another very interesting literature source about novel future high lift configurations was the one from T. Melin from Royal Institute of Technology in Sweden. This publication was focusing

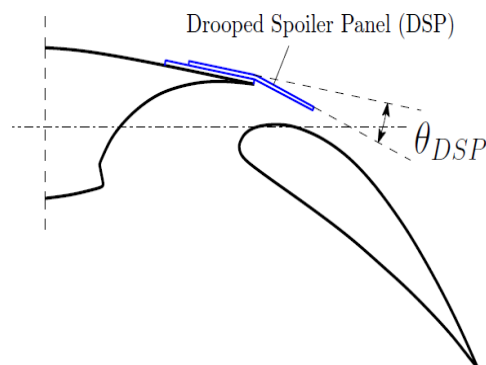


Figure 2.11: Schematic of drooped spoiler panel concept [36]

on the exploration of plenty innovative concepts for generating sufficient low speed aerodynamic performance for conventional transport aircraft [17]. All the concepts in this project, named **HELIX**, were assessed on three significant criteria:

1. Higher performance at same cost
2. Same performance at lower cost
3. Lower environmental impact at same cost

From this publication [17], one of the concepts was about multi-surface concepts. Specifically, this idea could be better demonstrated by the pop-up wing shown in Figure 2.12 and the hinged secondary wing concept. According to the author, this was a challenging project, as it had substantial differences from the conventional aircraft designs used nowadays. The secondary flying surface is buried in the primary wing structure during cruise flight. However, during the take-off and landing the surface is deployed above the primary surface in order to gain more lift. The main challenge of the scientists for this case was the best possible distance between these two wings and the optimum design of the secondary wing surface. For this purpose Euler and Navier-Stokes solvers have been used both in two (2D) and three (3D) dimensions, in order to calculate more than 20,000 solutions. Concluding, computational results showed that when the geometrical centre of the upper airfoil is close to the centre of the lower airfoil, the total coefficient of lift ( $C_L$ ) attained was the minimum one. However, placing the upper airfoil in a different horizontal position or by increasing the vertical distance between the two airfoils the values of lift coefficient increased. Nevertheless, the key result was that when the upper airfoil was used in close proximity to the secondary airfoil, as a slat or flap, then the values of  $C_L$  were the maximum. As a result, this concept did not offer any aerodynamic net gain [17].

Another interesting high lift project was involving the design and optimisation of the so called "Advanced Drooped Hinged Flap" [31]. Although the dropped hinge, or pivot, flap is not a new concept, it was investigated as an alternative high-lift device. The benefits of the dropped hinge flap promised to provide benefits in terms of weight, manufacture and maintenance costs. Furthermore, this could give the designer higher flexibility when designing for a steep approach

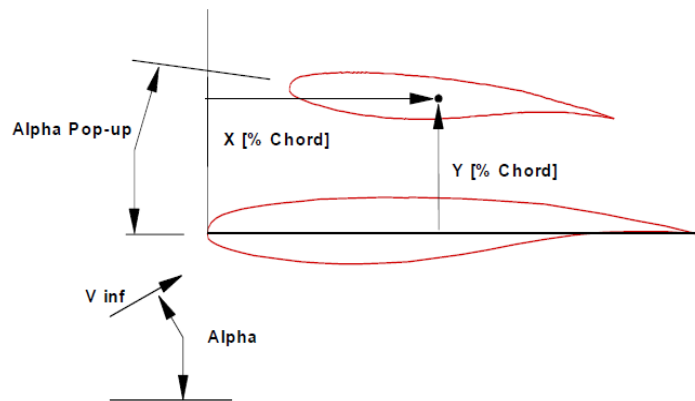


Figure 2.12: Pop-up secondary wing concept studied by Melin et al. [17] for HELIX project

capability. The advanced drooped hinged flap is shown schematically in Figure 2.13(b).

The main challenge during design of this high lift concept was the reduced freedom when designing appropriate take-off and landing settings in comparison to the well-known single slotted Fowler flap with track kinematics. The main problem according to the engineers was that due to the fact that the dropped hinge flap is deployed along a radius, the designer is only allowed to choose one target position in order to fully define the kinematics system. As it could be imagined, if an optimal take-off setting is chosen as the design criterion, then the landing configuration would be inferior and vice-versa. As a result, the biggest challenge of this concept was to find the best possible compromise between both cases.

To begin with, this concept was designed in order to improve the low speed performance of the main wing. In the beginning, two-dimensional (2D) calculations performed using panel methods for the high lift device, in addition to coupling of a 2-D method with a lifting surface scheme, in order to have a first estimate of the performance of the whole configuration. But then as the project was evolving more detailed 2D Navier-Stokes calculations used for the whole 3D high lift configuration, including most of the parts. However, in addition to CFD, low speed wind tunnel tests performed in the Airbus tunnels in Germany and UK for configuration evaluation and selection. Additional tests performed at DNW wind tunnel using large-scale complete model including also powered turbine simulation. Finally, more tests performed at high Reynolds number tunnels at Onera F1 and ETW for verification purposes.

Moreover, an aeroacoustic analysis carried out for this concept using CFD and wind tunnel data especially in the vicinity of a wing in the high lift configuration. According to the authors, apart from low noise levels, an efficient aerodynamic high lift performance could contribute significantly to a low noise aircraft. Although, the noise from the trailing edge is considerably lower than the noise generation from the leading edge, the design of the trailing edge devices could indirectly contribute to a lower total noise level, even if it's source noise increases.

In terms of the results, the maximum lift was insensitive to the overlap changes varying from -0.5 % to 0.5 %, tried on the configuration. This was also validated by the CFD results. However, the changes on the gap between the flap and the main wing showed a large influence

on the maximum lift, with the best aerodynamic performance obtained with the smallest gap value (Setting A), as it is shown in Figure 2.13(a). Unfortunately, these results did not validate the CFD data, which predicted the worst performance for this particular setting. The most obvious conclusion for this difference between the wind tunnel and CFD results was explained by the difference of the Reynolds number used for each test (CFD:  $20 \cdot 10^6$ , WT:  $1.4 \cdot 10^6$ ). More research about these miscorrelations asked by the authors.

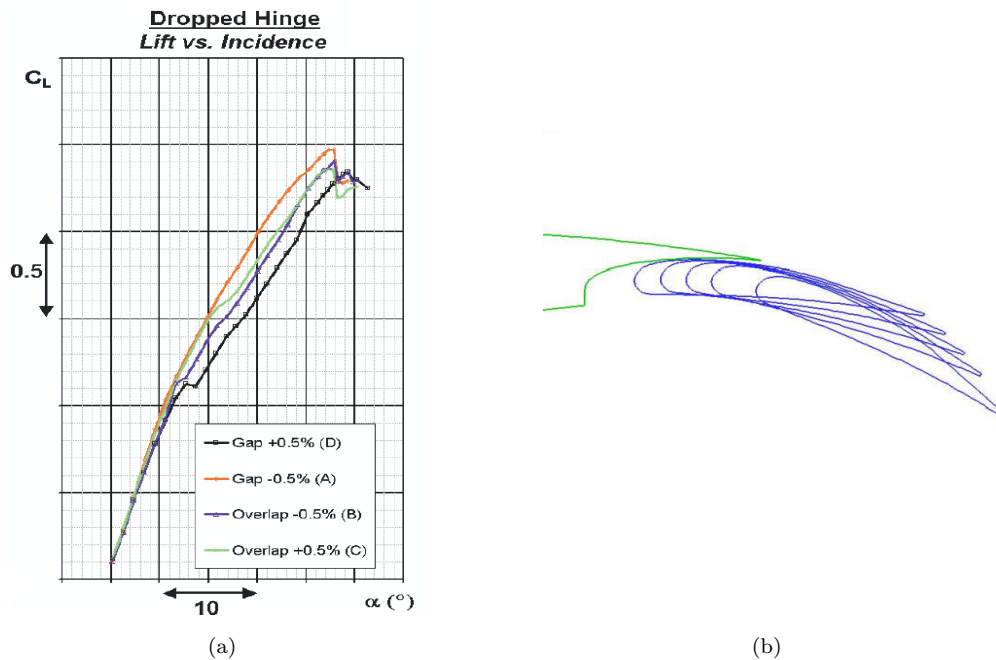


Figure 2.13: Gap and overlap variations (a), wind-tunnel results for ADHF and (b) Advanced Dropped Hinge Flap concept schematic [31]

As mentioned earlier, flow control is closely linked to high lift performance and it's also the main topic of this thesis work. That is why the next work discussed is about the active flow control of separation on the flap of a three-element high lift configuration by scientists at TU Berlin [13]. To begin with, the researchers tried active flow control by means of periodic suction and blowing as well as pulsed blowing into the flap's boundary layer to a 3D high lift configuration. This research was carried out experimentally in the wind tunnel and computationally using CFD. The numerical part mainly focused on understanding the process of separation control by analysing the flow field structures at different excitation parameters. On the other hand, the experimental investigation was mainly focused on the overall lift and drag improvement by measuring integral values. The experiments performed using a half-model with finite span, sweep and fuselage. The numerical investigation was carried on a swept wing of infinite span.

Firstly, experiments carried out on the configuration without excitation, in order to get an idea about the lift and drag figures. As it was expected, at large flap angles the lift and drag values increased. This is shown in Figure 2.14. In addition, it was realised that at very high flap angles (e.g.  $45^\circ$ ) the maximum value of lift coefficient ( $C_{L_{max}}$ ) was decreased. For validation reasons it was determined that at  $37^\circ$  of flap angle and  $6^\circ$  of the main wing, the flow was still

attached. A very important note from these tests, was the strong cross flow observed, especially on the separated flap caused from the sweep angle.

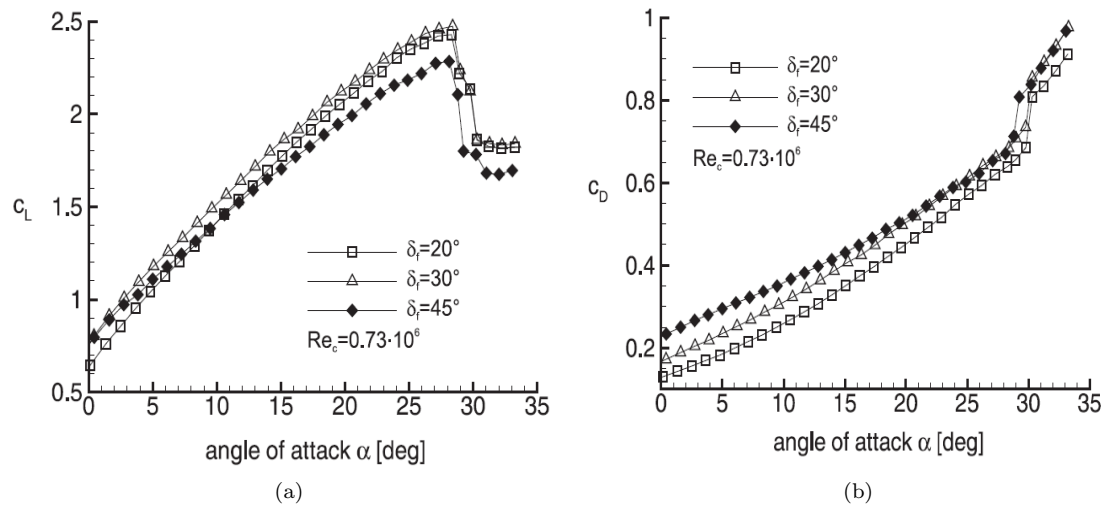


Figure 2.14:  $C_L$  (a) and  $C_D$  (b) vs.  $\alpha$  for the unexcited case [13]

Experimental data proved that unsteady blowing is more effective than steady blowing at a specific high lift setting. Active flow control was able to reattach the flow, resulting in an increased lift compared to base flow. The measured results of the finite wing presented an almost frequency-independent behaviour of gain in lift. The main lift coefficient of the 2D flow increased by 17%, for the infinite wing case, increased by 11% and for the finite wing case by 6%. The explanation about these changes in lift was accounted to three-dimensional effects. The numerical investigations with various momentum coefficients at a given excitation frequency have shown that the lift increased strongly when the intensity is smaller than  $C_\mu = 50 \cdot 10^{-5}$ . However, at higher angles of attack and especially near the maximum lift, the total drag in the excited case was slightly higher than the base flow. This is presented in Figure 2.15 and although unsteady forcing prevented separation and augmented the lift values, the higher induced drag amplified the drag as well.

The last thing to mention was that the largest part of the total lift, was produced from the main wing for both the unexcited and excited cases. In addition, the total gain in lift was not caused by the particular increase of lift on the flap but the enhanced circulation around the main airfoil generated by the decreased separation on the upper flap surface. The reason for the effectiveness of the excitation according to the authors, were the vortices generated by the perturbations. These vortices enabled the transport of energy from the main flow to the recirculation region near the wall and as a result the separation on the upper surface of the flap was postponed, giving an increase in lift values [13].

Another very well-known flow control technique, was about "Active vortex generators as a novel high lift device" [17]. The main reason mentioning this research into this part was that this passive control is one of the most reliable and as will be seen later in the report, it was also used in this thesis work. For this work, researchers used experimental and numerical means

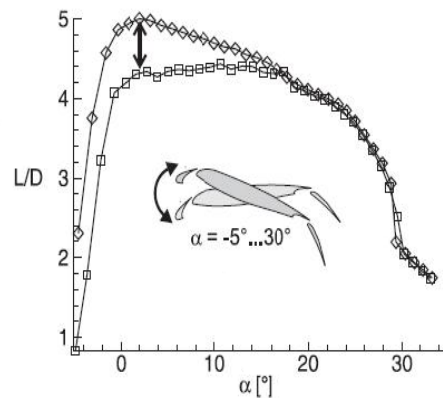


Figure 2.15: L/D vs.  $\alpha$  with (excited) and without flow control (unexcited) [13]

in order to simulate the aerodynamic behaviour of a transport wing equipped with deployable active vortex generators. The geometry shown in Figure 2.16 used consisted by a single row array of delta wings positioned above the upper surface of the airfoil close to the leading edge. The numerical simulations performed were (2.5D) and divided into take-off, cruise and landing configurations. Then, experimental tests conducted in order to validate the computational results. The main reason for this flow control use would be to replace the slat on a late generation wing profile.

From experimental results, the performance of the AVG's depended mainly on their position and shape. Moreover, the height placed above the surface was critical as long as the angles and density of vortex generators. For CFD results, the airfoil used had the same characteristics with the A-320 profile and two main parameters studied; the height of the AVG above the surface close to the leading edge and the angle of incidence. Firstly, three different angles tested each with four different angles of attack. However, after this computation there was not an overall increase in lift coefficient and stall behaviour, due to artificial high velocities in the leading edge. However, there was more understanding of the AVG configuration. But even for the next computations tried, it was found that the velocities close to the leading edge were very high, which was partly expected due to the missing leading edge device. The authors claimed that this problem could be solved by reducing the camber and the flap deflection but then a remarkable loss of lift would be occurring.

The main concentration point of this work was on the development of the vortex generated and understanding of how it could improve the efficiency of the system. On the other hand, the experimental results, were different compared to the numerical data in the take-off and landing configurations. These discrepancies could be explained by the fastening method used on the wind tunnel model. This caused disruption of the leading edge suction and created an under prediction of the stall angle of attack in the experiment. However, the agreement between experimental and computational results was fair enough in order to allow further work decisions. The main conclusion was that the base wing's performance was degraded by applying this configuration.

Another similar work was from researchers in India about passive flow control using vortex generators over a simple NACA 0012 airfoil using CFD [3]. The main part of the research was to test the NACA 0012 airfoil over a wide range of angles of attack with vortex generators attached

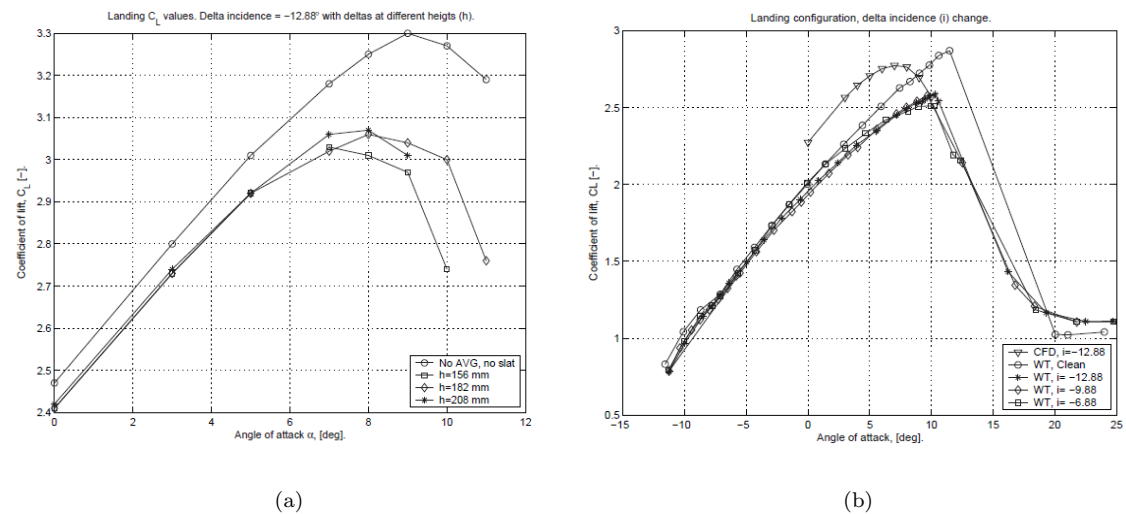


Figure 2.16:  $C_L$  vs. angle of attack (a) for clean wing and AVG configurations and (b) Comparison of WT and CFD results [17]

on it. Three dimensional RANS simulations with Spalart-Allmaras turbulence model used in Fluent and the main emphasis was put on how the addition of small vanes could help to delay the onset of stall. As flow control over an airfoil at high angles of attack was of strong interest, it was tried to simulate as best as possible the flow around the airfoil with and without vortex generators in order to show any possible effect of these passive devices. As the study was CFD related, the mesh generation was an important part of this work. Thus, having a denser mesh closer to the airfoil and especially at regions of adverse pressure gradient as necessary. The total cell number in the whole domain was 1,100,395 cells. A schematic of the geometry and of the mesh used close to the vortex generator is displayed in Figure 2.17 .

In order to demonstrate clearly the effect of vortex generators, the authors, first examined the clean wing configuration and then the wing fitted with vortex generators at the same Reynolds number, in order to compare the data. The range of angles of attack tested was from  $0$  to  $16^\circ$ . The results could be divided into two different categories; pre-stall and post stall. In the pre-stall case and for considerably lower angles the effect of the vortex generators was not significant and is shown from  $C_L$  and  $C_D$  plots. Hence, the flow was mainly attached on the upper surface of the airfoil. However, as soon as the angle of attack increased and the airfoil was in the post-stall region, the vortex generators helped considerably to reduce the length of the recirculating region, which starts from the leading edge in the clean wing case.

From data given, it is shown that the stall angle for the clean airfoil configuration is at  $14^\circ$ . However, as soon as the airfoil was fitted with vortex generators then the stall angle was increased to  $16^\circ$ . The values of  $C_L$  and  $C_D$ , both increase as would be expected. The reason that the maximum lift coefficient increased was the stall delaying effect of the passive devices at high angles of attack. However, there was a small increase of the drag coefficient as well. This was explained by the increase of the wetted surface area due to vortex generators. Nevertheless, it is shown that the drag induced by these devices was negligible, as the main source of drag which was pressure drag, reduced by the delayed separation on the upper surface of the airfoil. Concluding, authors advise for further Direct Numerical Simulations (DNS), in order to get more physical

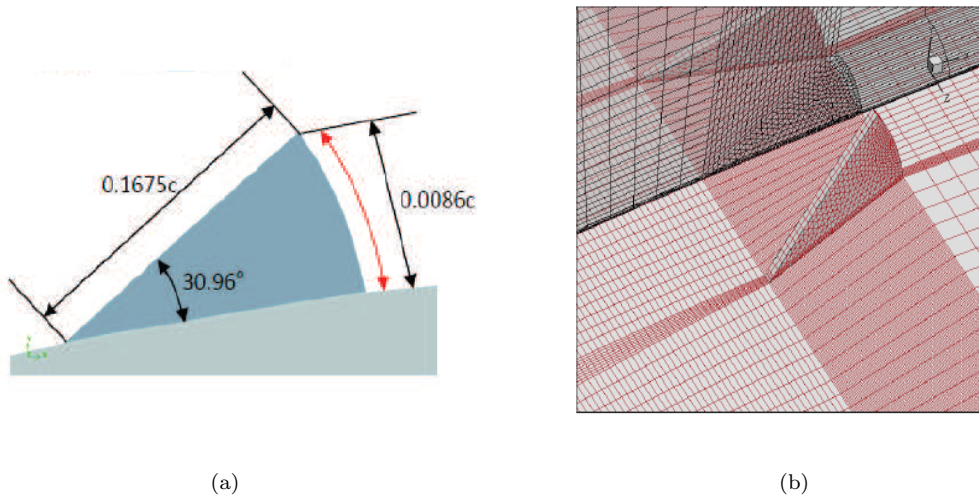


Figure 2.17: Illustration of the geometry and dimensions (a) of vortex generator and (b) Mesh of the vortex generator [3]

understanding of the modifications in the coherent structures induced by the vortex generators, in order to keep the flow attached on the upper surface of the NACA 0012 airfoil [3].

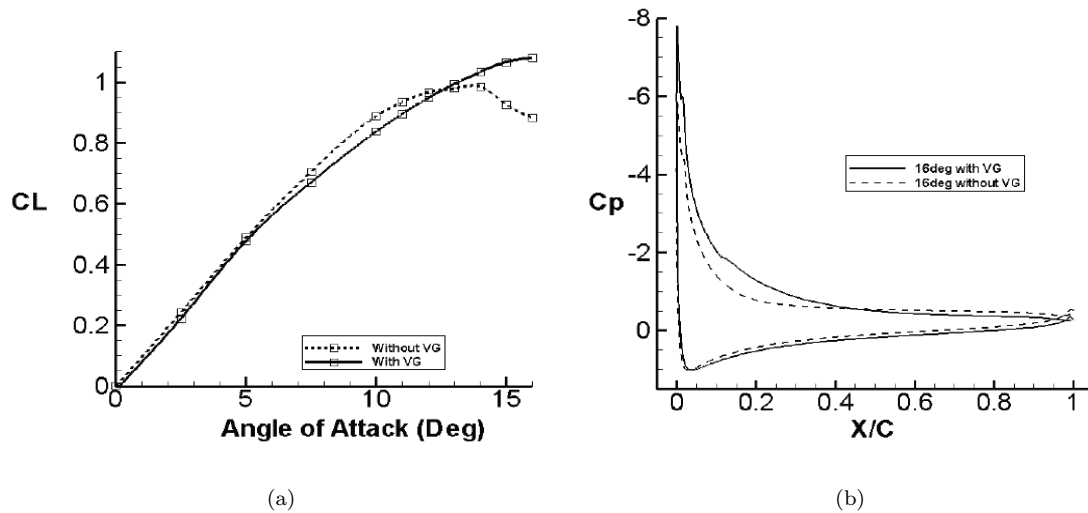


Figure 2.18:  $C_L$  vs.  $\alpha$  (a) comparison and (b)  $C_p$ -distribution comparison with and without VG's [3]

Another remarkable flow control trial on high lift devices was from researchers of Braunschweig University of Technology [24]. This work was an experimental and computational investigation of a gap-less high lift system using circulation control. Authors referred on the increased interest of reducing noise which is generated by high lift devices and insisted that "when air is blown from a slot directly upstream of a flap, the flow over it, can withstand great adverse

*pressure gradients without separation*". The flow around the model of a transonic airfoil in a low speed wind tunnel was analysed using pressure measurements and long distance macroscopic particle image velocimetry ( $\mu$ PIV). The Reynolds number used was  $1 \cdot 10^6$ . Moreover, particles seeded in the jet in order to measure the velocity in the vicinity of the slot and close to the surface.

Before wind tunnel experiments, numerical 2D simulations of the flow around profiles using circulation control were performed, in order to find favourable geometries with low momentum coefficients. For this purpose RANS simulations conducted and all these preliminary computations were undertaken assuming fully turbulent boundary layer and using a turbulence model. After that, the experiments started in a low speed tunnel at 50 m/s. One of the most noticeable results was the  $C_p$ -distribution presented for an angle of attack of  $0^\circ$  and different momentum coefficients. It was shown that without blowing the flow was separating from the very beginning of the flap. For smaller momentum coefficients the flow separated further downstream. Finally, when the momentum coefficient was more than  $C_\mu = 0.040$ , the flow stayed attached up to the trailing edge. According to the authors, an increase in the momentum coefficient always corresponds to an increase of the circulation around the complete airfoil and does not decrease the pressure on the flap. In addition to that it is also shown that, the velocity in the boundary layer, as well as the velocity in the jet is augmented for the higher momentum coefficient. Hence, for momentum coefficient  $C_\mu = 0.043$ , the momentum of the jet is large enough to keep attached up to the trailing edge of the airfoil. These two things are shown in Figure 2.19 for an angle of attack of  $0^\circ$ . The last step of this research was the numerical simulation of experimental work done. From pressure distributions presented in this paper, for momentum coefficients of  $C_\mu = 0.045$ , it was possible to compare the numerical and experimental results for angles of attack of  $-5$  and  $0^\circ$ .

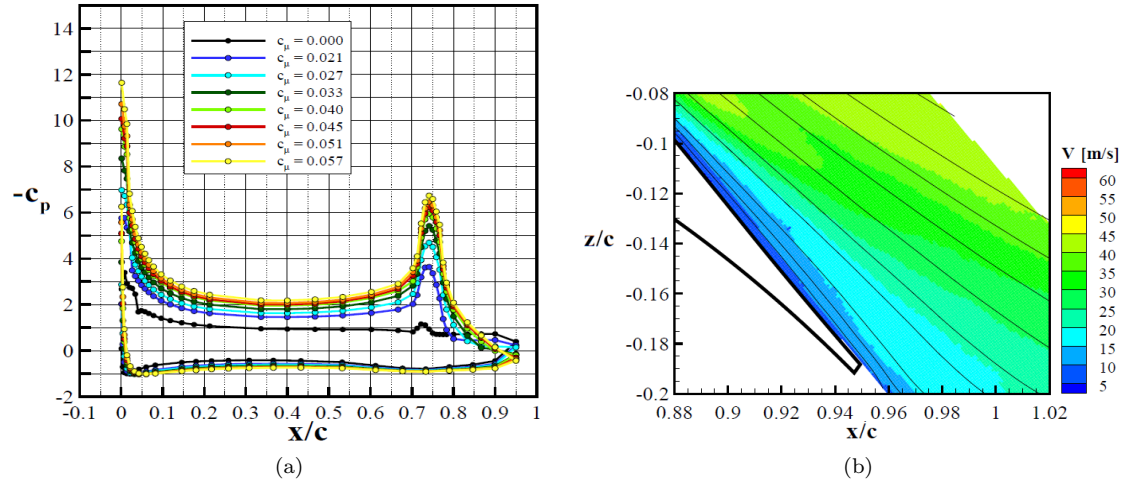


Figure 2.19:  $C_p$ -distribution (a) for various momentum coefficients and (b) Velocity field at the trailing edge region [24]

The agreement between the experimental and computational results was very good and demonstrates the capability of the used turbulence model to simulate the flow around a circulation control airfoil with a sharp trailing edge. Finally, the authors note that more simulations should be conducted to determine if this good agreement could also be achieved for maximum

lift and prediction of separation angle and momentum coefficient [24].

Another interesting study was from NLR (National Aerospace Laboratory) [34]. This was a CFD study of free flying delta array used as a passive flow control device. According to the authors, in order to achieve low speed performance or an enhancement on the performance of a high lift system, one has to avoid flow separation on the flow around the high lift system. Nevertheless, something which could link this study to this thesis work, is that maximum lift for high lift systems is a very complex phenomenon and especially at flight Reynolds number is not only governed by flow separation on the high lift device but by other effects as the wake breakdown of the main wing above the flap.

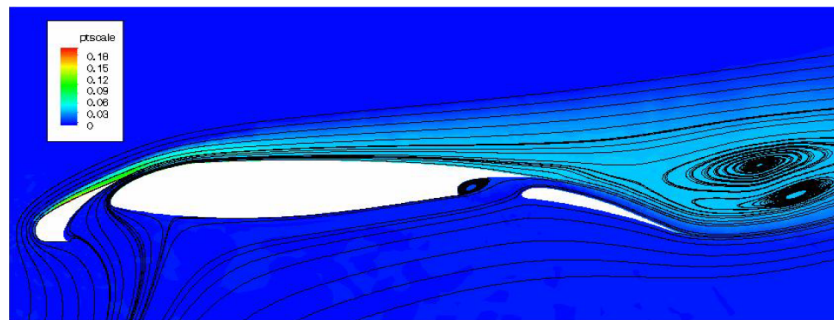


Figure 2.20: Illustration of wake break-up above the flap as computed for a HELIX baseline three element airfoil in take-off configuration at  $M_\infty = 0.20$ ,  $\alpha = 32^\circ$  and  $Re = 21.0 \cdot 10^6$  [34]

This was a CFD study of the free flying delta array (FFDA) that was aimed at controlling the flap boundary layer, as well as the wake of the main wing. In order to give a visual idea of this flow control device, it consisted of an array of delta wings placed in the gap between the main wing and the flap at take-off and landing settings. Three dimensional schematics of FFDA are shown in Figure 2.21. Each sharp edge delta wing generated a pair of counter rotating vortices. The effect of these vortices on the main wing wake flow, would be that the flow would be turned towards the flap surface.

The applicability of this flow control device in a real wing configuration was challenging. These delta wings could be stowed in the cove when the flap was retracted. However, this resulted in a reduced design freedom and as a result, these delta wings had to be placed to a region close to the leading edge of the flap. A graphical representation of this layout is presented in Figure 2.21 .

The design of the delta wings was based such as the vortices were strong enough to have the desired effects on the flap boundary layer at the main wing wake flow, but at the same time be limited to avoid vortex breakdown. That is why CFD simulations based on Navier-Stokes calculations took carried out. Looking at the results, according to the projected streamlines, giving a two-dimensional view of the phenomena happening, a trailing edge separation for the clean wing configuration observed starting at approximately 75% flap chord. On the other hand though, when the FFDA was applied, the separating region was greatly reduced to a small pocket of recirculating flow downstream of the flap trailing edge. The main wing wake was thickened in the centre plane due to a downward directed velocity induced by vortices. This was calculated for angle of attack of  $18^\circ$  and  $Re = 19 \cdot 10^6$  and is shown in Figure 2.22.

Moreover, even if maximum lift was not measured for the configuration with the FFDA, it

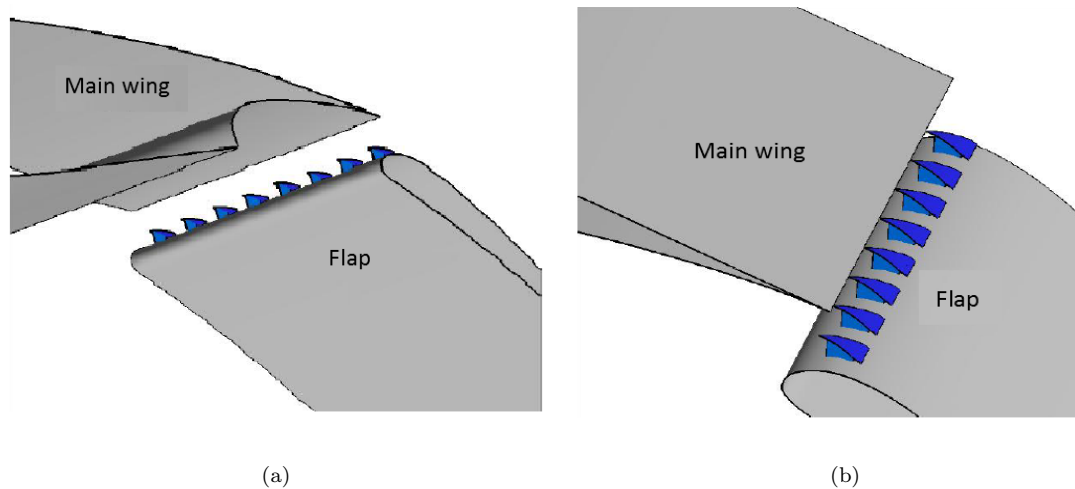


Figure 2.21: Schematic of the FFDA flow control device, mounted on top of the leading edge of the flap (a) bottom view (b) top view [34]

was expected that there would be an increase in maximum lift of approximately  $\Delta C_l = 0.0338$  at the safety take-off speed and a drag reduction of  $\Delta C_d = -0.0043$ . For the landing setting, the gain for maximum lift was  $\Delta C_l = 0.0348$  and the reduction of drag was  $\Delta C_d = -0.0089$ . The lift and drag polars are presented in Figure 2.23 for landing phase. As a final note, it could be expected that FFDA could offer greater gains to novel-high lift system designs aimed at increased aerodynamic performance or reduced geometrical complexity [34].

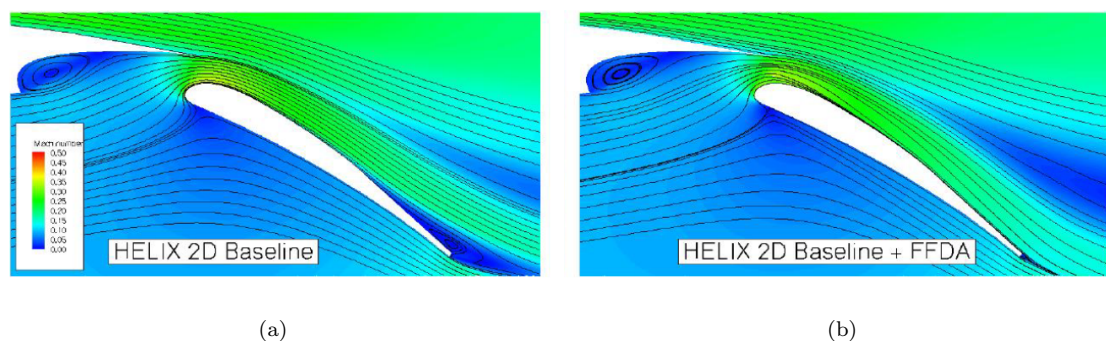


Figure 2.22: Comparison of stream patterns in the centre plane for the HELIX 2D baseline landing configuration with (b) and without (a) FFDA at  $M_\infty = 0.18$ ,  $\alpha = 18^\circ$  and  $Re = 19.0 \cdot 10^6$  [34]

The last part of literature study, presented was actually found from a paper published from J. C. Ross et al. with title ”*Lift-Enhancing Tabs on Multi-element Airfoils*” [27]. In this work the main topic is a different case of passive flow control, using flat-plate tabs, very similar to well-known Gurney flaps, to increase the lift force of multi-element airfoils. This is done by placing them on the pressure side and close to the trailing edge of the main wing. However, the

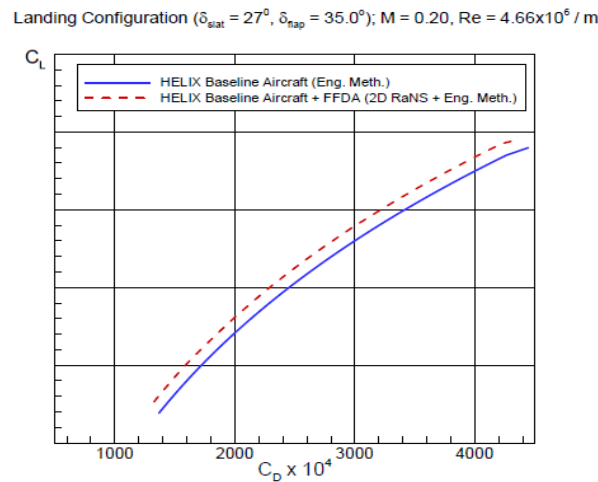


Figure 2.23: Estimated effect of the FFDA device on the drag polars of the HELIX baseline aircraft for landing configuration at ( $\delta_{\text{slat}} = 27^\circ$ ,  $\delta_{\text{flap}} = 35^\circ$ ),  $M = 0.20$  and  $\text{Re} = 4.66 \cdot 10^6$  [34]

most important point in this paper is where the authors present previous relevant work done, which is related to their study.

One of the referred previous studies done and was of great interest for this thesis, was the one of drooped shroud used on F/A-18 aircraft in landing configuration. Deflecting the upper surface of the cover or spoiler of the main element has been proposed for transport aircrafts and was used on F/A-18 combat aircraft. A schematic is presented in Figure 2.24(a). This was the only case found in literature, where there was a very close connection with what will be presented in this work.

Results of spoiler droop, on a transport aircraft airfoil, showed a decrease in maximum lift for deflections of  $5^\circ$  and  $10^\circ$  but an increase in the lift at a given angle of attack. As will be presented and discussed in the last part of literature study, the first estimate of decrease of maximum lift could be accepted from the authors. However, there are no possible reasons for this decrease in this paper, in this work, possible reasons will be presented and discussed according to additional literature found on the topic. The only reasoning presented in this paper and tried to explain this reduction of maximum lift was using the pressure distribution and comparing with the main study of this paper, the tabs. As can be seen from the plot in Figure 2.24(b), showing the pressure distribution for these two cases, the drooped-shroud case has a suction peak at the hinge point which limits the amount of deflection that could be used due to the large gradients downstream of the hinge. The pressure distribution for the tab case is much smoother and much less likely to cause premature flow separation than in the drooped spoiler case [27].

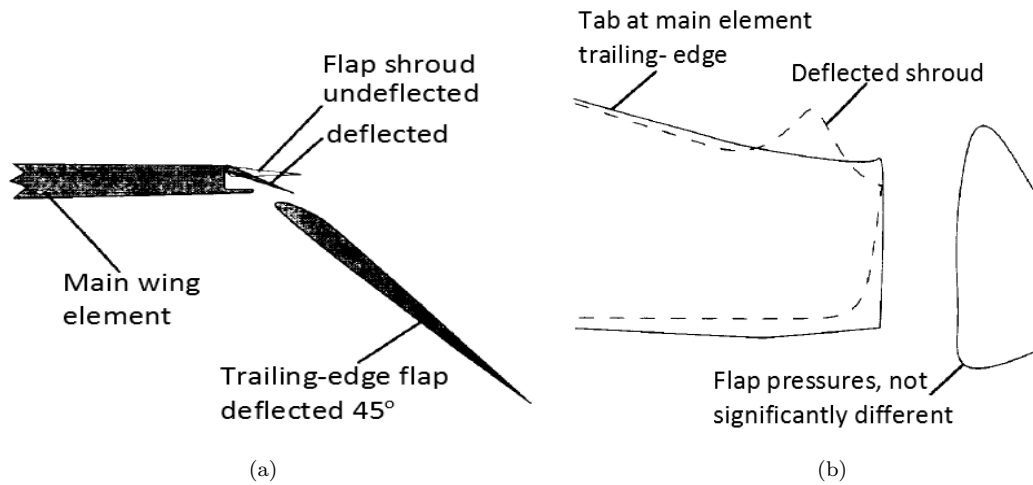


Figure 2.24: Flap shroud used on F/A-18 (a) [very similar to drooped spoiler panel case] and (b)  $C_p$ -distribution for drooped spoiler panel and cove tab [27]

## 2.3 Wake Flows & Flow Reversal

A well-known review of high lift aerodynamics is from A. Smith. In part of his report, Smith talks about the off-the-surface pressure recovery. The author tries to explain the phenomenon of wake bursting by distinguishing the different existing cases. Therefore, it is stated that up to now most of the studies were about fluid flowing into regions of higher pressure while it is in contact with a surface. This is also known as the decelerating boundary layer. However, there could be a different kind of flow, the flow of wakes, which might be out of contact with any wall into regions of high pressure. This kind of flow occurs usually on multi-element airfoils. In addition, it is believed that the phenomenon of wake bursting is a result of each forward element producing wake components over its downstream elements. It is underlined that the theory for this kind of wake flow is not so well developed as the theory of the boundary layer flow and called for attention to this complex phenomenon. Thus, if the rise of pressure is great enough then, flow reversal in the stream is possible, entirely of the surface.

Afterwards, Smith explains that off-surface flow reversal could be easily demonstrated by resorting to Bernoulli's equation and is also presented here as well as it was found very useful. Considering the flow case presented below on Figure 2.25, at station 0, the static pressure of the flow is constant across the stream, however it is clear that there is a wake-like zone where the velocities are deficient. The wake flows to a region of higher pressure at station 1. As very thin regions are considered with respect to any overall curvature of the flow, the static pressure at station 1 could also be assumed to stay constant across the boundary layer. As the velocity gradient on the vertical axis will be very small, the same will apply for the shear stresses as well and as a result, it could be assumed that each streamline maintains its total head between these two stations. Such an assumption was also confirmed by plenty of numerical analyses, including Stratford's.

A useful distinguish is made between potential regions (U) and energy deficient regions (u), in order to proceed with the equations for incompressible flow. Hence:

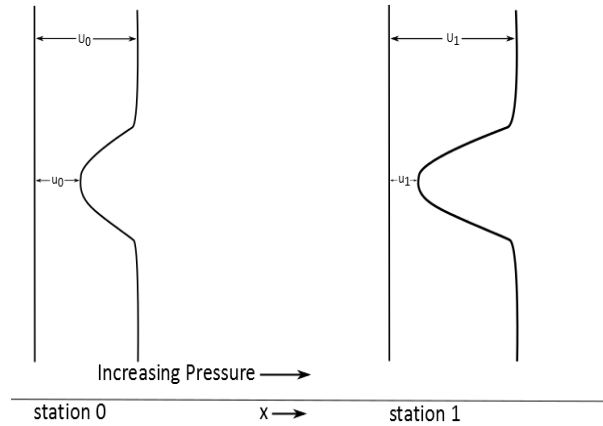


Figure 2.25: Flow of a wake into a pressure rise region [29]

For potential regions:

$$p_0 + \frac{1}{2}\rho U_0^2 = p_1 + \frac{1}{2}\rho U_1^2 \quad (2.11)$$

For energy deficient regions:

$$p_0 + \frac{1}{2}\rho u_0^2 = p_1 + \frac{1}{2}\rho u_1^2 \quad (2.12)$$

Solving for  $u$  and  $U$  at station 1 and obtaining their ratio:

$$\frac{u_1^2}{U_1^2} = \frac{p_0 - p_1 + \frac{1}{2}\rho u_0^2}{p_0 - p_1 + \frac{1}{2}\rho U_0^2} \quad (2.13)$$

Then, introducing canonical pressure coefficient into 2.13, results to:

$$\frac{u_1^2}{U_1^2} = \frac{\frac{u_0^2}{U_0^2} - \bar{C}_p}{1 - \bar{C}_p} \quad (2.14)$$

As the coefficient increases the ratio of velocities at station 1 could reach zero before the coefficient reaches the value of 1, as long as the ratio of velocities at station 0 is less than zero. Taking for example the value of the velocity ratio at station 0 as  $\frac{1}{2}$  and  $C_p = \frac{1}{2}$ , the value of the velocity ratio at station 1 is 0. Hence, the velocity-defect ratio is magnified and flow reversal could occur in the main stream. The effect of the viscosity is also mentioned as it helps to smooth out the wake velocity defect and as a result the Bernoulli approach is improperly conservative. In general it could be concluded that as the flow is in a region of higher pressure zone, the velocity defect ratio will always worsen. Finally, according to the author, in practical applications, where the adverse pressure gradients are not infinite, the wake instability problem should be rarely serious, which means that wakes should be able to withstand higher pressure gradients that a boundary layer can.

For multi-element airfoils there are two types of pressure recovery; the typical one which is the on-surface pressure recovery and the off-surface pressure recovery. Talking about a slatted

airfoil, the flow is accelerated and reaches a peak velocity, and then it decelerates in contact with the surface. At some point it detaches and continues to decelerate up to the trailing edge pressures are reached and then is accelerated again to free stream conditions. By the off-surface deceleration, recovery from very high pressure values can be made in much shorter distance that can be made when all the deceleration is in contact with the surface [29].

The next piece of literature was a paper published by researchers at Purdue University [15]. The authors made clear that the behaviour of wakes in adverse pressure gradients is very critical to the performance of high lift systems and that the phenomenon of wake bursting could happen even if the boundary layer is attached on a surface. This is shown schematically for a 2D airfoil in Figure 2.26. Although wake bursting is known for its importance on high lift systems, there are no detailed measurements reported for busted wakes, which makes this complex phenomenon even more vital.

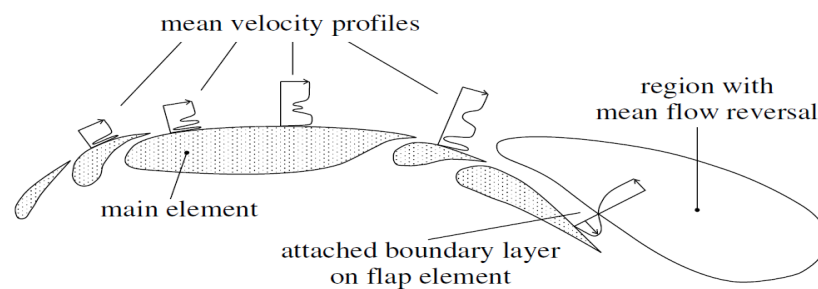


Figure 2.26: Flow phenomena over a 2D high lift airfoil configuration [15]

In their work, they managed to achieve wake bursting in the wake of a flat plate in a two dimensional (2D) diffuser. Measurements carried out using flow visualisation, pressure probes and Laser Doppler Velocimetry (LDV). The set up included a 1800 mm plate, in order to generate a wake and a variable angle diffuser, to create an adverse pressure gradient. The tunnel velocity used was 15 m/s. Moreover, tangential blowing was able to keep the boundary layers attached at large diffuser angles, in order to reverse the wake behind the flat plate. The flat plate-diffuser set-up is shown in Figure 2.27 .

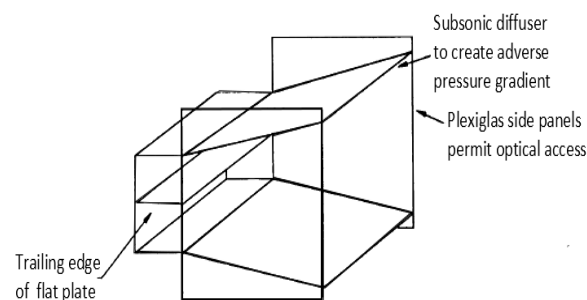


Figure 2.27: Flat plate-diffuser wind tunnel set-up used to create adverse pressure gradient [15]

Without adverse pressure gradient, the flow field behind the flat plate formed a regular two-dimensional turbulent wake as indicated by LDV. However, when the diffuser opened between 0

and  $6^\circ$ , the velocity defect in the centreline of the wake increased in magnitude and width due to adverse pressure gradient. The LDV measurements agreed well with Pitot pressure measurements and it was clear that increasing the diffuser angle up to  $6^\circ$  had not huge impact on the flow field. This was probably due to separations of the diffuser boundary layers. Nonetheless, with the aid of the blowing, it was managed to keep them attached and the Pitot measurements showed that the wake was reversed at an angle of  $11^\circ$ . Placing tufts on the trailing edge of the plate, the wake was totally attached there, and as a result, it was concluded that wake reversal was occurring somewhere in the diffuser. After smoke visualisation tests, it was shown that the bursting point was about half-way up the diffuser [15].

Another work, was from NASA researchers with title "Wake flow in adverse pressure gradient" [8]. A series of fundamental experiments conducted, to study the effects of adverse pressure gradient on a wake flow. Moreover, computations using various turbulence models performed in order to check the validity of these results. This work was done in the interest of improving the predictability of high lift systems. The authors explained that the off-the-surface separation could lead to decambering of the multi-element system and a great loss of lift. In addition, that turbulent mixing in the wake, controls the growth of the wake and dictates the extent to which the wake experiences flow reversal. The geometry used in the experiments included a flat plate, 6 mm thick, 381 mm wide and 419 mm long, mounted on the centre of the test section and parallel to the wind tunnel walls. The last 38 mm of the plate were symmetrically and linearly tapered to a 0.4 mm trailing edge and the upstream edge was rounded. In addition, the tunnel wall boundary layers were able to stay attached using tangential blowing from slots. Finally, the Reynolds number tested was  $1 \cdot 10^6$ . The set-up is shown schematically in Figure 2.28.

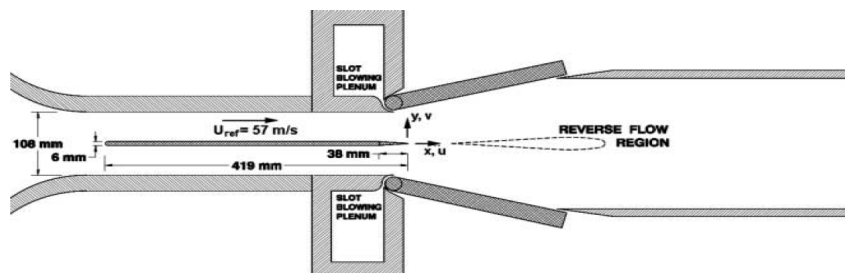


Figure 2.28: Schematic of the 2D wind-tunnel test section geometry used by Driver et al. [8], including geometrical information on the set-up and the expected wake reversal region behind the flat plate

The measurements included mean and fluctuating velocities using LDV and turbulent Reynolds shear stresses. The computations performed, solved the incompressible Navier-Stokes equations, using two different turbulence models, SA and SST. In the adverse pressure gradient cases, using a  $120 \times 81$  grid, the computations showed less velocity deficit than the experimental results. No reversed flow was seen in the small separation case and only small amount of reversal produced by the SST model in the extreme separation case. In terms of the shear stresses, for the straight wall case the experimental and numerical results agreed well. As the diffuser was diverged shear stresses were increased and the numerical results under predicted these values for adverse pressure gradients. Moreover, as the Reynolds shear stress gradient increased, the greater the flow ability to cope with adverse pressure gradients was. Moreover, in the centreline of the wake, the gradient did not alter even if the flow was separated.

Furthermore, for the small separation case, neither computation was able to reproduce the flow reversals seen in the experiments. The biggest deficiency in existing turbulence models is their tendency to overpredict the turbulent eddy-viscosity. This could be seen by the plot of streamwise distribution of local maximum in Reynolds shear stresses presented in Figure 2.29. The last thing studied, was a case where the splitter plate was enlarged by 38 mm in order to extend downstream into the adverse pressure gradient region and simulate the phenomenon of overhang in multi-element airfoils. The results showed that the separation was slightly more extensive than the shorter trailing edge case. This was attributed to the longer distance that the boundary layer spends in contact to the wall and its associated to the skin friction. To conclude, computations with turbulence models failed to capture the flow reversals and the associated displacement effects seen in the wind tunnel experiments [8].

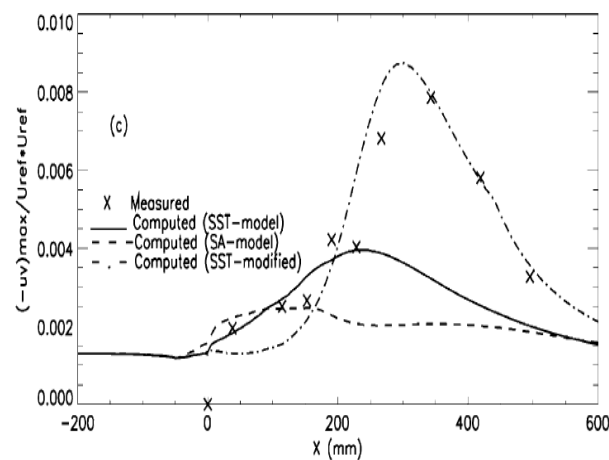


Figure 2.29: Reynolds shear stress evolution for the small separation case (expansion ratio = 2.25) as presented by Driver et al. [8]

The effects of curvature and pressure gradient on a turbulent wake are also discussed by Starke et al. [30]. Data gathered and compared with existing for the wake under zero pressure gradients. Mean velocities and Reynolds shear stresses measured and used as test cases for turbulence models. According to the authors, even a small curvature has a significant effect on mean velocities and turbulence in the wake. Hence, in order to get accurate experimental data, LDA technique used because of its non-intrusive nature. The test set-up included a flat plate of 600 mm length and 18 mm thickness. The nose was elliptic and the last 110 mm was tapered to form a sharp trailing edge of 0.2 mm. In addition, the plate was placed at zero angle of attack and its boundary layer tripped with wires close to the leading edge. The velocity was set at 10 m/s and Reynolds number at  $4 \cdot 10^5$ . Two types of experiments performed; one for zero pressure gradient wake and one for adverse pressure gradient wake by adjusting one of the side walls of the tunnel.

In the case of zero-pressure gradient wake, the static pressure remains constant in downstream direction, except for a short region near the trailing edge. On the other hand, the curved wake showed a normal pressure gradient over the initial part of the wake. Then this gradient stays constant. For the zero pressure wake case, the boundary layer at the trailing edge has a shape factor,  $H=1.6$ , which is slightly greater than the shape factor, for a turbulent boundary

layer in zero pressure gradient. This small difference is caused by the fact that the boundary layer is subjected to a mild adverse pressure gradient induced by the tapered part of the plate. In addition, the momentum-loss thickness decreases at the trailing edge to a constant value far downstream. The change of momentum-loss thickness in the near wake is caused by the tapering of the trailing edge as well. The local favourable pressure gradient resulted in local acceleration of the mean flow near the centreline and as a result a decrease of the momentum-loss thickness. This additional acceleration of the flow due to tapering, caused the increase of the centreline velocity of a zero pressure gradient wake behind a flat plate. This experiment did not extend far enough downstream to reach far-wake conditions.

For the curved wake, the side of the wake facing the parallel test section wall was destabilised by the curvature, whereas the side of the wake facing the diverging test section wall was stabilised. In this case, the velocity profiles were asymmetrical at the trailing edge region, caused by the adverse pressure gradient, induced in the boundary layer at the side facing the diverging wall. This is shown in Figure 2.30. An increased spreading of the wake downstream, due to curvature, was not apparent in this experiment. In terms of the displacement and momentum-loss thickness, the first decreases behind the plate and then increases further downstream. The second one grows steadily in the downstream direction. Hence, the decrease found in the zero pressure gradient was not encountered in the curved wake [30].

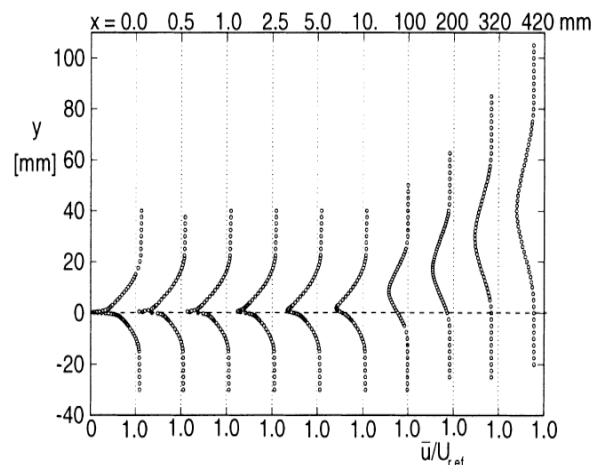


Figure 2.30: Mean streamwise velocity in the curved wake case as presented by Starke et.al. [30]

A more recent work by researchers at Delft University of Technology [33], included RANS numerical calculations for the near wake of a flat plate with and without the effects of an adverse pressure gradient. This investigation is related to the wake flow in the trailing edge of the main element. Because of the strong adverse pressure gradients, the problem was simplified to the wake analysis of a "thick" flat plate with a tapered trailing edge. In addition, the flow behind the plate was subjected to strong adverse pressure gradient, causing high turbulent intensities and local mean-flow reversal. These experiments conducted to compare the results of numerical calculations. The test set-up used was exactly the same used in the previous work presented, including suction slots to prevent boundary layer separation on the diffuser walls positioned at  $15^\circ$ . A schematic of the set-up used is shown in Figure 2.31.

RANS numerical calculations solved for two-dimensional, turbulent flow near wake for both for the constant pressure and adverse pressure gradient cases, using two turbulence models. For

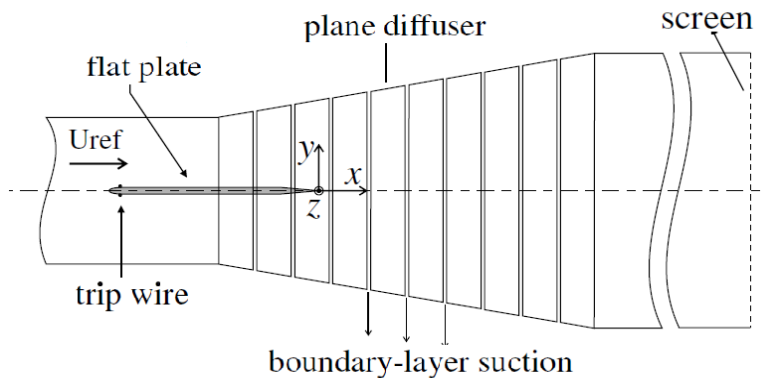


Figure 2.31: Wind tunnel set-up used for the investigation of the wake in adverse pressure gradient by Tummers et.al. Note that the origin of measurements is at the trailing edge of the plate [33]

the zero pressure gradient, the pressure variations induced by the taper, could have significant effects on the trailing edge flow zone. In addition, the measured and computed centreline velocity, as long as the turbulent kinetic energy on the centreline and the maximum value of the turbulent kinetic energy at different stations, indicated good agreement between experiments and the numerical calculations. Moreover, the computations reproduced accurately the measured decrease of the momentum thickness at the trailing edge further downstream. This was explained by the pressure decrease downstream of the trailing edge such that the near wake experienced a favourable pressure gradient and consequently the momentum thickness decreased. For the adverse pressure gradient wake, there were significant discrepancies between experiments and the predictions near the centreline of the wake. This is shown, for mean velocity and kinetic energy along the centreline in Figure 2.32.

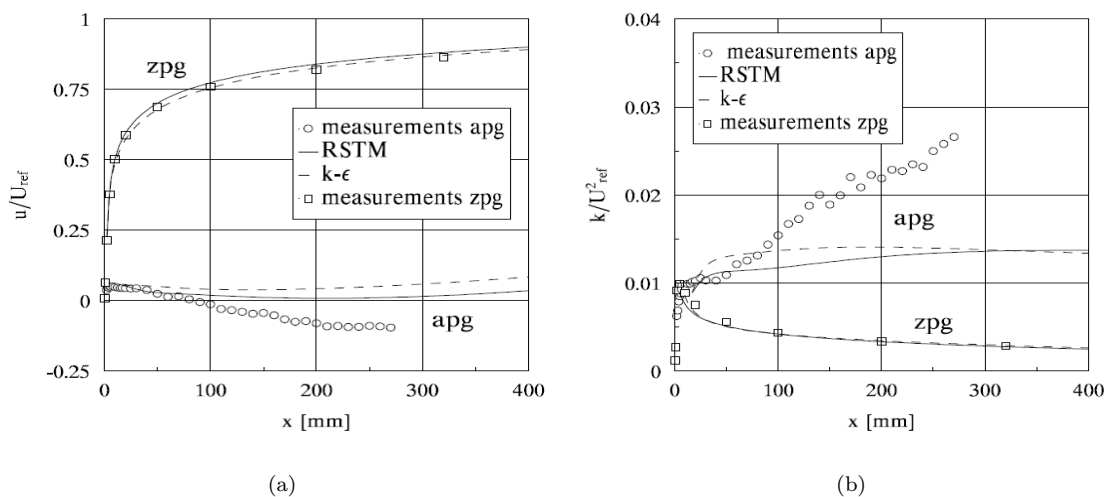


Figure 2.32: Measured and calculated mean velocity (a) and (b) kinetic energy along the centreline of the wake [33]

Another interesting work was an experimental study of the trailing edge flow of a supercritical NLR 7702 airfoil using LDA [1]. Detailed measurements of mean flow and turbulence performed close to the trailing edge region of this airfoil. The main target was to provide accurate and reliable data for turbulence models development for trailing edge flows and validate computational methods.

The Reynolds number based on model chord was  $1.47 \cdot 10^6$  and the tunnel speed was 35 m/s. The chord length was 600 mm and was placed at  $4^\circ$ . The airfoil used is presented in Figure 2.33. The thick upper surface turbulent boundary layer was close to separation at the trailing edge. The boundary layer on the lower surface was tripped by a small diameter wire at 30% chord position. The area of investigation was extended over an area of  $60 \times 60 \text{ mm}^2$  centred on the trailing edge. This zone was divided into a fine measurement grid, with fine steps near the model surface in order to capture the flow behaviour in the boundary layer and near the wake centreline. Coarser grid steps were used in the outer region, where flow phenomena were of less importance.

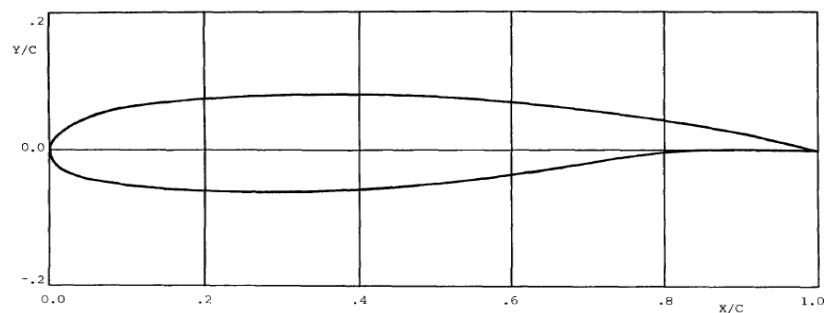


Figure 2.33: NLR 7702 airfoil 2D schematic [1]

All the quantities were scaled with the free stream speed, measured by a Pitot static tube at the entrance of the test section. Then as the uncorrected LDA data showed good agreement with hot-wire data, the researchers decide to ignore velocity bias corrections. Moreover, the law of the wall used to find the wall-distance correction and skin friction coefficients used to compare with theoretical data and agreed within  $\pm 5\%$ . The accuracy examined by comparing boundary layer and wake results at different stations and the agreement with LDA data was pretty good. Finally the two-dimensionality was also validated measuring mean velocity and turbulence profiles at different spanwise positions.

According to results, the difference in thickness of both boundary layers is outstanding. The upper surface boundary layer thickness increases while the lower stays constant. Hence, the upper is decelerated and the lower is accelerated. At the trailing edge, the two layers meet at an angle, resulting in a highly asymmetric near wake. Most of the lower surface boundary layer, the turbulence was suppressed by the favourable pressure gradient. Moreover, there is a rapid growth of normal and shear stresses near the wake centreline. In this region, the very intense mixing of the two merging layers controlled the turbulence mechanism. After a while the peaks start growing even more and dominate the lower half of the wake. This is shown for the far wake schematically in Figure 2.34(b).

Due to adverse pressure gradient, the displacement thickness and momentum thickness of the

upper surface boundary layer were considerably greater than the lower surface. It was also shown that in the near wall region both simple algebraic turbulence models of Michel and Cebeci & Smith, underestimated the experimental results, while in the outer zones, these models extremely overestimated the eddy viscosity and Prandtl mixing length by a factor of 2. The main conclusion was that LDA is a powerful tool for measuring various turbulence quantities, even in this kind of complex flows [1].

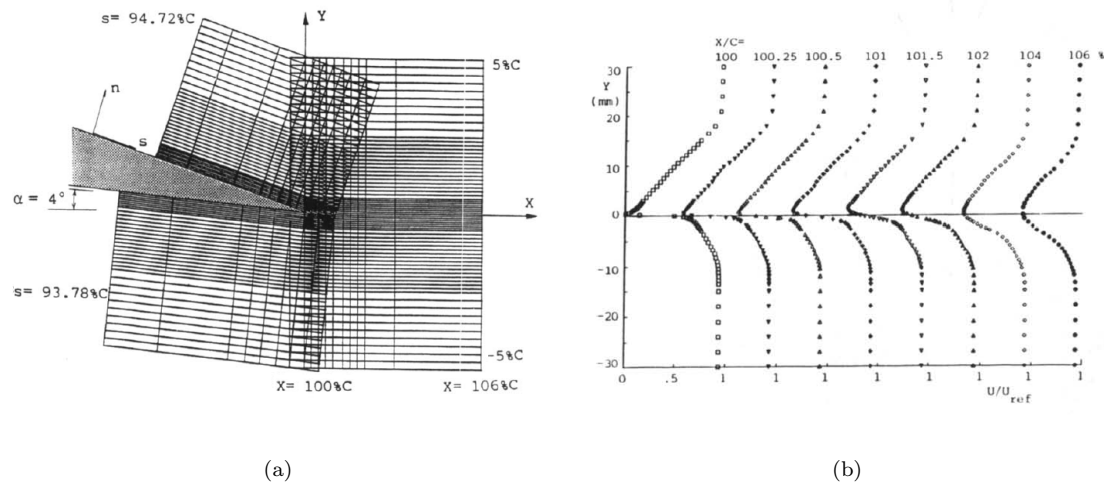


Figure 2.34: Measurement grid (a) and (b) Distributions of mean streamwise velocity in the wake [1]

The next work could be linked to the case of this thesis work, as the analysis of the flow-field was done for a two-element airfoil. During take-off and landing situations, the flow over the aft portion of a multi-element airfoil could be subjected to strong adverse pressure gradients, merging shear layers, strong interactions between viscous and non-viscous flows, streamline curvature and asymmetric wakes. The ability to calculate this kind of flows is not yet satisfactory due to the limited available measurements necessary for a better understanding of the flows in the neighbourhood of flap trailing edges [2].

The first test conducted was for a moderate flap deflection angle and had no-boundary layer separation, in which the wing-flap arrangement was mounted vertically in the wind tunnel. The second arrangement was mounted horizontally in the wind tunnel and had a flap deflection angle which lead to a massive separation over the aft 61% of the flap. To begin with the set-up, the test was conducted at NASA Ames Research. The NACA 4412 section used for the main airfoil section and a NACA 4415 for the flap section. The wind tunnel set-up used is presented in Figure 2.35

The chord length of the main airfoil was 0.9 m and the chord length of the flap was 0.36 m. The model's span was 3.05 m. The gap was set at 3.5% and the overlap at 2.8%. Moreover, the angle of the flap was set at  $21.8^\circ$  in comparison to the main wing angle of attack which selected to be at  $8.2^\circ$ . Boundary layer trips used on the suction and pressure surfaces of the main wing and flap to ensure uniform flow transition of the laminar boundary layer to a turbulent boundary layer across the span.

The test speed was 30 m/s and the Reynolds number was  $1.8 \cdot 10^6$ . Tufts and oil flow visualisation showed the flow to be two-dimensional over the central 65% of the main airfoil's span. Pressure measurements conducted using surface pressure taps with very good repeatability. In addition, sting-static Pitot tube used for pressure measurements in the tunnel and roof boundary layers. Upstream of separation and for most of the wake, the velocity was measured using hot wire anemometry. But for zones of reversed flow and high turbulence 3D laser velocimetry was used to obtain the velocities.

Presenting the main results of this work, in terms of the pressure, the suction decreased monotonically towards the trailing edge and the pressure was reasonably flat in this region. The rate of decrease of flap suction pressure was noted to reduce at 20% of flap chord, just downstream of the main airfoil trailing edge. In addition the  $C_l$  value was found as 3.19 and the  $C_d$  value was estimated as 0.066 using a velocity profile measured one chord length downstream from the flap trailing edge. The pressure distribution for both main wing and flap is presented in Figure 2.36.

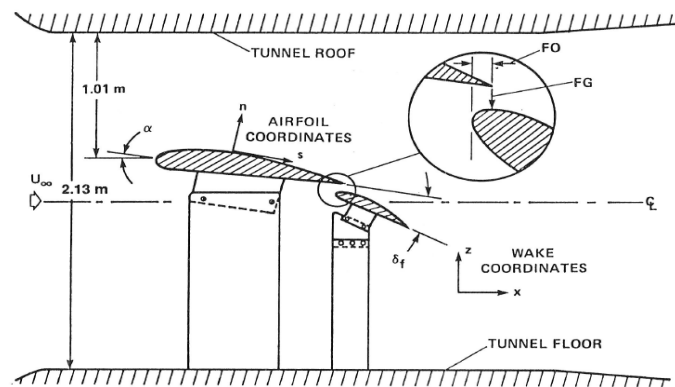


Figure 2.35: Installation of airfoil in the Ames 7- by 10-Foot wind-tunnel used for the experiments presented by D. Adair et al. [2]

Moreover, some corrections have been made to see the effect of tunnel wall interference, by doing calculations with and without the tunnel walls. In terms of velocity results, boundary layer separation was noted at 25 mm upstream of the flap trailing edge. Negative flow was also found to persist to about 27 mm beyond the trailing edge and a thin intermittent of negative flow covered the mean negative flow. The maximum height of the recirculation flow was found to be 10 mm. Moreover, the displacement and momentum thickness steadily increased as the shear layer met increasingly the adverse pressure gradient region. On the other hand, in the wake zone both these parameters decayed. From the velocity profile was quite clear that the profiles are in an adverse pressure gradient over the main airfoil. On the flap the boundary layer was thin but was gradually thickened in downstream distance. The magnitude of the reversed flow was found very small at the trailing edge with a maximum velocity of 1.2 m/s noted. This jet dominated the near wall flow over the flap. Finally, downstream, the main airfoil and flap, wakes fully merge and profiles showed an asymmetric wake development. Finally, it was recommended to consider the effects off the wind tunnel wall interference when calculating the flow field [2].

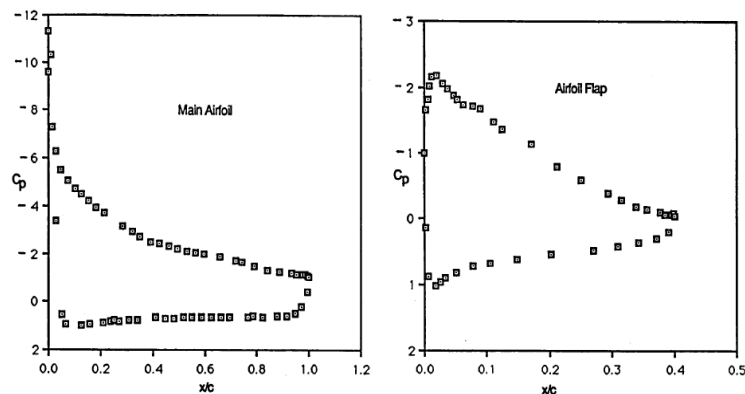


Figure 2.36: Surface pressure distribution for the whole configuration (wing & flap) [2]

The last work presented is from researchers in China [37]. The title of this work was "*Aerodynamic Characteristics of High-Lift Devices with Downward Deflection of Spoiler*". In this work, it was tried to improve the performance of landing through the method of downward deflection of the spoiler. The concept of downward deflection of the spoiler is shown schematically in Figure 2.37.

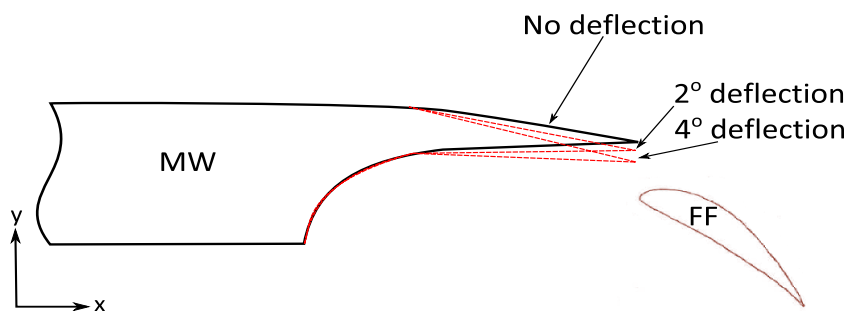


Figure 2.37: Downward deflection of the spoiler according to X. Wang et al. [37]

Using the CFD approach, the capability of downward deflection of a conventional spoiler as a device of increasing lift in landing was investigated. Most of the computational methods that have been used to compute the high-lift flow field since the 80's are integral boundary-layer (IBL) and Reynolds-averaged Navier-Stokes (RANS) methods. In this research, RANS method of commercial software Fluent applied, using SA turbulence model. More details on the CFD settings could be found on the paper itself [37]. To validate the numerical results, two different airfoils configurations used one three-element configuration in 2D and one 3D NASA trap wing. The results compared with experiments. For the 2D case, the slat angle was set at  $-30^\circ$  and the flap angle at  $30^\circ$ . The gap and overlap of the flap was  $0.0127c$  and  $0.0025c$  respectively. In addition, the configurations tested at two different Reynolds numbers, of  $5$  and  $9 \times 10^6$ . From the comparison, of experimental and numerical results, it was very clear that the lift coefficient was fairly accurate in the linear region of lift coefficient. However, the error increased in the region of stall angle. In terms of the drag, the calculated results are higher than the experimental ones.

For the 3D case, a landing setting of slat angle at  $30^\circ$  and flap angle at  $25^\circ$  is presented. The mean aerodynamic chord of the model was 1 m, the model semi-span was approximately 2.16 m and the reference area was  $6.71\text{m}^2$ . The flap gap and overlap values were set as  $0.005c$  and  $0.015c$  respectively. The configuration tested at  $\text{Re} = 4.3 \cdot 10^6$  and turbulent flows were assumed in the computations. The results indicated that numerical computations accurately predicted the lift and drag of the high-lift devices. The error was increased for high angles of attack but the trend was similar to experimental results. The results for the downward deflection of just the spoiler have shown that there was a decrease of lift with the increase of deflection angle. Moreover, they were only got worse with just the downward deflection of the spoiler.

Then, the results of downward deflection of the spoiler with the invariable parameters of gap and overlap of the flap. For this case, the aerodynamic characteristics will improve with the increase of angle of deflection of the spoiler. The last thing shown in this work was the effect of the downward movement of the spoiler in the 3D configuration by keeping the invariable parameters of gap and overlap of the flap. As it is shown in Figure 2.38, by using a spoiler deflection of 8 degrees, the lift coefficient and lift to drag ratio increase. Hence, it is predicted that the aerodynamic characteristics will improve with the downward deflection of the spoiler.

Concluding, if the spoiler deflects only downward, the aerodynamic performance will become worse than the original configuration. On the other hand, the aerodynamic performance will improve, if the spoiler is deployed downwards under the conditions of making the gap and overlap parameters of the flap the same as the original configuration [37].

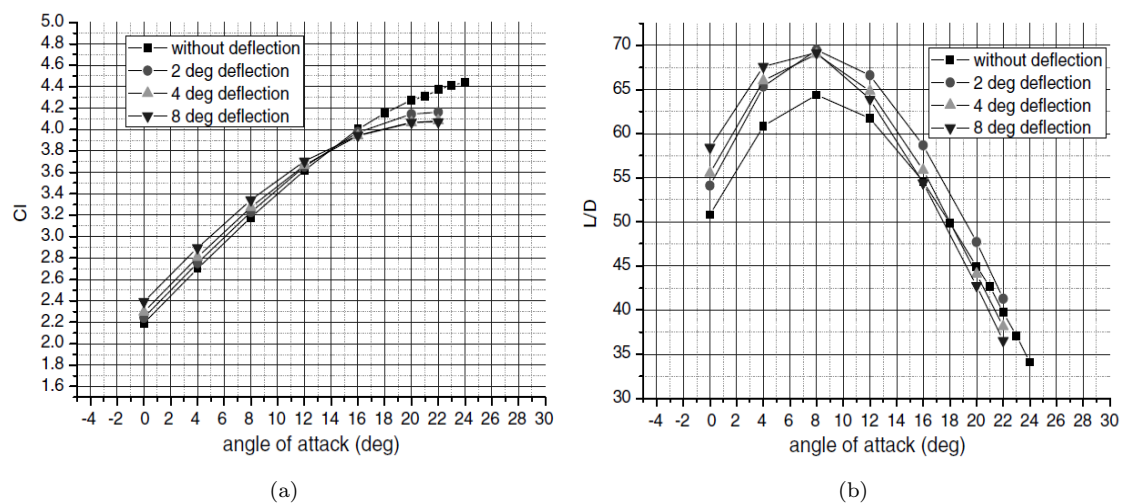


Figure 2.38: Lift coefficient (a) and lift-to-drag ratio (b) under the conditions of different angles of deflection of the spoiler [37]

## Chapter 3

# Wind Tunnel Testing Campaign I

This chapter presents all the relevant aspects with respect to experimental apparatus, set-up, procedures and results of this testing campaign. As the focus is on a two-element airfoil, a wing-flap model configuration which was already available for wind-tunnel testing, was chosen. This model, together with the flow facility (LTT) in which the experiments were carried out and the passive flow control device (DSP), will be discussed in detail in the next section. For additional information based on mentioned topics, the reader is also referred to Appendix A at the end of the report.

### 3.1 Experimental Apparatus

#### 3.1.1 Experimental Facility: Low Turbulence Tunnel (LTT)

The experiments of this research were conducted in the Low-Speed Low-Turbulence Wind tunnel (LTT) of Delft University of Technology. This atmospheric tunnel, is of closed-throat, single-return type and was constructed around and through a building, see Figure 3.1. A six-bladed fan is driven by a 525 kW DC motor, giving a maximum test section velocity of about 120 m/s. The maximum Reynolds number for two-dimensional testing is about  $4.8 \cdot 10^6$ , based on a chord model of 0.6 m [9].

The combination of anti-turbulence screens located in the settling chamber and a high contraction ratio of 17.8, results in an uniform velocity profile with a low free-stream turbulence level in the test section with variation from 0.015 % at 20 m/s to 0.07 % at 75 m/s. The interchangeable octagonal test-section is 1800 mm wide, 1250 mm high and 2600 mm long.

Mechanically actuated turntables flush with the test-section top and bottom wall, providing positioning and attachment for a two-dimensional model. The standard wind-tunnel testing equipment consists of an electronically read 200 tubes multi-manometer with fibre optic cells, a 6-component balance, a 192 ports electronic pressure scanner system, hot wire anemometry and PIV systems. For flow visualization purposes an infra-red camera system is also available. Data are recorded using an electronic data acquisition system and are on line reduced using the laboratory computer. To perform pressure measurements for a test model, the software package "Profmeas" was used. This program allows the user to measure, store and correct the data from each test. Below, a wind-tunnel layout schematic with a picture of the wind-tunnel's test section is presented in Figures 3.1 and 3.2.

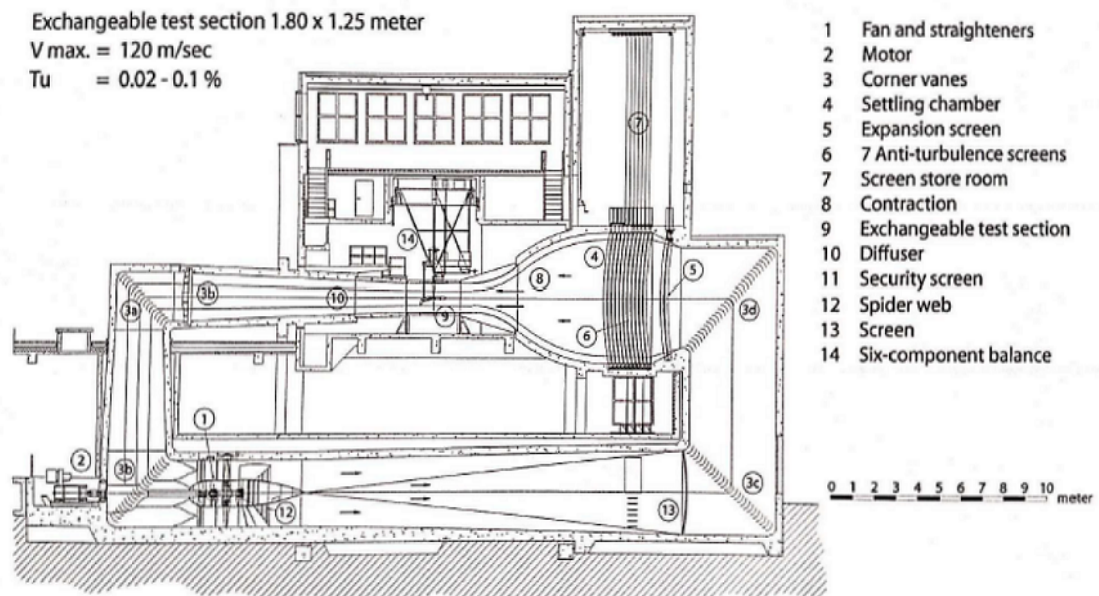


Figure 3.1: Schematic layout of the Low-Speed Low-Turbulence Wind-tunnel [9]



Figure 3.2: Low-Speed Low-Turbulence Wind-tunnel test section area overview [9]

### 3.1.2 X-400 Wing-Flap Configuration

The wing-flap model used for this research project has its roots in the early 90's when the Extra company started the EA-400 project in cooperation with Delft University of Technology. The airfoil's design requirements were defined as a  $C_{l_{max}} \geq 3.2$ , drag as low as possible at a  $C_{l_{design}} \geq 0.4$ , stall characteristics at least equal to the NLF 416 airfoil and the implementation of a flap. Finally, the end product of this cooperation was the Natural Laminar Flow airfoil. However, extensive testing of this model resulted in a redesign of the slot entrance combined with the application of a zig-zag tape just upstream of where the new flap cove starts (To eliminate a laminar separation bubble). These adjustments realized lower drag of the airfoil [9]. The new modified airfoil, which is also the model used for this research project, is shown in Figure 3.3.

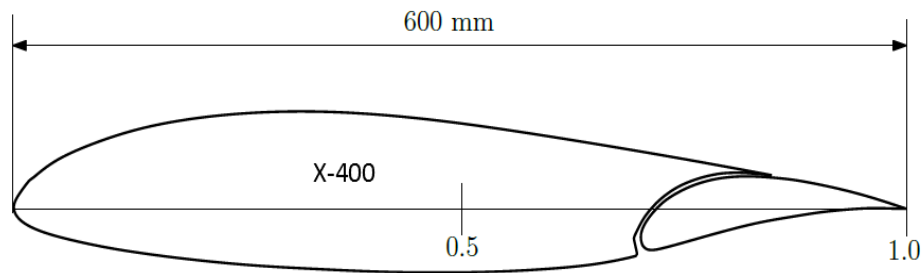


Figure 3.3: 2D schematic of the X-400 wing-flap configuration with retracted Fowler flap [9]

In the flap-nested configuration, the model has a chord of 600 mm and with its length of 1250 mm it spans the entire tunnel height as shown schematically in Figure 3.4. The model is installed vertically between rectangular end-plates which are flush with the turntables. The axis of rotation of the turntables was at 50% c. The flap is of a Fowler type with a chord length of 30% c. As shown in Figure 3.5, the geometric details of the flap settings are defined by the gap, overlap and deflection. The definition of the flap deflection, is set as the chord line of the flap in nested position.

Moreover, the X-400 is characterized by the sharp slot entry shape resulting in a small gap between the lower surface of the wing and the retracted flap. For pressure measurements, a total of 56 pressure orifices on the main wing and 28 on the flap (0.4 mm diameter) were located in diagonal rows between 450 mm and 550 mm from the bottom of the test section. This pattern was designed to minimize interference effects from upstream pressure orifices with downstream ones. To prevent three-dimensional separated flow near the tunnel walls as a result of early separation, boundary layer suction was applied through 5 mm diameter holes with centres spaced 10 mm apart. Near the flap surface the suction is applied through 4 mm diameter holes with centres spaced 8 mm apart, shown in Figure 3.6 .

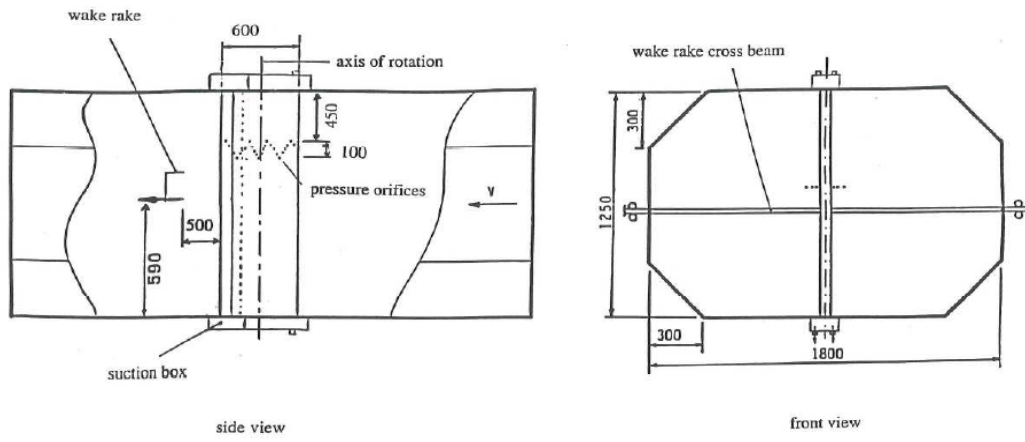


Figure 3.4: Model set-up and geometrical information with respect to the wind-tunnel section [9]

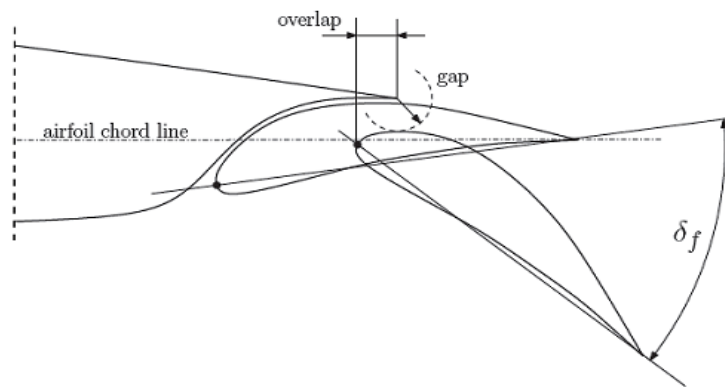


Figure 3.5: Gap and overlap definitions of the X-400 wing-flap configuration [9]

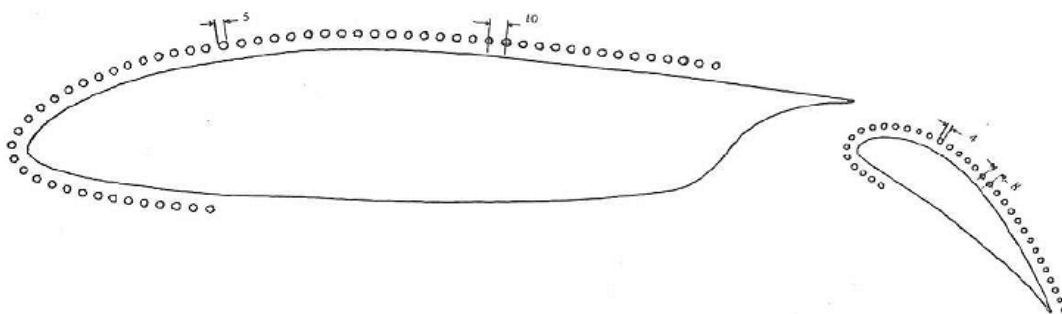


Figure 3.6: Suction orifices at the Low-Speed Low-Turbulence Wind-tunnel wall [9]

### 3.1.3 Drooped Spoiler Panel (DSP)

The drooped spoiler panel was a fundamental part of the flow control device and the most relevant information about it will be presented. In order to design these panels, literature information in combination with the X-400 wing-flap configuration coordinates were taken into account. In Table 3.1, the geometrical information of each spoiler panel is presented. Moreover, in Figure 3.7, a schematic of the drooped spoiler panel concept is shown.

DSP No.	$\theta_{dsp}$ [°]	t [mm]	$x_{straight}$ [mm]	$x_{inclined}$ [mm]
1	15°	1.5	48	30
h1&h2	15°	1.5	48	30
2	0°	1.5	48	30
3	6°	1.5	48	30
4	8°	1.5	48	30

Table 3.1: Drooped Spoiler Panel (DSP) geometrical definitions

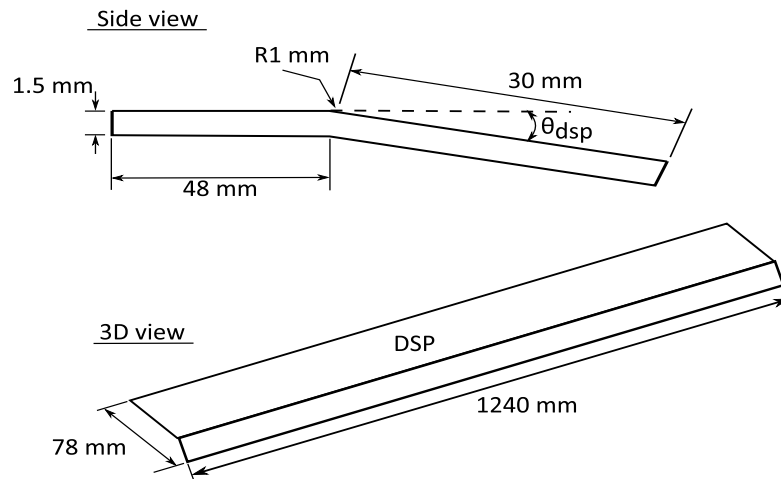


Figure 3.7: Drooped Spoiler Panel (DSP) concept schematic, including geometrical definitions

To begin with, the DSP as a flow control device was consisted of three different components, which had to be attached on the X-400 main wing model. The first one was the upper surface plate which included the holding support structures. The next two were the lower surface plate and the drooped spoiler panel which were all connected with small nuts and bolts. The drawing of the holding structure is presented in Figure 3.8. The straight part of the drooped spoiler panel was 48 mm, the inclined part was 30 mm and the thickness was strictly 1.5 mm, in order to fit in the holding structure gap.

When all the parts were ready, they were attached on the wing-flap configuration model. The upper and lower surface plates were placed first at the trailing edge of the main wing using double-sided tape. Then the drooped spoiler panel was also attached on the configuration and screwed with the plates using nuts and bolts. The wing model with the upper and lower surface plates attached could be seen in Figure 3.9.

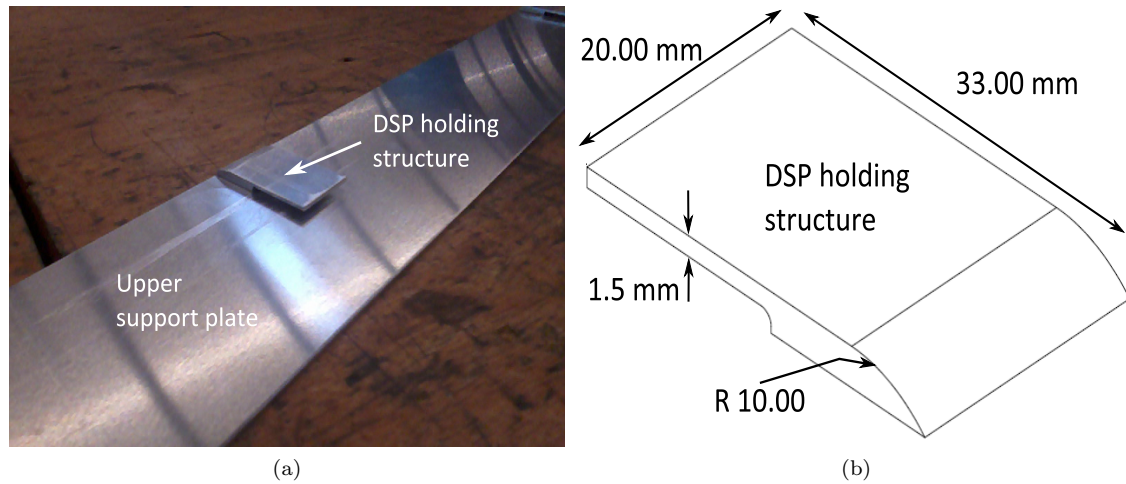


Figure 3.8: DSP holding structure (a) 3D actual component and (b) 3D drawing

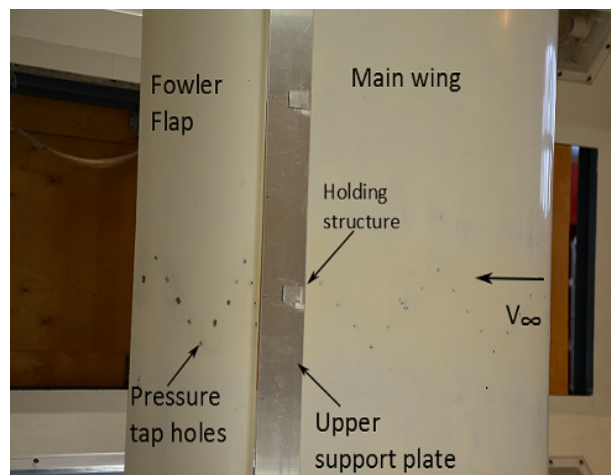


Figure 3.9: Upper surface plate attached on the X-400 wing-flap scale model

## 3.2 Pressure Measurements & PIV Set-up

As the wind-tunnel test section with the X-400 wing-flap model was placed in the wind tunnel, the Fowler flap was set at the right angle,  $\delta_f$ . It was decided to carry out the experiments at a flap angle of  $50^\circ$ . The reason for using this high angle of attack, was due to the fact that was already known from previous experiments, that with this configuration (X-400), the flow on the flap was separated from lower angles ( $< 40^\circ$ ). Thus, as the main objective of the testing campaign was to determine the effectiveness of the drooped spoiler panel (DSP) on the flap flow, this relatively high angle was selected.

The next step was to set the wanted overlap and gap values of the wing-flap configuration. The overlap was set at 0% c and the gap at 3.72% c. This information is also presented in Table 3.2. For further information on the detailed procedure for setting-up these parameters, the reader is referred in Appendix A.

$\tilde{\delta}_f [^\circ]$	$x_{\text{overlap}} [\%c]$	$y_{\text{gap}} [\%c]$
$50^\circ$	0	3.72

Table 3.2: X-400 Wing-Flap Model Settings as set for pressure measurement and PIV experiments

The last part of the first wind tunnel testing campaign, was to perform Particle Image Velocimetry (PIV) tests. This was done with the aim to get a deeper understanding of the flow in the main wing trailing edge-Fowler flap region. Anyone familiar with recent experimental techniques and especially Particle Image Velocimetry (PIV), would know that this is the most advanced in the field of aerodynamics. This non-intrusive technique, could give a great insight into the flow field and that is why was chosen for this research.

The first thing done, was to replace one of the quadrant parts of the lower circular disc wall, with a plexiglass transparent one, to allow for camera optical access in the test section. Moreover, the top circular disc, as well as the side section windows were covered using duct tape and the wing-flap configuration was painted black, to avoid reflections. The configuration was sprayed at the point where the laser beam was impinging the surface. The transparent quadrant of the lower disc and the tape covered top disc including the black painted configuration, are both shown in Figure 3.10.

The next step was to construct the holding structure of the laser. The structure, was placed parallel to the test section and on the right height with respect to the measurement plane. Then, the laser sheet was aligned according to the measuring position. Moreover, the laser lenses positioned in front of the laser head by placing two negative lenses, one positive and one cylindrical at the end, in order to spread the beam into the test section. The lenses placement is shown schematically in Figure 3.11. Additionally, the seeding was placed behind the test-section, through a tunnel's opening. Below, in Figure 3.12, a schematic overview of the PIV set-up is shown.

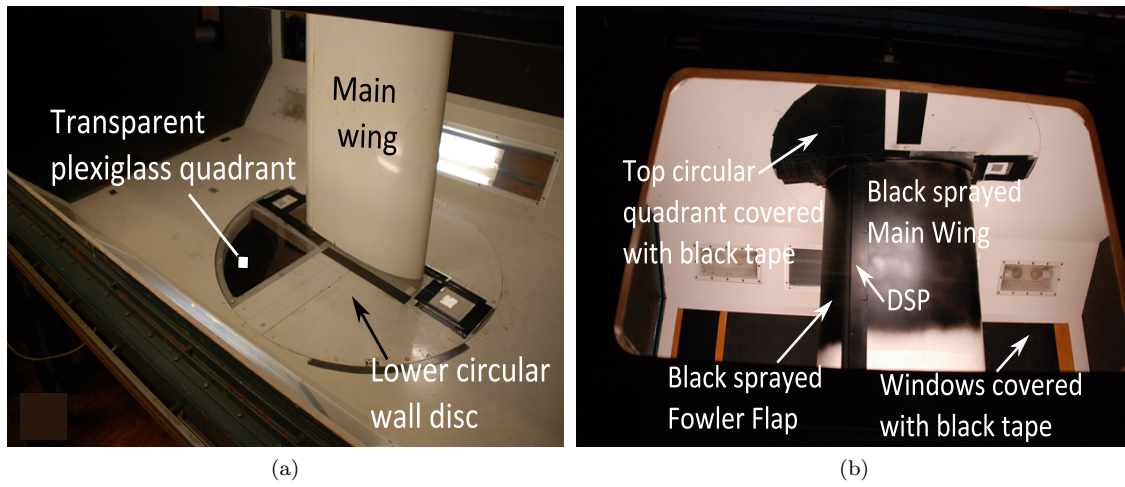


Figure 3.10: Transparent quadrant window on the lower circular disc of the LTT's test section (a) for visibility purposes and (b) Upper circular disc covered with duct tape and black painted configuration to avoid reflections

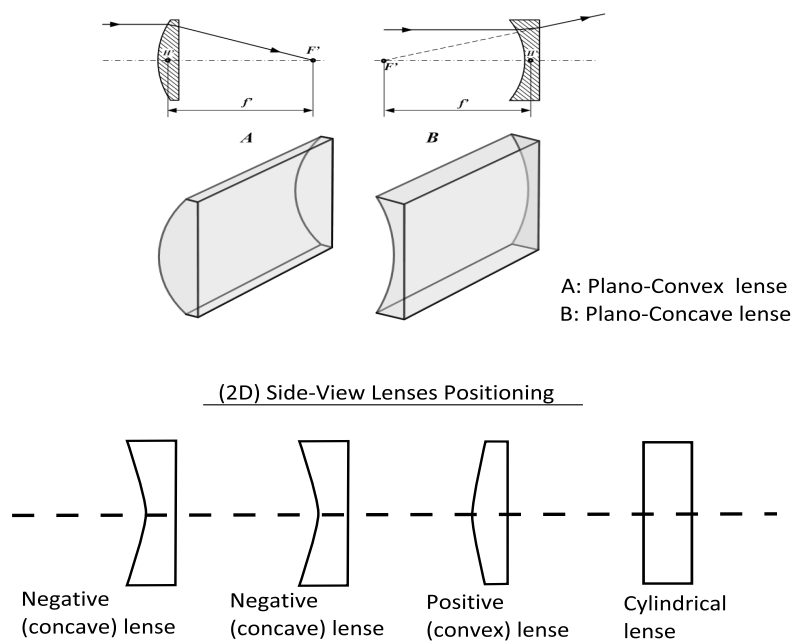


Figure 3.11: 2D lenses placement schematic in front of the laser head positioned from left to right

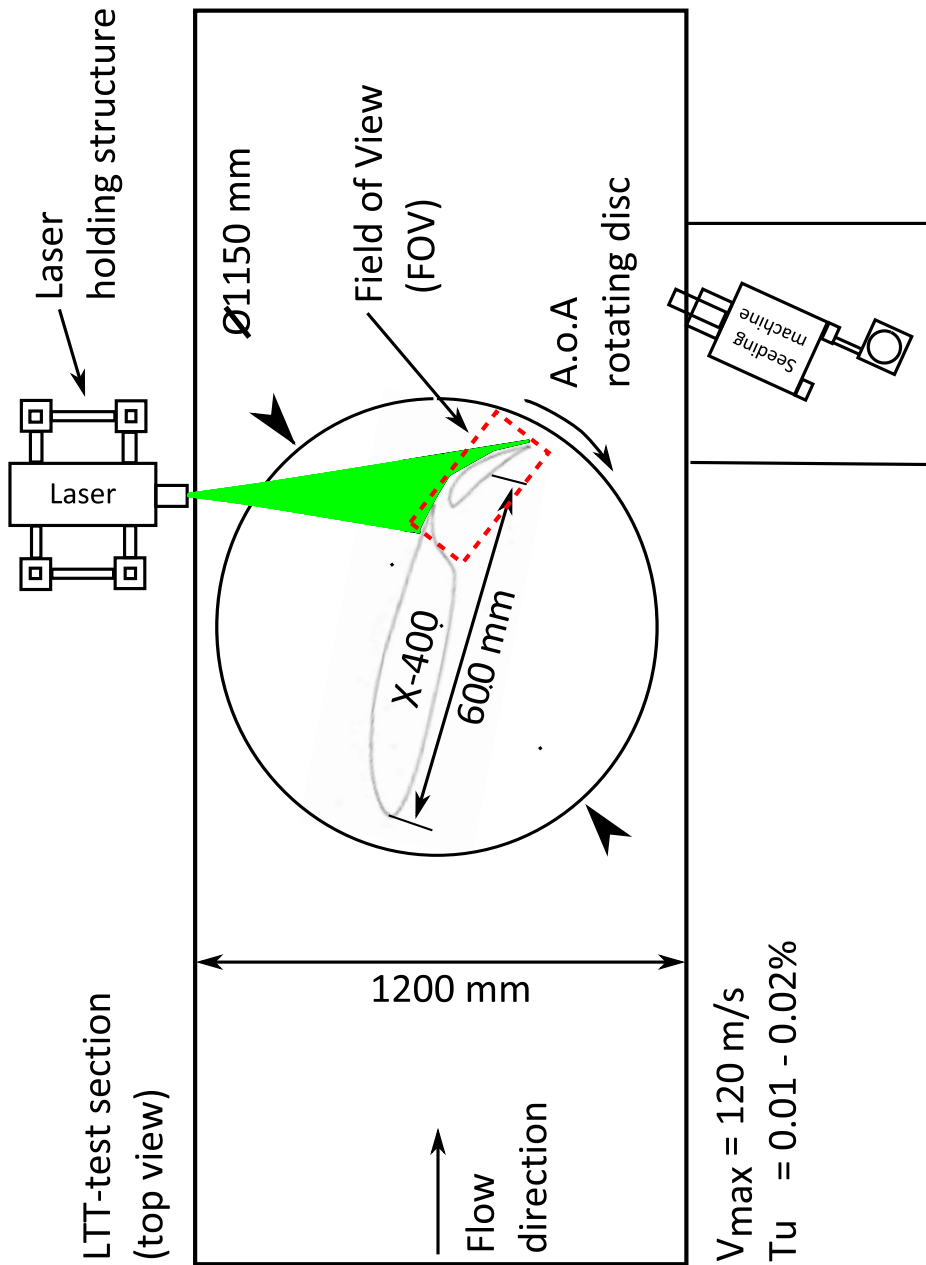


Figure 3.12: 2D schematic overview of the PIV set-up in top view, including geometrical information

Then, the camera was mounted on the lower circular disc of the test section with a simplified structure. The positioning of the camera is shown in Figure 3.13. By mounting the camera on the lower rotating disc, it would not be necessary to repeat the calibration procedure for each angle of attack, as the field of view (FOV) would remain the same, even if the whole configuration was moving. Moreover, this placement would allow the camera to be as close as possible to the measuring plane. The slight angle of the camera, was not an issue of having the plane out of focus, thus, the use of "scheinplug" was not necessary. Concluding, as the camera was in place, the calibration procedure carried out. For more detailed information on the PIV theoretical background, set-up, equipment used, and calibration procedure, the reader is referred to Appendix A.

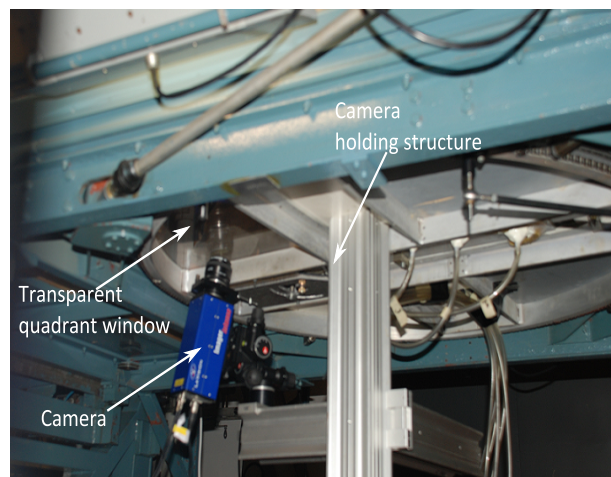


Figure 3.13: Camera placement below the wind tunnel test section

## 3.3 Experimental Procedure

### 3.3.1 Flow Visualisation Techniques

#### Tufts flow visualisation

The first thing done was flow visualisation using woollen tufts. Eighty-four black tufts positioned on the white surface of the X-400 model for contrast purposes. The length of the tufts was approximately 50 mm each and they were placed at a distance of 50 mm of each other and on the suction side of the model configuration. Then, they were tested for different speeds up to 40 m/s with and without the drooped spoiler panel (DSP) and at different main wing angles of attack. The final placement of the tufts on the wing-flap model is presented in Figure 3.14.

#### Oil flow Visualisation

Then, oil flow visualisation used, in order to have a broader idea of the flow phenomena with and without the drooped spoiler panel on the Fowler flap. To make the oil liquid needed, 50 cc of oil paraffin used. In general, there are three different types of paraffin liquid; thin, medium and thick and it's use depends on flow speed. For these tests, the thick paraffin liquid used as the tests performed at 40 m/s. Then 20 drops of fluorescent oil additive were mixed with the paraffin

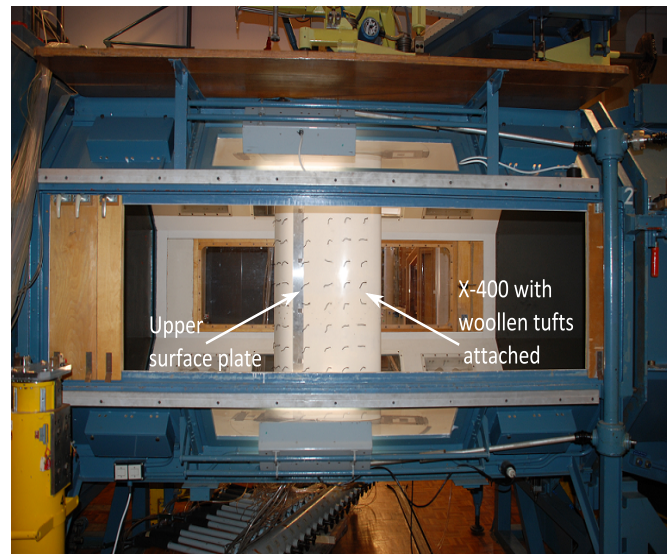


Figure 3.14: Woollen tufts placed on the upper surface of the X-400 wing-flap configuration

liquid followed by carefully application on the Fowler flap perpendicular to the flow. After that the tunnel was started and for each run, the angle of attack was changed first and then the oil liquid was applied on the region of interest. The application of paraffin oil on the model is shown in Figure 3.15. Before applying the paraffin oil, the wind tunnel model was cleaned carefully in order to have a very smooth surface and all the pressure taps and suction holes were covered with duct tape to prevent oil filling them.

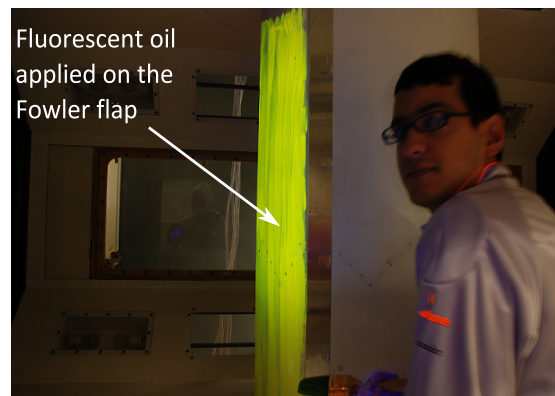


Figure 3.15: Paraffin oil applied on the Fowler flap of the X-400 configuration

The test matrix used for both flow visualisation tests is presented below in Table 3.3.

### 3.3.2 Pressure Measurement Techniques

#### Pressure tap measurements

The next part of testing, included surface pressure measurements in order to determine the pressure distributions and hence the lift of the wing-flap model. The drag was measured using

Flow Visualisation Test Matrix		
TestCase	$\alpha$ – Range[ $^{\circ}$ ]	$V_t$ [m/s]
Without DSP	0-2-4-6-8-10-12-14-15	40
DSP1	0-2-4-6-8-10-12-14-15	40

Table 3.3: Test matrix for flow visualisation tests (woollen tufts and oil flow)

the wake rake which was positioned behind the wing model. For these measurements, the clean wing configuration (CWC), DSP1 (at  $15^{\circ}$ ), DSP2 (at  $0^{\circ}$ ), DSP3 (at  $6^{\circ}$ ) and DSP4 (at  $8^{\circ}$ ) tested at tunnel speeds from 10 to 50 m/s, and all the other parameters such as flap angle, overlap and gap remained unaltered. The only parameter altered was the angle of attack of the whole configuration and is presented in Table 3.4.

Surface Pressure Tap Measurements Test Matrix					
<b>CWC</b>	<b>DSP1</b>	<b>DSP2</b>	<b>DSP3</b>	<b>DSP4</b>	<b>Settings</b>
AoA [ $^{\circ}$ ]	AoA [ $^{\circ}$ ]	AoA [ $^{\circ}$ ]	AoA [ $^{\circ}$ ]	AoA [ $^{\circ}$ ]	
0	0	0	0	0	$V_t = 10 - 50\text{m/s}$
2	2	2	2	2	
4	4	4	4	4	
6	6	6	6	6	$x_{\text{overlap}} = 0\%c$
8	8	8	8	8	
10	10	10	10	10	
12	12	12	12	12	$y_{\text{gap}} = 3.7\%c$
14	14	14	14	14	

Table 3.4: Test matrix for surface pressure tap measurements



Pressure Probe Measurements Test Matrix (1)			
Point No.	x [mm]	y [mm]	z [mm]
Pt.A	150	640	15
Pt.B	170	640	15
Pt.C	190	640	15
Pt.D	210	640	15
Pt.E	230	640	15
Pt.F	250	640	15
Pt.G	270	640	15
Pt.H	290	640	15
Pt.I	310	640	15
Pt.J	330	640	15
Pt.K	380	640	15
Pt.L	430	640	15
Pt.M	480	640	15
Pt.N	500	640	15
Pt.O	520	640	15
Pt.P	570	640	30
Pt.Q	620	640	60
Pt.R	670	640	60

Table 3.5: Test matrix (1) for pressure measurements at  $\alpha = 0^\circ$ ,  $\delta_f = 50^\circ$  and DSP1 (at  $15^\circ$ ) attached

points used as the wake area was of great interest. The same points and procedure followed for the  $8^\circ$  case. The probe set-up and location of measurement points, are both shown in Figure 3.17.

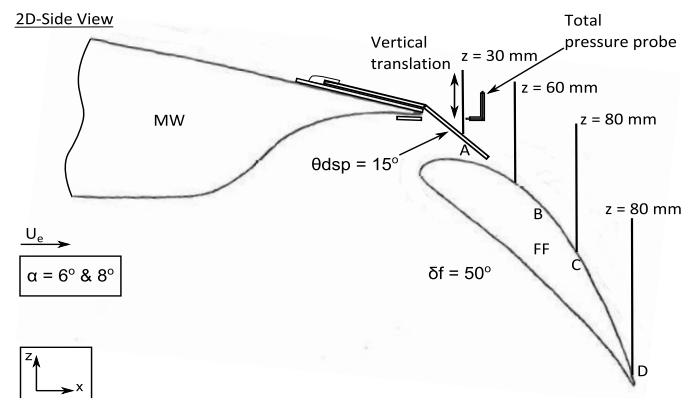


Figure 3.17: 2D schematic of the probe set-up and measurement points location for total pressure probe measurements at  $\alpha = 6^\circ - 8^\circ$ ,  $\delta_f = 50^\circ$  and DSP1 (at  $15^\circ$ ) attached

Finally, the test matrix of these measurements is presented in Table 3.6

Finally, some simple passive flow control solutions tested on this configuration to determine their influence on wake bursting phenomenon. The first test carried out was using counter-rotating pairs of sub-boundary layer vortex generators. Their height was equal to the boundary

Pressure Probe Measurements Test Matrix (2)			
Point No.	x [mm]	y [mm]	z [mm]
Pt.A	540	640	30
Pt.B	570	640	60
Pt.C	620	640	80
Pt.D	670	640	80

Table 3.6: Test matrix (2) for pressure measurements at  $\alpha = 6^\circ - 8^\circ$ ,  $\delta_f = 50^\circ$  and DSP1 (at  $15^\circ$ ) attached

layer thickness halved ( $h = \delta/2$ ) and they were placed 140 mm in front of the drooped spoiler panel, DSP1(VG1). In order to select the right height for the vortex generators, a careful study was carried out using the probe measurement data, in order to determine the boundary layer thickness, which was computed to be approximately  $\delta = 14\text{mm}$ . The vortex generators were evenly distributed on the wing model's span. A detailed schematic including all the geometrical information on vortex generators, as long as a picture of them is presented in Figure 3.18.

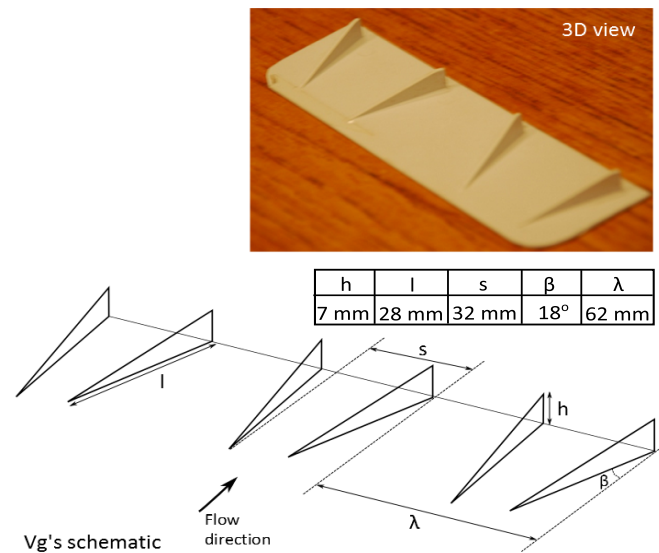


Figure 3.18: Vortex generators schematic and picture, used on the main wing of the X-400 wing-flap model configuration

To find the best position for the vortex generators, additional tests carried out, first by placing woollen tufts on the wing in front and behind of the drooped spoiler panel. It was realised that at low angles of attack the position was reasonably good, as there was no flow separation on the main wing of the model. But, as soon as the angle of attack increased, the vortex generators were inside the separated region. As a result, different positioning and number of rows had to be considered for better and more efficient mixing. At the end, the vortex generators placed 270 mm in front of the drooped spoiler panel, DSP1(VG2). At this position, they were outside the flow separation region on the main wing, especially at higher angles. The position of vortex generators on the X-400 wing-flap model configuration with respect to the drooped spoiler panel, is shown in Figure 3.19.

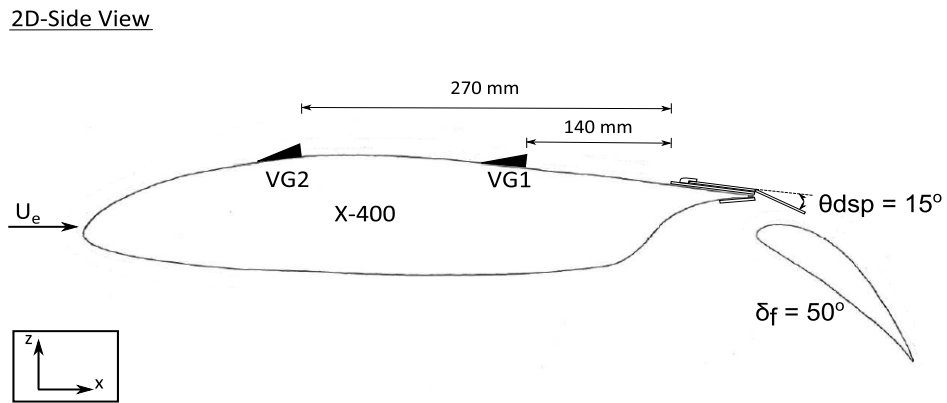


Figure 3.19: Vortex generators placement on the X-400 wing-flap model configuration with respect to the drooped spoiler panel (DSP1)

Concluding, the last passive control devices tested, were DSP1(h1) and DSP1(h2) with holes across their spanwise direction. Two different configurations tested at 40 m/s, keeping all the other parameters unaltered, having holes of 2 and 4 mm respectively. These holes were placed on the inclined part of the panel as is shown in Figure 3.37, including all the relevant geometrical information for these passive control devices. The reason for testing this configuration was that a pressure relief could be expected close to the leading edge of the Fowler flap, which should possibly reduce the effect of wake reversal.

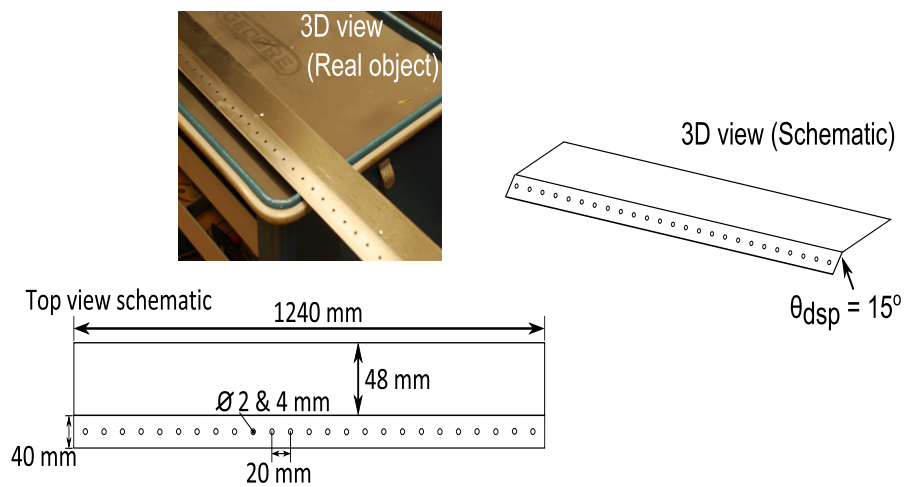


Figure 3.20: Schematic of DSP1, with 2 and 4 mm holes on it's inclined panel, including geometrical information

### 3.3.3 Particle Image Velocimetry (PIV)

The experimental procedure for PIV consisted of 15 different test cases. All test cases, included testing of the X-400 wing-flap model, with or without the drooped spoiler panel (DSP) at different wind tunnel velocities and three different angles of attack of  $0^\circ$ ,  $6^\circ$  and  $8^\circ$ . The settings of flap angle, overlap and gap of the slot, remained the same as for previous tests.

Thus, the first three cases included tests of the clean wing configuration (CWC), without the drooped spoiler panel attached, at eight different velocities, ranging from 5 to 40 m/s. The angles tested, mentioned earlier. The next three cases, included tests with the DSP1 (at  $15^\circ$ ) attached. Then, the next three, included tests with the same configuration, but this time with surface roughness, at the pressure side of the main wing. For the roughness, double-sided tape with carborundum grain size 24 (0.841 mm) placed close to the leading edge of the main wing as shown in Figure 3.21. The thickness of the double sided tape was 0.11 mm and it's width was 50 mm. The distance of the roughness from the leading edge ( $x = 0$ ,  $y = 0$ ), was measured to be 60 mm, covering the whole span of the model.

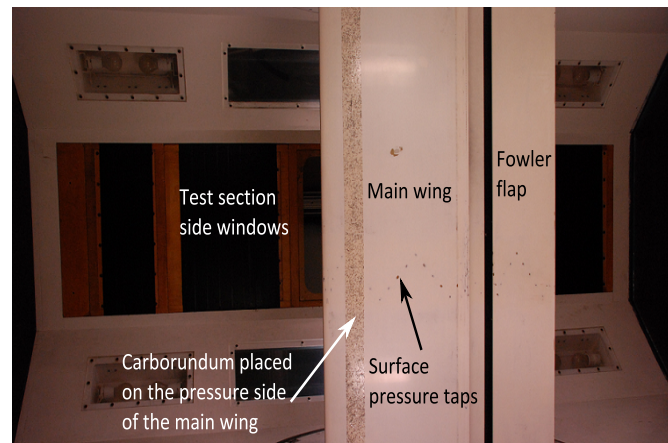


Figure 3.21: X-400 with carborundum roughness placed at the bottom side of the main wing

The range of wind tunnel speeds reduced from 20 to 40 m/s, for the cases where surface roughness applied on the model. Then, additional roughness was applied at the same position, but on the suction side, for symmetrical flow purposes. The last thing tested, was the upper surface roughness alone. The test matrix used for PIV experiments, is presented in Table 3.7. The matrix including Davis settings is presented in the Appendix A, at the end of the report.

PIV Test Matrix				
TestCase No.	Description	$\alpha$ [ $^{\circ}$ ]	$V_t$ Range [m/s]	Settings
TC.1	CWC	0	5-10-15-20-25-30-35-40	
TC.2	CWC	6	5-10-15-20-25-30-35-40	
TC.3	CWC	8	5-10-15-20-25-30-35-40	
TC.4	DSP1	0	5-10-15-20-25-30-35-40	$\delta_f = 50^{\circ}$
TC.5	DSP1	6	5-10-15-20-25-30-35-40	
TC.6	DSP1	8	5-10-15-20-25-30-35-40	
TC.7	DSP1 - (lower roughness)	0	20-25-30-35-40	$x_{\text{overlap}} = 0\%$
TC.8	DSP1 - (lower roughness)	6	20-25-30-35-40	
TC.9	DSP1 - (lower roughness)	8	20-25-30-35-40	
TC.10	DSP1 - (upper & lower roughness)	0	20-25-30-35-40	
TC.11	DSP1 - (upper & lower roughness)	6	20-25-30-35-40	
TC.12	DSP1 - (upper & lower roughness)	8	20-25-30-35-40	$y_{\text{gap}} = 3.7\%$
TC.13	DSP1 - (upper roughness)	0	20-25-30-35-40	
TC.14	DSP1 - (upper roughness)	6	20-25-30-35-40	
TC.15	DSP1 - (upper roughness)	8	20-25-30-35-40	

Table 3.7: Test Matrix for PIV experiments

## 3.4 Presentation & Discussion of Results

### 3.4.1 Flow Visualisation Techniques

#### Tufts flow visualisation

Firstly, the clean wing configuration (CWC) tested. At  $0^{\circ}$  and at 40 m/s tunnel speed, the flow was attached on the main wing but at the Fowler flap, flow separation occurred. However, the front part of the flap was unaffected from separated flow and this was possibly happening due to the upper surface plate presence. Hence, at low angles of attack of the main wing, the flap was affected by significant flow separation. As the angle of attack increased to  $10^{\circ}$ , it was clear that the flap was deloaded and the main wing was experiencing separated flow approximately after the aerodynamic centre ( $c/4$ ). Then, the flow at the Fowler flap looked attached compared to the angle of attack of  $0^{\circ}$ . At  $15^{\circ}$ , the main wing was separated and the flap flow was attached. A picture of this case is shown in Figure 3.22 (a).

Then placing the DSP1 on the main wing and keeping the tunnel speed at 40 m/s, for  $0^{\circ}$ , observing the movement of the woollen tufts, it was observed that the flow on the main wing and Fowler flap was attached, but with a slight unsteadiness. Increasing the angle of attack at  $2^{\circ}$ , the flow was attached on the main wing and flap. The same was observed at  $5^{\circ}$  as well, however, this time, the slight unsteadiness on the flap flow was not apparent, which could be explained by the increase of the angle of attack. Increasing further the angle to  $8^{\circ}$ , the flow was totally attached for both the main wing and Fowler flap. This is shown in Figure 3.22 (b). Finally, at  $10^{\circ}$ , the flow on the main wing separated at the last quarter of the wing's chord and was attached on the flap. Concluding, for  $15^{\circ}$  angle of attack, the main wing was separated after the aerodynamic centre of the wing ( $c/4$ ) and the flap flow was attached.

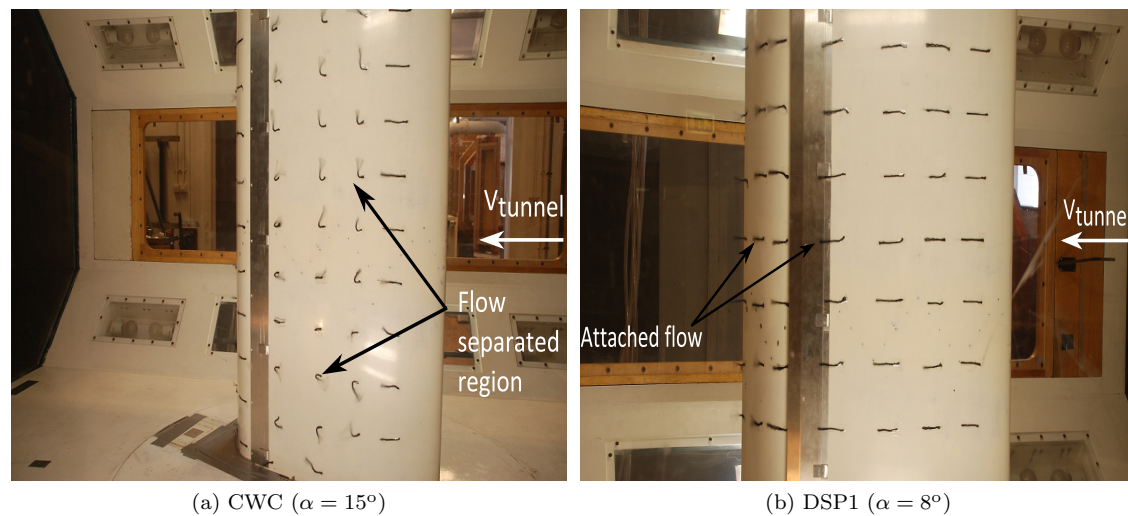


Figure 3.22: Flow visualisation using tufts (a) at  $\alpha = 15^\circ$  for CWC and (b) Attached flow observed at  $\alpha = 8^\circ$  with DSP1 attached on

### Oil flow Visualisation

Increasing the angle of attack at  $2^\circ$  for the CWC, the same phenomena observed, including attached flow, then a separation bubble, turbulent flow and finally flow separation at approximately half-chord length ( $c/2$ ). This is shown in Figure 3.23 (a). Then at  $5^\circ$ , the same observations made, but with three dimensional effects more pronounced, including vortices in the separated region. However, at  $8^\circ$ , different phenomena noticed, with flow staying attached up to the quarter chord ( $c/4$ ) of the flap, then a separation bubble appeared and then the flow was again attached up to the trailing edge. At the very end of the trailing edge, a small amount of the flap was close to separation or separated, however, the effect would be very small. At  $10^\circ$  and  $15^\circ$ , the flow was attached on the whole suction side of the flap.

Then, the DSP was attached on the wing-flap configuration and the paraffin oil was applied in front of the DSP and up to the trailing edge of the flap. Starting with an angle of attack of  $0^\circ$ , the flow was attached on the flap. Three-dimensional effects noticed very close to the trailing edge of the flap. The same situation observed at  $2^\circ$ . Increasing the angle of attack at  $5^\circ$ , the flow on the flap was still attached and an interesting feature noticed on the flow around the holding structures placed on the upper surface plate of the DSP. This is presented in Figure 3.23 (b). It could be said that these small parts work as fences in three-dimensional (3D) flow, delaying separation of the wing in the spanwise direction.

Increasing the angle of attack further to  $8^\circ$ , the flow remained attached up to the trailing edge of the flap. However, at  $10^\circ$ , it was observed that the main wing was separated in contrast to the flow on the flap which stayed attached. Moreover, there was an indication of flow reversal on the panel's inclined part. All these phenomena are shown in Figure 3.24. Finally at  $15^\circ$ , the same features noticed. The reversed flow on the DSP inclined part was even more pronounced, covering most of it as the angle of attack increased. After studying carefully the pictures, it was concluded that for both tests the results were very similar and the correlation between woollen

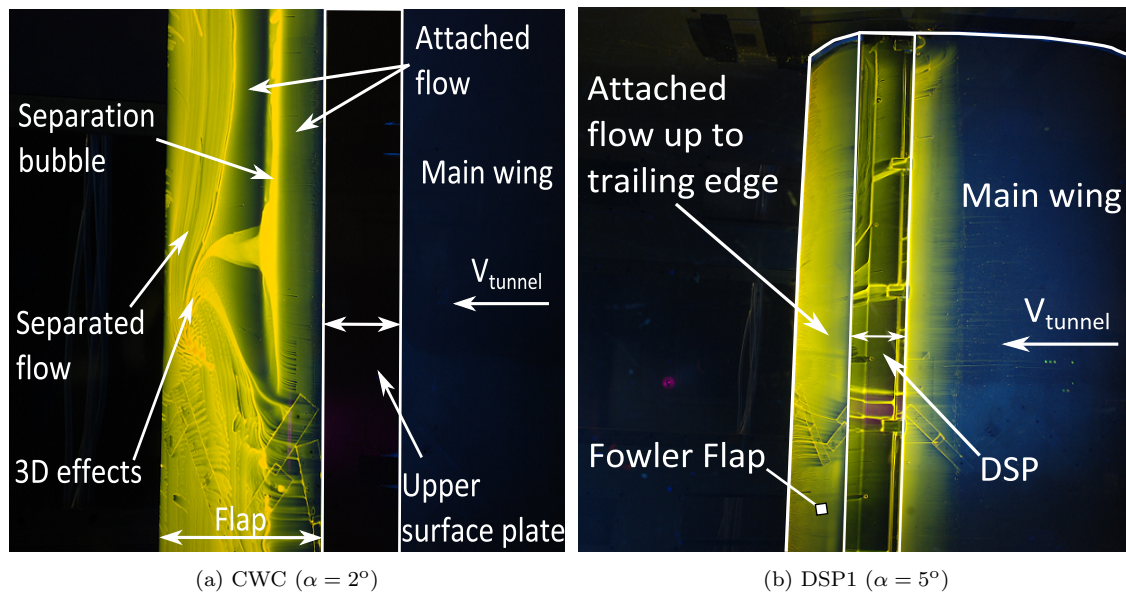


Figure 3.23: Flow features at  $\alpha = 2^\circ$  without DSP (a) and with DSP (b) at  $\alpha = 5^\circ$

tufts and oil-flow visualisation was acceptable. Both techniques showed accurately the attached flow on the flap, which was the main objective of the DSP flow control device. Thus, by measuring the lift and drag through pressure measurements, it was expected to see these effects on the lift and drag coefficients of the whole wing-flap model.

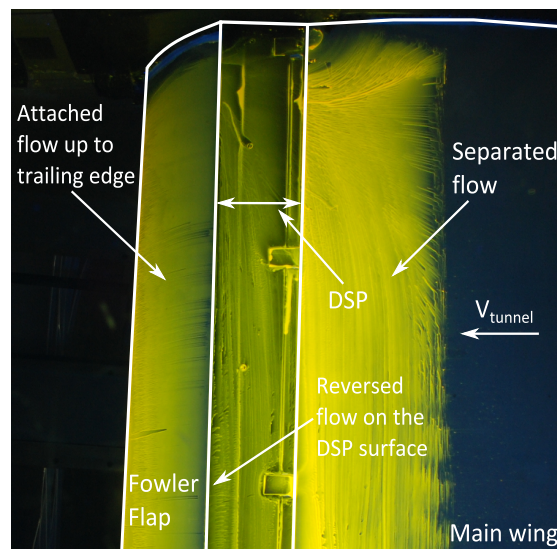


Figure 3.24: Flow features at  $\alpha = 10^\circ$  with DSP attached on the main wing of the X-400 model

Then, the wake rake was placed in the test section behind the wing model. The wake rake

and pressure taps were connected to the same pressure scanner, at the back side of the pressure scanner as the pressure tap tubes. This included 67 total pressure tubes and 16 static pressure tubes. The wake rake could be moved in the  $y$  and  $z$  but not in the  $x$ -direction. The last thing done was to check if all the pressure taps were working properly giving sensible readings. The wake rake position behind the wing-flap model is shown in Figure 3.25.

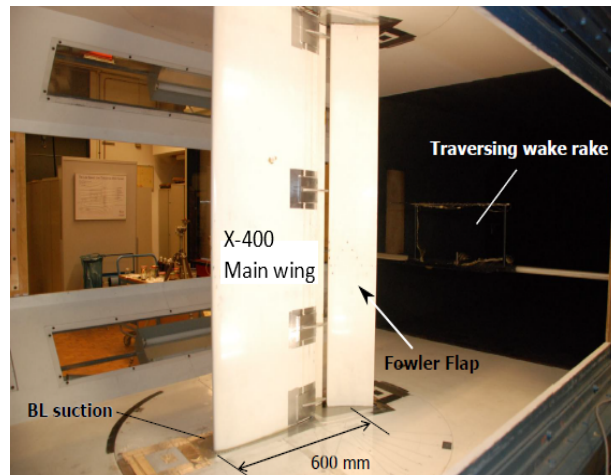


Figure 3.25: Wake rake placed behind the X-400 configuration in the LTT test section

### 3.4.2 Pressure Measurement Techniques

#### Surface pressure measurements

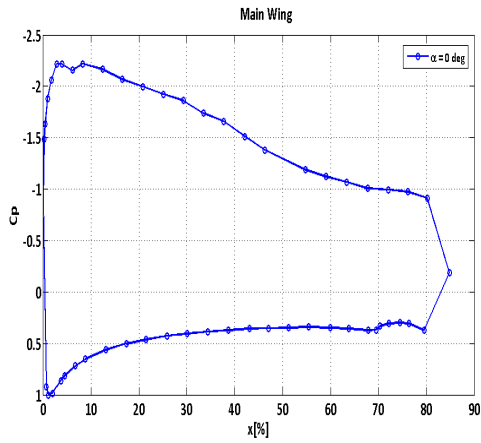
Starting with the clean wing configuration (CWC) at 40 m/s and considering the  $C_p$ -distribution plots, the main wing was staying attached and the Fowler flap was separated up to an angle of attack of  $10^\circ$ . The flap was separated from  $0^\circ$  up to  $10^\circ$  at approximately half-chord position ( $c/2$ ). After  $10^\circ$ , and up to  $14^\circ$ , the flow on the main wing was separated and on the Fowler flap was attached due to the deloading effect of the flap at this high angle of attack. These results, were to be expected, as the same were noticed from previous tests at lower angles of attack, (e.g.  $\delta_f = 40^\circ$ ). The  $C_p$ -distribution plots for angles of attack at  $0^\circ$ ,  $8^\circ$  and  $12^\circ$ , are presented in Figure 3.26.

For DSP1 ( $15^\circ$ ), at the same speed, the flap was attached for the whole range of angles of attack, as could be noticed from the  $C_p$ -distribution plots in Figure 3.27. On the other hand, the main wing was again attached up to  $10^\circ$  and then separated up to  $14^\circ$ . This was expected from the use of the drooped spoiler panel as a flow control device. The explanation for this very interesting result is, that the flow is accelerated on the suction side of the Fowler flap, due to the formation of a "convergent nozzle" by the panel's inclined surface and the flap's upper contour. This accelerates the flow in the boundary layer, and thus keeps the flow attached up to the trailing edge. Moreover, the pressure peaks on the flap, are reduced when the DSP is used, which makes easier for the flow to sustain the adverse pressure gradients. For the clean wing configuration (CWC), this is not the case, as there is an adverse pressure gradient due to the very high flap angle. As a result, the flow cannot follow the contour and finally is separated at half-chord ( $c/2$ ). The  $C_p$ -distribution plots for the same angles, using DSP1 (at  $15^\circ$ ), are

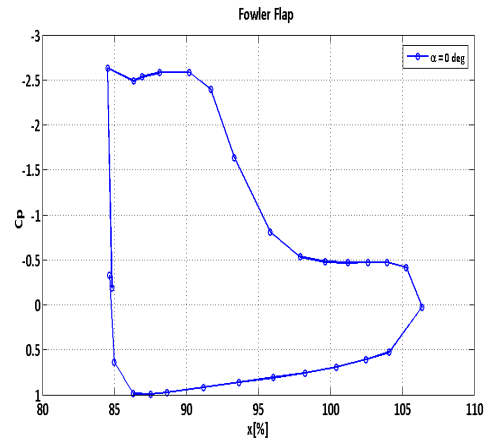
presented in Figure 3.27.

For DSP2 at ( $0^\circ$ ), again at the same speed, the flap was separated for angles of attack from  $0^\circ$  up to  $6^\circ$ , at approximately half-chord position ( $c/2$ ), as could be seen from the  $C_p$ -distribution plots in Figure 3.28. From  $8^\circ$  to  $14^\circ$ , the flap stayed attached. On the other hand, the main wing was attached up to  $10^\circ$  and then separated up to  $14^\circ$ . The behaviour noticed for DSP2 (at  $0^\circ$ ) could be compared as very similar to the clean configuration (CWC) case presented earlier. The effect of the drooped panel at  $0^\circ$  is not sufficient to keep the flow attached as is shown in Figure 3.28. This is probably because there is not any interaction between the panel and the Fowler flap. Thus, it could be concluded that this DSP angle ( $\theta_{dsp}$ ) was not beneficial, in terms of keeping the flap flow attached.

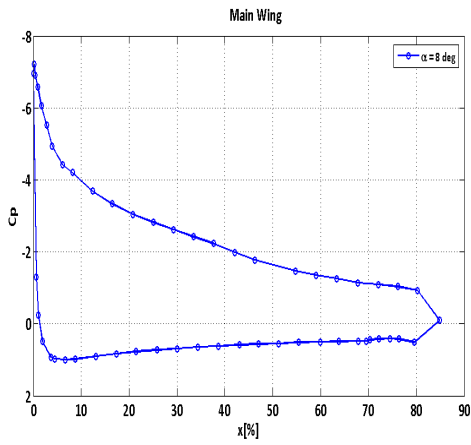
In terms of the DSP3 (at  $6^\circ$ ) and DSP4 (at  $8^\circ$ ), Figure 3.29 shows that the flap flow is separated at low angles of attack, up to  $2^\circ$ . The flap at low angles of attack is separated for the last 5% of the flap chord ( $c$ ). Then from  $4^\circ$  up to  $14^\circ$ , the flap stays attached. On the other hand, the main wing, stays attached up to  $10^\circ$  and after that it separates at higher angles of attack. The flow on the flap is explained by the presence of the drooped spoiler panel, which for both cases, manages to reduce the pressure peaks especially close to the leading edge of the flap. This leads to a better "response" of the flow to the adverse pressure gradient further downstream and the flow manages to stay attached. Nevertheless, the panel's angle, is not large enough as in the case of DSP1 (at  $15^\circ$ ), in order to achieve that at low angles of attack and as a result, the flow separates.



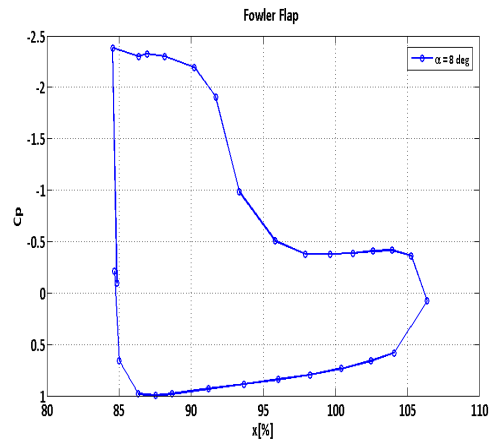
(a) Wing ( $\alpha = 0^\circ$ )



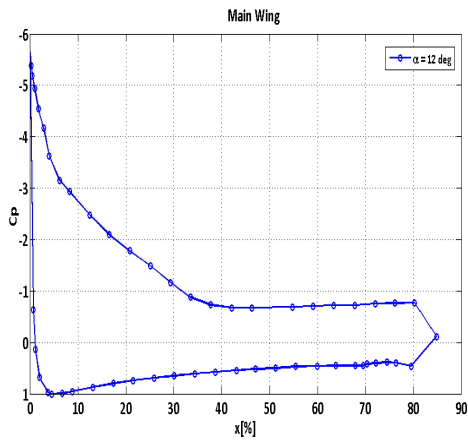
(b) Flap ( $\alpha = 0^\circ$ )



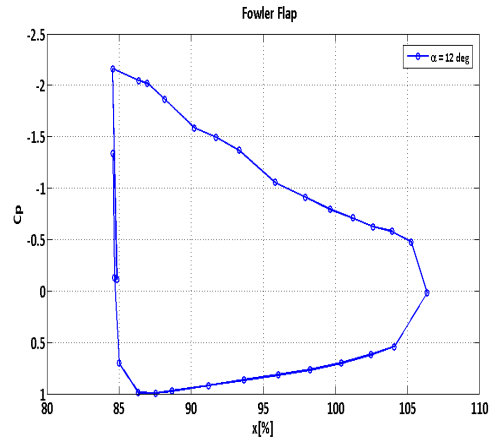
(c) Wing ( $\alpha = 8^\circ$ )



(d) Flap ( $\alpha = 8^\circ$ )

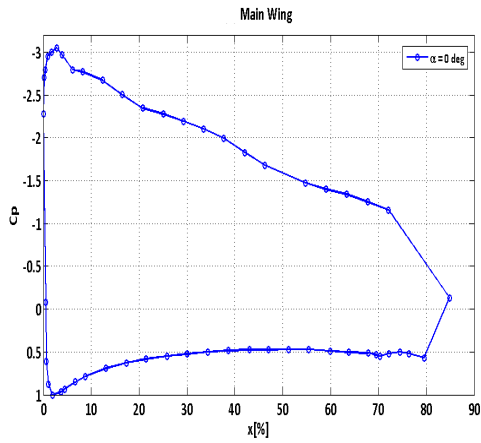


(e) Wing ( $\alpha = 12^\circ$ )

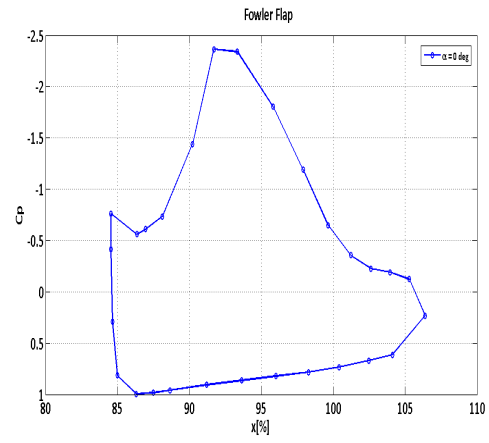


(f) Flap ( $\alpha = 12^\circ$ )

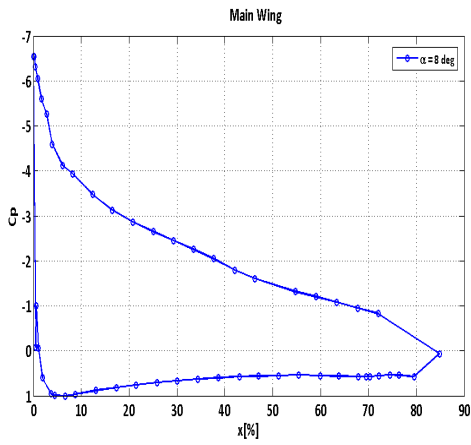
Figure 3.26: Wing (left) and flap (right)  $C_p$ -distribution plots for CWC at  $Re = 1.6 \cdot 10^6$  with  $\delta_f = 50^\circ$ ,  $x_{overlap} = 0\%$  and  $y_{gap} = 3.7\%$



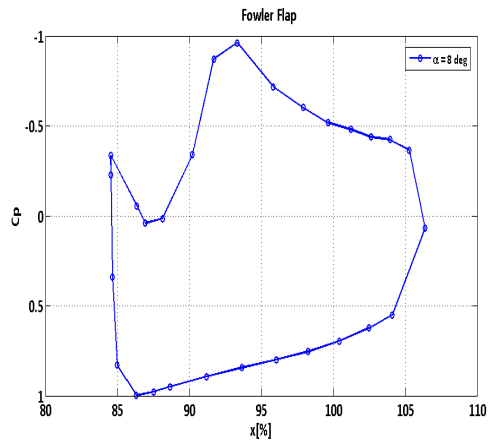
(a) Wing ( $\alpha = 0^\circ$ )



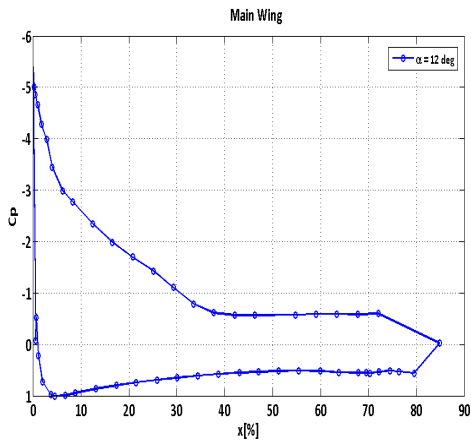
(b) Flap ( $\alpha = 0^\circ$ )



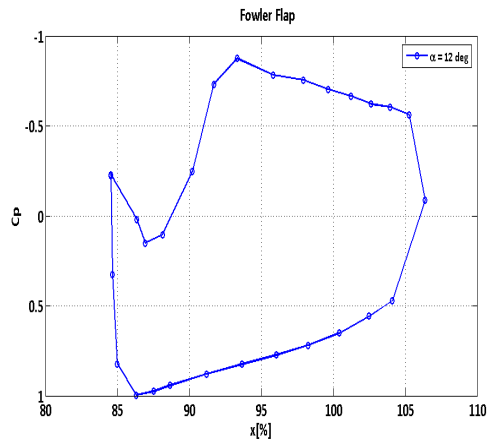
(c) Wing ( $\alpha = 8^\circ$ )



(d) Flap ( $\alpha = 8^\circ$ )



(e) Wing ( $\alpha = 12^\circ$ )



(f) Flap ( $\alpha = 12^\circ$ )

Figure 3.27: Wing (left) and flap (right)  $C_p$ -distribution plots for DSP1 at  $Re = 1.6 \cdot 10^6$  with  $\delta_f = 50^\circ$ ,  $x_{overlap} = 0\%$  and  $y_{gap} = 3.7\%$

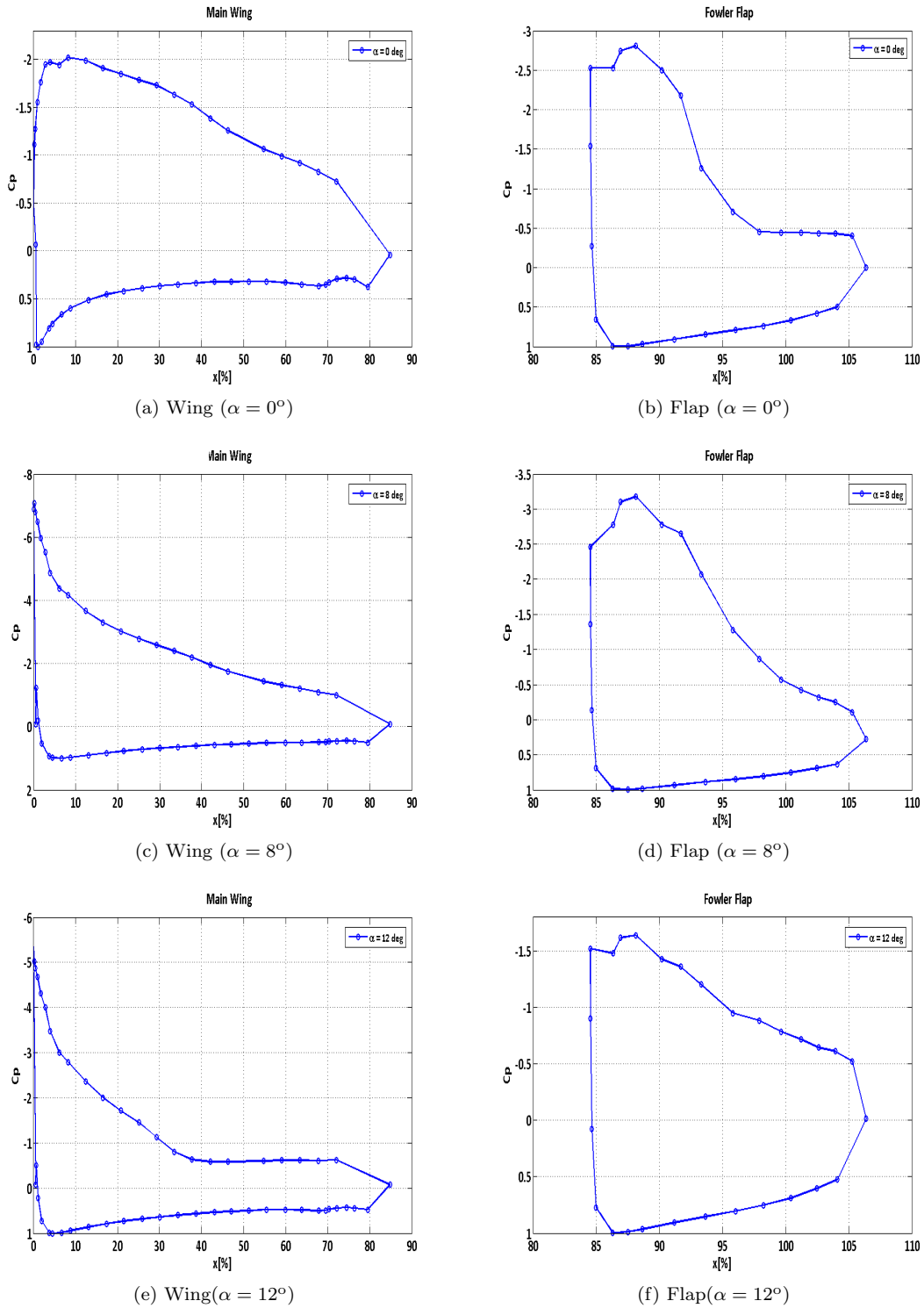
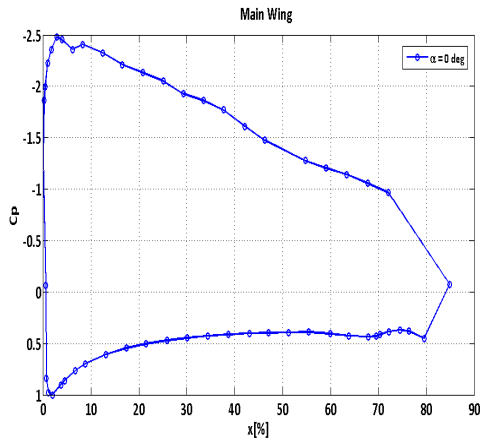
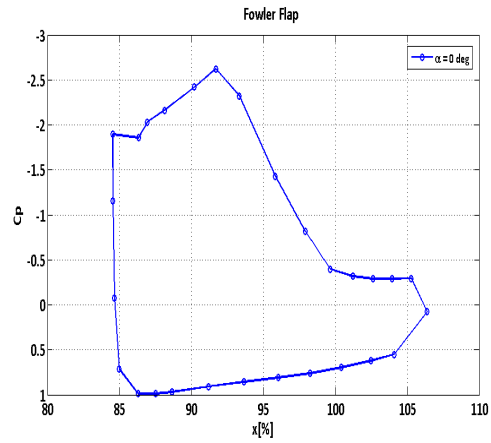


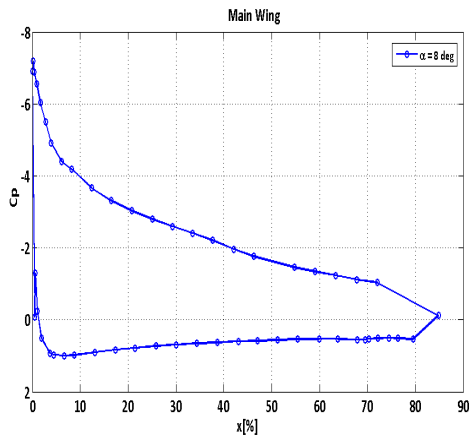
Figure 3.28: Wing (left) and flap (right)  $C_p$ -distribution plots for DSP2 at  $Re = 1.6 \cdot 10^6$  with  $\delta_f = 50^\circ$ ,  $x_{overlap} = 0\%$  and  $y_{gap} = 3.7\%$



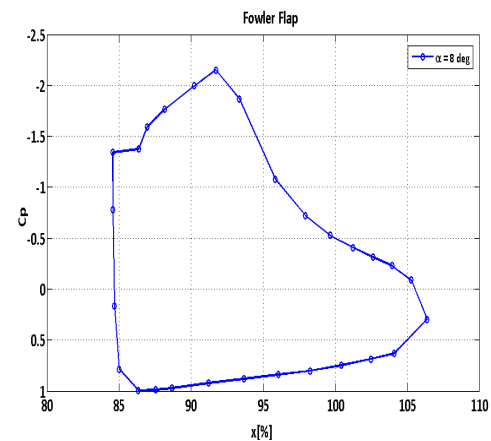
(a) Wing ( $\alpha = 0^\circ$ )



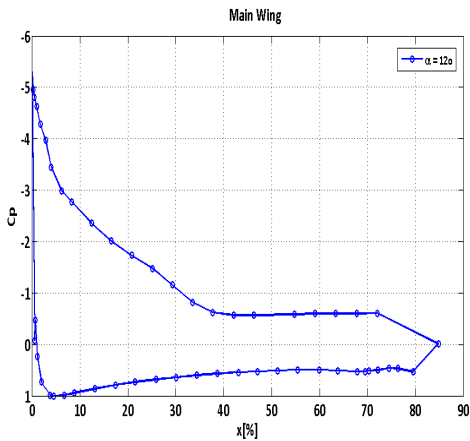
(b) Flap ( $\alpha = 0^\circ$ )



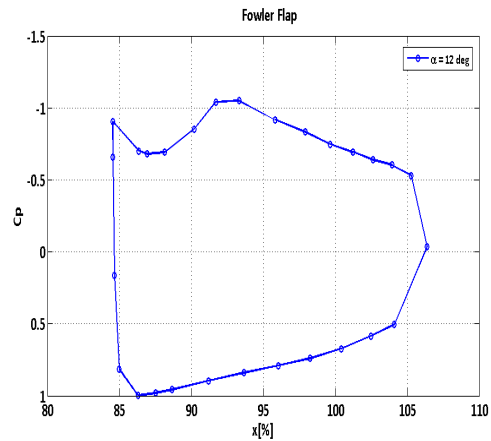
(c) Wing ( $\alpha = 8^\circ$ )



(d) Flap ( $\alpha = 8^\circ$ )



(e) Wing ( $\alpha = 12^\circ$ )



(f) Flap ( $\alpha = 12^\circ$ )

Figure 3.29: Wing (left) and flap (right)  $C_p$ -distribution plots for DSP4 at  $Re = 1.6 \cdot 10^6$  with  $\delta_f = 50^\circ$ ,  $x_{overlap} = 0\%$  and  $y_{gap} = 3.7\%$

From the surface pressure measurements, it was also possible to determine the lift of the X-400 model configuration. The lift was determined through pressure measurements from the surface pressure taps. The drag was measured using the wake rake which was positioned behind the wing model. Starting with the clean wing configuration (CWC), the lift increases linearly up to  $10^\circ$ , reaching a  $C_{Lmax}$  value of 3.054. After this angle of attack, the lift coefficient drops, showing an abrupt stall behaviour. For the case of DSP1 (at  $15^\circ$ ), the maximum lift coefficient is much lower than the clean configuration (CWC) lift data. This is shown in Figure 3.30 (a). For this case, the lift line is reaching it's maximum at a lower angle of attack, showing a flat plateau trend up to the point where the configuration is stalled due to the very high angle of attack and as a result there is a significant loss of lift. The maximum lift coefficient,  $C_{Lmax}$ , was 2.556 at an angle of  $8^\circ$ , and then for the remaining angles, the stall shows a linear trend. Moreover, looking at the drag coefficient  $C_D$  plot lines, the drag coefficient for the drooped spoiler panel case (DSP1), is lower than for the case of the clean wing configuration up to  $8^\circ$ . However for higher angles of attack, the drag coefficient of the drooped panel case increases significantly, possibly because the configuration is stalled earlier ( $8^\circ$ ), contrary to the clean wing which is stalled at a higher angle ( $> 10^\circ$ ). In addition, the stall behaviour of the clean wing is not as sudden as for the drooped panel case. All this information is presented in Figure 3.30.

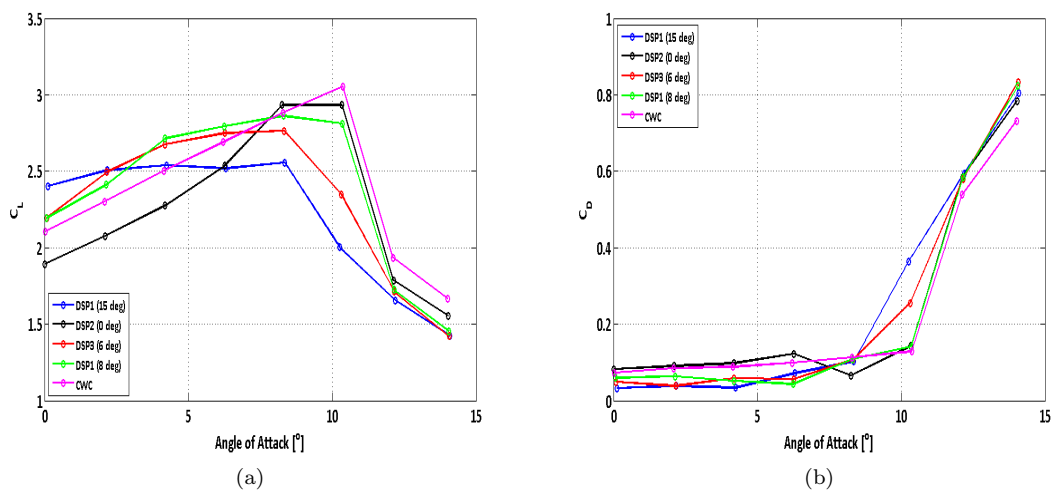


Figure 3.30:  $C_L$  (a) and  $C_D$  (b) vs. Angle of Attack (AoA) with (CWC) and without (DSP's) flow control at  $Re = 1.6 \cdot 10^6$  with  $\delta_f = 50^\circ$ ,  $x_{overlap} = 0\%$  and  $y_{gap} = 3.7\%$

For the DSP2 (at  $0^\circ$ ), and looking the  $C_L$  and  $C_D$  plots, presented in Figure 3.30, the maximum lift coefficient is achieved at the same angle of attack as for CWC, at  $10^\circ$ , however, it's value is a bit lower reaching 2.934 compared to the 3.054 value for the clean wing configuration. Moreover, at  $8^\circ$ , the lift coefficient is actually identical to the case of  $10^\circ$ , showing a constant trend. The post stall trend is the same as for the clean wing case. Hence, even if the panel used has not a significant effect at this small angle, this flat plateau for the lift coefficient is appeared but at a higher angle of attack than for the DSP1 case. Moving to the the drag coefficient plot, the trends with CWC are fairly similar, with a small increase in drag for the DSP2 case, which could be explained by the additional parasitic drag due to the panel.

For DSP3 (at  $6^\circ$ ) and DSP4 (at  $8^\circ$ ), looking at the lift coefficient plots in Figure 3.30, as

the panel angle increases, the lift line trend is showing a larger plateau starting at lower angles of angle of attack, but at the same time, the maximum lift drops significantly. This could be explained by the suppression of the pressure distribution on the flap when the panel is attached. This results to an attached flow on the flap, however, the lift is reduced especially at lower angles of attack. The drag coefficient trends are also similar to each other and as the panel's angle is increased the separation on the main wing is decreased or totally eliminated (DSP1 case) therefore, the  $C_D$  values for pre-stall regions are lower than for the clean wing case or the lower panel angle cases. The results were in great contrast to the expectations after the flow visualisation and initial pressure tests. This was due to the attached flow noticed on the Fowler flap surface, and thus it was expected that the  $C_L$  values would be greater for the drooped spoiler panel. As a result, the effect of the drooped spoiler panel (DSP) on the performance of the model, was in overall inferior compared to the clean wing configuration (CWC).

Considering the results from the tests carried out, the drooped spoiler panel at  $15^\circ$  (DSP1), was the one which satisfied the main objective of this passive flow control device. This was to keep the flow attached on the Fowler flap of the X-400 model. From pressure distribution plots, using DSP1, it was clear that the flow was able to stay attached on the whole range of angles of attack. As a result, it was decided to use this panel (DSP1), for the rest of the experimental campaign. The effect of Reynolds number on the lift and drag coefficients for the clean wing configuration (CWC) and DSP1, is presented in Figure 3.31. The  $C_L$  and  $C_D$  plots are shown, but this time for different Reynolds numbers representing speeds from 10 to 40 m/s.

Starting with the clean wing configuration and looking at the lift coefficient plot in Figure 3.31, is realised that as the Reynolds number increases, the  $C_L$  values increase up to  $Re_3$ . Moreover, for the  $Re_3$  case, the maximum lift value fairly increases to 3.326 but also the stall angle of attack is postponed to  $12^\circ$ , in contrast to all the other Reynolds numbers, where the stall initiates at  $10^\circ$ . This is explained by the thinner boundary layer formed as the Reynolds number increases. The thinner boundary layer on the wing and flap surfaces, mean less boundary layer displacement thickness,  $\delta^*$ , and effectively a higher camber, which would result in higher downwash and as a result lift for the whole configuration. This is also noticed in Figure 3.31, for the case of DSP1, where as the Reynolds number increases, the lift coefficients increase as well. On the other hand, moving back to the CWC case and for  $Re_4$ , it seems that the further increase of the tunnel's velocity, leads to a lower maximum lift value and earlier stall initiation. In addition, by observing the  $C_p$ -distribution plots of the CWC for the pre-stall angles of attack, it is obvious that for  $Re_4$ , there is a decrease of the pressure peak especially compared to the  $Re_3$  case. This is shown in Figure 3.32, presenting the pressure distribution on the main wing and flap for CWC at an angle of attack of  $6^\circ$ . Despite that, the separation point on the Fowler flap is the same as for the other Reynolds numbers tested.

Apparently, for the CWC as the Reynolds number increases there is more separated flow on the Fowler flap, which results to the lower lift and higher drag coefficient values, as is shown in Figure 3.31 for  $Re_4$ . Another possibility could be the three-dimensional effects on the flap flow. The thickening of the boundary layers on both tunnel walls could form a very adverse pressure gradient region especially close to the flap area. This could result to the lower pressure peaks shown in the  $C_p$ -plots in Figure 3.32 and as a result to lower lift values for  $Re_4$ . These effects were also observed during the oil-flow visualisation tests for the clean wing configuration at the same speed and flap angle, altering the angle of attack, as presented in subsection 3.4.1.

From the drag coefficient plot in Figure 3.31, up to  $Re_3$ , the drag coefficient decreases because

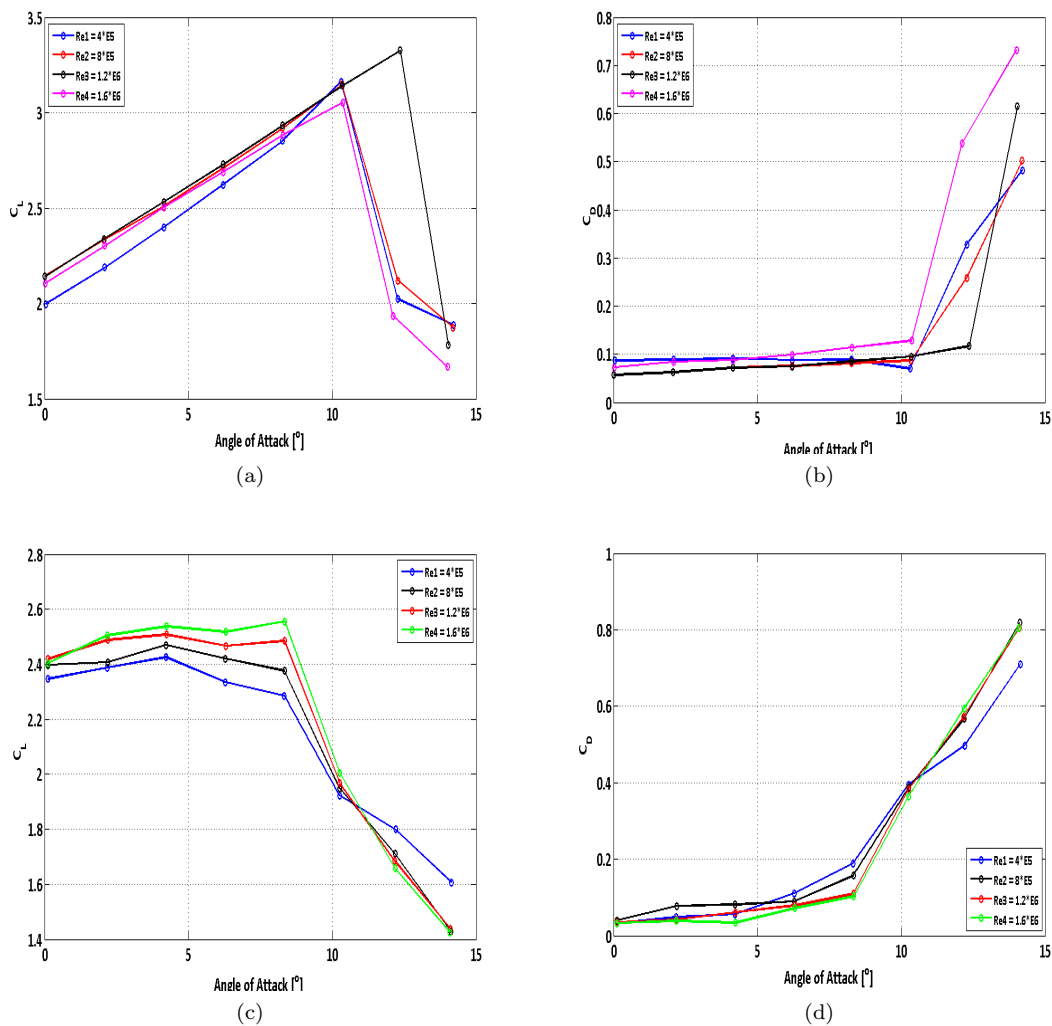


Figure 3.31:  $C_L$  (left) and  $C_D$  (right) vs. Angle of Attack (AoA) for CWC (upper) and DSP1 (lower) cases, for different Reynolds numbers (Re) with  $\delta_f = 50^\circ$ ,  $x_{overlap} = 0\%$  and  $y_{gap} = 3.7\%$

the boundary layer thickness becomes thinner and as a result the boundary layer displacement and momentum thickness will reduce too. Thus, the drag of the whole configuration will also reduce, resulting to lower drag coefficient values. This is also the case for DSP1, where as the Reynolds number increases the drag coefficient drops. For this case, the boundary layer is attached on the flap, due to the presence of the drooped spoiler panel and as a result there is not flow separation. However, for  $Re_4$ , the drag coefficients increase which could be explained by the three-dimensional effects described earlier, resulting in high pressure regions on the flap area and consequently higher drag values.

After the first measurements, it was clear that by using any drooped spoiler panel, the  $C_L$  values were in general lower compared to the clean wing configuration. This was not expected

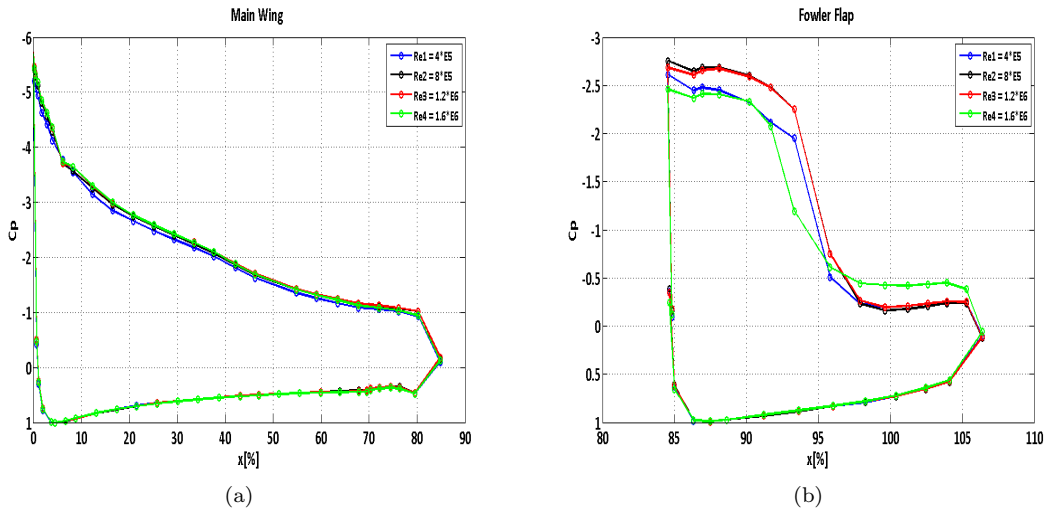


Figure 3.32: Wing (left) and flap (right)  $C_p$ -distribution plots for CWC for different Reynolds numbers ( $Re$ ) at  $\alpha = 6^\circ$  with  $\delta_f = 50^\circ$ ,  $x_{overlap} = 0\%$  and  $y_{gap} = 3.7\%$

after the flow-visualisation and  $C_p$ -distribution plots observations. Therefore, after further research, it was assumed that wake bursting or also called wake reversal was probably creating this problem. This phenomenon is shown schematically in Figure 3.33. The main reason for assuming that this great loss of lift was caused by wake bursting, was that after the flow visualisation analysis, an area of reversed flow noticed on the DSP inclined surface and this was quite strange as the flow on the Fowler flap was fully attached. That is why additional pressure measurements had to be done, in order to be sure about this phenomenon. These measurements carried out using a total pressure probe in close proximity to the vicinity of the airfoil's surface, in order to show boundary layer development across the chord of the whole configuration. The main reason of doing these tests with the total pressure probe was to determine if there would be an area of reversed flow somewhere close to the main wing or DSP.

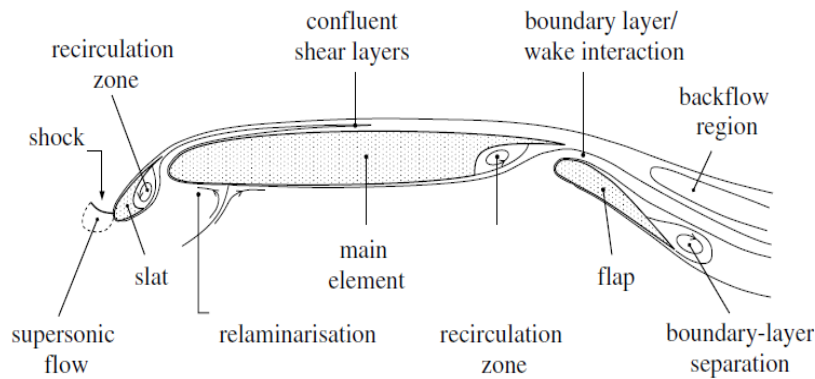


Figure 3.33: Phenomena that affect the flow around a multi-element airfoil. Note the reversed flow region above the Fowler flap surface [33]

### Probe pressure measurements

The data analysis of the probe pressure measurements, showed the development of the boundary layer on several stations along the model's chord. The measurement points placement could be found in Table 3.5 and a 2D schematic of their position on the actual wing-flap model presented in subsection 3.3.2 of this chapter, in Figure 3.16. For the case at an angle of attack of  $0^\circ$ , the boundary layer formation was normal and attached up to the trailing edge of the main wing. A brief proof of the very small loss in total pressure the boundary layer edge to the wall, is presented in Appendix A. In Figure 3.34, the boundary layer formation is presented for all the points measured on the wing-flap model. The boundary layer thickness, starts at a value of 4 mm at Point A, and reaches 10 mm at Point O, close to the trailing edge of the main wing. On the flap zone, the pressure measurements included more points (30 & 60 points respectively) in the vertical, (z), direction as it was necessary to have a better indication of the flow-field on the wake above the boundary layer. It would be helpful for the reader to note that the plots presented in Figure 3.34, are normalised total pressure data. Hence, the only sense they could make is with respect to their trend being similar to the velocity trend. The values of course could not be the same neither negative, in order to show flow or wake reversal as could be expected if velocity data was plotted. From plot (f) in Figure 3.34, showing the measurements on the Fowler flap, it's evident that the flow on the Fowler flap is attached up to half-chord ( $c/2$ ) by looking the trend of Point Q line. Moreover, a reduction of the normalised total pressure between  $y = 18$  to  $y = 38$  mm, could be a sign of wake bursting happening or being close to occur due to high pressure gradients on this wake region. Finally, from the trend of Point R line, it could be argued that the flow is on the verge of flow separation. Thus, a potential increase of the angle of attack, could possibly lead to the wake bursting phenomenon. As a result, additional tests performed at larger angles of attack of  $6^\circ$  and  $8^\circ$ , where the flat plateau of  $C_L$  values noticed, in order to get a clearer understanding of what could be the reason for this behaviour.

The results for these tests are presented in Figure 3.35 for both angles of attack of  $6^\circ$  and  $8^\circ$  respectively. An indication of flow reversal in the wake above the boundary layer of the Fowler flap is observed. Looking at the plots (b), (c) and (d) in Figure 3.35, covering the whole chordwise distance of the flap, the trend of the normalised total pressure lines, is showing a reduction of values, above the boundary layer region. Assuming that this trend could be related to velocity trends at these points, a drop in velocity in this region could be expected. Concluding, what could be stated with confidence is an obvious negative effect on the region above the flap, when the model's angle of attack was increased. This effect could possibly be wake bursting phenomenon. Finally, it could be understood that doing such measurements in regions of confluent layers and wakes, using simple probes could be very challenging and risky with respect to the accuracy of the results. Nevertheless, this data was quite helpful in order to get an overall idea of flow phenomena on this region, but the necessity of carrying out PIV measurements was fairly obvious.

### Surface pressure measurements (VG's/DSP(h))

The last tests carried out using surface pressure measurements, included further flow control devices with the DSP attached, in order to determine their effect on the wake bursting phenomena. Observing the first test, with vortex generators at the first position, DSP1(VG1), being 140 mm in front of the DSP1, the results were exactly as expected. Their performance at this position was not the best possible, as they were placed in the separated region of the main wing at higher angles of attack. As a result, their effect on wake bursting was neutral. Still, in terms of lift coefficients, even at this position, the lift values were increased compared to the DSP1 case as

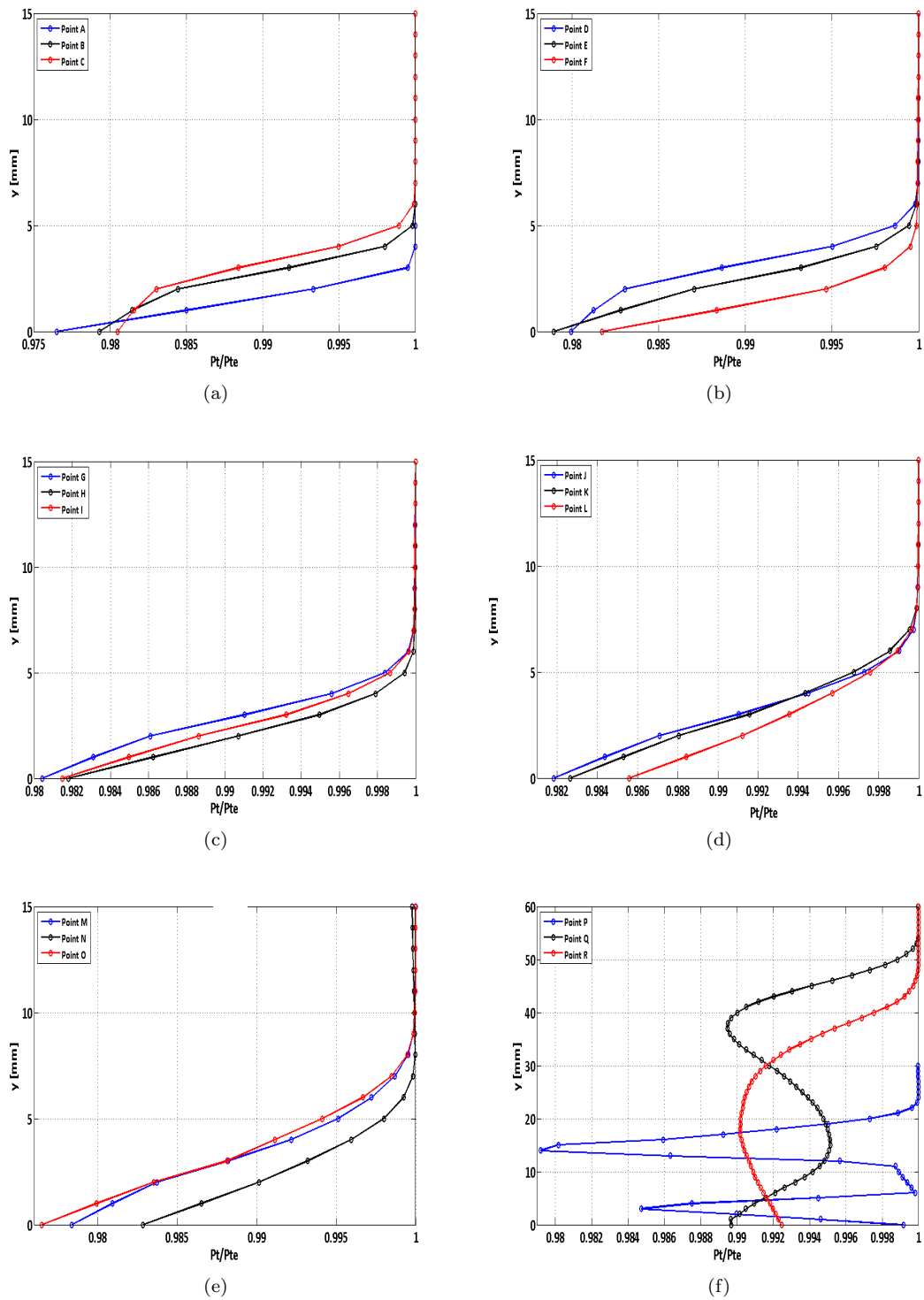


Figure 3.34: Total pressure measurements at different stations across the X-400 model at  $\alpha = 0^\circ$ ,  $Re = 1.6 \cdot 10^6$  with  $\delta_f = 50^\circ$ ,  $x_{overlap} = 0\%$  and  $y_{gap} = 3.7\%$

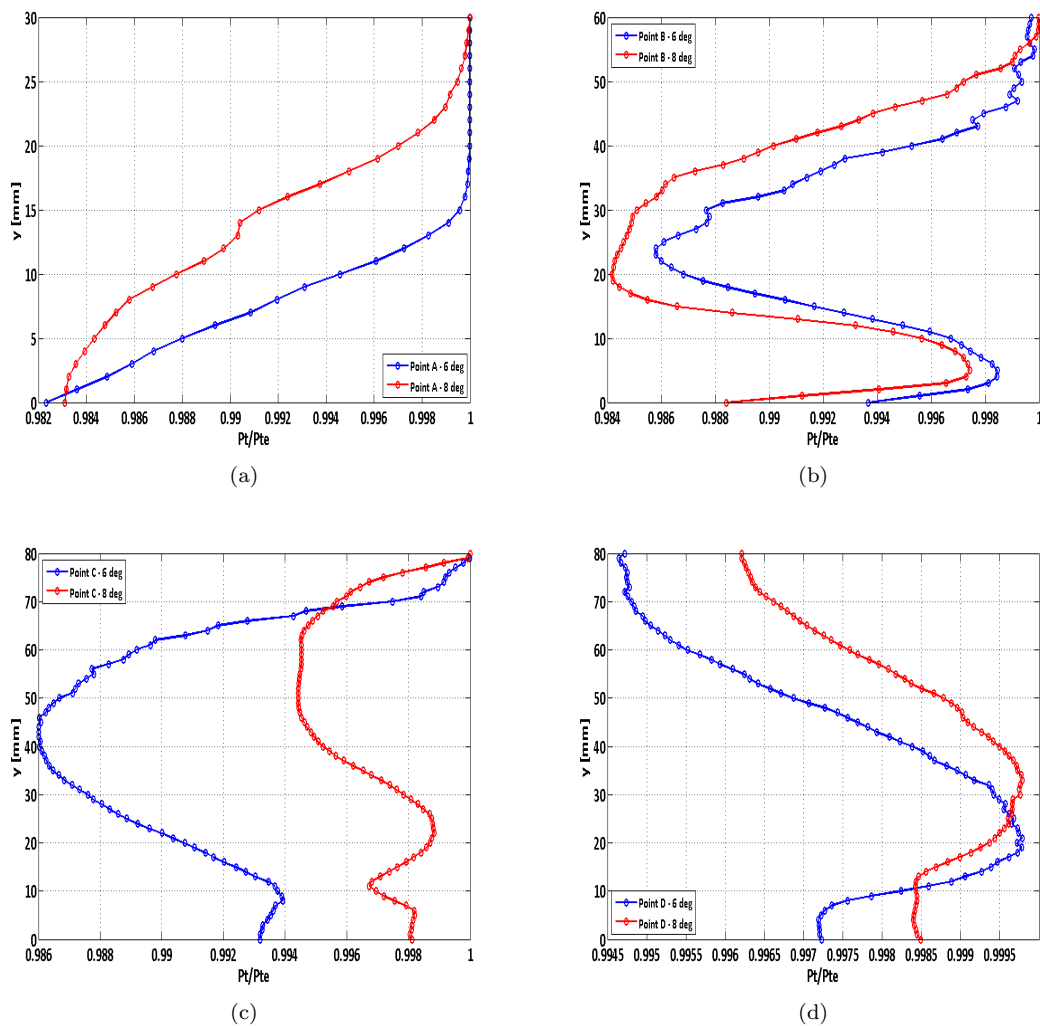


Figure 3.35: Total pressure measurements at different stations across the X-400 model at  $\alpha = 6^\circ$  and  $8^\circ$ ,  $Re = 1.6 \cdot 10^6$  with  $\delta_f = 50^\circ$ ,  $x_{overlap} = 0\%$  and  $y_{gap} = 3.7\%$

shown in Figure 3.36. However, observing the  $C_p$ -distribution plots for this case in Figure 3.36 (c) and (d), in particular at an angle of attack of  $4^\circ$  and  $6^\circ$ , it was very clear that the flap was separated at lower angle of attacks close to the trailing edge compared to the case without the vortex generators, where the flap flow was attached. This is explained by the thickening of the boundary layer on the main wing causing this separation on the flap.

For the second position, DSP1(VG2), being 270 mm in front of the DSP1, the maximum lift coefficient increased by 0.1 compared to the previous position (DSP1(VG1)) and the angle of attack where this maximum lift occurred was at  $6^\circ$  as presented in in Figure 3.36 (a). Hence, this position looked to give an additional performance. It is believed that by changing the vortex generators position, the effect of the vortices on the wake was significant enough to eliminate

the wake bursting phenomenon and increase the maximum lift coefficient. For drag coefficients, at the pre-stall region, the drag for the cases with vortex generators, is higher than for the case without them. Nevertheless, at the post-stall region the drag using the vortex generators is lower as shown in in Figure 3.36 (b), due to the fact that vortices postpone the flow separation on the main wing of the model and thus reduce drag coefficients. However, still the performance compared to the clean wing configuration is lower enough. Therefore, it could be concluded that even if the vortex generators helped to increase the lift, they were unable to eliminate the problem of wake reversal in significant grade.

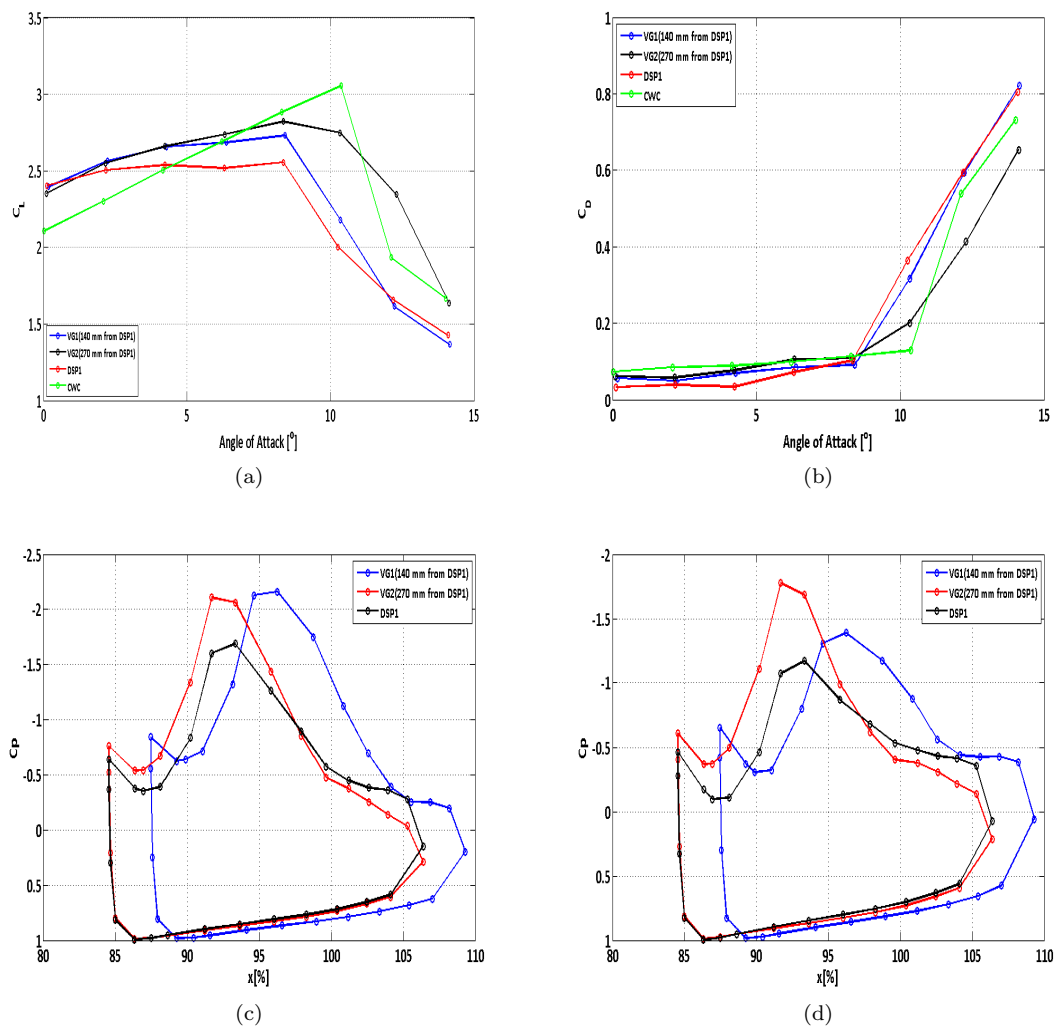


Figure 3.36:  $C_L$  (a) and  $C_D$  (b) vs. Angle of Attack (AoA) and Fowler flap  $C_p$ -distribution plots at  $\alpha = 4^\circ$  (c) and  $\alpha = 6^\circ$  (d) for DSP1, DSP1(VG1) and DSP1(VG2) with  $\delta_f = 50^\circ$ ,  $x_{overlap} = 0\%$  and  $y_{gap} = 3.7\%$

Finally, the drooped spoiler panels (DSPh's) with holes on the inclined surface tested. The  $C_L$  and  $C_D$  plots with respect to the angle of attack are shown in Figure 3.37 for both cases of

DSP1(h1) and DSP1(h2) with holes compared to DSP1(VG2) and DSP1 itself. The results of these passive devices were not successful and the lift coefficient plots presented in Figure 3.37 (a), showed that this solution did not alter anything compared to the DSP1 case. Comparing the two configurations with 2 mm (DSP1h1) and 4 mm (DSP1(h2)) diameter holes, the second one (DSP1(h2)), seemed to have lower lift coefficients compared to the other first one (DSP1(h1)). Despite that, both were achieved lower lift values from the best recorded test case of DSP1(VG2), with vortex generators as could be seen in Figure 3.37. In terms of the drag coefficients, at the pre-stall region, the drag for the cases with DSP1(h1), is higher than for the case with the drooped panel itself. Nevertheless, at the post-stall region, the drag seems to stay the same for both cases of panel with holes and panel itself. Hence, still the performance of these devices compared to the clean wing configuration is lower enough.

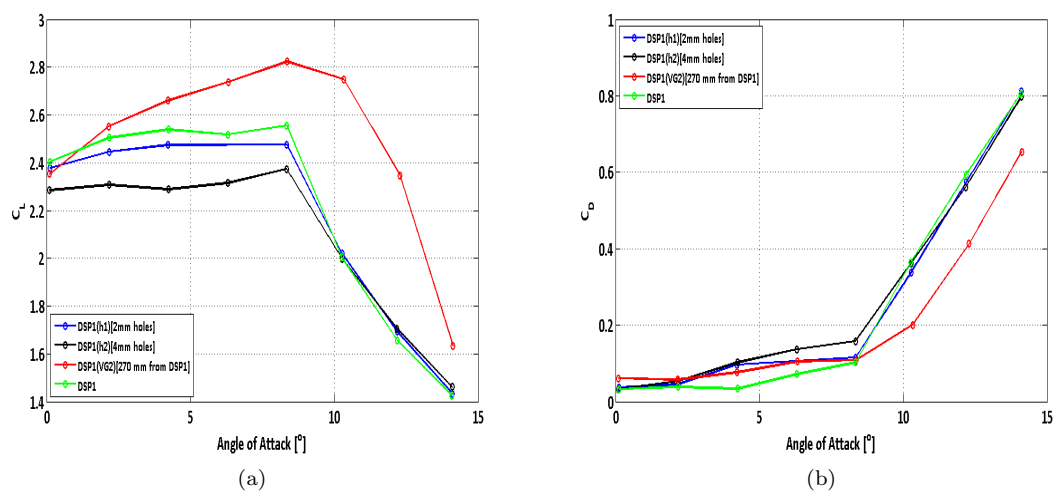


Figure 3.37:  $C_l$  (a) and  $C_d$  (b) vs. Angle of Attack (AoA) for DSP1, DSP1(h1), DSP1(h2) and DSP1(VG2) with  $\delta_f = 50^\circ$ ,  $x_{\text{overlap}} = 0\%$  and  $y_{\text{gap}} = 3.7\%$

### 3.4.3 Particle Image Velocimetry (PIV)

#### General Aspects

Prior to presenting and discussing the results from PIV experiments, additional information will be given on what will be shown in this section. Firstly, as it could be seen from the test matrix of these tests in subsection 3.3.3, the test cases were numerous with plenty of data, hence, only the ones giving an important insight on this research will be presented in detail in this subsection. Further results could be found in the Appendix A, at the end of the report. Therefore, after initial analysis, it was decided to present all the data related to the clean wing configuration but also the ones for the DSP1 (at  $15^\circ$ ), at an angle of attack of  $0^\circ$  and  $8^\circ$  and at wind-tunnel velocity of 40 m/s.

The reason for choosing those two angles of attack, was mainly to show the different flow features on the Fowler flap, as long as the wake bursting phenomenon was already initiated at  $8^\circ$ , according to the pressure measurement data. Moreover, the results for the drooped spoiler panel

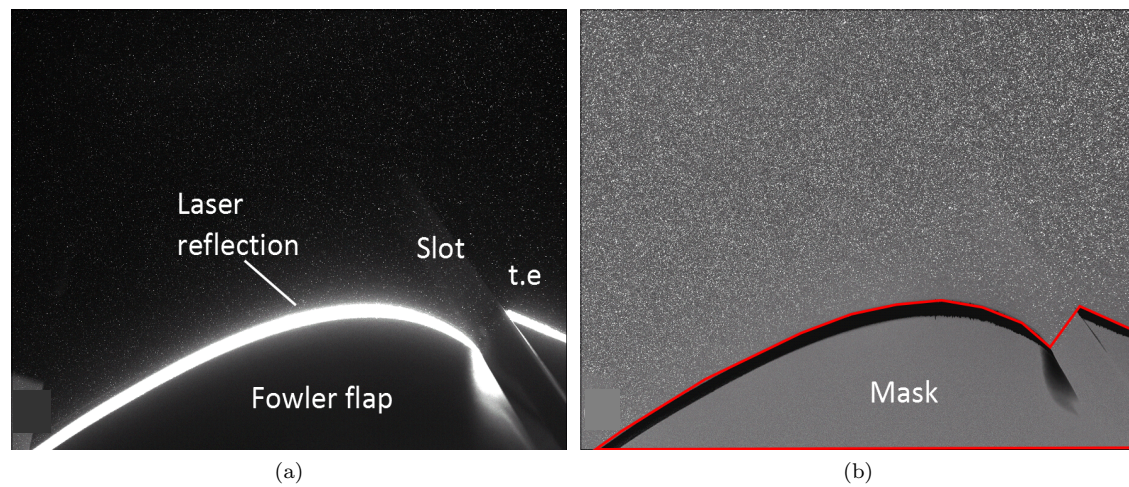


Figure 3.38: Post-processed image of the wing-flap configuration (a), showing the reflection due to the laser beam and (b) Mask out-layer as applied using Davis software 8.1 for clean wing configuration (CWC)

(DSP1) case, with surface roughness applied on the suction and pressure side of the main wing, were also examined. On the other hand, the reason for presenting only data at tunnel speed of 40 m/s was mainly for similarity reasons, but also because no significant features noticed, apart from a smaller separated region due to the thinner boundary layer at higher Reynolds numbers. Finally, the total velocity field with streamlines, the wake velocity profiles and the displacement as well as momentum thickness plots, will be presented.

The field of view (FOV) was 273 mm x 214 mm and it is possible to capture a small part of the main wing's trailing edge and the whole Fowler flap. The cove area is not visible at all, however, the slot between the wing and the flap could be slightly noticed as could be seen in Figure 3.38 (a). Despite that, the flow through the slot was very difficult to be captured as there was no light going in that particular area, but its effect on the suction side of the flap was obvious, as will be seen later in the total velocity plots.

Another issue, was the reflection of the laser beam when it was in contact with the wing and flap's surface. This is clear in Figure 3.38 (a) and on the right image (b), one could see the mask's out-layer, represented by the red line. On the plots presented later, all this region is covered with a black mask.

Concluding, for all the calculations of each test case, namely, the displacement,  $\delta^*$  and momentum,  $\theta$ , thickness, as well as for the velocity profiles, the calculations carried out along perpendicular lines being at  $90^\circ$  to the streamlines. The white lines shown in Figure 3.39 indicate the positions of the velocity profiles.

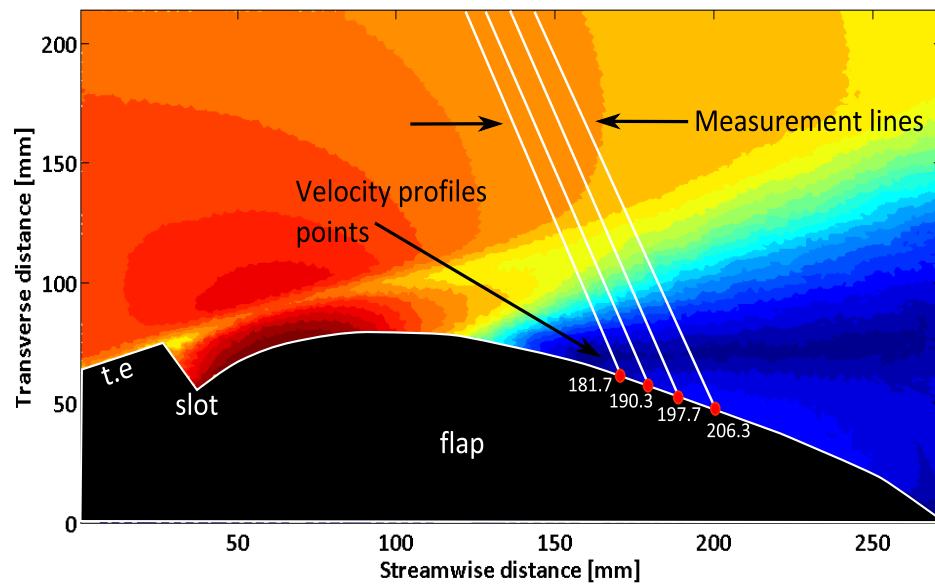


Figure 3.39: Field of View (FOV) including the lines (in white) for the positions of the velocity profiles

### Test Case (1): Clean Wing Configuration (CWC) at $0^\circ$

The first test case is for the clean wing configuration at an angle of attack of  $0^\circ$  and tunnel velocity at 40 m/s. The first plot presented in Figure 3.40, is the total velocity field with streamlines. One could notice the highest velocity region immediately after the slot, on the suction side of the Fowler flap. This increase of the speed is expected and is much higher than the free-stream velocity, as shown in the colorbar. The second important feature of this plot is the separated region, initiated approximately after the mid-chord position ( $x=135$  mm in the streamwise direction), as could be seen in Figure 3.40. The area coloured in blue, represents a very low velocity or high pressure region, where the flow is separated. This behaviour was expected, as the flap angle is so large ( $\delta_f = 50^\circ$ ) that the flow cannot cope with the adverse pressure gradient and finally separates as is also indicated by the white streamlines.

The next two plots presented in Figure 3.42, are the displacement and momentum thickness plot (a), as well as the velocity profiles plot (b), at four different stations, selected in the separated region, as this was the area of interest for these tests. From plot (a), both displacement,  $\delta^*$ , and momentum,  $\theta$ , thickness seem to have negative values up to quarter chord distance ( $c/4$ ), where the highest velocities occur on the suction side of the Fowler flap. The negative values noticed for both quantities could be explained with the aid of Figure 3.41. It is very clear that the flow above the flap, is very complex as, interaction and merging of multiple wakes and flows occurs. Thus, if one would try to plot the velocity profile from flap's surface to the free stream across a line perpendicular to the streamlines, would result in the velocity profile shown at the bottom of Figure 3.41. Then, in order to calculate the displacement and momentum thickness, using the equations given in Figure 3.41, it's clear that due to the slot flow, the velocity value at this area will be higher than the free-stream value. This will consequently lead to negative values for both

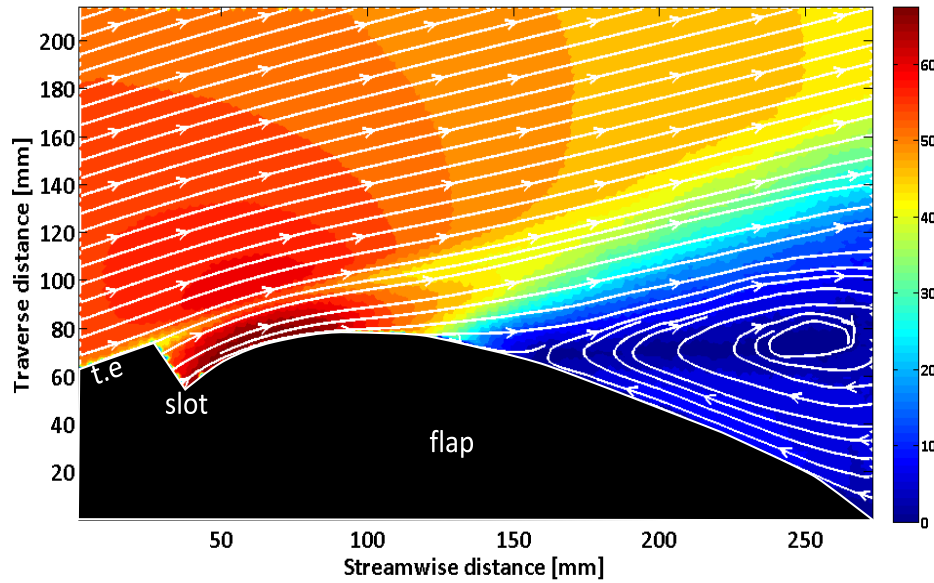


Figure 3.40: Total velocity field with streamlines for CWC at  $\alpha = 0^\circ$  and  $V_t = 40\text{m/s}$

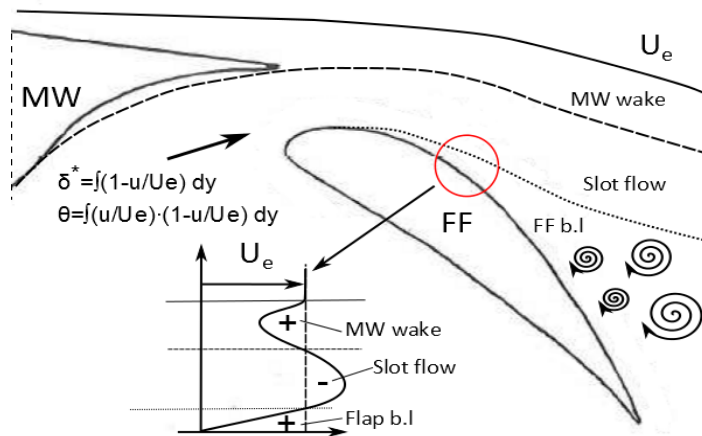


Figure 3.41: Explanatory schematic, showing the Fowler flap region flow field as well as the interaction and merging of main wing wake, slot flow and flap’s boundary layer

variables, as long as  $u$  is higher than  $U_e$ .

After this point these two quantities both increase due to the separated region, following approximately after the mid-chord position ( $c/2$ ). In particular, the displacement thickness,  $\delta^*$ , increases considerably more than the momentum thickness,  $\theta$ , around 20 mm, as the flow separates from the flap’s surface. From the other plot (b) in Figure 3.42, the velocity profiles at four different stations show what was observed from the total velocity field plot in Figure 3.40. The flow is separated for all the stations

selected. Finally, there is not any sign of wake bursting happening.

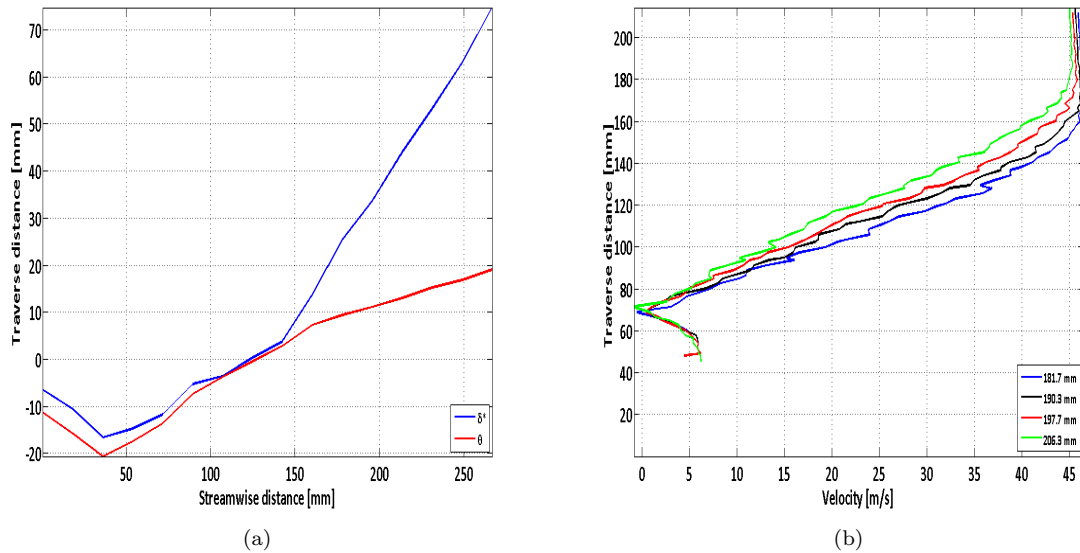


Figure 3.42: Displacement,  $\delta^*$ , and momentum,  $\theta$ , thickness (a) plot and Wake velocity profiles (b) at 4 different stations for CWC at  $\alpha = 0^\circ$  and  $V_t = 40\text{m/s}$

### Test Case (2): Clean Wing Configuration (CWC) at $8^\circ$

The second test case is for the clean wing configuration at an angle of attack of  $8^\circ$  and tunnel velocity at 40 m/s. From the total velocity field plot with streamlines in Figure 3.43, three main features could be noticed. Firstly, the velocity region immediately after the slot, on the suction side of the Fowler flap is not as high as it was observed for the first test case at  $\alpha = 0^\circ$ . The decrease of the speed could be explained by the greater angle of attack of the model configuration. The second important feature of this plot is the separated region, which increased in size. Moreover, it is still initiated approximately after the mid-chord position ( $x=135$  mm in the streamwise direction), as could be seen in Figure 3.43. The area coloured in blue, represents the very low velocity in the region where the flow is separated. The last thing noticed, is that the flow velocity on the trailing edge of the main wing, is not as high as on the first case, and this could indicate that the main wing is close to flow separation as the velocity at this region reduces significantly compared to  $\alpha = 0^\circ$  case.

The next two plots shown in Figure 3.44, are the displacement and momentum thickness plot (a) as well as the velocity profiles plot (b), at the same four stations. From plot (a), it is clear that both the displacement and momentum thickness increase on the main wing's trailing edge. This could be explained by the decrease in speed close to the trailing edge which would cause the increase in both variables. Then both keep increasing abruptly, especially after the mid-chord position, where the flow is totally separated and the separation region is large enough. This is why, at this case the displacement thickness gets higher values than for the first case at  $\alpha = 0^\circ$ . On the other hand, the momentum thickness seems not to increase further. From the velocity profiles plot (b) at the four different stations, all show what was expected from the total velocity

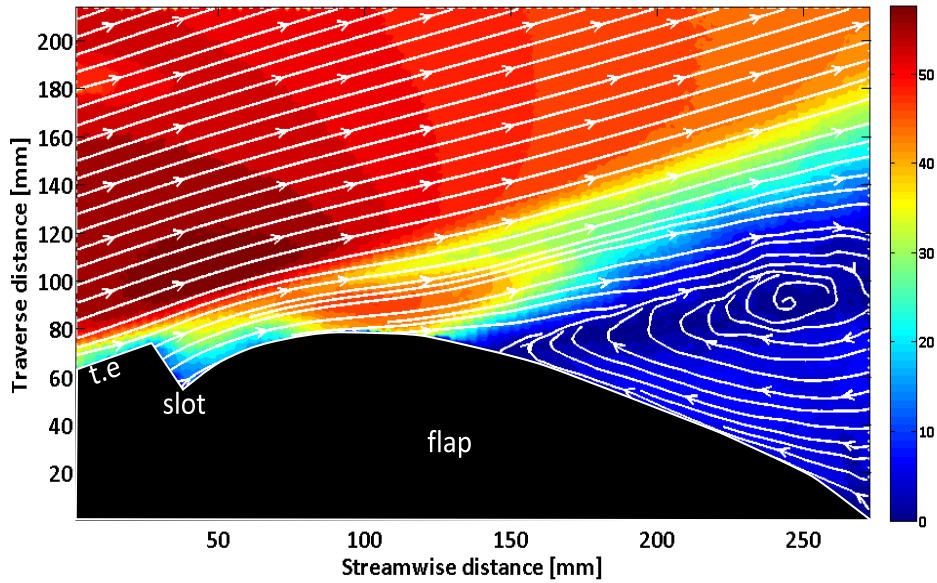


Figure 3.43: Total velocity field with streamlines for CWC at  $\alpha = 8^\circ$  and  $V_t = 40\text{m/s}$

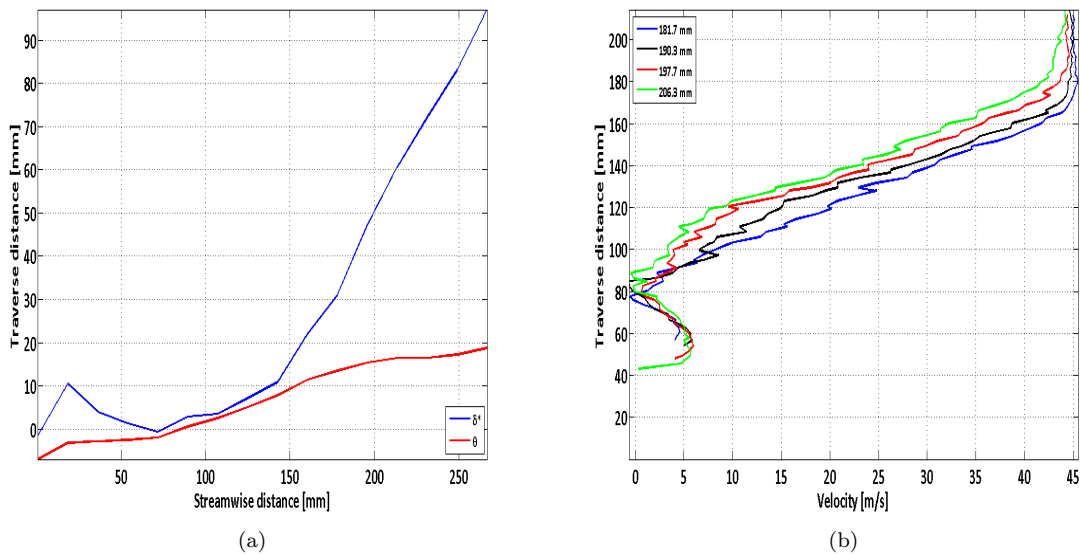


Figure 3.44: Displacement,  $\delta^*$ , and momentum,  $\theta$ , thickness (a) plot and Wake velocity profiles (b) at 4 different stations for CWC at  $\alpha = 8^\circ$  and  $V_t = 40\text{m/s}$

field plot observations. The flow is separated for all the stations selected. Once more, there is not any sign of wake bursting happening.

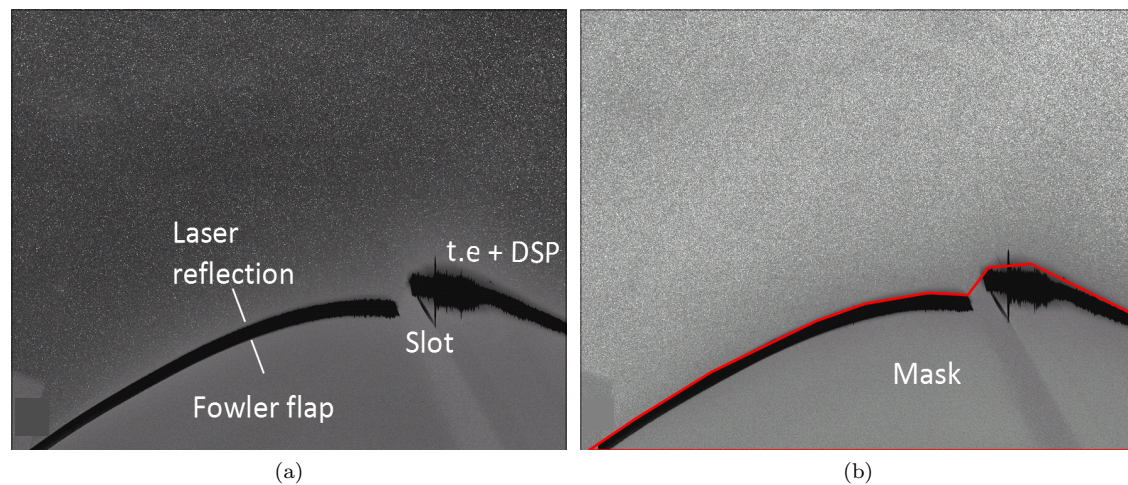


Figure 3.45: Post-processed image of the wing-flap configuration (a), showing the reflection due to the laser beam and (b) Mask out-layer as applied using Davis software 8.1 for drooped spoiler panel (DSP1)

### Test Case (3): Drooped Spoiler Panel (DSP1) at $0^\circ$

For this case, the DSP1 (at  $15^\circ$ ) was attached and observing the field of view (FOV = 273 mm x 214 mm), a small part of the main wing's trailing edge with the drooped panel attached and the whole Fowler flap were captured. As for the case without the DSP, the cove area, was not visible at all, however, the slot between the wing and the flap could be slightly noticed. Despite that, the flow through the slot was very difficult to be captured as there was not light going in that particular area, but it's effect on the suction side of the flap was obvious, as will be seen later in the total velocity plots. Another issue, was the reflection of the laser beam when it was in contact with the wing and flap's surface. This is clear in Figure 3.45 (a) and on the right image (b), one could see the mask's out-layer, represented by the red line. On the plots presented later, all this region is covered with a black mask.

The third test case presented, is the one with the drooped spoiler panel attached at  $0^\circ$  and tunnel velocity at 40 m/s. From the total velocity field plot with streamlines, two main features could be noticed. The first one, is that the flow velocity close to the proximity of the wall is increased significantly and the flow stays attached on the Fowler flap as shown in Figure 3.46, in contrast to the clean wing configuration (CWC) case, where the flow is clearly separated, shown in Figure 3.40. Hence, it could be said with confidence that the drooped spoiler panel keeps the flow attached on the Fowler flap's surface. The second observation is that above the attached flow on the Fowler flap, it seems that an area of very low velocity exists, after mid-chord ( $c/2$ ) distance, and this could be an indication of wake bursting occurring at higher angles of attack of the model configuration.

From displacement and momentum thickness (a) plot presented in Figure 3.47, both variables have negative values up to mid-chord distance ( $c/2$ ), where the highest velocities take place on the suction side of the Fowler flap. This behaviour was noticed for CWC at the same angle of attack and was explained analytically. Afterwards, both increase but much less than for the clean

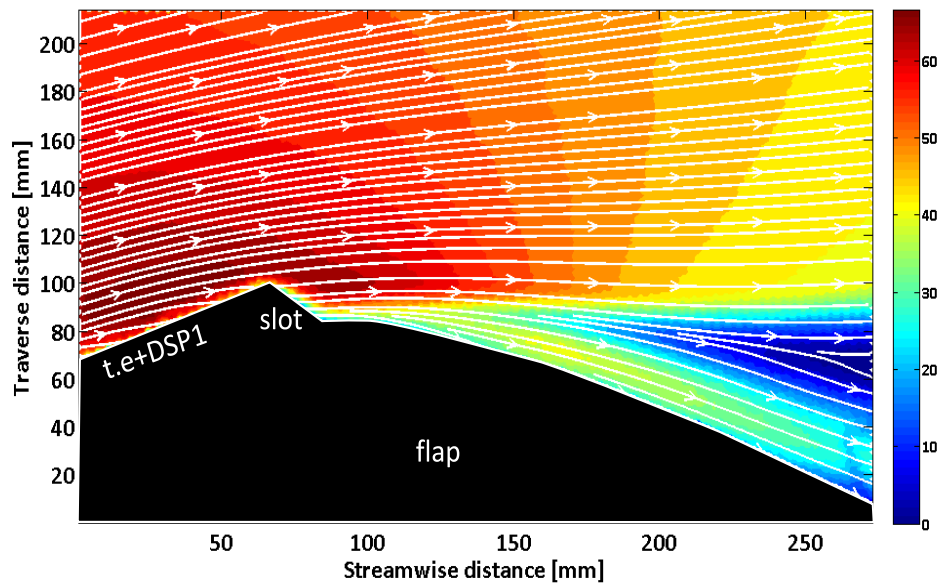


Figure 3.46: Total velocity field with streamlines for DSP1 at  $\alpha = 0^\circ$  and  $V_t = 40\text{m/s}$

wing configuration (CWC) case presented earlier. In particular, the displacement thickness,  $\delta^*$ , increases considerably more than the momentum thickness, at approximately 32 mm, which is nearly half from the clean wing (CWC) case. On the other hand, the momentum thickness,  $\theta$ , increases around 15 mm, which is nearly 5 mm less than the clean wing case. From the other plot (b), the velocity profiles at the four different stations show normal behaviour from the flap's surface up to the edge of the boundary layer. Then, a very low velocity region above the boundary layer, having a significant drop in velocity covering approximately 20 mm, is very obvious as it was observed in the total velocity field plot in Figure 3.46.

#### Test Case (4): Drooped Spoiler panel (DSP1) at $8^\circ$

The fourth test case presented, is the one with the drooped spoiler panel attached at  $8^\circ$  and tunnel velocity at 40 m/s. From the total velocity field plot with streamlines in Figure 3.48, two main features could be noticed. Firstly, the flow on the flap's surface seems to be attached, however, the flow above the boundary layer, in the wake is reversed. This is what expected and called wake bursting phenomenon. Interestingly, it seems the flow is kept attached close to the wall, due to the wake bursting, as it could be observed by the direction of the streamlines. Hence, there is a serious indication that the wake bursting keeps the flow attached on the surface. Moreover, the flow on the trailing edge of the main wing seems to have lower velocity values than for the case with DSP1 at  $\alpha = 0^\circ$ , and this could be expected due to the higher angle of attack of the whole configuration. The interesting bit comes from the drooped spoiler panel (DSP1), where the reversed flow seems to influence. This could be linked to the flow visualisation observations presented in subsection 3.4.1, which showed reversed flow on the inclined surface of the drooped spoiler panel. All these phenomena could be seen in Figure 3.48.

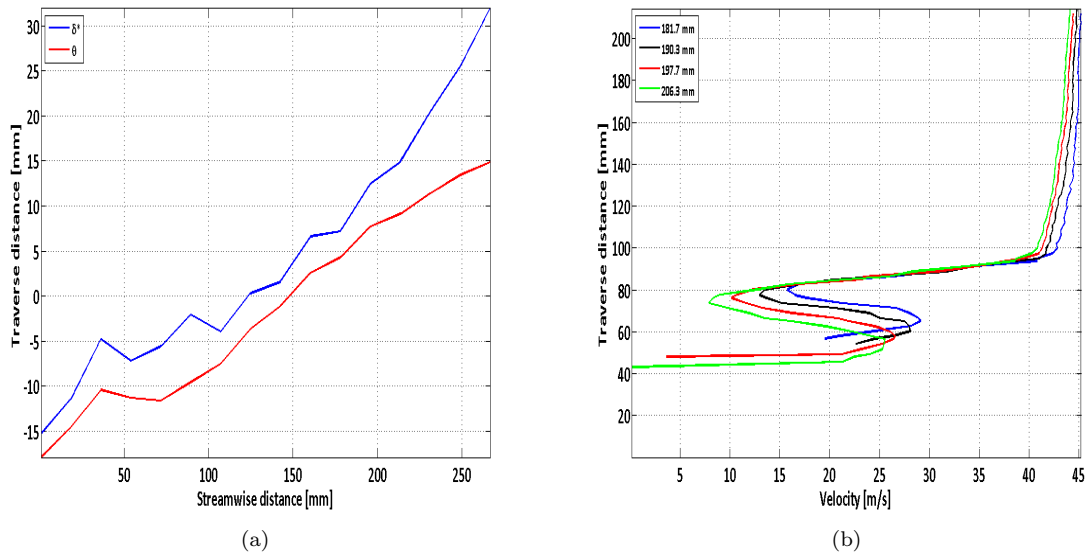


Figure 3.47: Displacement,  $\delta^*$ , and momentum,  $\theta$ , thickness plot (a) and Wake velocity profiles (b) at 4 different stations for DSP1 at  $\alpha = 0^\circ$  and  $V_t = 40\text{m/s}$

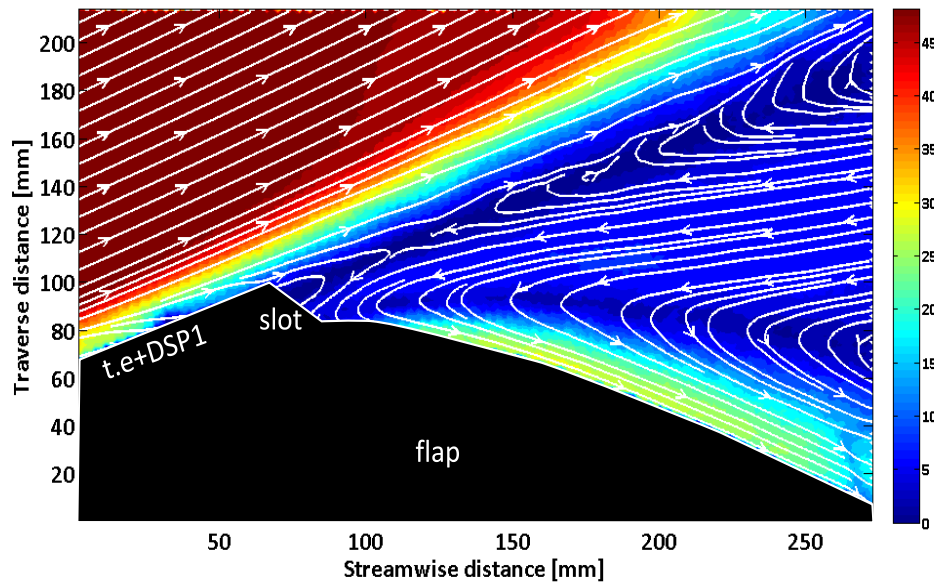


Figure 3.48: Total velocity field with streamlines for DSP1 at  $\alpha = 8^\circ$  and  $V_t = 40\text{m/s}$

From the next two plots presented in Figure 3.49, the displacement and momentum thickness plot (a) as well as the velocity profiles plot (b), at four different stations, several comments could be made. From plot (a), both displacement,  $\delta^*$ , and momentum,  $\theta$ , are increasing across the chordwise distance. It comes without surprise that both increase and they get their highest values compared to all the other cases mentioned so far. However, close to the trailing edge it seems that there is a decrease possibly due to the flow reversal. From the wake velocity plot (b), further information could be extracted for the wake bursting phenomenon. Flow seems to diverge, as pressure increases, moving to opposite directions, as shown by the streamlines. Part of the flow moves towards the wall of the Fowler flap and the other part towards the free stream area. This is the reason that wake bursting phenomenon, could be argued to keep the flow attached on the surface of the flap.

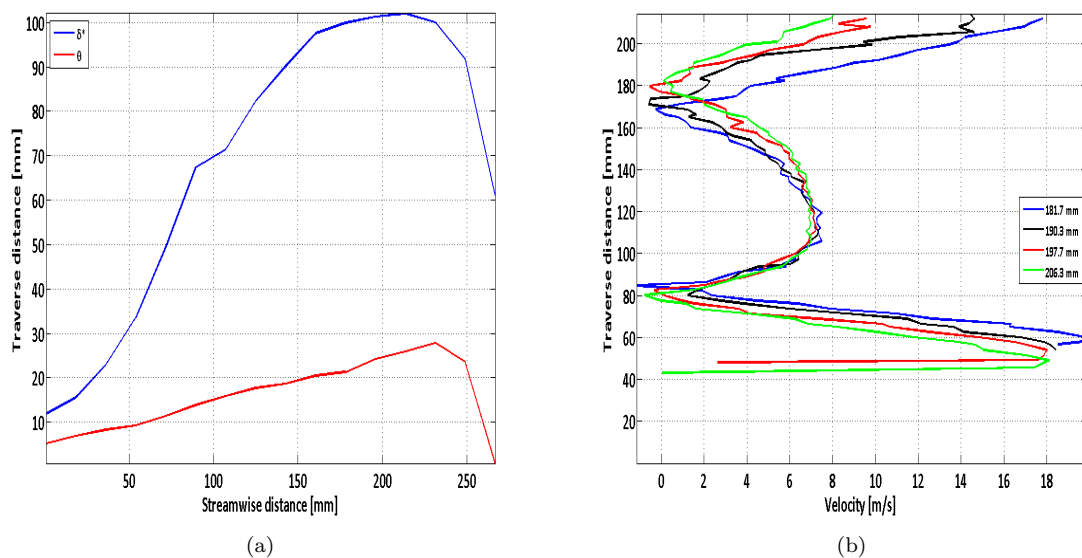


Figure 3.49: Displacement,  $\delta^*$ , and momentum,  $\theta$ , thickness (a) plot and Wake velocity profiles (b) at 4 different stations for DSP1 at  $\alpha = 8^\circ$  and  $V_t = 40\text{m/s}$

#### Test Case (5): Drooped Spoiler panel (DSP1) with (upper + lower) roughness at $0^\circ$

The next test case presented, is with DSP1 attached and surface roughness on the upper and lower sides of the main wing, at  $\alpha = 0^\circ$  and tunnel velocity of 40 m/s. From the first plot, the total velocity field with streamlines shown in Figure 3.50, the flow is clearly attached on the surface of the Fowler flap due to the effect of the drooped spoiler panel. However, it is very obvious that above the boundary layer, the area of very low velocity is larger for this case than for the case without the roughness, and reversed flow exists as it could be noticed by the white streamlines in Figure 3.50. Therefore, this off-the-surface reversal, could be explained by the extra thickness of the boundary layer caused by the surface roughness on top and bottom sides of the main wing.

From the next two plots presented in Figure 3.51, the displacement and momentum thickness plot (a), as well as the velocity profiles plot (b), at four different stations, several comments could be made. From plot (a), both displacement,  $\delta^*$ , and momentum,  $\theta$ , are both increasing

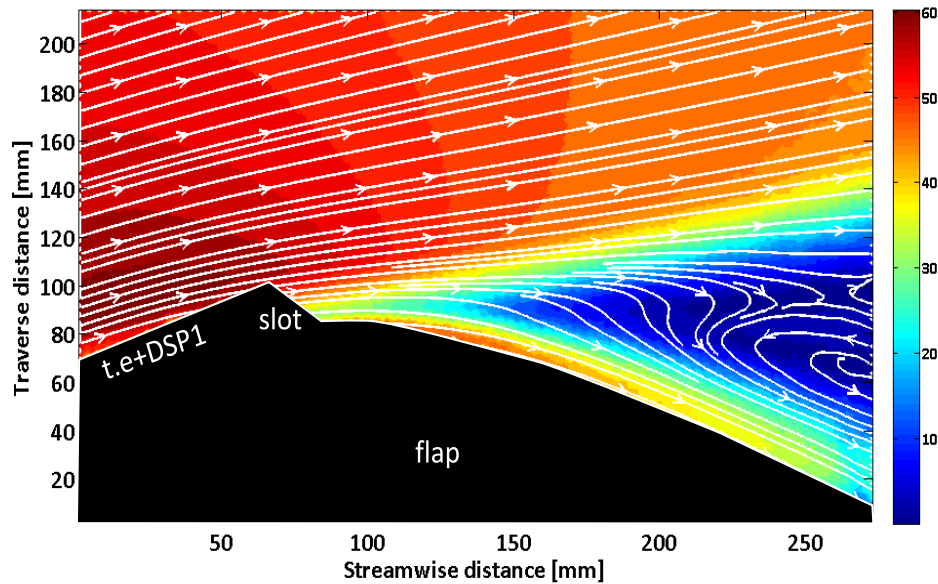


Figure 3.50: Total velocity field with streamlines for DSP1 with upper and lower surface roughness on the main wing, at  $\alpha = 0^\circ$  and  $V_t = 40\text{m/s}$

across the chordwise distance. However, one could notice that the value of the displacement thickness is doubled again compared to the simple drooped spoiler panel case (Test Case (3)). Of course, this is explained by the roughness on both sides of the main wing, increasing the displacement thickness and leading to wake bursting above the flap, which in turn causes this great increase. On the other hand, the momentum thickness seems to stay the same, not showing further increase. From the wake velocity plot (b), it is very clear that the flow is attached on the surface of the Fowler flap but moving upwards on the wake region, there is a great reduction in flow velocity and increase in pressure, which causes the flow to reverse abruptly. Then, the flow velocity increases again as moving to the free-stream region.

#### Test Case (6): Drooped Spoiler panel (DSP1) with (upper + lower) roughness at $8^\circ$

The last test case presented, is with DSP1 attached and surface roughness on the upper and lower sides of the main wing, at  $\alpha = 8^\circ$  and tunnel velocity of 40 m/s. From the first plot, the total velocity field with streamlines presented in Figure 3.50, there are not very important differences noted, especially compared to the case with the drooped spoiler panel at  $\alpha = 8^\circ$  (Test Case 4). The features presented are the same, showing severe wake bursting happening above the boundary layer region. Once more, it seems that the wake bursting has an effect on keeping the boundary layer attached due to the divergence of the reversed flow, as it could be noticed by the white streamlines in Figure 3.52.

From the next two plots, in Figure 3.53, showing the displacement and momentum thickness plot (a), as well as the velocity profiles plot (b), at four different stations, there are not much to discuss. From plot (a), both displacement,  $\delta^*$ , and momentum,  $\theta$ , are increasing across the

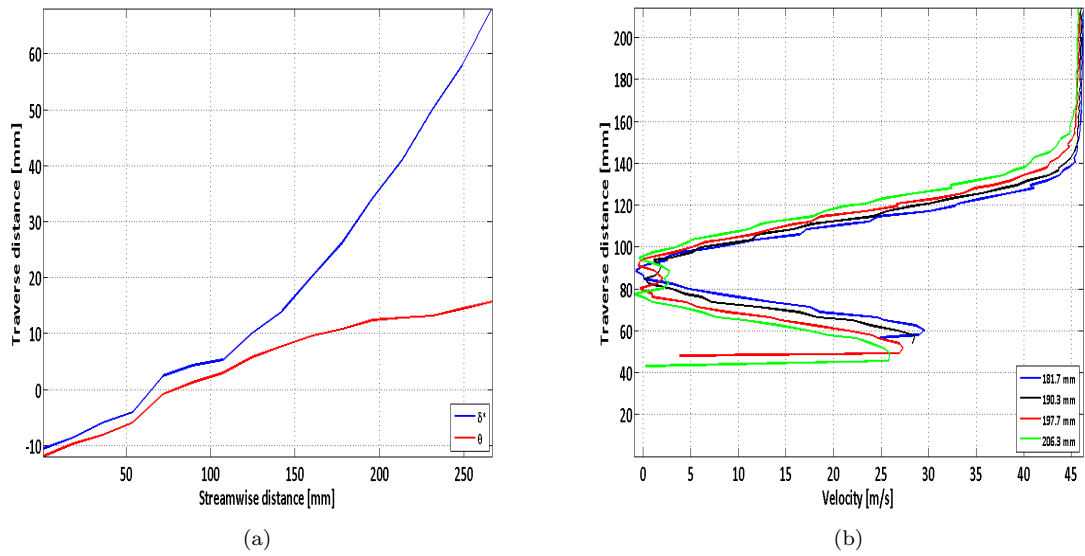


Figure 3.51: Displacement,  $\delta^*$ , and momentum,  $\theta$ , thickness (a) plot and Wake velocity profiles (b) at 4 different stations for DSP1 with upper and lower surface roughness on the main wing, at  $\alpha = 0^\circ$  and  $V_t = 40\text{m/s}$

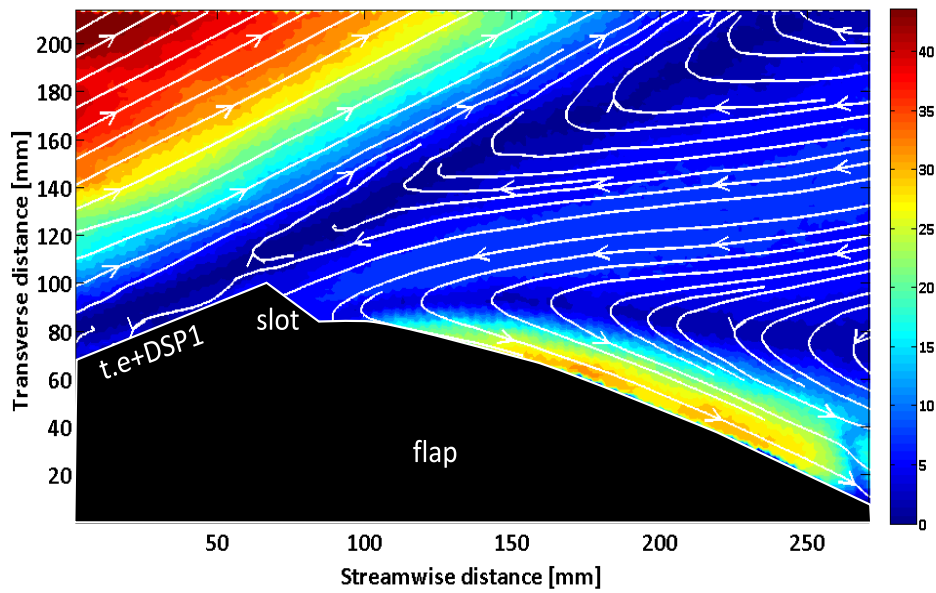


Figure 3.52: Total velocity field with streamlines for DSP1 with upper and lower surface roughness on the main wing, at  $\alpha = 8^\circ$  and  $V_t = 40\text{m/s}$

chordwise distance. However, one could notice that the value of the displacement thickness is very similar compared to the simple drooped spoiler panel case (Test Case 4). As a result, when wake bursting is very strong, such as at  $\alpha = 8^\circ$ , the contribution of surface roughness on the main wing to the displacement thickness in the wake could be thought as negligible.

From the wake velocity plot (b), the wake bursting phenomenon is clear. Flow seems to diverge, as pressure increases, moving to opposite directions, as shown by the streamlines in Figure 3.52 and part of the flow moves towards the wall of the Fowler flap and the other part to the free stream region. This is the reason that wake bursting phenomenon, may be the reason for having attached flow on the surface of the flap. This is shown by the two negative peaks in velocity in Figure 3.53, which represent reversed flow in different directions, one towards the boundary layer and the other towards the free-stream.

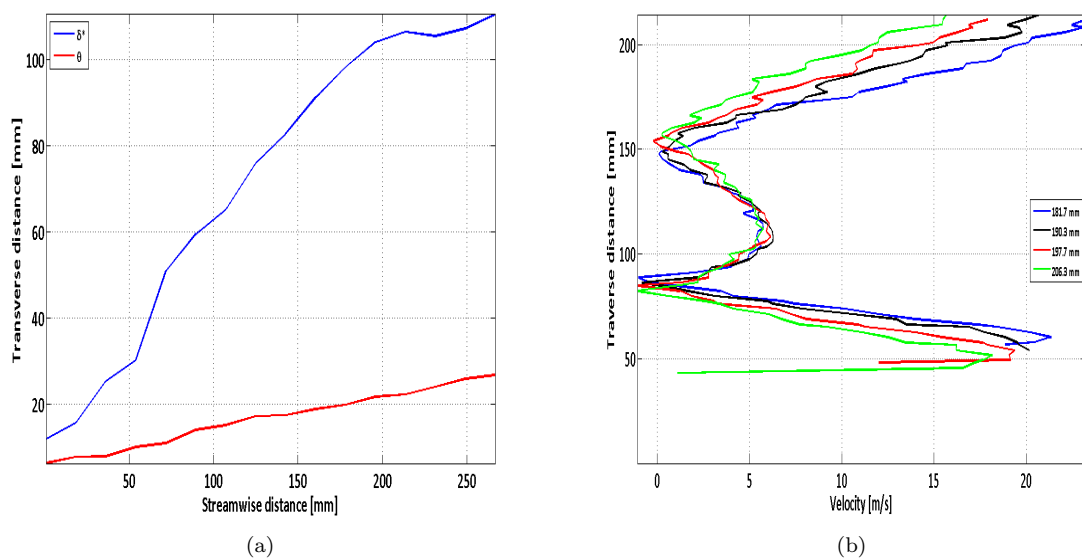


Figure 3.53: Displacement,  $\delta^*$ , and momentum,  $\theta$ , thickness (a) plot and Wake velocity profiles (b) at 4 different stations for DSP1 with upper and lower surface roughness on the main wing, at  $\alpha = 8^\circ$  and  $V_t = 40\text{m/s}$

### 3.5 Experimental Campaign I Conclusions

The first experimental campaign was performed in the Low Turbulence Tunnel (LTT) of the Low Speed Laboratory (LSL) at Delft University of Technology and included tests with the X-400 wing-flap model configuration. The initial objective of these tests was to study the clean wing configuration performance at flap angle of  $\delta_f = 50^\circ$ , but also to simulate a drooped spoiler panel (DSP) and determine its effect as a passive flow control device, in order to postpone or eliminate flow separation on the Fowler flap. However, after the first tests, the main goal was to perform some applied research on wake bursting, which was the cause of considerable loss of lift on the overall performance of the configuration, using the flow control device compared to the clean wing configuration.

From the results of this testing campaign numerous conclusions were drawn and will be presented briefly in this section. Flow visualisation tests carried out using woollen tufts and fluorescent oil, with the clean wing configuration, showed clear flow separation on the Fowler Flap from low angles of attack at mid-chord position. On the other hand, placing the drooped panel spoiler (DSP1) on the main wing, the flow on the Fowler flap was totally attached at this high flap angle of  $\delta_f = 50^\circ$ . Hence, the effect of this passive flow control device was positive from early testing.

Then moving to pressure measurements, from pressure taps data and the  $C_p$ -distribution plots, the same phenomena observed. For the clean wing configuration, the Fowler flap was separated up to  $\alpha = 10^\circ$ . Beyond that, the main wing was separated and the Fowler flap attached. On the other hand, when the drooped spoiler panel (DSP) was attached, the Fowler flap was attached for the whole range of angles of attack up to  $14^\circ$  and the main wing was separated after  $10^\circ$ . More DSP devices used with different geometric characteristics, but none seemed as efficient as DSP1 (at  $15^\circ$ ), keeping the flow attached on the surface of the flap.

From lift and drag calculations, it was very clear that CWC had higher  $C_L$  values compared to DSP cases. Specifically for DSP1,3 and 4, a flat plateau  $C_L$  line was noticed from  $\alpha = 6^\circ$  onwards accompanied by significant loss of lift. On the other hand the drag coefficients were lower for the DSP1 case compared to CWC, up to  $\alpha = 8^\circ$ .

As the angle of the DSP was reduced, the lift coefficient was increasing significantly but the flow on the surface of the Fowler flap was not attached any more, as for the case of DSP1 (at  $15^\circ$ ). This was the reason for choosing this panel as the one to continue the tests with the X-400 model. This device was able to keep the flow attached for the whole range of angles of attack tested, up to  $14^\circ$ . Continuing with the DSP1, the effects of Reynolds number examined. Increasing the Reynolds number, it was noticed that the lift was increased possibly due to the thinner boundary layer thickness. However, at higher Reynolds numbers, the separation and the three-dimensionality (3-D) of the flow was quite strong on the Fowler flap. Moreover, the drag was also decreased as the Reynolds number increased.

The explanation for this sudden loss of lift was that wake bursting or also called off-the-surface separation is happening. The reason for that was from the observation of reversed flow region on the drooped panel's surface during the oil flow visualisation tests, while at the same time the Fowler flap surface was fully attached. Therefore, in order to validate this initial thought, further pressure measurements carried out on the Fowler flap surface. The most interesting results noticed at the angles of  $6^\circ$  and  $8^\circ$ , where wake bursting was indicated according to  $C_1$  plots. Then total pressure probe tests gave further indication that above the boundary layer region the flow was reversed and that wake bursting was indeed occurring at these angles of attack with the DSP1 attached. Finally, additional passive control techniques tested, in order to see their effect on wake bursting phenomenon. The first one was the use of vortex generators at different positions on the main wing, and the second one, different drooped spoiler panels (DSP1) with different hole diameters on the inclined side of the panel, in order to relieve pressure distribution in this area. The main conclusions from these trial and error tests, were that even if vortex generators helped to increase the lift slightly, these passive control devices were unable to eliminate the wake reversal significantly.

After these tests, PIV data would be essential in order to study and try to understand the nature of wake bursting phenomenon. At tunnel velocity of 40 m/s and flap angle of  $\delta_f = 50^\circ$ , for

the clean wing configuration at  $\alpha = 0^\circ$ , the Fowler flap is separated as expected approximately at the mid-chord as shown from the pressure measurements. As the angle of attack of the whole configuration increased to  $\alpha = 8^\circ$ , the flow separation region above the Fowler flap is increased in size. Of course, both the momentum and displacement thickness increased significantly compared to the  $0^\circ$  case, as the angle of attack increased too. For this case, no wake bursting was observed for any angle of attack tested. Placing the drooped spoiler panel and setting the whole configuration at  $0^\circ$ , the PIV data showed the ability of the panel to keep the flow attached on the Fowler flap. However, above that, even at  $0^\circ$ , a small region of very low velocity was apparent, on top of the boundary layer and could be described as an indication of wake bursting happening at larger angles of attack. Moreover, for this case at  $\alpha = 0^\circ$ , as the flow is kept attached on the Fowler flap, the displacement and momentum thickness were much lower than for the clean wing configuration, where severe flow separation is happening. Thus, even at this low angle with the drooped panel attached, there was still no sign of wake bursting. However, increasing the angle of attack at  $8^\circ$ , where according to pressure measurement data wake bursting initiated, it was very clear that things are totally different. The flow on the flap surface was still attached but the region of low velocity above the boundary layer was much greater in size. The most interesting observation of PIV, was the divergence of the reversed wake flow which could be the reason of attached flow on the Fowler flap's surface. This divergence causes the flow to brake in two parts. One moving towards the boundary layer and one towards the free-stream. Therefore, the part moving towards the boundary layer, could increase the momentum in the boundary layer even further, keeping the the boundary layer attached on the surface. The displacement and momentum thickness, both increase slightly more than the clean wing configuration case, which could be explained as normal due to the very large area of reversal region in the wake.

The last data presented were about the case of drooped spoiler panel in combination with roughness on top and bottom of the main wing. The only interesting difference, was that the roughness would increase the thickness of the wake much faster, hence even at  $0^\circ$ , where there was no wake bursting just with the DSP attached, now the off-the-surface separation is obvious above the boundary layer of the Fowler flap. Thus, it seems that increasing the displacement thickness,  $\delta^*$ , the wake bursting was initiated much earlier, which could mean that these two are very related. On the other hand, the momentum thickness,  $\theta$ , was not showing such a behaviour. However at larger angles of attack, the contribution of the displacement and momentum thickness to wake bursting looked negligible compared to the lower case, as the phenomenon is already very strong due to the very large angle of the configuration and as a result of the great divergence of the flow causing this phenomenon to happen.

## Chapter 4

# Wind Tunnel Testing Campaign II

In order to study and potentially understand the wake bursting phenomenon, it was decided to proceed by carrying out further fundamental tests. This route was chosen firstly to validate some of the findings of the first wind-tunnel campaign and secondly in order to link these fundamental studies to the more practical application of main wing-high lift devices interaction, which is what is missing from the literature. As a result, this chapter presents all the relevant aspects with respect to experimental apparatus, set-up, procedures and results of this testing campaign carried out in a more fundamental set-up.

### 4.1 Experimental Apparatus

#### 4.1.1 Experimental Facility: M-Tunnel

The M-tunnel is a model tunnel of the Low turbulence tunnel facility and it can be used as both an open jet or a closed wind tunnel. Depending on whether it is used as an open or closed tunnel, the maximum velocity can reach 35 m/s or 50 m/s respectively. The test section of the tunnel is 0.4 m x 0.4 m square and due to the large contraction ratio, the turbulence level of the flow in the test section is low [22]. An overview of the M-tunnel is presented in Figure 4.1.

In the beginning, several items which would consist the wind tunnel set-up for these tests manufactured. The experimental set-up was very important and it's quality was detrimental for the success of the experiments. The experimental set-up for this fundamental campaign consisted of a flat plate, half of it placed in a diffuser, in order to create the necessary pressure gradient and simulate the effect of wake reversal behind it. Of course the items needed for the complete set-up were much more than a flat plate and a diffuser and will be discussed in detail in the next sub-sections. In Figure 4.2, a 3D schematic of the generic set-up used for these tests is shown.

#### 4.1.2 Plexiglass Flat Plate

The flat plate used for the experimental set-up, was a plexiglass flat plate from previous experiments, but it was modified according to the needed dimensions and surface quality standards.

The dimensions of the plexiglass flat plate are presented in Table 4.1.



Figure 4.1: Schematic overview of the M-tunnel, used for the second experimental campaign [22]

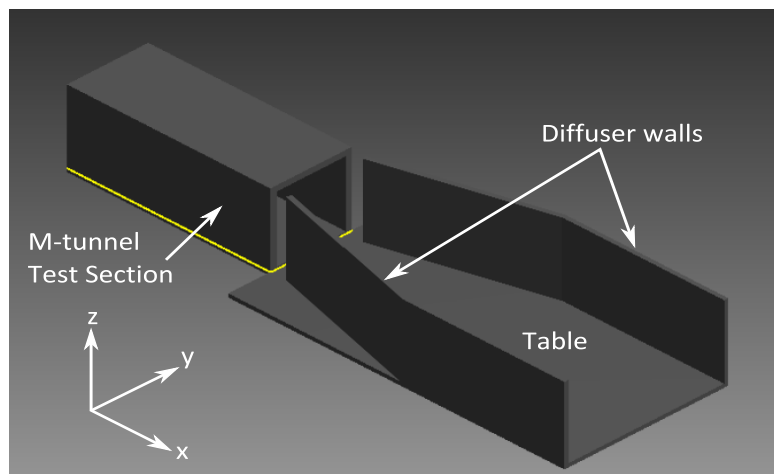


Figure 4.2: 3D wind-tunnel set-up schematic, including test section of the M-tunnel, diffuser walls and support table

Length (l) [mm]	Height (h) [mm]	Thickness (t) [mm]
950	400	20

Table 4.1: Plexiglass flat plate geometrical definitions

Then, the rear part of the plexiglass plate (last 100 mm) was tapered and the leading edge (first 45 mm) was rounded as shown in Figure 4.3, in order to simulate airfoil-smooth flow across the flat plate, avoiding any possible separations due to geometrical imperfections.

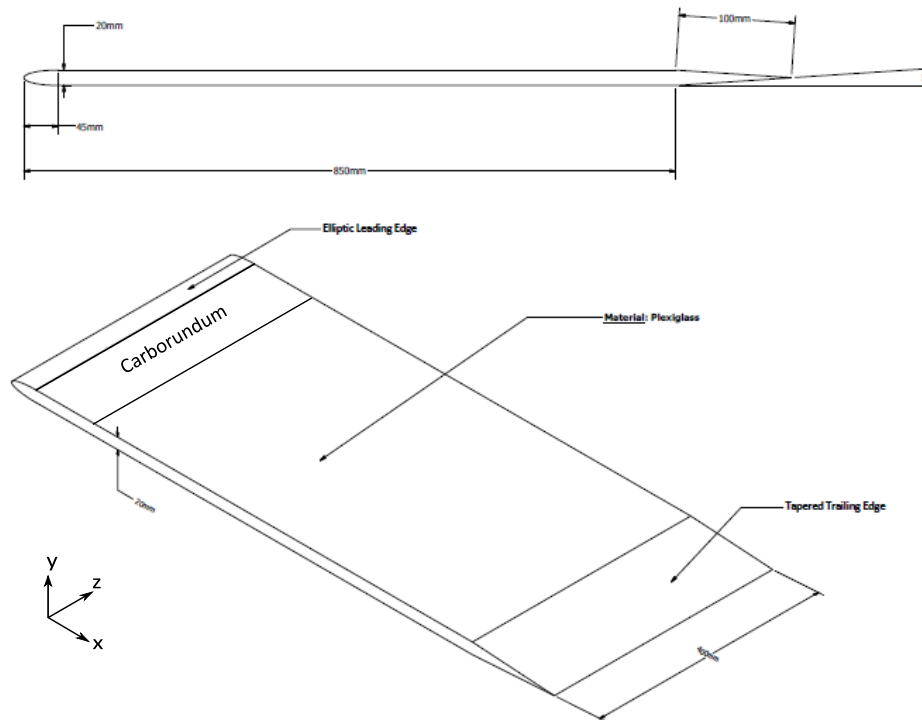


Figure 4.3: Final plexiglass flat plate drawing with rounded leading edge and tapered trailing edge including geometrical information

As the leading edge of the plate was rounded and the trailing edge tapered according to the drawing shown in Figure 4.3, surface roughness was placed close to the leading edge region, in order to trigger the boundary layer and force transition from laminar to turbulent boundary layer, as would happen to airfoil case. This was done using sand paper tape and carborundum grains distributed on it. The length ( $x$ -axis) of the sand paper tape on the plexiglass plate was decided to be 160 mm on both sides of the plate, covering the whole span distance ( $z$ -axis). Finally, the determination of the critical roughness height was important in order to select the correct carborundum grain size. According to literature [36], the critical roughness height,  $k$ , is defined as presented in equation 4.1.

$$k = \frac{x}{Re^{\frac{3}{4}}} \sqrt{\frac{Re_k}{0.332}} \quad (4.1)$$

where,  $x$  = size of the model used, hence, in our case  $x = 950$  mm

Therefore,

$$Re_x = \frac{1.225 \cdot 28 \cdot 0.95}{1.85 \cdot 10^{-5}} \approx 1.6 \cdot 10^6 \quad (4.2)$$

It is also known that  $Re_k = 600$  for 3D roughness. Thus,

$$k = \frac{0.95}{(1.6 \cdot 10^6)^{\frac{3}{4}}} \sqrt{\frac{600}{0.332}} = 8.97 \cdot 10^{-4} \approx 0.89 \text{ mm} \quad (4.3)$$

As a result, a carborundum grain size of 0.84 mm used, as it was the closest size available to the calculated theoretical value. However, the thickness of the double-sided tape was also taken into account having a measured thickness of 0.22 mm. Therefore, the critical roughness height,  $k$ , was approximately 1 mm which was thought as acceptable in order to achieve transition on the flat plate. Then the carborundum grains were distributed uniformly along the span of the plate. In Figure 4.4, the carborundum grains applied on the plate's surface close to the leading edge are shown.

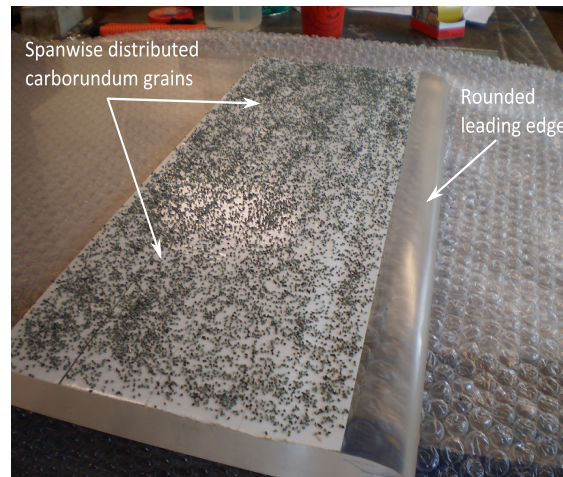


Figure 4.4: Carborundum grains applied on the flat plate's surface, close to the rounded leading edge region

### 4.1.3 Diffuser Walls

The diffuser section consisted of two diverging walls followed by two straight walls, as it is illustrated in Figure 4.2. For the divergent walls, wooden rectangular blocks placed in line with 5 mm slots between each other, in order to form the wall. These slots used to create suction with the aid of the screen, placed at the end of the diffuser section and as a result to avoid flow separation at the wall's surface due to adverse pressure gradients. The other two walls, used for the straight part of the diffuser, were rectangular continuous sections.

Finally, as it was intended to perform measurements using pressure probes and as the wind-tunnel/set-up configuration was quite complex, it was decided to drill holes on one of the diverging diffuser walls. This was done in order to insert an aluminium rod (with the probe attached on it) through these holes and thus carry out the measurements. The diameter of the aluminium rod

was 9.5 mm, so the diameter of these holes was approximately 10.5 mm. These holes would be covered with duct tape while not used, in order to avoid further suction. In total 13 holes were drilled, 8 on the diverging wall and 5 on the straight section wall of the diffuser. A schematic showing the diverging and straight wall sections is presented in Figure 4.5. Notice, the small pressure tap holes on the top surface of the wall on blocks 2, 4, 6 and 8 measuring from left to right. In total eight pressure taps (four on each wall) used, in order to measure the static pressure on the diffuser walls at different stations.

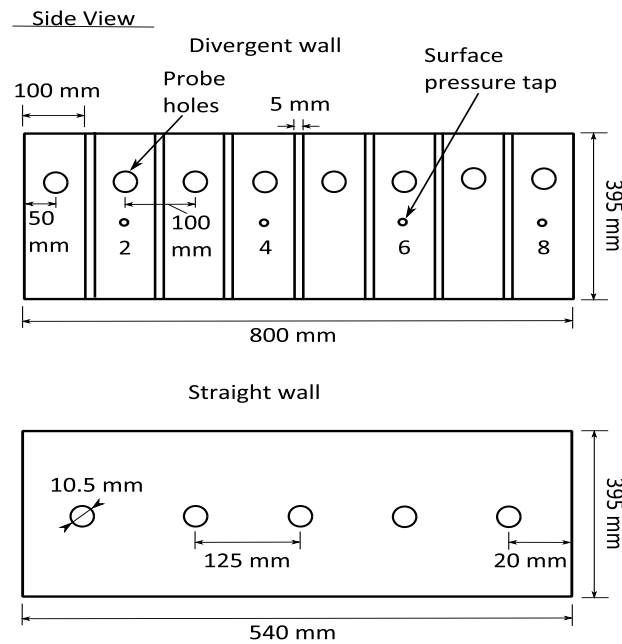


Figure 4.5: Schematic of the diffuser diverging and straight wall sections with pressure taps on blocks No. 2, 4, 6 and 8 measuring from left to right, including geometrical information

The next thing done after surface smoothing, in order to have the best possible surface quality, was to place woollen tufts on the diverging diffuser walls, in order to perform flow visualisation tests. Thus, 12 tufts were placed on each wall in four different rows of 3 tufts each, hence 24 tufts in total for both divergent walls. The length of the each tuft was measured as 50 mm. In Figure 4.6, one diverging diffuser wall is presented with all the woollen tufts placed on it's surface and ready to be mounted in the wind tunnel. Further pictures of the wind-tunnel set-up with the diffuser walls attached could be found in **Appendix B**.

#### 4.1.4 Wind-Tunnel Screen, Supporting Table & Top Walls

Using this set-up, adverse pressure gradients expected between the two diverging diffuser walls. This of course would lead to flow separation on the walls placed approximately at an angle of  $15^\circ$ . As a result, by placing a screen at the end of the straight walls, over pressure would be created and in combination with the slots on the diverging walls, suction would take place there and as a result the boundary layer could stay attached. Moreover, a horizontal slot was cut in the centre of the screen to be used for the PIV experiments. This slot needed to allow access for the laser beam due to the limited accessibility of the current set-up. The length of this slot

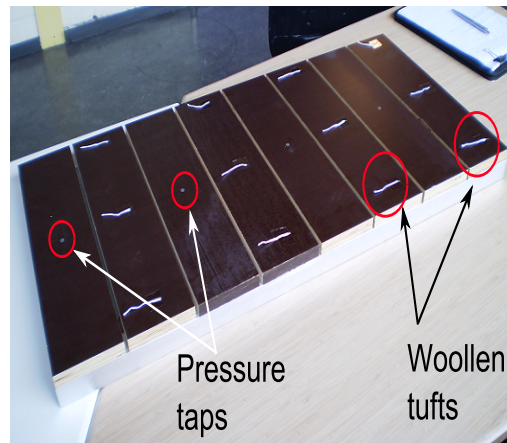


Figure 4.6: Diffuser diverging wall with woollen tufts attached on it's surface

was  $l_s = 200\text{mm}$  and it's thickness,  $t_s = 20\text{mm}$ . Finally, the screen was attached on the two straight wall sections by two L-shaped aluminium structures, which were screwed on the walls. The screen used looks like a mesh and is made out of copper. A schematic of the screen used for these tests is shown in Figure 4.7.

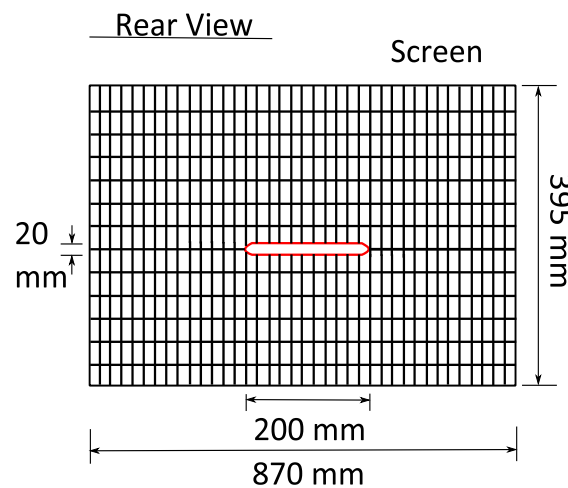


Figure 4.7: Schematic of the screen placed at the end of the diffuser section including geometrical information

Furthermore, a table was used as a support for the whole set-up with  $l = 1850\text{ mm}$  and  $w = 930\text{ mm}$ . Finally, on the top of the set-up, two transparent plexiglass plates placed in order to cover the diffuser area. The reason for placing these transparent walls was initially to have visual contact with the set-up during testing, but additionally, to have optical access for the camera, in order to perform PIV tests. The dimensions of these plates were  $l = 777\text{ mm}$ ,  $w = 904\text{ mm}$  and  $t = 5\text{ mm}$ . The final set-up could be seen in Figure 4.8.

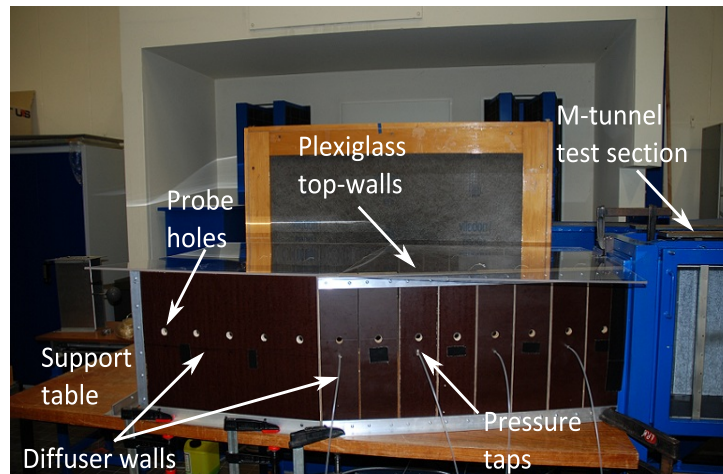


Figure 4.8: Schematic of the screen placed at the end of the diffuser section including geometrical information

## 4.2 PIV & Pressure Measurements Set-Up

### 4.2.1 Pressure measurements set-up

After all the mentioned parts of the generic experimental set-up were in place, the set-up for pressure measurements was prepared. The first thing to do was to connect all the tubes to the pressure tap exits. Then these tubes were connected to the inlets of a scanning valve device and then to a pressure sensor which was connected to a computer in order to record the data gathered. As mentioned in section 4.1.3, there were eight pressure taps, four on each wall. Hence, it was decided to name them for practical reasons. The first pressure tap hole (closest to the test section) was named as pt.1, the second one, as pt.2 and so on. The tubes for each point of each wall were finally connected to each other using a T-junction and then connected to the scanning valve's inlets. A diagram of the pressure tap tube connections could be seen in Figure 4.9.

Four different tubes from each point were connected to the back side of the scanning valve. The scanning valve had two different rotary switches. One of them, was used to select the wanted channel and the other was used in order to select the appropriate tube. For this case, the right channel was set at number 3 and the other rotary switch could be set from 1 to 4, depending on which point it was desired to record static pressures. The tubes used for the pressure measurements were of 55.5 mm diameter. As it is shown in Figure 4.9, a Pitot-tube inside the test section used in order to record a reference pressure value.

The holding structure and the traverse system which would be used in order to move the pressure probe in the test section was the last thing to prepare. The aluminium rod was attached on the traverse system and at its edge, a pressure tube could be placed. Moreover, a tube was also connected to the probe and then to the scanning valve at position 5. As a result, in order to check the static pressure at each station on the walls, the switch could be rotated from position 1 to 4. On the other hand, in order to measure the total pressure from the probe, the switch had to be rotated at position 5. A picture of the traverse system, is presented in Figure 4.11.

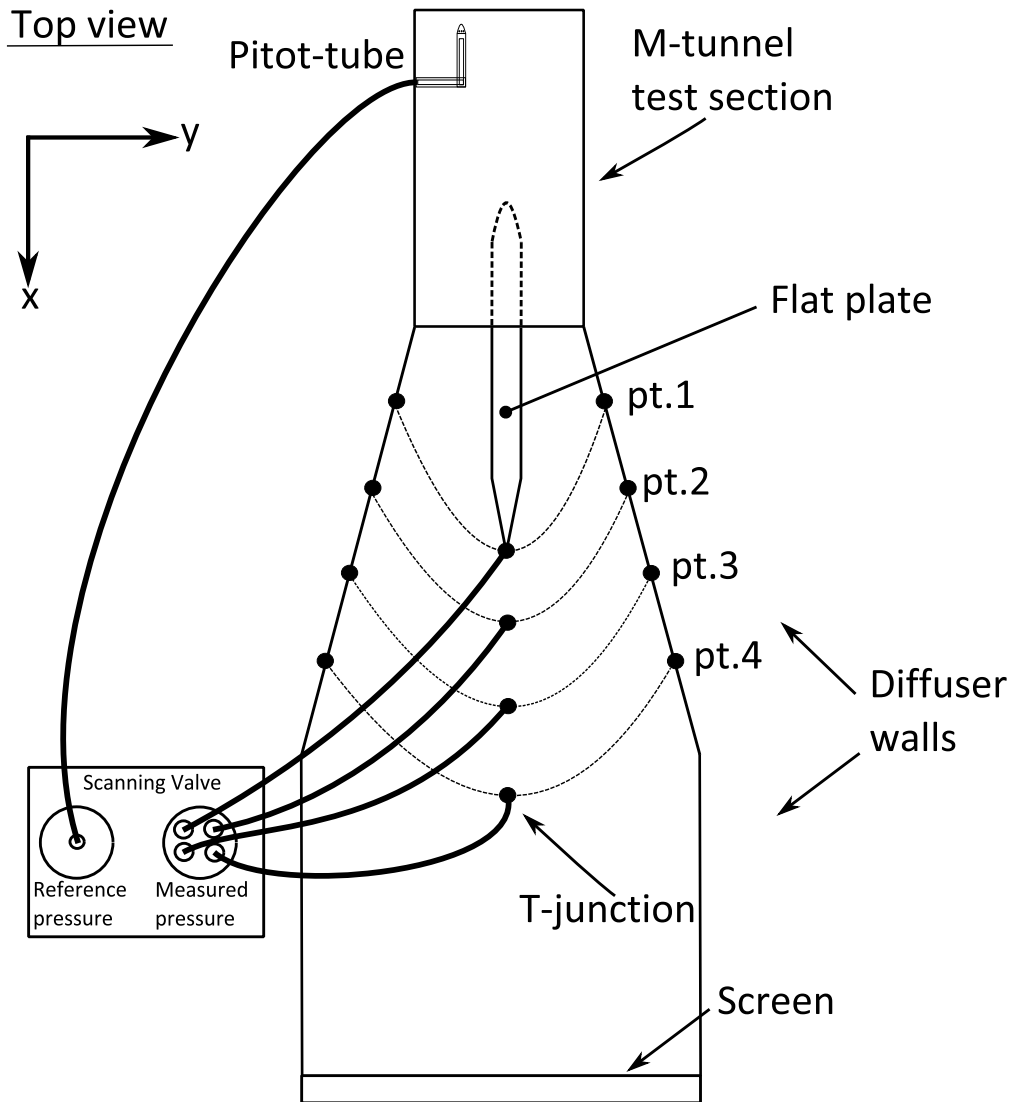


Figure 4.9: Schematic diagram of pressure tap tube connections

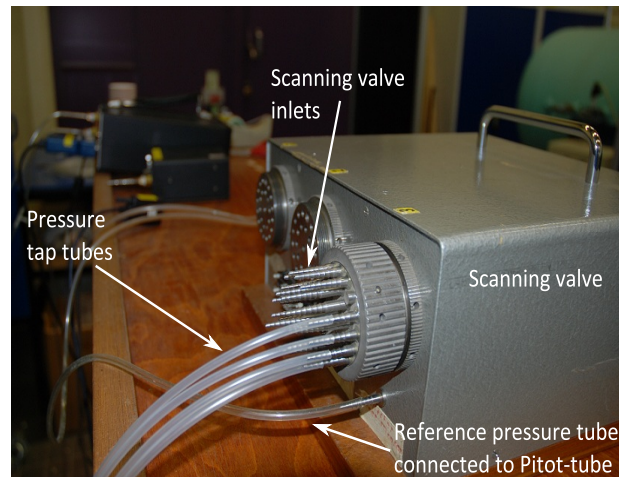


Figure 4.10: Scanning valve rear view with total pressure tubes connected, including explanations of individual parts

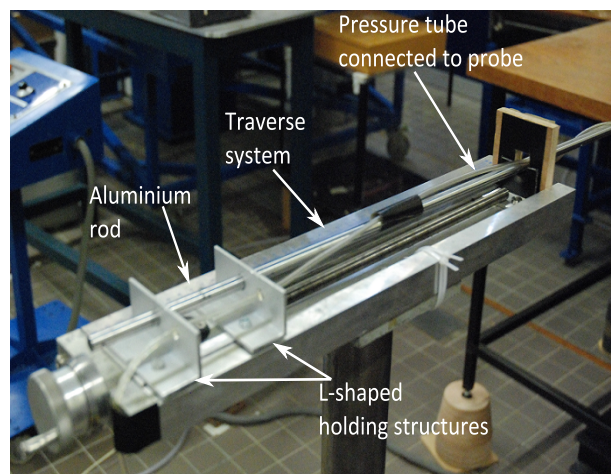


Figure 4.11: Probe traverse system picture, including explanations of individual parts

### 4.2.2 PIV set-up

The first thing done was to create a holding structure for the camera which was placed on top of the diffuser area, as this was the only possible placement allowing optical access. Thus, the holding structure had to be quite highly placed and stable enough and that is why a tripod was used, where the whole structure was attached on it. In addition, the BNC cables of the camera, had to be also long enough, in order to be connected to the computer used for PIV data acquisition. The final version of the camera holding structure with the camera attached on it, is presented in Figure 4.12.

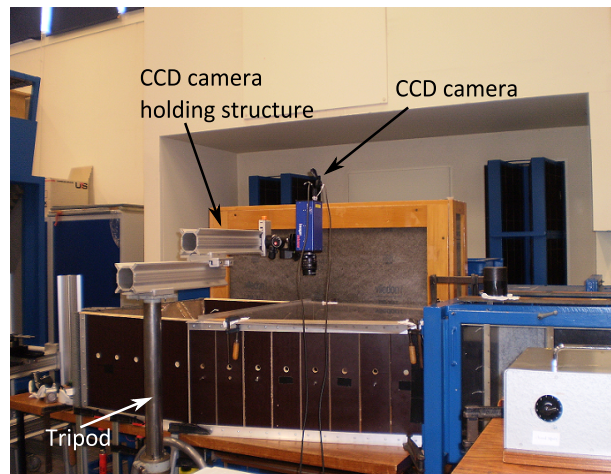


Figure 4.12: Final camera placement for PIV tests, including explanations of individual parts

The next step was to construct the laser holding structure. As shown in Figure 4.13, the laser structure, was placed behind the diffuser screen and the laser placed on it. The laser beam was able to "insert" in the diffuser area through a slot on the screen as described in section 4.1.4. As the laser was placed on the structure, the laser sheet was aligned with the measuring plane, as even a small angle on the beam could lead to non-accurate results. Moreover, the laser lenses positioned in front of the laser head by placing two negative lenses, one positive and one cylindrical at the end, in order to spread the beam into the test section. The exact position of the lenses is exactly as positioned for the PIV tests in wind-tunnel testing campaign I and a schematic of it is presented in Figure 3.11. Finally, the seeding generator position decided to be on the top of the transparent walls, as there was not any other alternative based on the complex set-up and space available.

Concluding, the whole set up was covered with black blankets, in order to keep the measurement regions as dark as possible, to avoid possible reflections. The laser holding structure, with laser attached on it and the lenses placed in front of it's head, together with the the alignment process of the laser beam through the screen slot are presented in Figure 4.14. More pictures of the CCD camera and laser could be found in **Appendix B** at the end of the report.

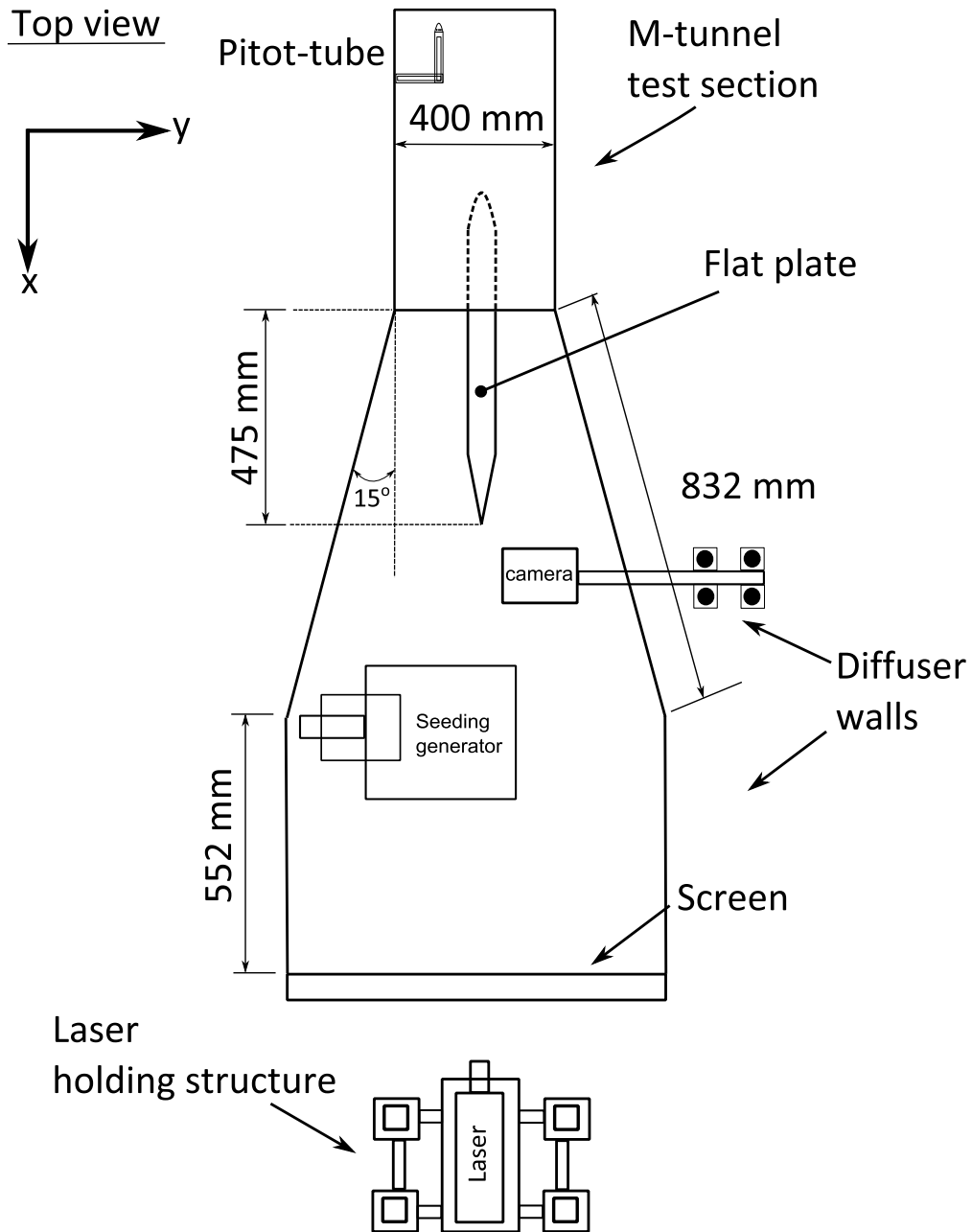


Figure 4.13: Schematic of the PIV set-up in top view including geometrical information and explanations of individual parts

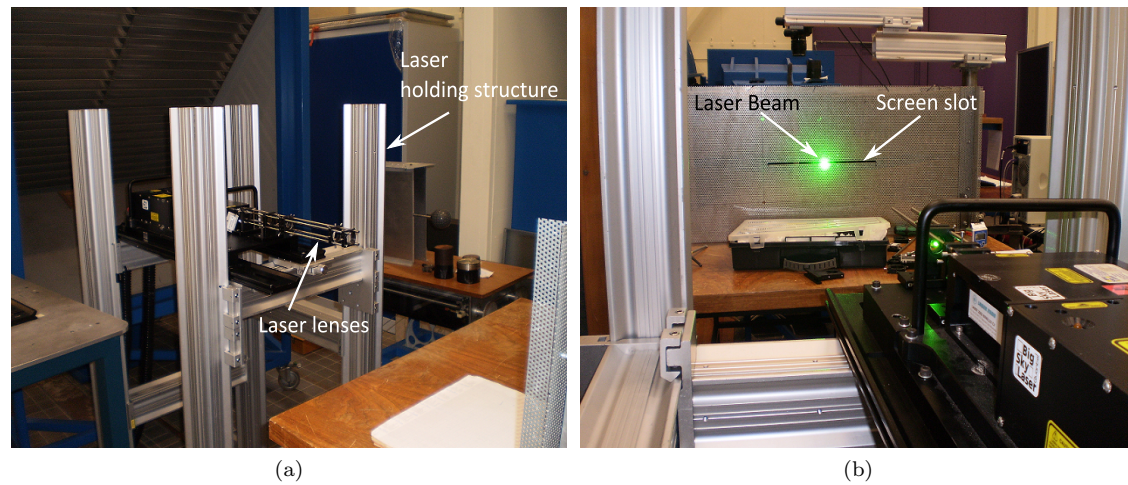


Figure 4.14: Laser holding structure (a) with laser attached on it and the lenses placed in front of it's head and (b) Alignment process of the laser beam through the screen slot

### 4.3 Experimental Procedure

The first thing done was running the tunnel at different speeds between 5 and 20 m/s, in order to carry out visual checks with respect to the set-up. The first problem realised was that the top transparent plexiglass plates, were lifting as the speed of the tunnel increased. As a result, weights placed on top of these walls, in order to keep them in place while running the tunnel at higher speeds. These weights created visibility issues, however, they were essential, since there was a serious danger of lifted walls during the experiments. Because of that, the running speed of the tunnel was limited to 22 m/s.

#### 4.3.1 Flow Visualisation

The next part of this experimental procedure, was to carry out quantitative flow visualisation tests to observe the flow on the walls of the diffuser. The woollen tufts already placed on the diffuser walls during the set-up were used. Flow visualisation also performed on the plexiglass flat plate in order to check if there was any flow separation and in the wake region behind it, to notice whether wake reversal was happening or not. Flow visualisation was carried out at two different speeds. The first was at 12 m/s and the second at the maximum speed tested, at 22 m/s as shown in Table 4.2 .

<b>Flow Visualisation Test Matrix</b>			
<b>Position</b>	Diffuser Walls	Flat Plate	Wake Region
$V_{t1}$ [m/s]	12	12	12
$V_{t2}$ [m/s]	22	22	22

Table 4.2: Woollen tufts flow visualisation test matrix

### 4.3.2 Surface Static Pressure Measurements

After flow visualisation tests, several static pressure data recorded for the four different stations on the diverging diffuser walls using the pressure taps positioned there. These measurements carried out in order to record the pressure values on the diverging walls of the diffuser due to the adverse pressure gradients. The static pressure data were recorded at all points from 1 to 4, ten different times during different measurements. This sample thought reliable enough in order to give a clear indication of how the pressure is changing in the diffuser area. The  $N$  value, which is in the test matrix in Table 4.3, represents the number of samples that recorded each time a measurement test was carried out. For all these measurements, this value was 200 with the time needed to record all these data measured at approximately  $t = 7$  seconds. Hence, 200 values were recorded for each measurement and then were averaged to give the mean. The test matrix for these ten measurements is presented in Table 4.3.

Surface Static Pressure Measurements Test Matrix				
PT No.	$V_t$ [m/s]	Measurements No.	$N$	$t$ [sec]
PT.1	22	10	200	7
PT.2	22	10	200	7
PT.3	22	10	200	7
PT.4	22	10	200	7

Table 4.3: Diffuser surface static pressure measurements test matrix

### 4.3.3 Boundary Layer Total Pressure Measurements

Then, boundary layer measurements carried out on the plexiglass flat plate surface. The points of measurements could be seen schematically in Figure 4.16 and in Table 4.4. In this table, on the second column, the  $x$ -position of each measuring point is given in mm, measuring from the trailing edge, as this point is assumed to be  $(0,0)$ . The negative signs represent the streamwise probe direction with respect to the coordinate system used for these measurements, as presented in Figure 4.15. From the trailing edge backwards to the plate the sign is negative and towards the wake becomes positive. In the same column of Table 4.4,  $N=1000$ . Once more,  $N$ , represents the number of samples gathered from **LabView** software each time a measurement was carried out. The time for gathering the 1000 samples and get the mean value was measured to be  $t = 26.5$  seconds.

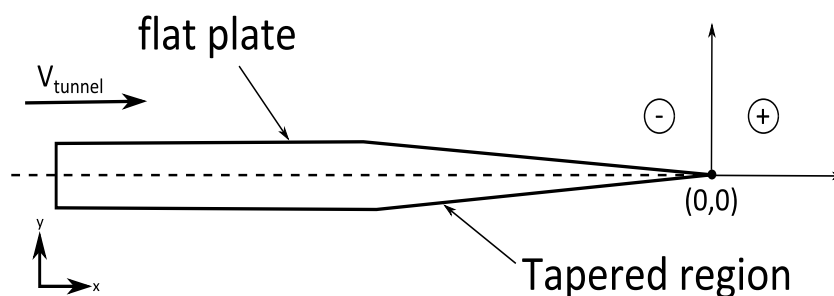


Figure 4.15: Coordinate system used for boundary layer measurements

The third column in Table 4.4, similarly includes the  $y$ -direction translation of the probe for each measurement. For all the measuring stations in  $x$ -direction, the total pressure was

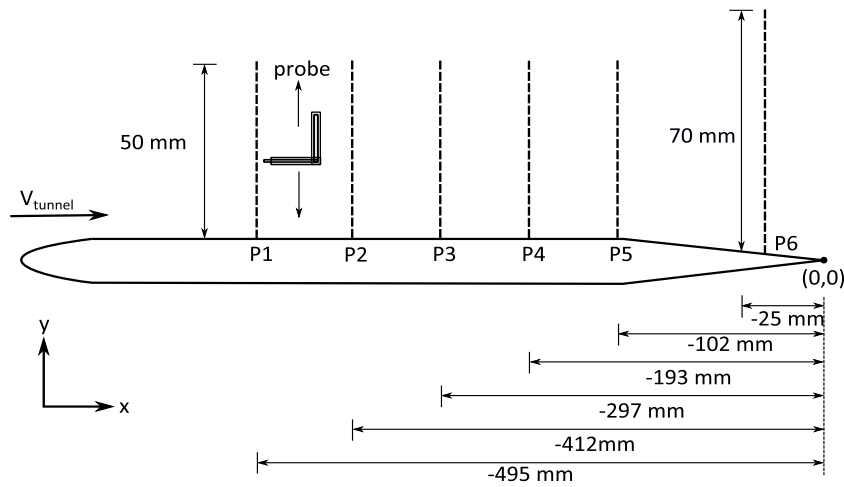


Figure 4.16: Schematic of the flat plate positions where boundary layer total pressure measurements carried out, including geometrical information

recorded at 50 different points in the  $y$ -direction with a step of 1 mm each. It is clear that point 0 represents the surface of the flat plate. For the fourth and fifth columns, the distance of measuring stations from the top transparent wall and the speed of the tunnel for each run are presented.

Boundary Layer Total Pressure Measurements Test Matrix				
Point No.	x [mm] [N=1000]	y [mm] [step = 1 mm]	z [mm] (from top wall)	$V_t$ [m/s] Maximum available
Point 1	-495	0-50	168	15
Point 2	-412	0-50	168	15
Point 3	-297	0-50	168	15
Point 4	-193	0-50	168	15
Point 5	-102	0-50	168	15
Point 6	-25	0-70	168	15

Table 4.4: Boundary layer total pressure measurements test matrix

### 4.3.4 Wake Total Pressure Measurements

The last part of pressure probe measurements was to carry out wake measurements. In the Table 4.5, the test matrix used for these measurements, with all the needed information with respect to the measuring points are presented. In contrast to boundary layer measurements, the points showing the streamwise distance ( $x$ ) from the trailing edge of the plate (0,0), have a positive sign. From the second column of Table 4.5, one could notice that  $N = 200$ . The time for gathering these 200 samples and get the mean value was measured  $t = 5.3$  seconds.

The third column similarly includes the  $y$ -direction translation of the probe for each measurement. For all the measuring stations in  $x$ -direction, the total pressure was recorded at 200 different points in the  $y$ -direction with a step of 5 mm each. It is clear that point 100 represents

<b>Wake Total Pressure Measurements Test Matrix</b>				
<b>Point No.</b>	<b>x [mm]</b>	<b>y [mm]</b>	<b>z [mm]</b>	<b><math>V_t</math> [m/s]</b>
	<b>[N=200]</b>	<b>[step = 5 mm]</b>	<b>(from top wall)</b>	<b>Maximum available</b>
Point 0	30	100 to -100	168	15
Point 1	100	100 to -100	168	15
Point 2	132	100 to -100	168	15
Point 3	222	100 to -100	168	15
Point 4	265	100 to -100	168	15
Point 5	320	100 to -100	168	15
Point 6	425	100 to -100	168	15
Point 7	520	100 to -100	168	15
Point 8	639	100 to -100	168	15

Table 4.5: Wake total pressure measurements test matrix

the distance being 100 mm above the flat plate, with 0 being at the trailing edge imaginary axis and -100, 100 mm below the flat plate. For the fourth and fifth columns, the distance of measuring stations from the top transparent wall and the speed of the tunnel for each run are presented. In Figure 4.17, a schematic of positions where wake total pressure measurements carried out with respect to flat plate, is presented.

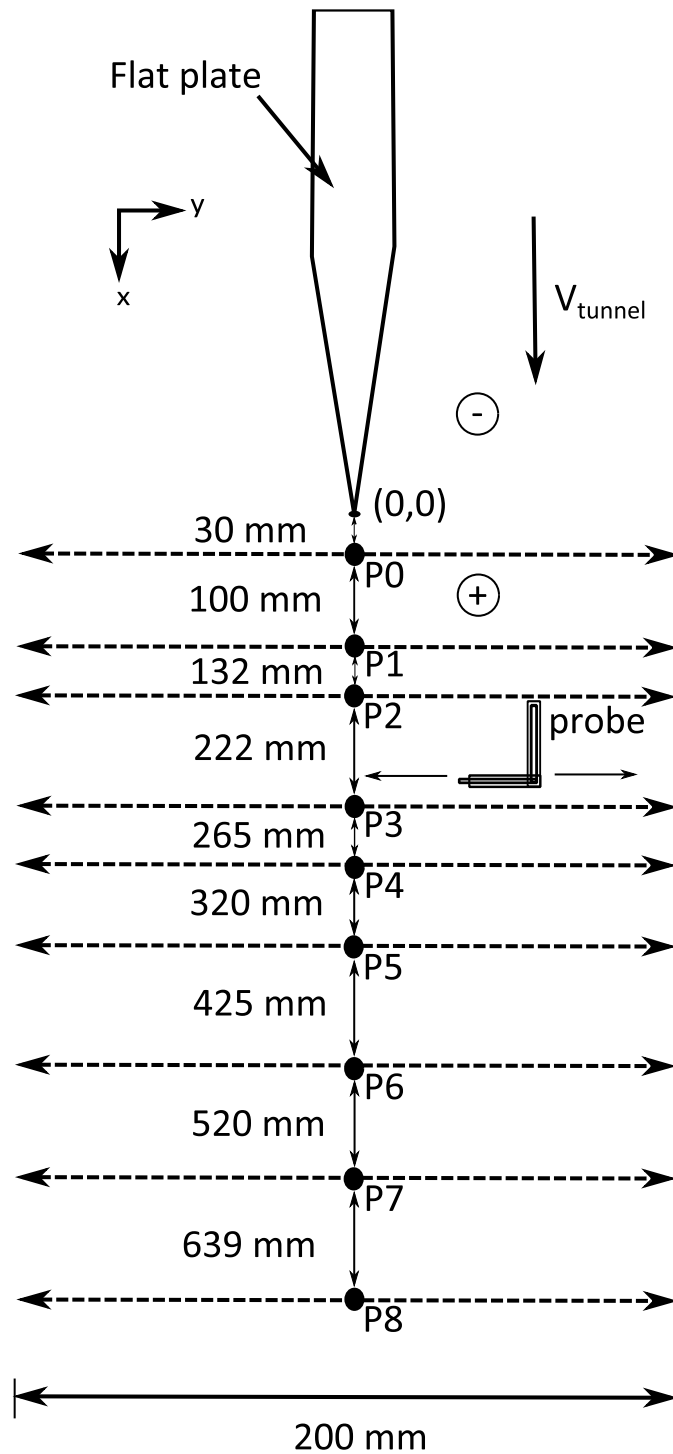


Figure 4.17: Schematic of the positions where wake total pressure measurements carried out with respect to the flat plate, including geometrical information

### 4.3.5 PIV

The PIV experimental procedure included measurements at three different velocities (5, 14 and 21 m/s), for each placement of the camera. For this testing campaign, three different positions of the camera were chosen, because of accessibility reasons. The first position was at the trailing edge (0,0) of the flat plate having a field of view (FOV) equal to 90 x 120 mm (90 mm to the y-axis and 120 to the x-axis), as for the other two camera positions. The second camera placement was 315 mm behind the flat plate's trailing edge and located in the diverging walls region. The last measurement position was 500 mm behind the trailing edge of the plate and located in the straight diffuser section after the diverging walls. More information with respect to Davis settings for each test case, could be found in **Appendix B**, at the end of the report. In Table 4.6, the test matrix of PIV tests is presented.

PIV Test Matrix		
Test Case No.	FOV No. & Position	$V_t$ [m/s]
TC.1	FOV 1 [t.e]	5.1
TC.2	FOV 1 [t.e]	14.1
TC.3	FOV 1 [t.e]	21.0
TC.4	FOV 2 [315 mm from t.e]	5.1
TC.5	FOV 2 [315 mm from t.e]	14.1
TC.6	FOV 2 [315 mm from t.e]	21.0
TC.7	FOV 3 [500 mm from t.e]	5.1
TC.8	FOV 3 [500 mm from t.e]	14.1
TC.9	FOV 3 [500 mm from t.e]	21.0

Table 4.6: PIV Test Matrix

Below, in Figure 4.18, a schematic of the experimental set-up used for the Wind Tunnel Testing Campaign II is presented including information on experimental set-up dimensions and FOV's position with respect to the plexiglass flat plate and diffuser section.

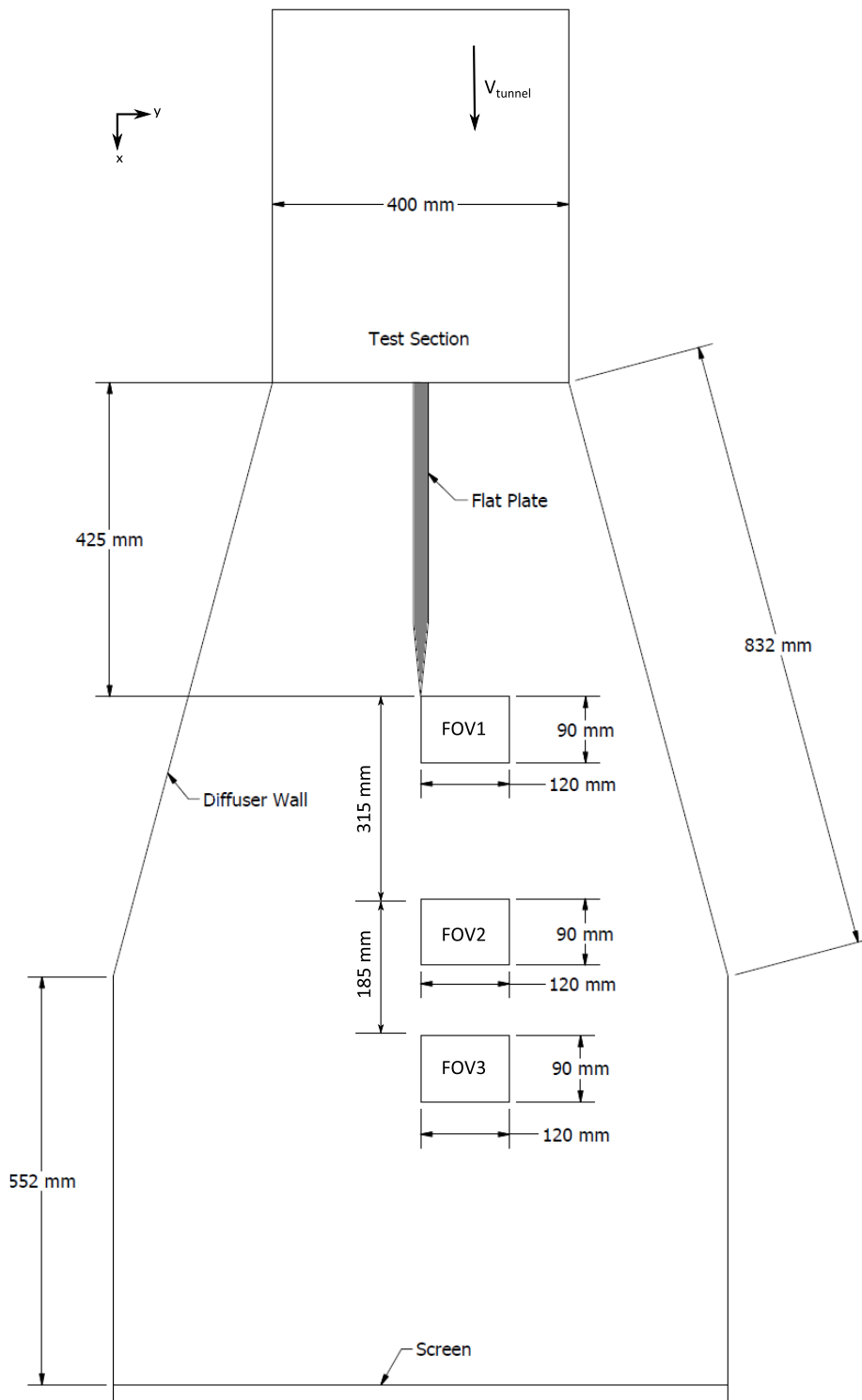


Figure 4.18: PIV measurement positions schematic

## 4.4 Presentation & Discussion of Results

From the first flow visualisation tests, running the tunnel between 5 and 20 m/s, and observing the tufts on the diverging diffuser walls, it was very clear that the flow was initially separated. Therefore, it was decided to use an additional aluminium screen and place it behind the initial copper one. This additional screen was placed in order to eliminate the problem of flow separation on the walls by creating greater overpressure. However, as soon as the aluminium screen was positioned behind the other one, there was not any sign of flow separation. Therefore, the extra overpressure was able to make the diffuser wall slots work more efficiently and suction was strong enough to eliminate flow separation.

### 4.4.1 Flow Visualisation

The flow on the flat plate and on the wake region was checked. This was done by observing the tufts on the flat plate and by moving a tuft attached on a rod, across the wake region. At 12 m/s, the flow on the diffuser walls was attached and turbulent as was indicated by the slight move of the woollen tufts. With respect to the flat plate, the flow seemed to be attached and turbulent as could also be expected due to the presence of roughness close to the leading edge of the plate. Finally, using the rod with the tuft at its end, it was also possible to check the flow behind the flat plate and get an idea of the flow behaviour in the wake. At this particular speed there was not any sign of wake reversal. At 22 m/s, the flow on the diffuser was again attached and turbulent as was observed by the slight move of the tufts for the first case. Moreover, the flat plate flow was also attached but it was realised that close to the trailing edge region (tapered part), it could be close to separation or separated. To conclude, behind the plate's trailing edge and using the rod with the tuft, it was noticed that there was extensive wake reversal for this velocity. The wake reversal region was determined to be up to the very end of the diffuser straight walls, as was observed by moving the rod across the wake area. Pictures taken during the flow visualisation tests, are presented in Figure 4.19 and show the flow behind the trailing edge of the flat plate for both velocities tested.

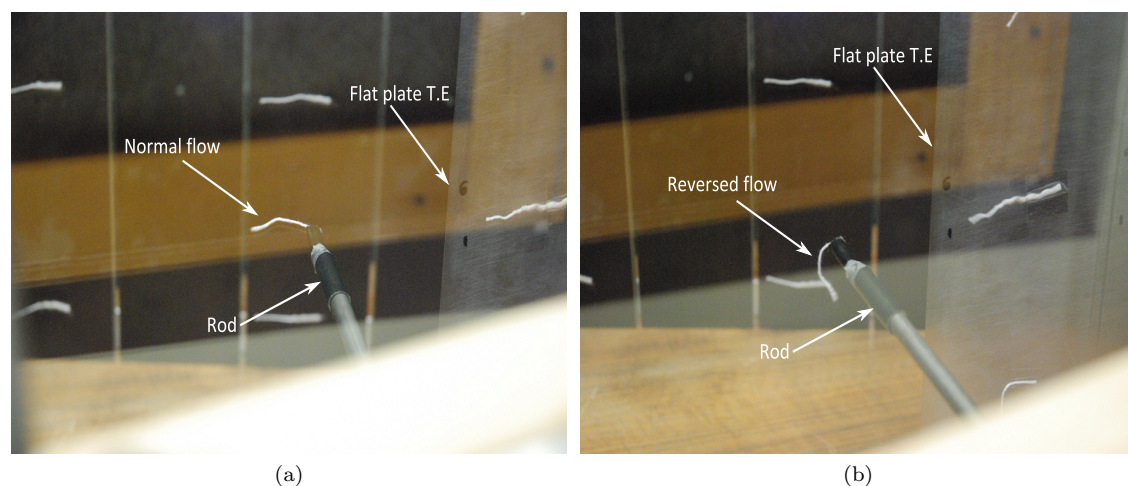


Figure 4.19: Woolen tuft behind flat plate at 12 m/s (a) showing no wake reversal and (b) at 22 m/s showing wake reversal

## 4.4.2 Pressure Measurements

### Surface Static Pressure Measurements

Each diffuser wall, had four pressure taps on it's surface, in order to record static pressures and to determine the pressure behaviour in the diffuser area. In Table 4.7, one could find all the data recorded by the surface pressure taps. As mentioned in section 4.2.1, ten different measurements carried out and then averaged in order to calculate static pressures in the diffuser area. By calculating the mean value for each station (pressure tap), it was possible to plot the pressure values for each station accurately enough.

Measurement No.	PT.1	PT.2	PT.3	PT.4
1	33.936	106.462	130.131	171.551
2	30.916	108.59	131.719	175.075
3	23.309	100.491	130.729	171.361
4	25.611	106.327	134.149	175.953
5	24.719	102.348	130.555	171.700
6	24.677	102.818	129.254	167.816
7	24.214	103.09	129.891	173.231
8	25.816	103.286	129.446	172.035
9	26.234	103.631	130.411	173.524
10	22.759	100.861	129.847	173.590
<b>Mean</b>	26.219	103.790	130.613	172.584

Table 4.7: Surface static pressure measurements

Then, the static pressure at each station was plotted against the streamwise distance in millimetres. As presented in Figure 4.20, the gauge pressure gradient increases steeply from station 1 to station 2. Then from station 2 to station 3 the gradient drops. Nevertheless, from station 3 to station 4, the gradient seems to have an approximately linear increase. The pressure gradient is compared with a red dotted line representing a basic linear fitting command in MatLab. This trend could be explained by the extreme overpressure due to the additional screen at the end of the diffuser. Hence, it could be argued that the overpressure is "felt" significantly closer to the tunnel's section exit (closer to PT.1) and as one moves forward, this effect is eliminated. That is why from point 2 to point 3, the gradient is reduced and up to point 4 the change in pressure is fairly linear.

### Boundary Layer Total Pressure Measurements

The boundary layer measurements carried out with the intention of getting a clear idea of the flow evolution before it reaches the wake region. As observed from the plots presented in Figure 4.21 for all the measured points, it is quite obvious that moving from leading edge to the trailing edge of the flat plate, the boundary layer is growing in thickness due to adverse pressure gradients in the diffuser region. From plot (e) for **Point 5**, one could notice that the boundary layer is close to separation by the looks of it. However, for the last point close to the trailing edge, **Point 6** (-25 mm), it could be argued that the flow is separated at the tapered part of the flat plate. Moreover, observing the data for this point is quite obvious that there is a quite significant wiggling on the gauge pressure values recorded. This could possibly be due to the unsteadiness of the flow being separated at this region. Otherwise, it could also happen due to vibrations of the total pressure probe measuring because of the reversed flow in this area which

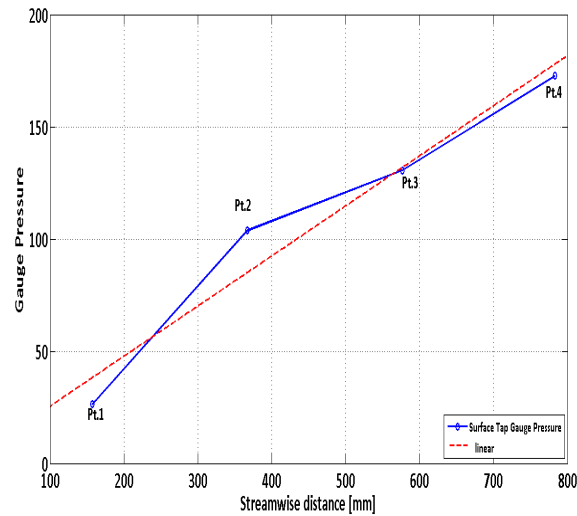


Figure 4.20: Gauge pressure vs. streamwise distance (mm) in the diffuser, based on surface pressure tap measurements

is a common error for intrusive measurement techniques. This was the reason of recording more data points for this particular station as could be seen from the Table 4.4. Concluding, the separated flow close to the trailing edge of the flat plate was not intended, as it was expected to have attached flow on the flat plate with reversed wake flow behind it. However, this was not of major importance. This was something which could be avoided by using lower grain size carborundum or a shorter distance with surface roughness. It is believed that the main cause for the separated flow, was the size of the grains which caused a thicker boundary layer and as a result of the adverse pressure gradient created by the diffuser, the boundary layer was finally separated close to the trailing edge.

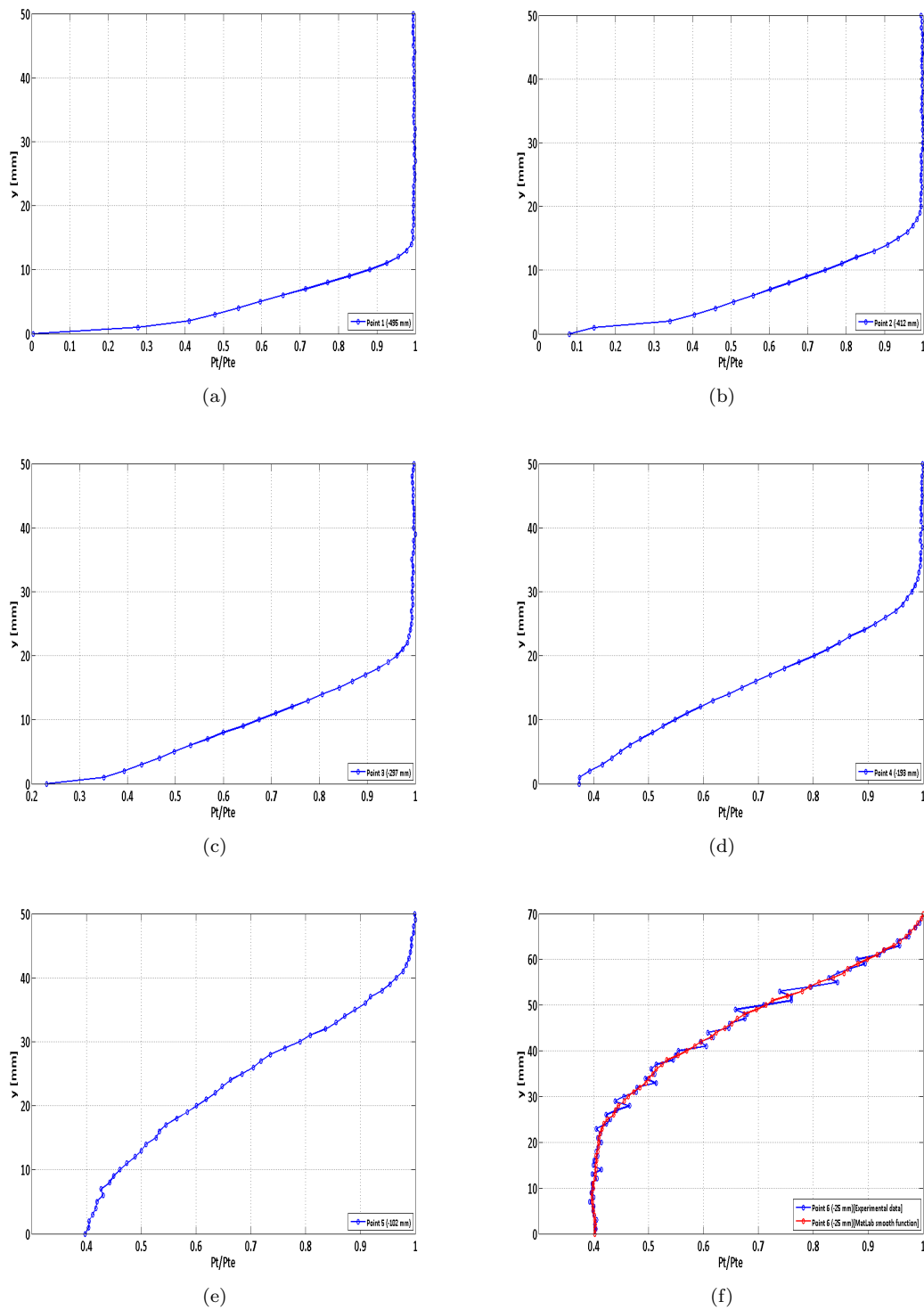


Figure 4.21: Flat plate total pressure boundary layer plots at points (a) Point 1 (-495 mm), (b) Point 2 (-412 mm), (c) Point 3 (-297 mm), (d) Point 4 (-193 mm), (e) Point 5 (-102 mm) and (f) Point 6 (-25 mm)  
 MSc. Thesis

C.Kounenis

### Wake Total Pressure Measurements

Observing very carefully all the plots presented in Figure 4.22, for all the points measured in the wake region, it is quite clear that moving from the trailing edge of the flat plate towards the end of the diffuser section, wake reversal occurred. For all the points presented in Figure 4.22, the wake reversal region, is represented by the part of the line where the gauge pressure values are nearly constant. It is obvious from most of the plots that there is very significant wiggling on the gauge pressure values probably due to the unsteadiness of the flow being reversed. Otherwise, it could also happen due to probe vibrations because of the highly reversed flow in this region. This is why for all the measured points, two different lines were plotted as shown in Figure 4.22. The blue line represents the experimental data recorded using the probe and the red line is a MatLab average filter line, avoiding the large fluctuations of the pressure values.

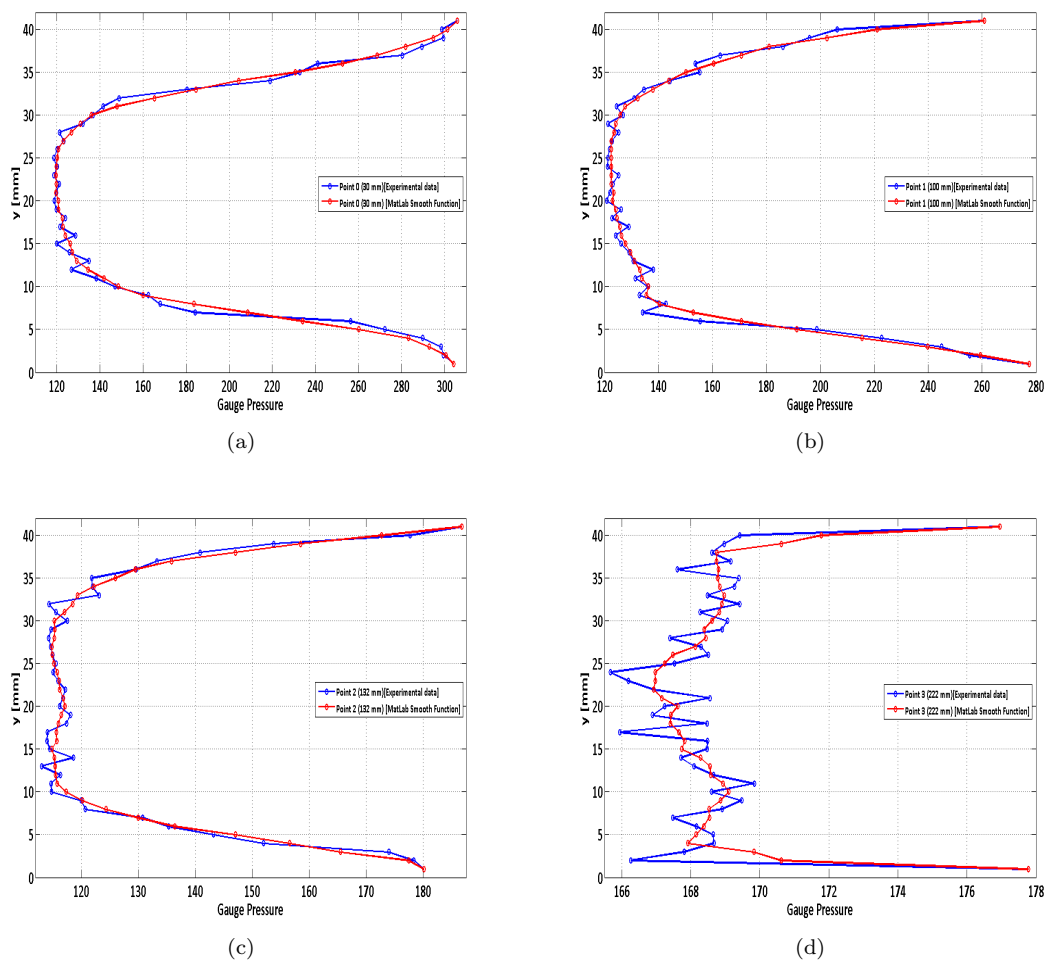
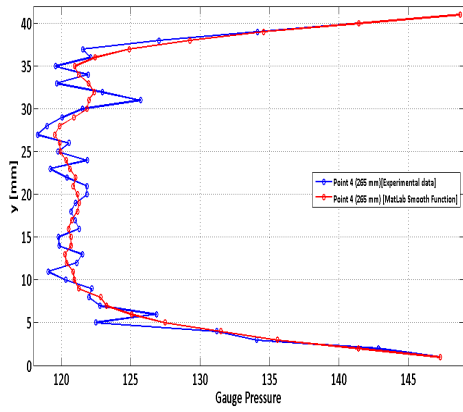
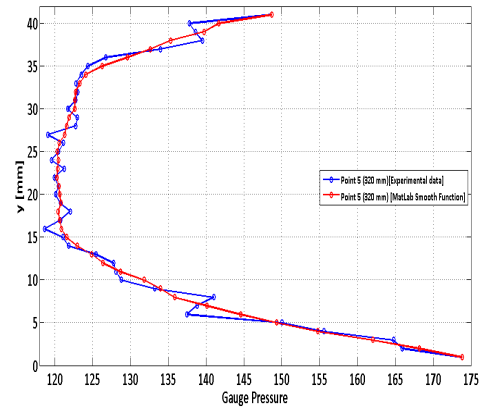


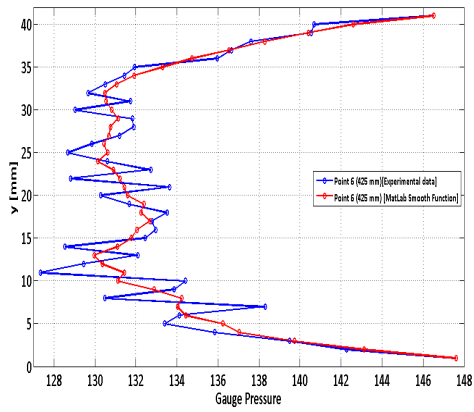
Figure 4.22: Wake total pressure plots at points (a) Point 0 (30 mm), (b) Point 1 (100 mm), (c) Point 2 (132 mm) and (d) Point 3 (222 mm)



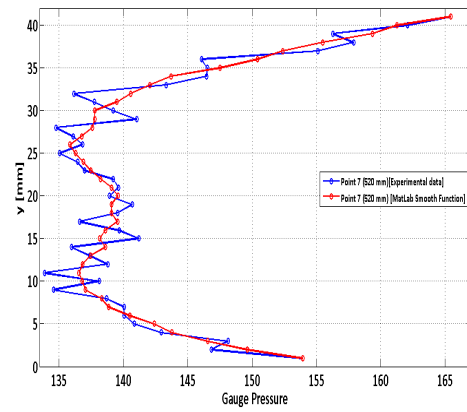
(e)



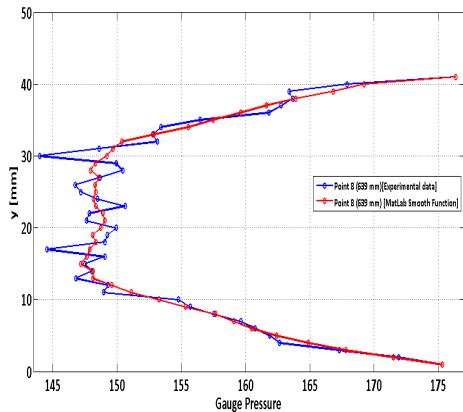
(f)



(g)



(h)



(i)

Figure 4.22: Wake total pressure plots at points (e) Point 4 (265 mm), (f) Point 5 (320 mm), (g) Point 6 (425 mm), (h) Point 7 (520 mm) and (i) Point 8 (639 mm)

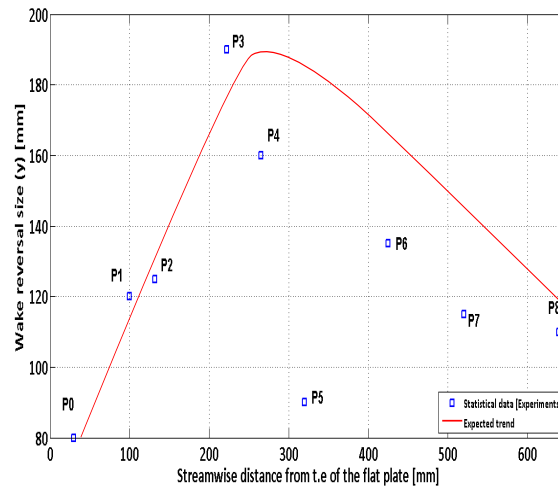


Figure 4.23: Wake reversal width vs. downstream distance from trailing edge

Concluding, the last thing to do using the wake measurement data was a simple statistical study, in order to determine the size of the reversed flow region behind the trailing edge of the flat plate as moving towards the diffuser section's end. In Table 4.8, the values of wake reversal size width as measured from pressure data of each station, are presented.

Point No.	y (wake reversal size) [mm]
Point 0 (30 mm)	80
Point 1 (100 mm)	120
Point 2 (132 mm)	125
Point 3 (222 mm)	190
Point 4 (265 mm)	160
Point 5 (320 mm)	90
Point 6 (425 mm)	135
Point 7 (520 mm)	115
Point 8 (639 mm)	110

Table 4.8: Statistical data with respect to wake reversal size

Observing the plot in Figure 4.23, is quite clear that the wake reversed flow size increases, moving towards the end of the diffuser's diverging walls. Then, a decrease could be noticed still in the divergent part of the diffuser at points 4 and 5, possibly due to the size of the measurement plane which apparently was not great enough to illustrate the actual reversed region area. Hence, the values at these 2 points could not be thought as accurate. Finally, for the last three points (Points 6, 7 and 8), the decrease in width could be explained by the reduction in pressure as the flow enters the straight wall diffuser part, further downstream. In the straight diffuser wall region, the velocity increases and the pressure drops from its greater values in the diverging section. The red line plotted represents the trend expected with respect to the wake reversal size across the whole diffuser length, taking into account that the pressure at points 4 and 5 keeps increasing further.

### 4.4.3 Particle Image Velocimetry (PIV)

At this section, the PIV results will be presented. As the amount of data gathered was considerably large and the results and plots obtained were also numerous, only the results for the first camera position (FOV 1) will be presented. This camera position was probably the most significant related to this research as it was placed in the region of the greatest overpressure. As a result, for this field of view, the results for all the tunnel velocities tested, will be presented and discussed thoroughly. The other field of views and the subsequent results, will be presented in *Appendix B* at the end of the report.

#### Test Case 1: FOV 1- $V_t = 5.1\text{m/s}$

The first set of plots presented in Figure 4.24, are for FOV 1, and tunnel velocity of 5.1 m/s. The first plot (a) presented is the total velocity field in combination with streamlines. This plot is mirrored across an imaginary axis that extends from the trailing edge downstream, represented by the thick white line in the centre of the figure. The reason for mirroring, was that the same flow characteristics were expected on the other side of the flat plate/diffuser section. As it could be seen from plot (a) in Figure 4.24, the flow close to the diffuser walls looks to be normal and gets it's greatest velocity values, as is also observed by looking the white streamlines. However, the velocity values are significantly lower than the tunnel speed measured in the test section. This is explained by the great overpressure created due to the wide diffuser angle of  $15^\circ$  and the screen at the end of it. Nevertheless, as one moves to the centre of this field plot, the flow seems to get it's lowest velocity values at this region, even negative values and as shown by the streamlines, which are totally reversed, showing symmetrical vortices, this could lead to the conclusion that wake reversal occurs in the centre region behind the tapered trailing edge of the flat plate.

The next two plots presented in Figure 4.24, are the U and V-velocity component fields. From the U-component velocity plot (b), it could be said that the flow moves from a region of higher velocity (closer to the diffuser walls) to a region where the velocity decreases significantly towards the centre of the field of view, even at values than zero, where reversed flow occurs behind the trailing edge of the flat plate. As could be seen, the velocity values are quite low as well. As mentioned earlier, this happened due to the great overpressure created by the additional screen placed at the end of the diffuser, in combination with the wall slots which created large suction forces and as a result the speed in the test section was decreased significantly.

As this was realised, it was decided to perform an analytical study of the velocity deficit in the whole diffuser area all the tunnel velocities tested. Hence, the velocity deficit study for the case of tunnel velocity equal to 5.1 m/s is presented. To begin with, in this study, the theoretical velocity deficit was calculated for each position in the diffuser area, using the Venturi effect. According to the governing laws of fluid dynamics, a fluid's velocity must increase as it passes through a constriction in order to satisfy the principle of continuity, while its pressure must decrease to satisfy the principle of conservation of mechanical energy. Thus, any gain in kinetic energy a fluid may experience due to it's increased velocity through a constriction is negated by a drop in pressure [4]. An equation for the drop in pressure due to the Venturi effect may be derived from a combination of Bernoulli's principle and the continuity equation. However, in this case, there was an interest in calculating the velocity deficit for the whole diffuser area, therefore, using the volumetric flow rate, the velocity at the point of interest,  $V_2$ , could be calculated by using the speed in the tunnel's tests section,  $V_1$ , as stated in the Equation 4.6:

$$Q_1 = Q_2 \quad (4.4)$$

$$V_1 \cdot A_1 = V_2 \cdot A_2 \quad (4.5)$$

$$V_2 = \frac{V_1 \cdot A_1}{A_2} \quad (4.6)$$

Then, the actual velocity deficit calculated, using geometrical information and data gathered by integrating the wake velocity profiles at specific positions and getting the velocity values all across the diffuser area. The theoretical and actual case velocity deficit trends across the set-up, compared with the tunnel's test section speed, which at this case was 5.1 m/s and are shown at plot (f) in Figure 4.24. From the theoretical continuity law calculation, it is very clear that as one moves in the diffuser area and up to the end of the divergent walls, the velocity drops, being significantly lower than the tunnel's test section values. Then, in the straight part of the diffuser after the diverging section, the velocity values remain constant as there is not any change in area for this region. On the other hand, for the actual case, the trend of the velocity deficit is different as the speed seems to have a very slight increase, which seems to drop abruptly to very low values of speed possibly due to the strong suction effect described earlier. Finally, as the flow reaches the straight part of the diffuser, the speed increases noticeably, which could be explained by the drop in pressure at this region compared to the diverging section of the diffuser. As it could be understood, the reduction in velocity in the diffuser area is large enough and possibly this could be avoided by altering the screen at the end of the diffuser, and substitute it with a different one which would create less overpressure. The other way to eliminate this velocity deficit would be to minimize the slot width on the diffuser diverging walls, in order to avoid the great suction occurring. The best solution, if such an experiment would be repeated, might be to take both into consideration and possibly carry out trial and error tests, by observing the state of the flow on the walls but at the same time recording the velocity values in the diffuser region.

For the V-component velocity field plot (c), the conclusions are very similar to the ones for the total velocity field plot, as the velocity close to the diffuser wall gets its largest values, while decreasing close to the centre of the field, reaching even negative values, which represent wake reversal.

In plot (d), the displacement and momentum thickness are presented. It could be observed that there is an increase of both quantities. In detail, the displacement thickness is increasing from 114.30 mm to 155.30 mm. A total increase of 41 mm. The reason for this large increase in displacement thickness could be explained by the diffuser, which diverges and therefore the streamlines would also be displaced by significant amount due to increase in pressure and the drop in velocity values. For the momentum thickness, there is also a very slight increase from 21.06 mm at the trailing edge to 23.93 mm at the end of the field of view. A total increase of 2.87 mm. A possible explanation for this slight increase in momentum thickness is the adverse pressure gradient in the wake region.

To conclude, in plot (e), the wake velocity profiles are presented for three different positions within the field of view, behind the trailing edge of the flat plate. For the first position behind the trailing edge at 22.5 mm, represented by the blue line, there is a slight reversed flow region which is covering the traverse distance from -18.34 mm to 18.34 mm. A total distance of 36.68 mm. At 45 mm behind the trailing edge, represented by the red line, there is a slight increase in reversed flow region covering the distance from -22.57 to 22.57, a total distance of 45.14 mm.

Finally, at 67.5 mm represented by the black line, there is even greater wake reversal, from -24.69 to 24.69 mm, a total distance of 49.38 mm. This could indicate that as one moves deeper in the wake region, the wake reversal width increases as the size of the wake grows as well.

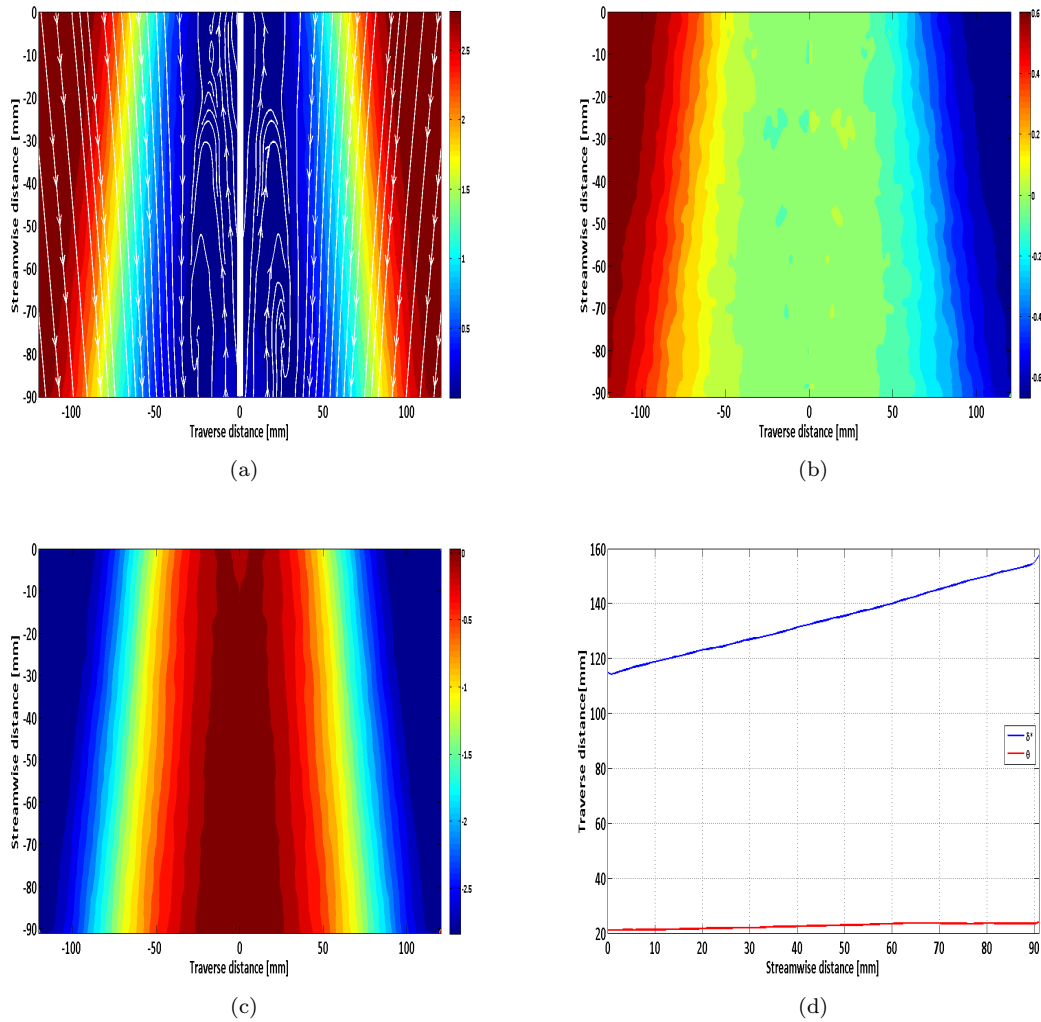


Figure 4.24: Total velocity (a) field with streamlines, (b) U-component velocity field, (c) V-component velocity field and (d) Displacement and Momentum loss thickness for FOV 1 and  $V_t = 5.1\text{m/s}$

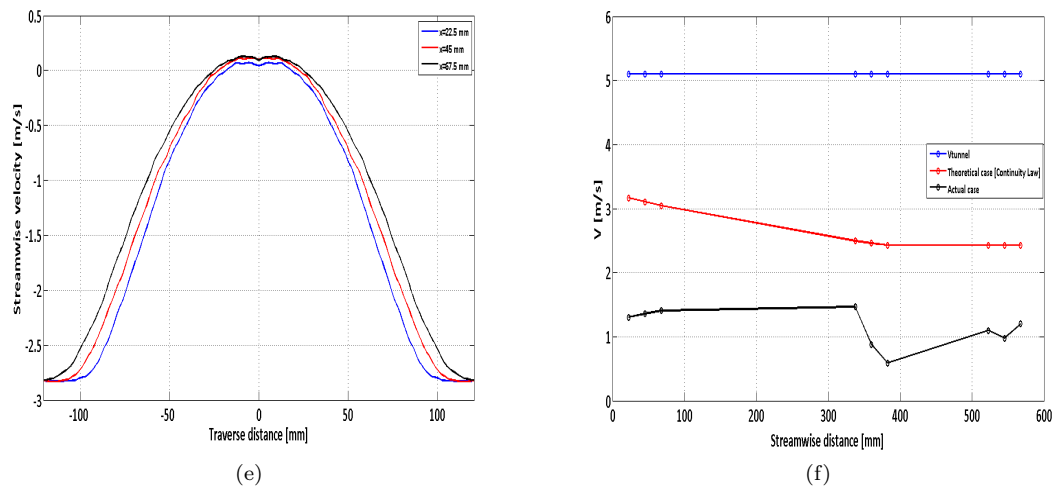


Figure 4.24: Wake velocity profiles (e) and Velocity deficit study (f) for FOV 1 and  $V_t = 5.1\text{m/s}$

#### Test Case 2: FOV 1- $V_t = 14.1\text{m/s}$

The first set of plots presented in Figure 4.26, are for FOV 1, and tunnel velocity of  $14.1\text{ m/s}$ . The first plot (a) presented Figure 4.26, is the total velocity field in combination with streamlines. This plot is mirrored across an imaginary axis that extends from the trailing edge downstream, represented by the thick white line in the centre of the figure. The flow close to the diffuser walls looks to be normal and gets its greatest velocity values, as is also observed by looking at the white streamlines. However, the velocity values are lower again than the tunnel speed measured in the test section and the region of lower velocities is now even larger than before. This is explained by the even greater overpressure created due to the wider diffuser angle of  $15^\circ$  in combination with the speed increase and the screen placed at the end of it. Nevertheless, as one moves to the centre of this field plot, the flow seems to get its lowest velocity values at this region, even negative values and as shown by the streamlines, which are reversed in a greater area than for the previous case, showing symmetrical vortices, this could lead to the conclusion that wake reversal size is now significantly increased.

The next two plots presented in Figure 4.26, are the U and V-velocity component fields. From the U-velocity component plot (b), it could be seen that the flow moves from a region of higher velocity (close to the diffuser wall) to a region towards the centre of this field, where the velocity decreases significantly even at values less than zero, where reversal occurs behind the trailing edge of the flat plate. The velocity deficit study was carried out for this case as well. By observing plot (f) in Figure 4.26, it is very clear that still the flow velocity in the diffuser area is considerably lower in the order of three times less than the tunnel's test section velocity. However, the trend in this case decreases in the diffuser diverging section of the diffuser and then increases as expected in the straight wall section due to lower pressure values in this region.

Moving to the V-component field plot (c), the observations are very similar to the ones for the total velocity field plot, as the velocity close to the diffuser wall gets its largest values, while decreasing close to the centre of the field, reaching even negative values, which represent wake

reversal occurring.

In plot (d), the displacement and momentum thickness are presented. From this one, one could observe that there is an increase of the displacement thickness and a decrease of the momentum thickness. In detail, the displacement thickness increases from 151.30 mm to 202.90 mm. A total increase of 51.6 mm. The reason for this additional increase in displacement thickness compared to the first case at tunnel speed of 5.1 m/s, is explained by the further increase in pressure in the diffuser area which results to lower velocities and hence to higher displacement thickness values. On the other hand, for this case, the momentum thickness, presents a decrease from 4.224 mm at the trailing edge to 1.474 mm. A total decrease of 2.75 mm. This decrease is very small compared to the increase in displacement thickness and of course could be within the range of statistical error. However, this small decrease could not be explained, as it would be expected to increase as the pressure gradient increases further in the diffuser area.

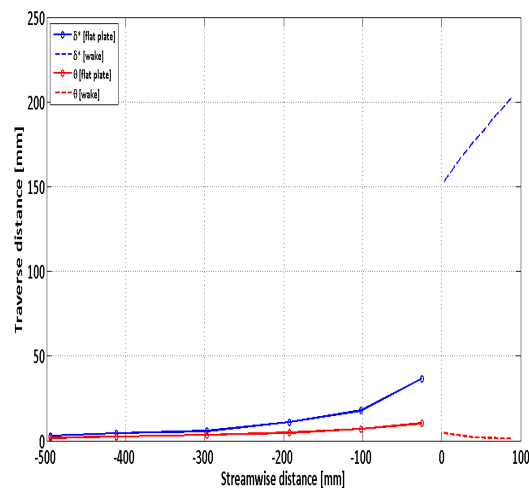


Figure 4.25: Displacement and momentum thickness for flat plate and wake

Based on all the data gathered from pressure measurements and PIV, another interesting thing to present would be the displacement and momentum thickness evolution on the flat plate and up to the end of FOV 1. Hence, as presented in Figure 4.25, it's possible to notice the gradual increase of displacement thickness on the flat plate. The increase of the boundary layer displacement thickness on the flat plate was approximately 34 mm starting at 3 mm on the first measurement point and increasing to 37 mm at the trailing edge of the plate. Moving to the wake region, the displacement thickness has already a value of 151.3 mm and increases to 202.90 mm at the end of FOV 1. As a result, the difference of size is visible and expected due to the greater pressure gradient in the wake than in the boundary layer, where also the skin friction could influence this variable. For the momentum thickness, it is obvious that for the boundary layer the momentum thickness increases from approximately 2 mm to 10 mm. This could be expected due to the adverse pressure gradient experienced as the flow moves downstream but also from the skin friction which also increases due to turbulent boundary layer on the flat plate. On the other hand, for the wake region, the momentum thickness decreases slightly by approximately 4 mm. As already mentioned, this behaviour could not be accepted as accurate enough and is

possibly within the range of statistical error.

Concluding, in plot (e), the wake velocity profiles are presented for three different positions within the field of view, behind the trailing edge of the flat plate. For the first position behind the trailing edge at 22.5 mm, represented by the blue line, there is a slight reversed flow region which is covering the traverse distance from -45.14 mm to 45.14 mm. A total distance of 90.28 mm. At 45 mm behind the trailing edge, represented by the red line, there is a slight increase in reversed flow region covering the distance from -49.37 to 49.37, a total distance of 98.74 mm. Finally at 67.5 mm represented by the black line, there is even greater wake reversal, from -53.60 to 53.60 mm, a total distance of 107.20 mm. As a result, by increasing the speed of the tunnel, the wake reversal size seems to be doubled in size in the traverse direction.

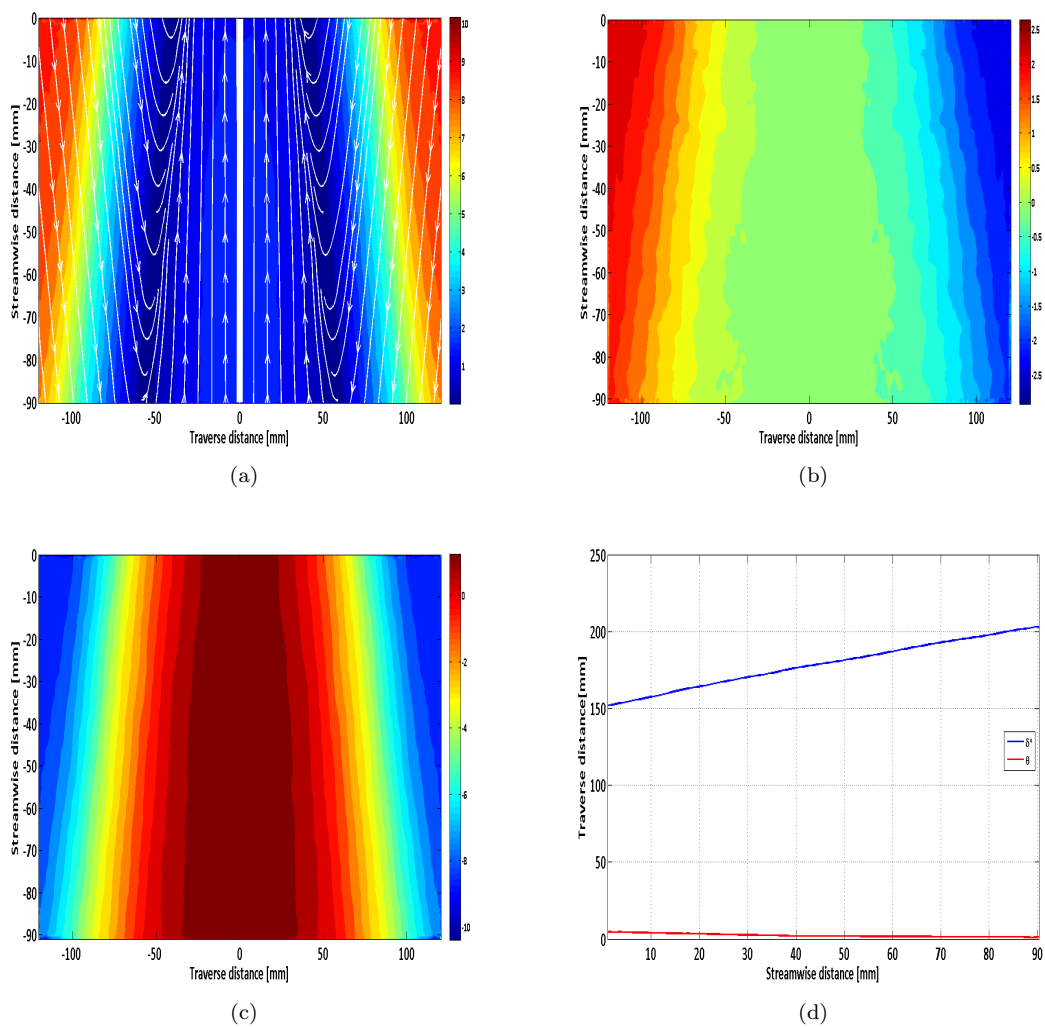


Figure 4.26: Total velocity (a) field with streamlines, (b) U-component velocity field, (c) V-component velocity field and (d) Displacement and Momentum loss thickness for FOV 1 and  $V_t = 14.1\text{m/s}$

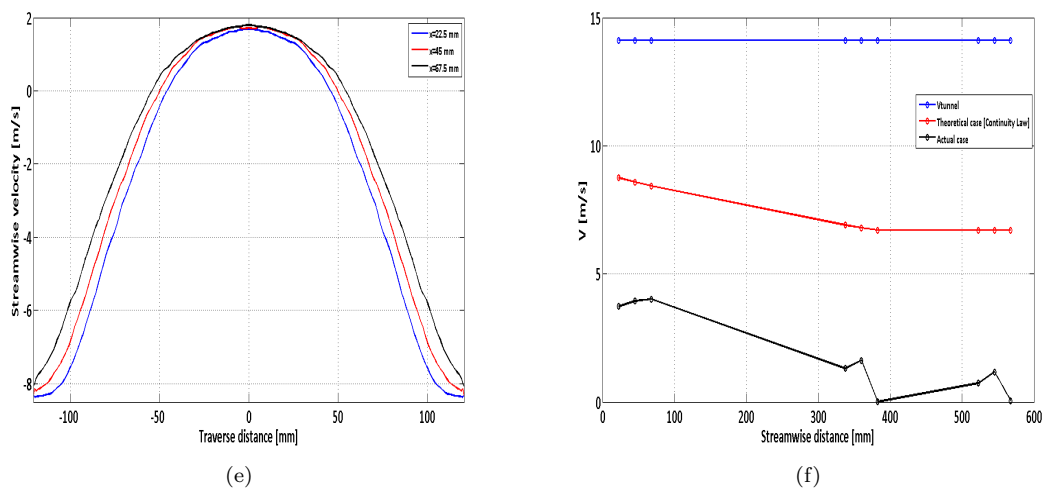


Figure 4.26: Wake velocity profiles (e) and Velocity deficit study (f) for FOV 1 and  $V_t = 14.1\text{m/s}$

### Test Case 3: FOV 1- $V_t = 21.0\text{m/s}$

The first set of plots presented in Figure 4.27, are for FOV 1, and tunnel velocity of  $21.0\text{ m/s}$ . The first plot (a) presented in Figure 4.27, is the total velocity field in combination with streamlines. As it could be observed, the flow close to the diffuser walls looks to be normal and gets its greatest velocity values, as is also confirmed by the streamlines. However, the velocity values are again lower than the tunnel speed in the test section and the region of lower velocities is now even larger than the two previous cases at  $5.1$  and  $14.1\text{ m/s}$ . This is explained by the greatest overpressure created due to the wide diffuser angle of  $15^\circ$  in combination with the further speed increase and the screen placed at the end of it. Nevertheless, as one moves at the centre of this field, the flow seems to get its lowest velocity values at this region, even negative values. Also observing by the streamlines, they are reversed in a greater area than for the two previous cases, showing symmetrical vortices and this could lead to the conclusion that wake reversal size flow region is now increased even more. As a result, it seems that as the velocity increases, the wake reversal region increases as well in traverse direction.

The next two plots presented in Figure 4.27, are the U and V-velocity component fields. From the U-velocity component plot (b), it could be seen that the flow moves from a region of higher speeds (close to the diffuser walls) to a region where the velocity decreases significantly even at values less than zero towards the centre of this field where wake reversal occurs behind the trailing edge of the flat plate. On the other hand, from the velocity deficit study carried out and presented at plot (f) in Figure 4.27, it is very clear that still the flow velocity in the diffuser area is considerably lower in the order of three times less than the tunnel's test section velocity. However, the trend is similar to the second case ( $V_t = 14.1\text{m/s}$ ), decreasing in the whole diverging section of the diffuser and then increasing as expected in the straight wall section due to lower pressure values in this region.

Moving to the V-component field plot (c), the conclusions are very similar to the ones for the total velocity field plot (a) presented in Figure 4.27, as the velocity close to the diffuser wall

gets its largest values, while decreasing close to the centre of the field, reaching even negative values, which represent wake reversal.

In plot (d) of Figure 4.27, the displacement and momentum thickness are presented. From this one, it could be observed that there is an increase of the displacement thickness and a decrease of the momentum thickness. In detail, the displacement thickness increases from 145.90 mm to 198.20 mm. A total increase of 52.3 mm. The reason for this additional increase in displacement thickness compared to the first (5.1 m/s) and second case (14.1 m/s), could be explained by the further increase in pressure in the diffuser area which results to lower velocities and thus to higher displacement thickness values. However, the momentum thickness, presents a decrease from 4.224 mm at the trailing edge to 1.474 mm. A total decrease of 2.75 mm. This decrease is very small compared to the increase in displacement thickness again for this case and of course could be between the range of statistical error as well. However, as mentioned earlier, this decrease could not be explained, as it would be expected to increase, as the pressure gradient increases further in the diffuser area.

Concluding, in plot (e), the wake velocity profiles are presented for three different positions in the FOV 1, behind the trailing edge of the flat plate. First of all for the first position behind the trailing edge at 22.5 mm, represented by the blue line, there is a slight reversed flow region which is covering the traverse distance from -42.32 mm to 42.32 mm. A total distance of 84.64 mm. At 45 mm behind the trailing edge, represented by the red line, there is a slight increase in reversed flow region covering the distance from -47.26 to 47.26, in total a distance of 94.52 mm. Finally at 67.5 mm represented by the black line, there is greater reversed wake flow, from -52.19 to 52.19 mm, a total distance of 104.38 mm.

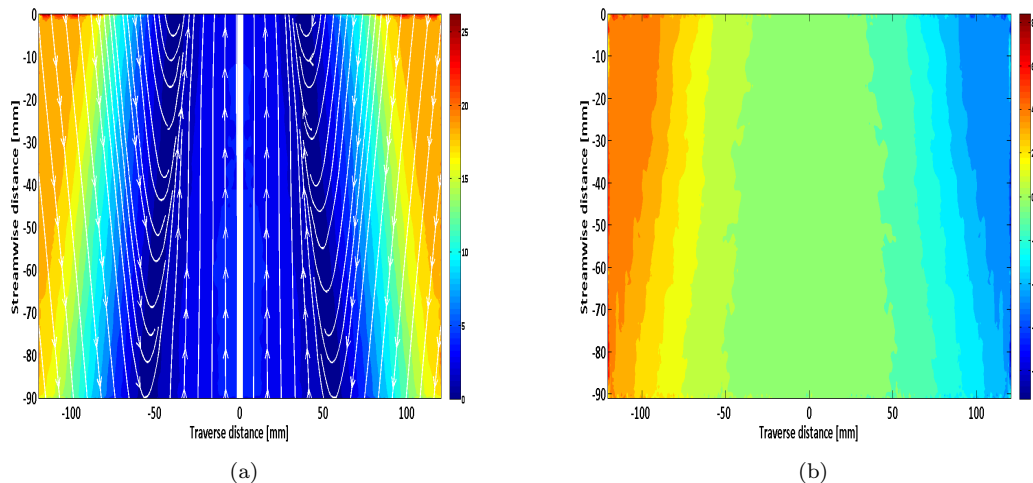


Figure 4.27: Total velocity field with streamlines (a) and U-component velocity field (b) for FOV 1 and  $V_t = 21.0\text{m/s}$

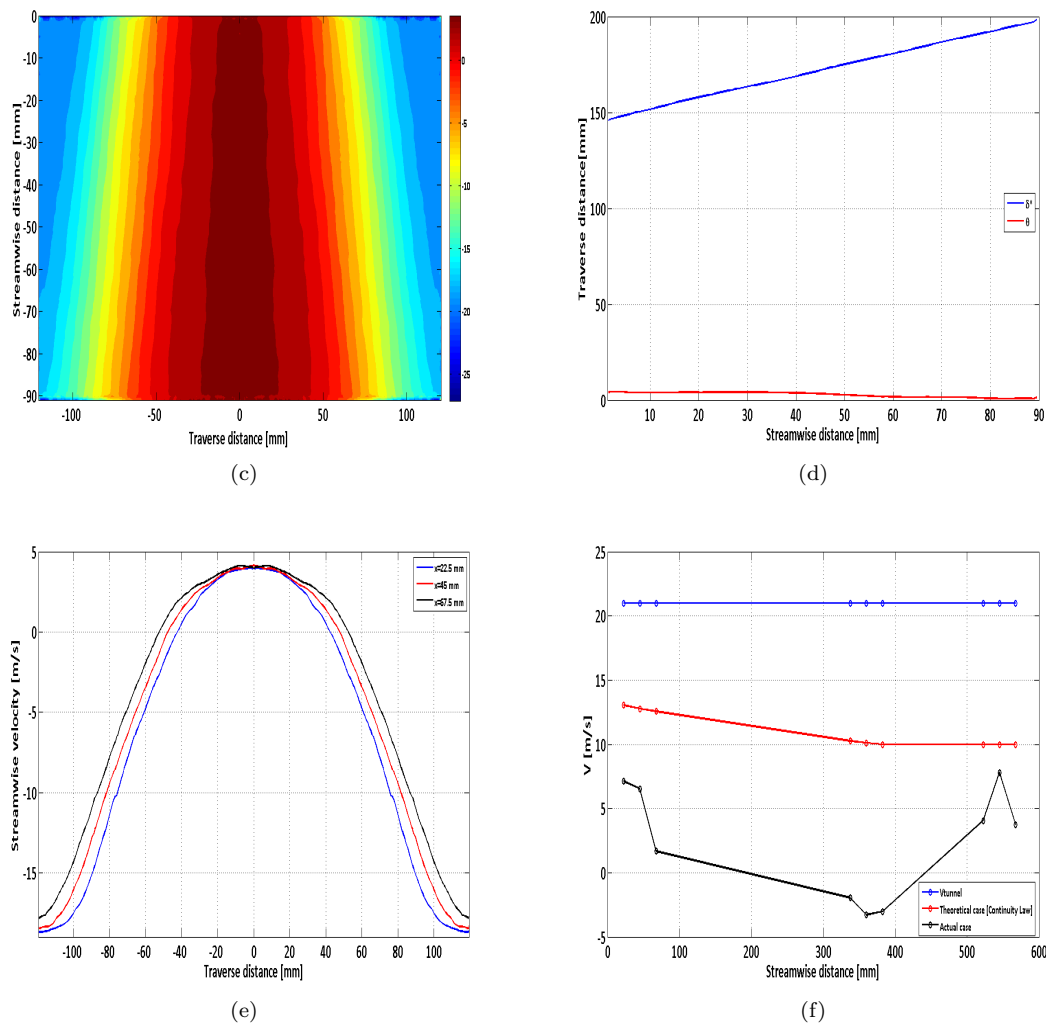


Figure 4.27: V-component velocity field (c), Displacement and Momentum loss thickness (d), Wake velocity profiles (e) and Velocity deficit study (f) for FOV 1 and  $V_t = 21.0\text{m/s}$

#### 4.4.4 Gartshore’s Wake Behaviour Relation

Concluding the work done for the second wind tunnel testing campaign, the last thing to present in this chapter is a theoretical study based on Gartshore’s relation. This study was based on experimental data gathered during these tests and used in order to determine the validity of this relation for this experimental work and decide whether it could be used as a future reference for wake behaviour. This relation was presented in the Background Theory, in Chapter 2, but a short explanation will also be given here.

Considering a streamline that leaves the slat of a multi-element airfoil, if the pressure rise is great enough, we could have flow reversal in the stream, entirely off-the surface. This could be

easily demonstrated by resorting Bernoulli's equation in Equations 4.7 to 4.10. Note, that  $u$  is the velocity at energy deficient regions and  $U$  is the velocity at potential regions.

$$P_0 + \frac{1}{2} \cdot \rho \cdot U_0^2 = P_1 + \frac{1}{2} \cdot \rho \cdot U_1^2 \quad (4.7)$$

$$p_0 + \frac{1}{2} \cdot \rho \cdot u_0^2 = p_1 + \frac{1}{2} \cdot \rho \cdot u_1^2 \quad (4.8)$$

$$\frac{u_1^2}{U_1^2} = \frac{p_0 - p_1 + \frac{1}{2} \cdot \rho \cdot u_0^2}{P_0 - P_1 + \frac{1}{2} \cdot \rho \cdot U_0^2} \quad (4.9)$$

$$\frac{u_1^2}{U_1^2} = \frac{\frac{u_0^2}{U_0^2} - \overline{C_p}}{1 - \overline{C_p}} \quad (4.10)$$

Some of the key things stated were that as the canonical pressure coefficient ( $\overline{C_p}$ ) increases the ratio of  $\frac{u_1^2}{U_1^2}$  could reach zero values before  $C_p$  reaches +1, provided that  $\frac{u^2}{U^2} < 1$ . However, the effect of viscosity, smooths the effect. Finally, as the  $\overline{C_p}$  increases, the velocity defect ratio is magnified and the flow reversal could occur in the mainstream [29].

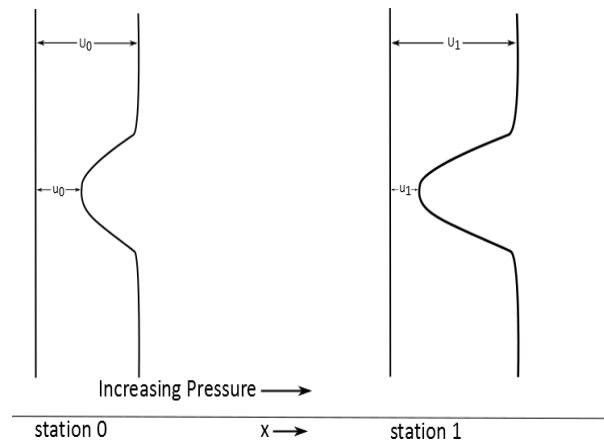


Figure 4.28: Flow moving to a region of increasing pressure

Gartshore has derived an approximate test as to whether the wake grows or decays. This relation is introduced in Equation 4.11 and could be used for the flat plate - diffuser experiments in order to check whether the wake grows or not [29].

$$\frac{1}{1 - C_p} \cdot \frac{dC_p}{dx} = \frac{1}{1 - \overline{C_p}} \cdot \frac{d\overline{C_p}}{dx} > \frac{0.07}{\delta^*} \quad (4.11)$$

Where  $\delta^*$  is the displacement thickness of the wake at the point being considered.

If the left hand side (LHS) of this relation is greater than the right hand side (RHS), then the wake grows. But if the left hand side (LHS) of the relation is smaller than the right hand side (RHS), then the wake decays. Some very interesting notes, from Gartshore's theory [29], were that a potential Reynolds number increase will increase the RHS of the equation as displacement thickness will decrease, but the effect is weak. According to his analysis, a boundary layer is more

prone to separation than the wake is to instability. Finally, by the off-the-surface deceleration, recovery from very high negative  $C_p$  values can be made in much shorter distance than could be made when all the deceleration is in contact with a surface. By using all this information, it could be possible to try to use the equation 4.11 and check whether the wake grows or decays for the fundamental experiments carried out in this research.

In order to do so, the highest test speed at  $V_t = 21\text{m/s}$  selected for FOV 1 position. Then, first the pressure coefficient ( $C_p$ ) and it's gradient ( $\frac{dC_p}{dx}$ ) plotted against the streamwise distance. However, in order to determine the pressure coefficients for each position, the static pressures measured on the diffuser walls used, in combination with the total pressure values recorded using the probe. Then, it was possible to calculate the pressure coefficients using Equation 4.12.

$$C_p = \frac{p - p_\infty}{\frac{1}{2} \cdot \rho_\infty \cdot V_\infty^2} \quad (4.12)$$

As presented at plot (a) in Figure 4.29, the displacement thickness in the wake increases in the streamwise direction as could be expected due to adverse pressure gradient caused by the diffuser. Similarly, the pressure coefficient line increases as moving downstream which was also expected for the same reasons. However, for the pressure coefficient gradient plot (c), it could be observed that there is a decrease as one moves downstream. Hence, by substituting numbers from these three plots in the Equation 4.11, it is possible to determine whether the wake grows or not. Using all points for the whole FOV 1 would be too many, hence, it was decided to pick one value in the middle of the FOV,  $x = 45\text{ mm}$ , in order to examine what happens there.

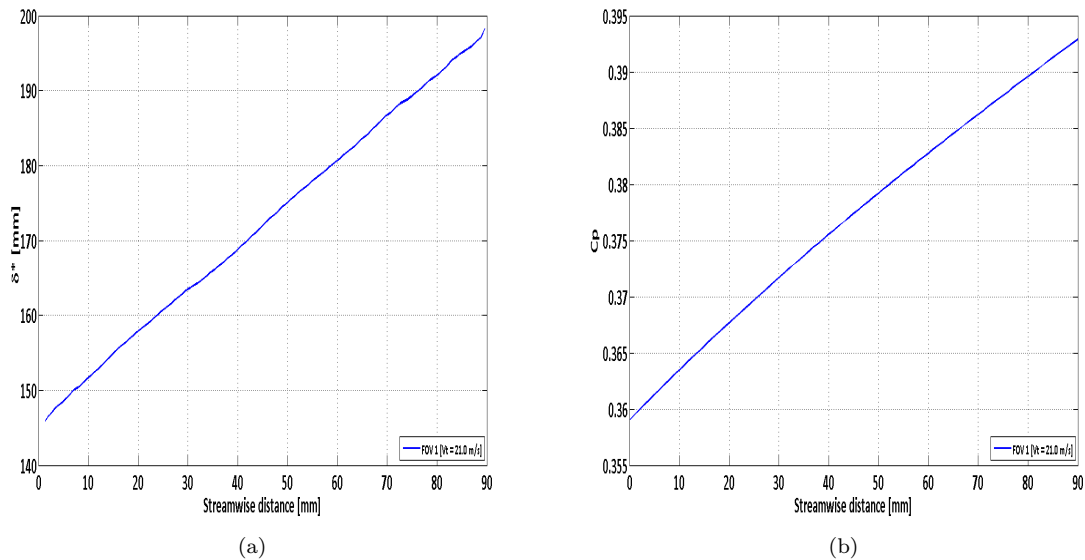


Figure 4.29:  $\delta^*$ , (a)  $C_p$  (b) vs. streamwise distance (mm) plots for FOV 1 and  $V_t = 21.0\text{m/s}$

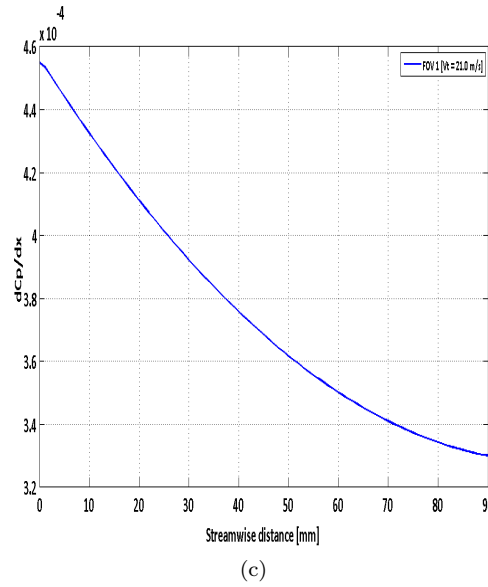


Figure 4.29:  $\frac{dC_p}{dx}$  vs. streamwise distance (mm) plot (c) for FOV 1 and  $V_t = 21.0\text{m/s}$

$$\frac{1}{1 - 0.3774} \cdot (3.7 \cdot 10^{-4}) > \frac{0.07}{172.1} \quad (4.13)$$

$$5.92 \cdot 10^{-4} > 4.06 \cdot 10^{-5} \quad (4.14)$$

As a result, it could be said that as both the  $C_p$  and  $\delta^*$  increase, the wake grows. This is validated by equation 4.14, for this point but also for all the other ones for this field of view. This was done by preparing a simple algorithm in MatLab which could return a **”True”** or **”False”** statement depending on whether the LHS is greater than the RHS or not.

## 4.5 Experimental Campaign II Conclusions

The second experimental campaign performed in the M-tunnel of the High Speed Laboratory (HSL) at Delft University of Technology. This experimental campaign included tests with a fundamental set-up, consisted of a flat plate - diffuser configuration. The reason of conducting these tests was to try and understand the wake bursting phenomenon further by simulating the same effect with a simple set-up in contrast to the actual wing-flap case used in the first testing campaign. Moreover, the aim was to get a reasonable amount of data, which could also be used to compare with the actual case and draw final conclusions.

Flow visualisation tests performed using woollen tufts at different wind-tunnel speeds, showed attached flow on the difuser walls and the flat plate. However, at lower speed there was no sign of reversed flow behind the plate, but at higher speed the reversed wake flow was pretty clear. Then, from static pressure data gathered from pressure taps placed on the diffuser walls, it was concluded that the pressure increase in the diffuser area was approximately linear as could be expected.

Then, from boundary layer measurements carried out on the flat plate's surface, the evolution of the boundary layer was normal, with boundary layer thickness increasing as the probe was moving towards the trailing edge. However, at the last measurement point, at the tapered part of the plate, the flow was separated. This was possibly happening due to the size or the distribution of the carborundum grains used as surface roughness for boundary layer transition. This was not expected and was not very welcomed, as attached flow was intended on the plate and then reversed flow behind the trailing edge. Nevertheless, this was not a big issue for the success of these tests. From wake measurements, the main conclusion was that moving streamwise in the diffuser area, the wake reversal region was increased in size. This was also validated by a statistical study performed.

Furthermore, PIV experiments carried out with the aim of gathering more accurate data which could be used in order to understand the wake bursting phenomenon nature and its possible causes, but also in order to compare with the data gathered during the first experimental campaign. In the report, only the data for the position immediately behind the trailing edge were presented as they were more related on what was of interest. For this position, three different speeds (5.1, 14.1 and 21 m/s) tested and the main conclusions from these cases were that as the speed increased, the wake reversal behind the trailing edge of the flat plate was increased significantly showing symmetrical vortical regions behind the plate. In addition, looking at the U and V- velocity components, for all the cases it was very clear that there was a great reduction in speed, especially inside the divergent part of the diffuser possibly happening due to the great overpressure created by the additional screen placed at the end of the diffuser in combination with the wall slots, in order to keep the flow attached on the walls. Thus, this great overpressure created large suction forces through the slots and as a result the speed in the diffuser area was decreased significantly.

Then with respect to the displacement thickness, for all the velocities tested, it was increasing as expected due to divergence of the streamlines which were displaced by significant amount due to increase in pressure and reduction in velocity. However, for the momentum thickness, the results were not as clear. For the lowest speed, the momentum thickness seemed to increase slightly, which could be explained by the adverse pressure gradient in the wake region. But for the other two speeds (14.1 and 21.0 m/s), there was a slight decrease which could not be explained. However, as these changes were minor, they could be explained as within the error range estimate. Finally, from the wake velocity plots, at three different positions in the filed of view, it was very obvious that as moving in the streamwise direction, the size of the reversed flow was increased significantly. Hence, from these results, it could be stated that there was an agreement between the pressure and PIV measurements with respect to the wake reversal region increase.

The last thing done was a theoretical study using Gartshore's wake behaviour relation, found in literature and it could be used to predict the wake bursting phenomenon. This relation is based on three different parameters namely the pressure coefficient  $C_p$ , the rate of change of pressure coefficient  $\frac{dC_p}{dx}$  and the displacement thickness of the wake,  $\delta^*$ . By using these three parameters it is possible to determine whether or not the wake grows or decays. Of course, if the wake grows, it means that there is great increase in pressure moving in the streamwise direction, which is the main cause of the wake bursting or reversal phenomenon. Thus, applying Gartshore's relation for this test, it seems that worked fine for the prediction of the growth of the wake for this particular case. As a result, it could be further used in order to predict the state of the wake which is strongly linked to wake bursting phenomenon.

## Chapter 5

# MSES Code For Maximum Lift Prediction

A relatively simple and fast tool in order to try and predict the high lift performance of multi-element airfoils, is the MSES code. MSES code is a CFD - design program for multi-element airfoils, developed at MIT, by Dr. M. Drela [7]. It allows the user to calculate the maximum obtainable lift for ideal flow control i.e. Euler, in comparison with (real life) viscous flow calculations.

In this thesis work, MSES code, used as a tool to analyse the overall lift performance of the X-400 model configuration with the same settings as tested in the wind-tunnel, with the intention to validate these results. Moreover, it was of great interest, to determine whether this code could predict the wake bursting phenomenon, at very high flap deflections. In the first section, general information about MSES are introduced, including part of it's background theory. Then, a brief insight on the validation procedure carried out for the MSES Linux version is presented, followed by the obtained numerical results. Finally, a brief conclusions part is located at the end of this chapter.

### 5.1 Introduction to MSES Version 3.07

MSES was originally distributed for all Unix and Linux platforms. For this research a Linux-compatible MSES version had been used, made available by Delft University of Technology. In the next subsection, the theory behind MSES code will be discussed, followed by the user interface and the required input files to run a complete simulation.

#### 5.1.1 Theory

The theory behind the numerical simulation of MSES can be divided into several topics. The following topics will briefly discussed:

1. The flow-field related equations
2. Discretisation and grid generation
3. Boundary layer equations covering the viscous part of the flow-field

#### 4. The solving method

##### Euler equations

MSES is an interactive program for the design, analysis and optimization of single and multi-element airfoil sections in subsonic and transonic flow conditions. It consists of a two-dimensional code based on the steady state conservative Euler equations [9].

##### Conservation of mass:

$$\oint_{\partial V} \rho(\vec{q} \cdot \hat{n}) = 0 \quad (5.1)$$

##### Conservation of momentum:

$$\oint_{\partial V} \rho(\vec{q} \cdot \hat{n})\vec{q} + p\hat{n}ds = 0 \quad (5.2)$$

##### Conservation of energy:

$$\oint_{\partial V} \rho(\vec{q} \cdot \hat{n})h_o ds = 0 \quad (5.3)$$

The integration is over the control volume boundary  $\partial V$ , with unit normal  $\hat{n}$ . For the meaning of the remaining symbols in these conservation laws, one is referred to the nomenclature. The MSES code, is set up by assuming that the viscous effects are restricted to a thin boundary layer and wake, and that the Euler equations cover the inviscid portion of the flow-field. Boundary layer theory describes the viscous part of the flow which is discussed later on in this section.

##### Grid Generation

An intrinsic grid is used for the discretisation of the equations in which a family of grid lines corresponds to the streamlines around the same body. Using this method, the continuity equation 5.1, simply states that the mass flux along each streamtube is constant:

$$m = \rho_1 \cdot q_1 \cdot A_{n1} = \rho_2 \cdot q_2 \cdot A_{n2} \quad (5.4)$$

Here,  $A_n$ , denotes the normal area of a conservation cell. Similarly the energy equation 5.3 reduces to a statement that the total enthalpy does not vary along a streamtube:

$$h_o = \frac{\gamma}{\gamma - 1} \frac{p_1}{\rho_1} + \frac{1}{2}q_1^2 = \frac{\gamma}{\gamma - 1} \frac{p_2}{\rho_2} + \frac{1}{2}q_2^2 \quad (5.5)$$

with  $\gamma$ , being the ratio of specific heats. Consequently the number of unknowns per grid node could now be reduced from four to two.

##### Boundary layer equations

The viscous portion of the flow is simulated, by assuming that the effect of the boundary layer is to displace the inviscid flow away from the physical body to create a new displacement body. As long as the ratio of boundary layer thickness and streamline radius of curvature remains small, this assumption has been shown to be acceptable. This is the case for a great deal of aerodynamic flows except e.g. near the trailing edge region. The boundary layer simulation starts with the

**Prandtl** boundary layer equations [40]:

**Continuity:**

$$\frac{\partial \rho}{\partial t} + \frac{\partial}{\partial x}(\rho u) + \frac{\partial}{\partial y}(\rho v) = 0 \quad (5.6)$$

**Momentum:**

$$\rho \left( \frac{\partial u}{\partial t} + u \frac{\partial u}{\partial x} + v \frac{\partial u}{\partial y} \right) = -\frac{\partial p_e}{\partial x} + \frac{\partial}{\partial y} \left( \mu \frac{\partial u}{\partial y} \right) \quad (5.7)$$

**Energy:**

$$\rho \left( \frac{\partial h}{\partial t} + u \frac{\partial h}{\partial x} + v \frac{\partial h}{\partial y} \right) = \frac{\partial p_e}{\partial t} + u \frac{\partial p_e}{\partial x} + \frac{\partial}{\partial y} \left( k \frac{\partial T}{\partial y} \right) + \mu \left( \frac{\partial u}{\partial y} \right)^2 \quad (5.8)$$

Assuming that we are dealing with a perfect gas and steady flows, these equations reduce to:

**Continuity:**

$$\frac{\partial}{\partial x}(\rho u) + \frac{\partial}{\partial y}(\rho v) = 0 \quad (5.9)$$

**Momentum:**

$$\rho u \frac{\partial u}{\partial x} + \rho v \frac{\partial u}{\partial y} = -\frac{\partial p_e}{\partial x} + \frac{\partial}{\partial y} \left( \mu \frac{\partial u}{\partial y} \right) \quad (5.10)$$

**Energy:**

$$\rho u \frac{\partial h}{\partial x} + \rho v \frac{\partial h}{\partial y} = u \frac{\partial p_e}{\partial x} + \frac{\partial}{\partial y} \left( \frac{\mu}{Pr} \frac{\partial h}{\partial y} \right) + \mu \left( \frac{\partial u}{\partial y} \right)^2 \quad (5.11)$$

with the Prandtl number defined as  $Pr = \mu \cdot c_p / k$ .

Moreover, the velocity could be eliminated using the continuity equation 5.9, by substituting for  $v$  into 5.10 and 5.11. The momentum and energy equations, are then integrated from the wall to infinity. By neglecting cross-stream pressure variation and considering only adiabatic free-stream flow, the final simplified equations for MSES are presented:

$$\frac{d\theta}{d\xi} + (2 + H - M_e^2) \frac{\theta}{u_e} \frac{du_e}{d\xi} = \frac{C_f}{2} \quad (5.12)$$

$$\theta \frac{dH^*}{d\xi} + (2H^{**} + H^*(1 - H)) \frac{\theta}{u_e} \frac{du_e}{d\xi} = 2C_D - H^* \frac{C_f}{2} \quad (5.13)$$

These two equations, for momentum and energy, are also referred as the shape parameter equation in this form and are valid for laminar and turbulent boundary layer regions, as well as for wakes. As a final step, the boundary layer calculation and the rest of the flow are coupled by making the solution at the edge of the boundary layer, a boundary condition for the inviscid calculation. This finally encloses the whole system for performing viscous simulations.

### Newton solution procedure

To conclude, the system of non-linear equations is solved by using the Newton solving method. More information about this can be found in [7].

### 5.1.2 User Interface

MSES is part of a set of programs to design, analyse and optimize single and multi-element airfoils. The basic programs required to run a simulation for this thesis work will be discussed in this subsection together with the specific input files needed for each single program. For the latter, each has its own objective. For information about all other programs or extra background information about the topics discussed hereafter, one is referred to the MSES User's Guide [7].

#### Input file **blade.xxx** - grid domain and airfoil geometry

The **blade.xxx** input file is a coordinate file created by the user containing the name of the profile (optionally), the four grid-boundary locations and the airfoil coordinates. This file is used in the initialization program MSET and in the airfoil manipulating program AIRSET. The "**xxx**" is a variable extension defined by the user, and is generally used to distinguish the case being run. For a multi-element airfoil the individual elements are separated by a line including "999.0 999.0". The exact format of this input file can be found in Appendix C.

#### Input file **mSES.xxx** - runtime parameters

The **mSES.xxx** input file is the run-time-parameter file used by the solver programs MSES and MSIS. Also here, the variable extension "**xxx**" defines a particular case. In this file all the variables together with the corresponding constraints are defined. It contains geometric and free-stream flow data like the angle of attack, the Reynolds number and the Mach number. The user can define the kind of simulation by a selection of several parameters such as inviscid flow, fully isentropic or a combination of isentropic and dissipative. More information about the format of this input file could be found in Appendix C.

#### Airfoil geometry manipulating program AIRSET

AIRSET is a menu-driven program for manipulating multi-element airfoil configurations and reads **blade.xxx** or a combination of several **blade.xxx** files as input. AIRSET, permits actions such as splitting off a flap and modifying the contour of a profile using the screen cursor. Furthermore, element translation, rotation or scaling can readily be performed with immediate graphical feedback. An inviscid panel method, with compressibility correction, is provided for a quick sanity check on any modification.

#### Grid and flow-field initialization program MSET

MSET is the program used to initialize the grid, the flow-field and a variety of other variables. It reads the airfoil coordinate input file **blade.xxx** and the **gridpar.xxx** file if available (optionally). MSET is menu-driven and allows the user to iteratively generate a good initial grid. By specifying the angle of attack a panel solution is generated which is used to trace a pair of stagnation streamlines just above and below each element, as well as the upper and lower far field streamlines. Once a good node distribution on each element is obtained, MSET proceeds to modify all the spacings to resolve conflicts between adjacent elements. An elliptic grid smoother can be used in order to eliminate grid imperfections such as kinks, overlaps and to make the grid

streamlines correspond to those of the incompressible inviscid flow. This final grid then serves as an initial guess for the MSES solver.

### Flow solver program MSES

MSES is the main program that solves the Euler equations. It requires two input files: **mdat.xxx** and **m ses.xxx**. The output file is written back to **mdat.xxx** which means that **mdat.xxx** can either be a restart file from an old calculation or a file created by MSET. When starting MSES the user is asked for the number of iterations to be performed. This value serves as a limit since MSES will terminate earlier if the average changes of several parameters between two iterations drop below the convergence tolerance limits and the maximum changes drop below 10 times these limits.

### Flow solver program MSIS

MSIS is functionally the same as MSES except that MSIS solves the Euler equations with one of the momentum equations replaced by an isentropic condition. Consequently, the Newton matrix used by MSIS is slightly changed which makes it about twice-four times as fast as MSES. Furthermore, MSIS is also advantageous as it can calculate flows with extremely low free-stream Mach numbers ( $M_\infty \approx 0.001$  or less). An important note is that MSIS can only be used for sub-critical cases. If any part of the flow-field in the solution becomes supersonic, MSIS will fail [7].

### Solution plotter MPLOT

MPLOT is the program which displays the solution in **mdat.xxx** at any time, whether the solution is converged or not. It allows plotting of most of the airfoil's surface and wake boundary layer variables. Force coefficients and amplitude amplifications for transition prediction could also be shown.

## 5.2 Validation of MSES Linux Version

As long as there was a familiarity with the way MSES works, it was time to perform a validation study for the Linux version of MSES. Different single element airfoil models used with the aim to determine their characteristics and compare them with data gathered from previous wind-tunnel experiments on the same airfoils. The reason behind this validation process was to check if the results obtained by the code, were accurate enough but also agreeing with experimental data, before proceeding to multi-element simulations simulations.

The MSES calculation data were compared with experimental data from wind-tunnel tests that Dr. W.A. Timmer performed at LTT with airfoils mainly used for wind energy purposes. Moreover, some NACA airfoils tested and compared with experimental data, found in literature and Internet sources [21]. A number of airfoils used in this study are presented in Table 5.1

Simulations of the flow-field around the airfoil using MSES were carried out for a range of angles of attack for each airfoil as shown in the table above. The first airfoils to be tested were NACA 0012, 4412 and 64<sub>2</sub>10. Then additional simulation tests carried out by using the rest of the airfoils that also tested by Dr. W.A. Timmer experimentally. The focus of the study was

<b>Airfoil Type</b>	<b>AoA Range [°]</b>	<b>Reynolds Number [Re]</b>
NACA 0012	0-2-4-6-9-10-12-16-20	$2.6 \cdot 10^6$
NACA 4412	0-1-2-3-5-6-7-8-9-10-12	$1.0 \cdot 10^6$
NACA 63 <sub>4</sub> 18	0-2-4-6-8-10-12-14	$1.6 \cdot 10^6$
NACA 63 <sub>4</sub> 21	0-2-4-6-8-10-12-14	$1.6 \cdot 10^6$
NACA 63 <sub>6</sub> 18	0-2-4-6-8-10-12-14	$1.6 \cdot 10^6$
NACA 64 <sub>2</sub> 10	0-1-2-3-4-5-6-7-8-9-10	$2.6 \cdot 10^6$
NACA 64 <sub>4</sub> 18	0-2-4-6-8-10-12-14	$1.6 \cdot 10^6$
NACA 64 <sub>4</sub> 21	0-2-4-6-8-10-12-14	$1.6 \cdot 10^6$

Table 5.1: MSES validation study matrix for Linux version

mainly on the airfoil's pressure distributions, lift and drag coefficients.

The presentation of data for this study, will include the most important plots for the first three airfoils tested, namely NACA 0012, 4412 and 64<sub>2</sub>10. Further data could be found in the Appendix C at the end of this report. In Figures 5.1, 5.2 and 5.3, the following graphs are presented: Airfoil's contour,  $C_1$  versus  $\alpha$ ,  $C_1$  versus  $\alpha$  and selected  $C_p$ -distribution plots for different angles of attack.

As one could observe from the plots in Figures 5.1, 5.2 and 5.3, for all the airfoil types tested using MSES, the pre-stall lift values of MSES simulations match the ones from wind-tunnel tests. Then for post-stall angles of attack, MSES simulations data seem to overestimate the lift values. The drag coefficient values from MSES simulations seem to underestimate the experimental data, but also the stall angles, showing earlier stall angles of attack compared to the wind-tunnel data. Moreover, for the MSES simulations, the solution was always converged using very few iterations, in order to get the final results. However, near the stall region, at higher angles of attack, the number of iterations needed was increasing significantly and MSES seemed to have difficulty in predicting the right solutions while most of the time it was unable to converge. This could be observed from  $C_p$ -distribution plots in Figures 5.1, and 5.3, where significant wiggling on the trends is noticeable. This could be explained as a not converged solution, hence, these results could not taken into account as they are not accurate enough.

With respect to the experimental data, the lift curves were very similar to that from MSES (up to stall region) whereas a small discrepancy was noticeable in drag coefficients specifically for post stall angles of attack. In addition, further check performed for the experimentally measured pressure distributions, compared with those calculated by MSES for certain angles of attack. One could clearly see that the distributions were as good as the ones from the code especially at low angles of attack and definitely for pre-stall regions. For the post-stall regions, the MSES code plots were showing great divergence compared to the experimental results.

As a result, from this validation study using the Linux Version of MSES, it could be concluded that:

1. Satisfying results and agreement with experimental data for pre-stall angles of attack
2. Low number of iterations and convergence for pre-stall regions
3. Not accurate results for post-stall regions with great divergence from wind-tunnel data

4. Greater number of iterations needed, not always converged solutions
5. MSES could be used accurately for pre-stall regions for single or multi-element airfoils
6. MSES could not be used accurately for post-stall regions especially at regions of great separation
7. The user should be very careful in the interpretation of MSES results, especially, where separation regions expected for single or multi-element airfoils

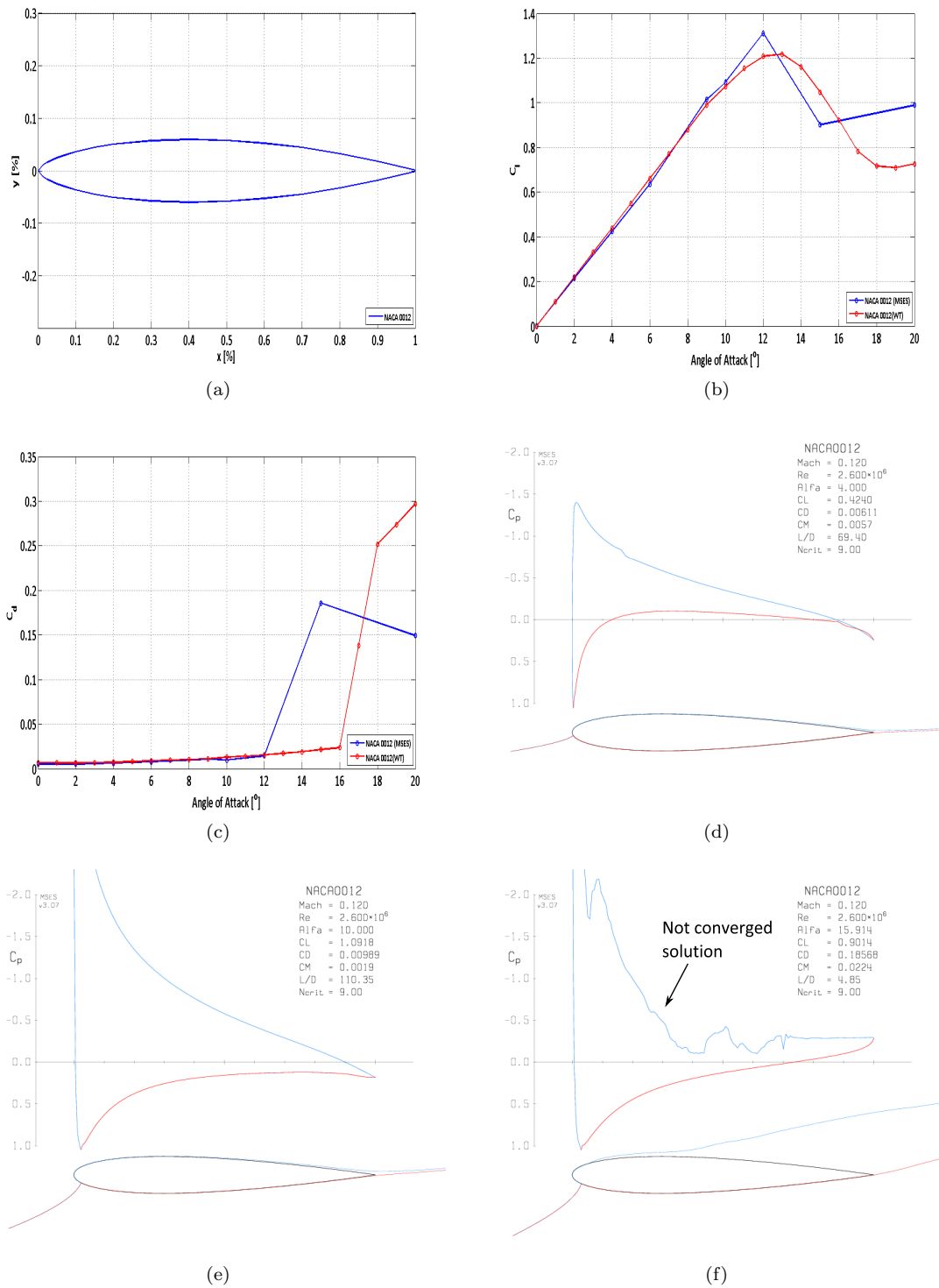


Figure 5.1: NACA 0012 study plots where (a) NACA 0012 shape, (b)  $C_L$  vs.  $\alpha$ , (c)  $C_D$  vs.  $\alpha$ , (d)  $C_p$ -distribution plot at  $\alpha = 4^\circ$ , (e)  $C_p$ -distribution plot at  $\alpha = 10^\circ$ , (f)  $C_p$ -distribution plot at  $\alpha = 15^\circ$   
 MSc. Thesis C.Kounenis

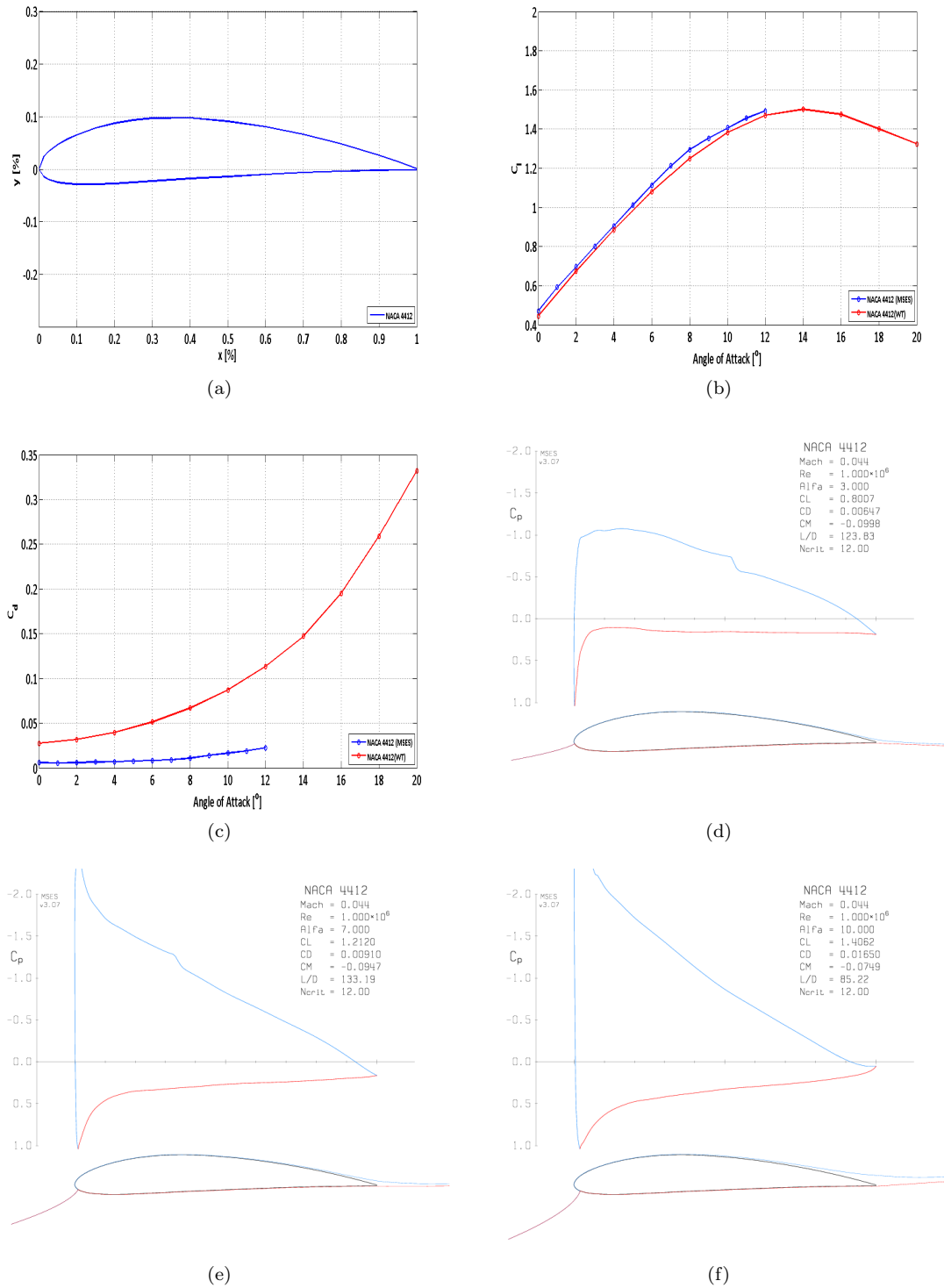


Figure 5.2: NACA 4412 study plots where (a) NACA 4412 shape, (b)  $C_L$  vs.  $\alpha$ , (c)  $C_D$  vs.  $\alpha$ , (d)  $C_p$ -distribution plot at  $\alpha = 3^\circ$ , (e)  $C_p$ -distribution plot at  $\alpha = 7^\circ$ , (f)  $C_p$ -distribution plot at  $\alpha = 10^\circ$   
 MSc. Thesis C.Kounenis

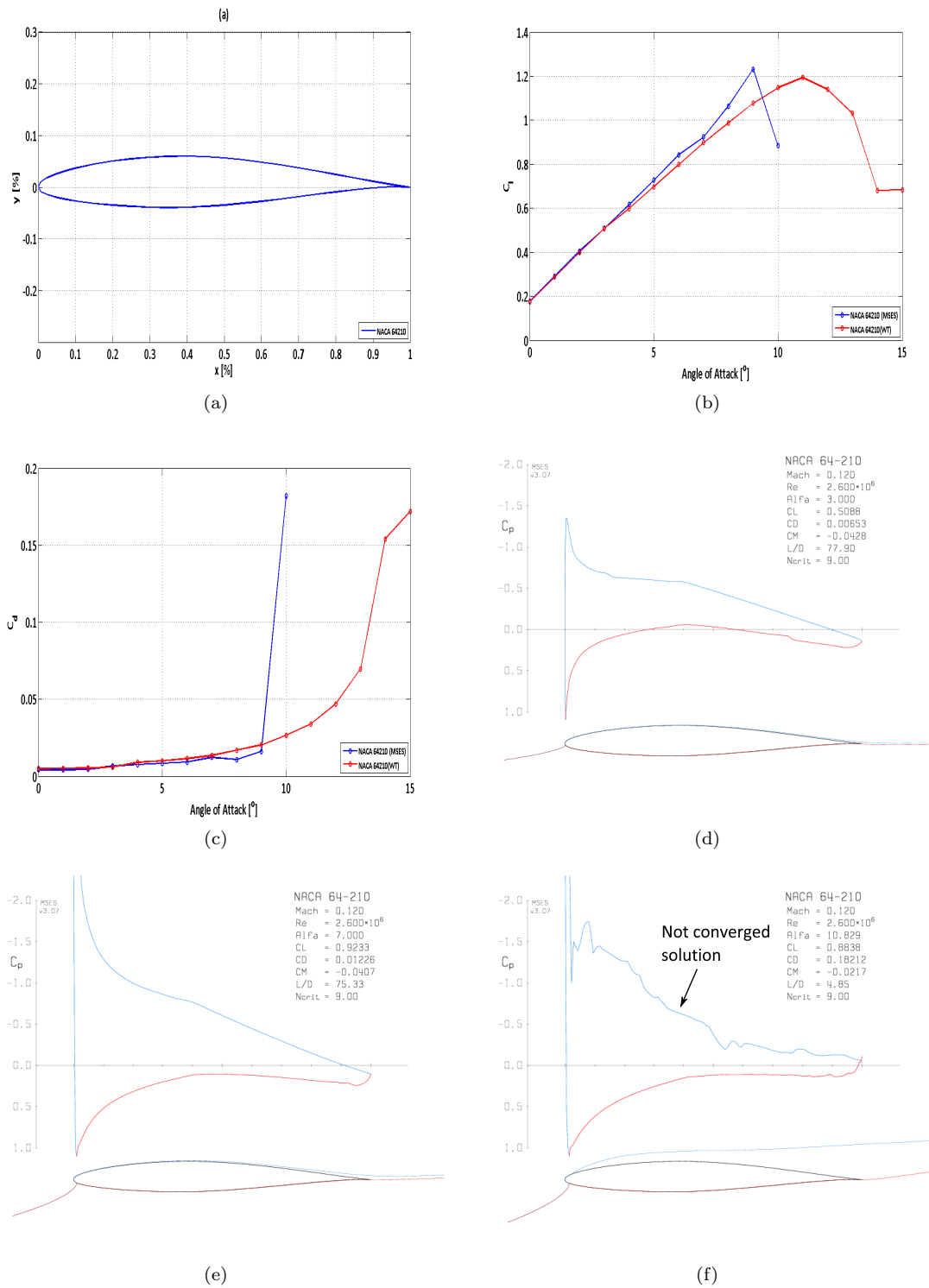


Figure 5.3: NACA 64<sub>2</sub>10 study plots where (a) NACA 64<sub>2</sub>10 shape, (b)  $C_l$  vs.  $\alpha$ ,  $C_d$  vs.  $\alpha$ , (d)  $C_p$ -distribution plot at  $\alpha = 3^\circ$ , (e)  $C_p$ -distribution plot at  $\alpha = 7^\circ$ , (f)  $C_p$ -distribution plot at  $\alpha = 11^\circ$   
 MSc. Thesis C.Kounenis

### 5.3 X-400 Wing-Flap Model Configuration

The next part of this computational work, was to model the X-400 wing-flap configuration, in order to check it's characteristics and compare the results with those obtained during previous MSES work found in literature [9]. Moreover, performing these calculations, it could be possible to predict the wake bursting phenomenon experienced in the wind-tunnel tests.

Since MSES encountered convergence problems, when a model contained sharp edges, the profile used for the calculations, shown in Figure 5.4, was given great attention in terms of smoothness of it's contour and for this reason, the coordinates of the airfoil were connected using splines. This was vital, in regions of great curvature, as for example in the cove area and slot entrance between the main wing and flap.

The profile was investigated for two different flap angles of  $\alpha = 40^\circ$  and  $50^\circ$  respectively, with overlap and gap settings presented in Table 5.2. By using two different angles, it would be possible to determine how the maximum lift influenced with increasing  $\delta_f$ , but also in order to compare how MSES code was performing for combinations of high angles of attack and flap deflections. All the calculations performed with the program MSIS, since the Mach number for the calculations was very low ( $M = 0.123$ ) and therefore isentropic conditions could be assumed. Consequently, the advantages of the use of this tool were twofold:

1. Extremely fast convergence time
2. The ease to calculate for larger angles of attack,  $\alpha$

$\delta_f$ [°]	$x_{\text{overlap}}$ [%]	$y_{\text{gap}}$ [%]
40	0.0	3.0
50	0.0	3.7

Table 5.2: X-400 wing-flap model setting parameters used for MSES calculations

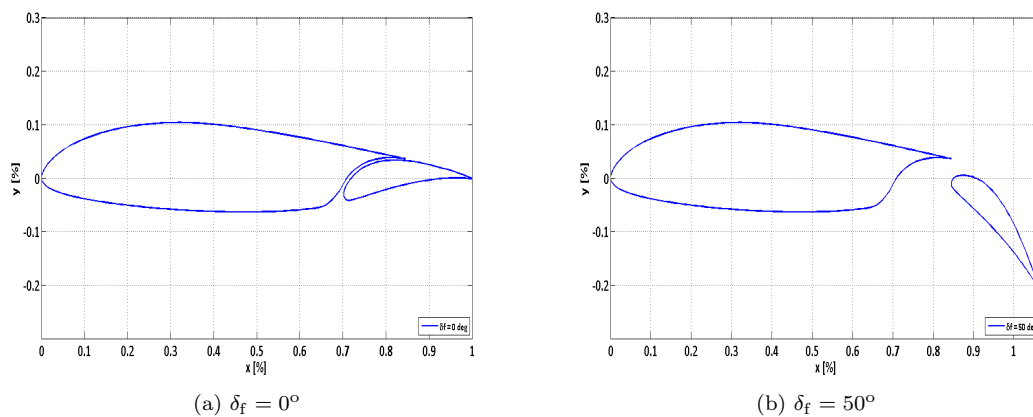


Figure 5.4: 2D X-400 wing-flap model configuration at (a)  $\delta_f = 0^\circ$  and (b)  $\delta_f = 50^\circ$

## 5.4 Presentation and Discussion of Results

During this computational work, using the X-400 wing-flap model, it was tried to understand whether the flow phenomena observed in the wind-tunnel, could also be validated from these simulations. This is why, this work could be described as a study of the potential limits of MSES code for combination of very high angles of attack and flap angles.

The profile was tested at two different flap angles of  $\alpha = 40^\circ$  and  $50^\circ$  respectively. The angle of attack was altered by a step of one degree each time up to maximum possible angles (post-stall angles as well). The Reynolds number selected to be  $1.7 \cdot 10^6$  and remained unchanged for all simulations. This Reynolds number picked for similarity purposes with the wind-tunnel data. The simulations performed for both flap angles by altering some parameters each time. These parameters were, the curvature exponent,  $c$ , but also the upper and lower surface transition points for both elements, namely  $XTR_u$  and  $XTR_l$ .

The curvature exponent, is a parameter which by change it, the number of nodes for both airfoils could be increased, where geometrical curvature exists and as a result could contribute in a more accurate solution. On the other hand, the top and bottom transition points for both elements, could also be altered in order to give the user more freedom. Consequently, by altering these three parameters, it was tried to determine, which case would give the best possible results and manage to predict the aerodynamic characteristics of this configuration at such a combination of high angles of attack and flap angles.

### 5.4.1 Case (A): $\delta_f = 40^\circ$

In this case, it was tried to determine which settings, from the ones mentioned in section 5.4, would give the closest match to the data published from a previous literature thesis work [9]. This work was done using MSES code as well, with the same configuration, flap angle and Reynolds number. As a result, it would be possible, to judge the results obtained from the Linux version, used for this work, in comparison with an identical work and then apply these, in order to proceed at  $50^\circ$  angle of attack simulations, which were of the main interest. Below, in Table 5.3, the simulation matrix used for  $\delta_f = 40^\circ$ , is presented.

By looking the simulation matrix in Table 5.3, three different cases tested by altering the settings, mentioned in section 5.4. Thus, these cases are numbered below:

- **Case 1:** Curvature exponent maximum refinement set as  $c = 0.1$ , with upper and lower transition points set as  $XTR1 = 0.1$  for the main wing and  $XTR2 = 0.1$  for the Fowler flap.
- **Case 2:** Curvature exponent medium refinement set as  $c = 0.5$ , with upper and lower transition points also changed for both elements close to mid-chord position,  $XTR_u$  and  $XTR_l = 0.5$ .
- **Case 3:** Curvature exponent unaltered, as  $c = 1$ , with upper and lower transition points also unaltered for both elements,  $XTR_u$  and  $XTR_l = 1.0$ .

Observing the results in Table 5.3, for all the cases presented, it seems like the MSES code, was unable to return any results for high angles of attack mainly at post-stall angles. The first case of maximum refinement, where  $c = 0.1$ ,  $XTR1 = 0.1$  and  $XTR2 = 0.05$ , was able to converge for all the pre-stall angles up to  $8^\circ$ . Then, for higher angles of attack, as happened for the other two cases, the convergence failed and the simulation was crashed. This could be possibly due to

Case	Re	A.o.A [°]	$\delta_f$ [°]	$x_{\text{overlap}}$ [%c]	$y_{\text{gap}}$ [%c]	c	XTR <sub>u1</sub>	XTR <sub>l1</sub>	XTR <sub>u2</sub>	XTR <sub>l2</sub>	Iterations No.	Convergence	Result
1	$1.7 \cdot 10^6$	0	40	0.0	3.0	0.1	1.0	1.0	1.0	1.0	300	No	Not Crashed-Not Accurate
2	$1.7 \cdot 10^6$	0	40	0.0	3.0	0.5	1.0	1.0	1.0	1.0	300	No	Crashed-Not Accurate
3	$1.7 \cdot 10^6$	0	40	0.0	3.0	1.0	1.0	1.0	1.0	1.0	300(35)	Yes	Accurate
4	$1.7 \cdot 10^6$	0	40	0.0	3.0	0.1	0.5	0.5	0.5	0.5	300	No	Crashed-Not Accurate
5	$1.7 \cdot 10^6$	0	40	0.0	3.0	0.5	0.5	0.5	0.5	0.5	300(19)	Yes	Accurate
6	$1.7 \cdot 10^6$	0	40	0.0	3.0	1.0	0.5	0.5	0.5	0.5	300(34)	Yes	Accurate
7	$1.7 \cdot 10^6$	0	40	0.0	3.0	0.1	0.1	0.1	0.05	0.05	300	No	Not Crashed-Not Accurate
8	$1.7 \cdot 10^6$	0	40	0.0	3.0	0.5	0.1	0.1	0.05	0.05	300	No	Crashed-Not Accurate
9	$1.7 \cdot 10^6$	0	40	0.0	3.0	1.0	0.1	0.1	0.05	0.05	300	No	Not Crashed-Not Accurate
10	$1.7 \cdot 10^6$	1	40	0.0	3.0	1.0	1.0	1.0	1.0	1.0	300(25)	Yes	Accurate
11	$1.7 \cdot 10^6$	1	40	0.0	3.0	0.5	0.5	0.50	0.5	0.5	300(19)	Yes	Accurate
12	$1.7 \cdot 10^6$	1	40	0.0	3.0	1.0	0.5	0.50	0.5	0.5	300(28)	Yes	Accurate
13	$1.7 \cdot 10^6$	2	40	0.0	3.0	1.0	1.0	1.0	1.0	1.0	300(27)	Yes	Accurate
14	$1.7 \cdot 10^6$	2	40	0.0	3.0	0.5	0.5	0.50	0.5	0.5	300	No	Crashed-Not Accurate
15	$1.7 \cdot 10^6$	2	40	0.0	3.0	1.0	0.5	0.50	0.5	0.5	300(24)	Yes	Accurate
16	$1.7 \cdot 10^6$	3	40	0.0	3.0	1.0	1.0	1.0	1.0	1.0	300(28)	Yes	Accurate
17	$1.7 \cdot 10^6$	3	40	0.0	3.0	0.5	0.5	0.50	0.5	0.5	300(19)	Yes	Accurate
18	$1.7 \cdot 10^6$	3	40	0.0	3.0	1.0	0.5	0.50	0.5	0.5	300(24)	Yes	Accurate
19	$1.7 \cdot 10^6$	4	40	0.0	3.0	1.0	1.0	1.0	1.0	1.0	300(29)	Yes	Accurate
20	$1.7 \cdot 10^6$	4	40	0.0	3.0	0.5	0.5	0.50	0.5	0.5	300(20)	Yes	Accurate
21	$1.7 \cdot 10^6$	4	40	0.0	3.0	1.0	0.5	0.50	0.5	0.5	300(28)	Yes	Accurate
22	$1.7 \cdot 10^6$	5	40	0.0	3.0	1.0	1.0	1.0	1.0	1.0	300(23)	Yes	Accurate
23	$1.7 \cdot 10^6$	5	40	0.0	3.0	0.5	0.5	0.50	0.5	0.5	300(23)	Yes	Accurate
24	$1.7 \cdot 10^6$	5	40	0.0	3.0	1.0	0.5	0.50	0.5	0.5	300(29)	Yes	Accurate
25	$1.7 \cdot 10^6$	6	40	0.0	3.0	1.0	1.0	1.0	1.0	1.0	300(34)	Yes	Accurate
26	$1.7 \cdot 10^6$	6	40	0.0	3.0	0.5	0.5	0.50	0.5	0.5	300(24)	Yes	Accurate
27	$1.7 \cdot 10^6$	6	40	0.0	3.0	1.0	0.5	0.50	0.5	0.5	300(28)	Yes	Accurate
28	$1.7 \cdot 10^6$	7	40	0.0	3.0	1.0	1.0	1.0	1.0	1.0	300(34)	Yes	Accurate
29	$1.7 \cdot 10^6$	7	40	0.0	3.0	0.5	0.5	0.50	0.5	0.5	300	Not	Crashed-Not Accurate
30	$1.7 \cdot 10^6$	7	40	0.0	3.0	1.0	0.5	0.50	0.5	0.5	300(29)	Yes	Accurate
31	$1.7 \cdot 10^6$	8	40	0.0	3.0	1.0	1.0	1.0	1.0	1.0	300(34)	Yes	Accurate
32	$1.7 \cdot 10^6$	8	40	0.0	3.0	0.5	0.5	0.50	0.5	0.5	300	Not	Crashed-Not Accurate
33	$1.7 \cdot 10^6$	8	40	0.0	3.0	1.0	0.5	0.50	0.5	0.5	300	Not	Crashed-Not Accurate
34	$1.7 \cdot 10^6$	9	40	0.0	3.0	1.0	1.0	1.0	1.0	1.0	300(34)	Yes	Accurate
35	$1.7 \cdot 10^6$	9	40	0.0	3.0	0.5	0.5	0.50	0.5	0.5	300	Not	Crashed-Not Accurate
36	$1.7 \cdot 10^6$	9	40	0.0	3.0	1.0	0.5	0.50	0.5	0.5	300	Not	Crashed-Not Accurate
37	$1.7 \cdot 10^6$	10	40	0.0	3.0	1.0	1.0	1.0	1.0	1.0	300(49)	Yes	Accurate
38	$1.7 \cdot 10^6$	10	40	0.0	3.0	0.5	0.5	0.50	0.5	0.5	300	Not	Crashed-Not Accurate
39	$1.7 \cdot 10^6$	10	40	0.0	3.0	1.0	0.5	0.50	0.5	0.5	300	Not	Crashed-Not Accurate

Table 5.3: Simulation matrix using X-400 wing-flap configuration at  $\delta_f = 40^\circ$ , including settings used and the results of these computations

the fact that the transition point was forced to move further upstream and as a result the solver was facing difficulties to converge.

Moving to the case of medium refinement, the curvature exponent was changed to  $c = 0.5$  and forced transition around the mid-chord of the airfoil ( $XTR1 = 0.5$  and  $XTR2 = 0.5$ ). For the pre-stall angles of attack, the convergence of the simulations was satisfying, however, for this case it lasted up to  $\alpha = 7^\circ$ . For higher angles, the solution could not converge or was again crashing and was quite strange that the angle of attack, where convergence was happening was reduced, as there was a significant lower refinement of the already mentioned parameters compared to **Case 1**. The reason for that, could possibly be that as the solution was further refined the transition point was moving forward for both elements, and thus, stronger wakes and separated regions existed, which MSES could not deal with, especially for combinations of high angles of attack and flap deflections.

To conclude, the last case without any curvature refinement,  $c = 1$ , and without forced transition ( $XTR1 = 1.0$  and  $XTR2 = 1.0$ ), performed better compared to the other two, as for all the angles tested in the pre-stall region, from  $0^\circ$  to  $10^\circ$ , the solution converged with a small number of iterations, mentioned in brackets next to the number of iterations tried. However, as mentioned before, after  $10^\circ$ , the simulations could not converge or were crashing. As a general conclusion, for all these cases, it could be argued that MSES, was unable to predict the flow characteristics at combinations of high main wing and flap angles, hence, it could hardly predict

large areas of separated flow. Consequently, the results in the pre-stall region, might be used and thought to be accurate, however, for the post-stall region, the results were not accurate and could not be taken into account.

At this point, the plots presented in Figure 5.5 will be discussed. To begin with the  $C_l$  plot (a), **Case 3** agrees very well with the most refined case (**Case 1**). However, this happens up to  $\alpha = 7^\circ$  where, there are not enough data for **Case 1**. However, both show a linear trend of  $C_l$  increase as angle of attack increases. On the other hand, the literature data agree very well with **Case 2** refinement. Once more, this happens up to  $\alpha = 6^\circ$ , where data exist for this case. One interesting thing to note is that the lift line from the literature data, was plotted based only on four points representing  $\alpha = 0^\circ, 4^\circ, 8^\circ$  and  $12^\circ$ . Moreover, up to  $\alpha = 8^\circ$ , it's linear and then the gradient drops, thus the accuracy of this result is questionable. By looking the  $C_l$  lines, it could be seen that the second refinement, **Case 2**, over predicts the lift coefficients compared to the other two cases (**Case 1** and **Case 3**). This could be explained from the earlier transition, which would lead to postponement of flow separation and as a result an increase in lift coefficients. On the other case of the maximum refinement, **Case 1**, an even earlier transition, would not have the same effect as the  $C_l$  values are lower.

Moving to  $C_d$  (b) plot, the discussion done for the  $C_l$  plot, could also be linked with the  $C_d$  data. **Case 2**, showing the highest lift possibly due to separation postpone, has also the lowest drag values from the other two. It comes with no great surprise that **Case 3** has the highest drag. **Case 3**, on the other hand, has higher drag coefficient values than **Case 2**. A possible explanation for that, could be given by observing the  $C_p$  plots (e) and (f), presented in Figure 5.5. For both **Case 2** and **Case 3**, it seems that a separation bubble exists. Thus, as the lift for the **Case 2** is higher and drag lower, it could be argued that the size of the separation bubble region is smaller for this case than for the other one. The other two plots shown in this figure (c) and (d), are the momentum coefficient against the angle of attack and the coefficient of lift against the drag coefficient plot. Both of them show reasonable trends with respect to the discussion done for the lift and drag plots earlier.

In general, for all the results presented for the case with  $\delta_f = 40^\circ$ , it could be said that the second refinement case (**Case 2**) seems to be the optimal to keep, for simulations with flap angle at  $\delta_f = 50^\circ$ . However, it was decided to try the same procedure and test the same cases as before, as the flow features would be significantly altered and further refinements could be essential.

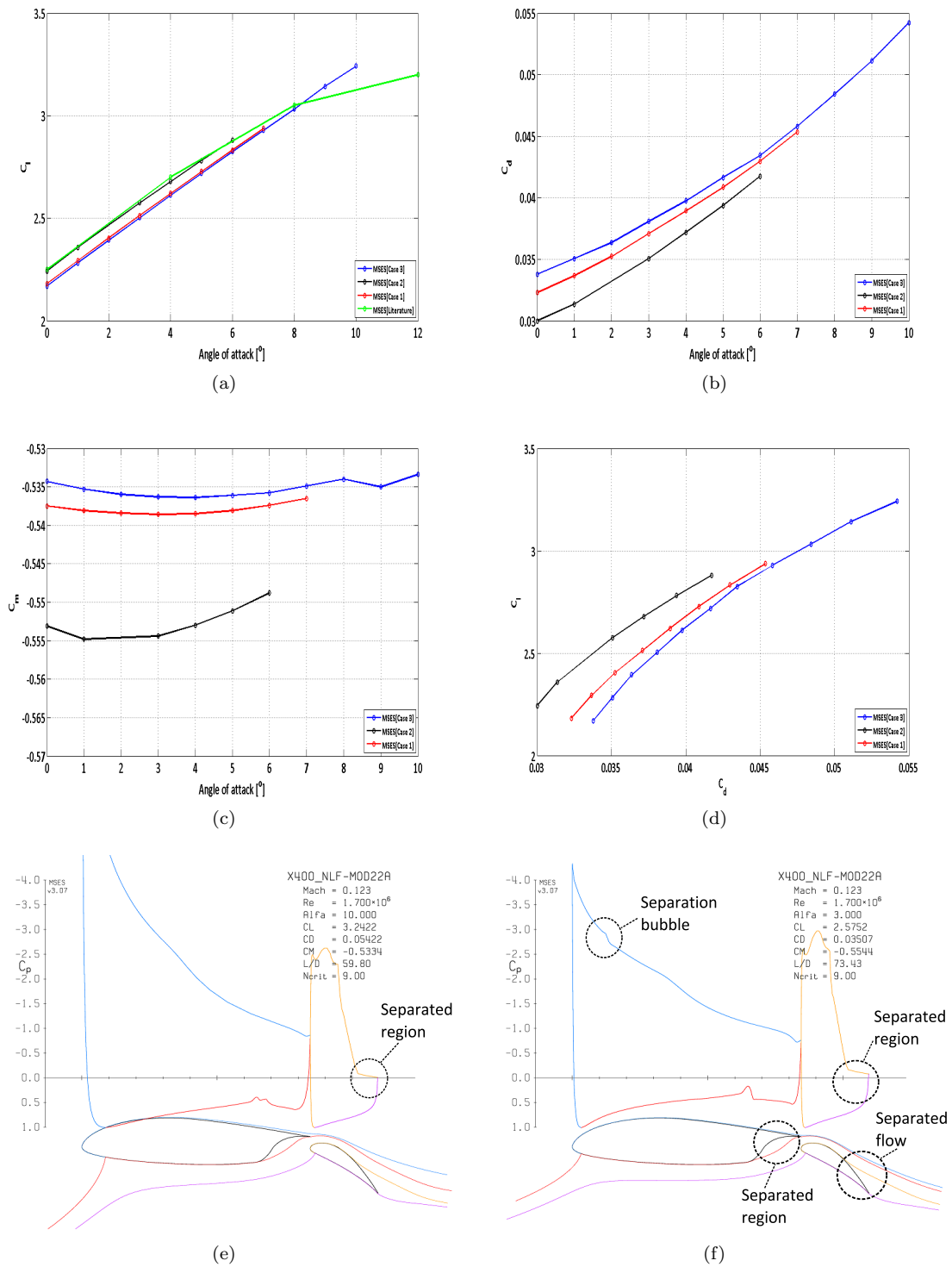


Figure 5.5: (a)  $C_l$  vs.  $\alpha$ , (b)  $C_d$  vs.  $\alpha$ , (c)  $C_m$  vs.  $\alpha$ , (d)  $C_l$  vs.  $C_d$ , (e)  $C_p$ -distribution plot at  $\alpha = 10^\circ$  for Case 1, (f)  $C_p$ -distribution plot at  $\alpha = 3^\circ$  for Case 2 for X-400 wing-flap configuration at  $\delta_f = 40^\circ$   
 MSc. Thesis C.Kounenis

### 5.4.2 Case (B): $\delta_f = 50^\circ$

Below in Table 5.4, the simulation matrix used for flap angle of  $\delta_f = 50^\circ$ , is presented.

Case	Re	A.o.A [°]	$\delta_f$ [°]	$x_{overlap}$ [%c]	$y_{gap}$ [%c]	c	XTR <sub>i,1</sub>	XTR <sub>r,1</sub>	XTR <sub>i,2</sub>	XTR <sub>r,2</sub>	Iterations No.	Convergence	Result
1	$1.7 \cdot 10^6$	0	40	0.0	3.7	0.1	1.0	1.0	1.0	1.0	300	No	Crashed-Not Accurate
2	$1.7 \cdot 10^6$	0	40	0.0	3.7	0.5	1.0	1.0	1.0	1.0	300	No	Not Crashed-Not Accurate
3	$1.7 \cdot 10^6$	0	40	0.0	3.7	0.5	1.0	1.0	1.0	1.0	500	No	Crashed-Not Accurate
4	$1.7 \cdot 10^6$	0	40	0.0	3.7	1.0	1.0	1.0	1.0	1.0	300	No	Crashed-Not Accurate
5	$1.7 \cdot 10^6$	0	40	0.0	3.7	1.0	1.0	1.0	1.0	1.0	500	No	Crashed-Not Accurate
6	$1.7 \cdot 10^6$	0	40	0.0	3.7	0.1	0.5	0.5	0.5	0.5	300	No	Crashed-Not Accurate
7	$1.7 \cdot 10^6$	0	40	0.0	3.7	0.5	0.5	0.5	0.5	0.5	300	No	Crashed-Not Accurate
8	$1.7 \cdot 10^6$	0	40	0.0	3.7	1.0	0.5	0.5	0.5	0.5	300	No	Not Crashed-Not Accurate
9	$1.7 \cdot 10^6$	0	40	0.0	3.7	1.0	0.5	0.5	0.5	0.5	500	No	Not Crashed-Not Accurate
10	$1.7 \cdot 10^6$	0	40	0.0	3.7	0.1	0.1	0.1	0.05	0.05	300	No	Crashed-Not Accurate
11	$1.7 \cdot 10^6$	0	40	0.0	3.7	0.5	0.1	0.1	0.05	0.05	300	No	Crashed-Not Accurate
12	$1.7 \cdot 10^6$	0	40	0.0	3.7	1.0	0.1	0.1	0.05	0.05	300	No	Crashed-Not Accurate

Table 5.4: X-400 wing-flap configuration MSES simulation result at  $\delta_f = 50^\circ$

As it could be noticed from Table 5.4, none of the already mentioned cases worked. For all the cases, the solution was either crashing or was not converged. This was of great surprise, as for all different cases, it seems that MSES could not return any solution. However, at  $\delta_f = 50^\circ$ , it could be expected that the separated regions especially close to the flap region would be even greater than the  $\delta_f = 40^\circ$  case. Hence, if MSES could not return a solution at low angles of attack, it would be imagined that a combination of high angles of attack and flap deflections, would be even harder to converge.

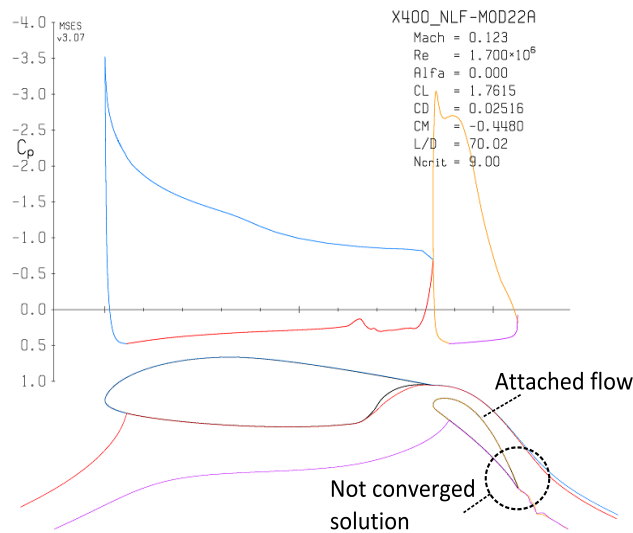


Figure 5.6: MSES simulation results at flap angle of  $\delta_f = 50^\circ$

This is also indicated from one of the plots of the X-400 wing-flap configuration, at  $\delta_f = 50^\circ$ , gathered from a not converged solution at  $\alpha = 0^\circ$ . As it could be noticed, the flow in the cove region area shows part of separation as would be expected but at the Fowler flap, there is not any separated region as would be expected at such large flap deflection. Moreover, if one looks carefully at the trailing edge of the flap, will see a significant wiggling happening in the wake, proving that the solution is not converged.

Concluding, as it was impossible to get accurate results for the clean wing configuration (CWC), the implementation of drooped spoiler panel (DSP) case at such high angles of attack and flap deflections, would be even more difficult to converge. Additionally, after discussing with very experienced users of MSES code, it could be concluded that the modeling of the drooped spoiler panel in the configuration would also be challenging, as it could have a significant thickness, which would be very hard to implement on MSES, resulting in crashed simulations and large errors.

## 5.5 MSES Conclusions

This computational study using MSES code was performed with initial aim the validation of the experimental data gathered in the wind-tunnel using the X-400 wing-flap model configuration. Therefore, an additional study carried out, using single element airfoils, in order to check whether the Linux MSES version was working as expected, returning accurate results. From this study, it seemed that MSES was working accurately enough in the pre-stall regions, where there was not any severe separated regions. However, for post-stall regions, the results were not accurate at all, as the solution was not always converged and most of the times was crashing.

Then moving to the actual case of the X-400 wing-flap configuration, it was decided to run simulations with this configuration at two different flap angles of  $\delta_f = 40^\circ$  and  $\delta_f = 50^\circ$ . The reason for that, was first of all to start with a lower flap angle, where some literature data existed, and then apply all these at  $\delta_f = 50^\circ$  case, which was of main interest. From the very first tests with the  $\delta_f = 40^\circ$  case, it was tried to test different settings as the curvature exponent and transition position, in order to check which one would give the best possible results.

The main conclusions were that MSES was able to predict the flow characteristics at pre-stall regions but at the post-stall regions, the solutions were not converged or instead were crashed. This possibly happened due to the fact that MSES code could not predict flow phenomena for combination of high angles of attack and flap deflections. Nevertheless, looking the data presented earlier, for **Case 2** tested with  $c = 0.5$  and  $XTR = 0.5$ , seemed to have the best results and could be used for the  $\delta_f = 50^\circ$  case. Moving to simulations with flap angle at  $\delta_f = 50^\circ$ , all the settings re-tested but this time for all cases the solutions were crashed or failed to converge.

As a result, it was impossible to get any results for this test case which was of main interest. The biggest possibility for this failure of MSES returning any accurate results, could be due to the large flap deflections and severe separation regions happening on the flap region which could not be predicted. As a result, further tests with drooped spoiler panel would have been even worse to simulate as could be imagined and as a result MSES cannot be used for validation of experimental results for this thesis work.

## Chapter 6

# Final Conclusions

The research on high lift systems showed that multi-element airfoils develop towards a circular arc to achieve maximum lift force. Nevertheless, flow control techniques become crucial in order to overcome the loss of lift due to flow separation. Within the scope of lift improvement, the effect of drooped spoiler panel (DSP) application, was investigated for a wing-Fowler flap model, the X-400 configuration. The main focus was on critical flight conditions, i.e. a high flap deflection angle of  $50^\circ$  and  $Re = 1.6 \cdot 10^6$ .

Clean wing configuration experiments, showed that the airfoil is characterized by some interesting features. At low angles of attack, the main element deals with attached flow, whereas on the Fowler flap, the flow is partially separated. Increasing the angle of attack towards the stalled condition, the flow on the main element separates while due to the displacement effect of the main airfoil wake, the flow around the flap gets fully attached. This observation indicated that the drooped spoiler panel (DSP) concept, could show benefit at lower angles of attack, as at higher ones the flow around the flap is already fully attached.

Separation delay by means of passive flow control was investigated using different drooped spoiler panels, attached close to the trailing edge of the main wing. The difference between the panels tested, was the angle of the inclined part, ranging from  $0^\circ$  up to  $15^\circ$ . The most successful device tested was the DSP1 (at  $15^\circ$ ), where the flow was able to stay fully attached on the surface of the Fowler flap up to its trailing edge. However, it was noticed that by reducing the panel's angle, this effect was reduced. The reason for that, is the convergent nozzle created by the inclined part of the panel and the Fowler flap's suction surface, increasing the flow velocity at this region as was also validated by PIV experiments. Thus, as the drooped spoiler panel angle was reduced this effect was not as powerful and consequently the flow was separated on the Fowler flap.

After the first pressure measurements, it was apparent that at low angles of attack and up to  $4^\circ$ , the lift coefficients were higher and drag coefficients lower for the case with the dropped spoiler attached, compared to the clean wing configuration. However after  $4^\circ$ , the lift coefficients were lower, presenting a flat plateau trend and drag coefficients presented a sudden increase. This was not expected and after analysing of all data gathered, it was realised that wake bursting was occurring. This rare phenomenon, which is not easily detectable, could be described as reversed flow on the wake above the boundary layer, due to an adverse pressure region on this area. The reason for which this phenomenon is not easily detectable, is the state of the boundary layer, which is still attached on the flap's surface, showing no sign of separation. This was experienced

during oil-flow visualisation tests in this case. As long as wake bursting was confirmed, it was decided to focus on wake bursting research, trying to understand its nature and possible causes.

Part of wake bursting research included Particle Image Velocimetry (PIV) tests on the wing-flap configuration. The most interesting data, showed that for clean wing configuration there was not any sign of wake bursting, but instead separated flow on the Fowler flap, which was growing in size as the angle of attack of the whole configuration was increased. Then with drooped spoiler panel attached on the main wing, for angle of attack of  $0^\circ$ , it was very obvious that the flow on the Fowler flap was attached and there was still no sign of wake bursting. However, it was clear that above the boundary layer there was a region of very low velocity, which could be a "warning" that wake bursting would occur as the angle of attack would increase further. Increasing the angle of attack at  $8^\circ$ , wake bursting occurred, showing attached flow in the boundary layer as expected, close to the wall of the flap, but above that, a very low velocity region existed, with reversed flow. The interesting fact, is that wake reversal could be the reason for the attached flow on the surface of the Fowler flap. This is because the reversed flow, above the boundary layer, seems to be split in two parts, one moving towards the boundary layer and the other towards the free stream. Moreover, it could be said that as soon as the wake bursting phenomenon initiated, there was a dramatic increase in wake displacement thickness,  $\delta^*$ , nearly doubled, compared to the  $0^\circ$  case, where there was still not any sign of it. Finally, it should be also added that further increase in boundary layer thickness could lead to wake bursting much faster especially at lower angles of attack of the whole configuration, however, at larger angles, where the wake bursting phenomenon is already initiated, an additional increase in boundary layer thickness would not cause a huge effect.

The second part of this research included a fundamental approach of testing, using a flat plate inside a diverging wall diffuser. This was done in order to further understand the wake bursting phenomenon in a simpler configuration but also try to link that with the actual wing-flap case. In order to simulate the wake reversal phenomenon, a flat plate with a tapered end, to simulate the flow leaving the trailing edge on a wing, was put inside a diffuser with diverging walls at an angle of  $15^\circ$ . These tests included some flow visualisation tests, in order to check the quality of the flow on the diffuser walls, on the flat plate's surface and behind the plate in the wake region. From these tests, it was realised that at higher tunnel velocities, there was flow reversal behind the flat plate's trailing edge. From boundary layer tests on the flat plate, a small part of the tapered region was separated, which was not exactly what expected but it was not also a big issue. Then moving to the wake measurements using pressure measurements and PIV, it was very clear that as the tunnel speed was increased the size of the reversed flow behind the flat plate was also increasing in size. Moreover, it was noticed that there was also a very large reduction in velocity in the diffuser area due to the great overpressure created by the walls and the screen at the end of the diffuser. Hence, this decrease of velocity and the great overpressure could be explained as the cause of wake reversal behind the plate. This is also the cause of wake bursting in the actual wing-flap configuration, where very low velocity was observed above the boundary layer of the Fowler flap. Finally, the displacement thickness was also observed to increase significantly due to the displacement of the streamlines in the wake region, which was also observed on the X-400 configuration tests.

The final thing done was a theoretical study using Gartshore's wake behaviour relation found in literature and it could possibly be used in order to predict the wake bursting phenomenon. This relation is based on three different parameters namely the pressure coefficient  $C_p$ , the rate of change of pressure coefficient,  $dC_p/dx$  and the displacement thickness of the wake,  $\delta^*$ . By using

these three parameters it was possible to determine whether or not the wake grows or decays. Of course, if the wake grows, it means that there is great increase in pressure which could also lead to wake reversal. Thus, applying the rule for this test, it seemed that the relation worked fine for the prediction of the growth of the wake for this particular case. As a result, this relation could be used in order to predict the state of the wake and if possible the wake bursting phenomenon.

Finally, a computational study using MSES code was carried out, with initial aim the validation of the experimental data gathered in the LTT testing campaigns using the X-400 wing-flap configuration. The main conclusions were that, MSES was able to predict the flow characteristics at pre-stall regions but at the post-stall regions the solutions were not converged or instead were crashed. This possibly was happened due to the fact that the MSES code could not predict flow phenomena for combination of high angles of attack and flap deflections. Nevertheless, looking the data presented earlier, **Case 2** tested with  $c = 0.5$  and  $XTR = 0.5$ , seemed to have the best results and could be used for the  $\delta_f = 50^\circ$  case. Moving to the  $\delta_f = 50^\circ$  flap angle simulations, once more all the settings re-tested but this time for all cases the solutions were crashed or failed to converge. As a result, it was impossible to get any results for this case which was of main interest. The biggest possibility for this failure of MSES returning any accurate results, could be due to the large flap deflections and severe separation regions happening on the flap region which could not been predicted. As a result, further tests with drooped panel would be even worse to simulate as could be imagined and as a result MSES could not be used accurately for validation of experimental results for this thesis work.

We could conclude that the selected configuration tested for flow separation delay was partially successful. The relatively large model, high Fowler flap deflection and large Reynolds number appeared not to be a huge obstacle in order to achieve flow separation elimination on the Fowler flap of the configuration. However, the potential of lift improvement was strongly limited due to wake bursting effects. From this work, one should realise the wake bursting existence at high angles of attack and the potential limits this phenomenon could set for high lift devices.

Therefore, a better understanding of the wake bursting phenomenon is necessary. This thesis work was a small piece in a great and unknown field. Literature was limited and the tests done for this work has shown that there are very important factors which could lead to the cause of this unwanted phenomenon and explanations on how it could be avoided in the design process of multi-element airfoils. For multi-element airfoils, this phenomenon could be the cause of great loss of performance and as a result, it would be very helpful to continue this kind of research in order to further understand it and possibly find solutions in order to deal with it.

## Chapter 7

# Future Work & Recommendations

As it could be understood by the reader, this work was a very small step towards an unknown "path". The initial objective of this thesis work was to study the effect of drooped spoiler panel (DSP) on a high lift configuration, however, it was eventually changed into gaining a deeper understanding on the wake bursting or so called off-the-surface separation phenomenon, which up to date seems not to be exploited in depth. The literature found was very limited, especially with respect to the actual case (wing-flap) problem. Many people know it's existence and presented it's great application in high lift devices, but very few tried to go deeper, trying to explain it, finding it's potential causes and possibly manage to prevent or postpone it. Moreover, most of the published research carried out with simplified models such as flat plates and diffusers, but none experimented with a wing-flap configuration, which is the real-life case, and the one of main interest.

This was the potential contribution of this thesis work. To present the existence of this phenomenon and try to link the fundamental test findings with the actual (wing-flap) case results. However, a period of 11 months would not be enough to fully exploit this phenomenon. Thus, this chapter could be thought as one of the most valuable parts of this report for any researcher planning to take this work a step further. This chapter consists of what should be done in the future, to get a greater insight in the wake bursting phenomenon. The future work recommendations, thought as the most relevant and vital for this research, are presented as noted during this work period of 11 months.

- Further wind-tunnel testing with the X-400 wing-flap model would be essential, in order to determine it's limits with respect to wake bursting phenomenon having the drooped spoiler panel (DSP) attached. This could be done, by testing the wing-flap configuration at different combinations of angles of attack and flap angles. Specifically, the change in flap angles, would consequently alter the overlap and gap values, which are thought as very important with respect to the flow phenomena leading to wake bursting. Additional tests with a different model including a slat and possibly more flap elements, would be valuable as the extent of wake bursting is expected to be reduced or even eliminated and hence the performance of the dropped spoiler panel on the overall configuration could be superior.
- Another area where more work could be done, is with respect to boundary layer displacement thickness,  $\delta^*$  and pressure coefficient gradient,  $\frac{dC_p}{dx}$ , relation with wake bursting phenomenon. It would be useful to create a "law" or rule, predicting the wake bursting

for a wing-flap configuration based on these parameters. Additionally, further exploit of Gartshore's relation, used in this thesis work, would be also very useful with respect to wake calculations and wake bursting prediction.

- Further particle image velocimetry (PIV) experiments on the wing-flap configuration, with a great attention to the boundary layer and wake regions, but also the wake and boundary layer interaction, would be ideal. It is believed, that additional PIV tests could give a great insight in the actual wing-flap configuration case of the whole phenomenon process.
- With respect to fundamental tests, it would be very significant to perform numerous flat-plate diffuser tests, but this time paying a lot of attention to the set-up by using already known data to avoid velocity deficit in the divergent section of the diffuser. Moreover, keeping the flow attached on the flat plate would also be desirable, in order to simulate the trailing edge flow of a wing-flap configuration. Moreover, the range of speeds tested could be increased, in order to have Reynolds number similarities.
- Furthermore, additional diffuser angles could be tested and by performing the same experimental techniques (Pressure measurements and PIV), gathering more data would allow to determine the effect on the wake reversal.
- Moving to computational work, further MSES work and simulations would be desirable. If wake bursting could be predicted by MSES code, then the prediction of this phenomenon would be much easier and could be incorporated much faster to the design process of a wing-flap configuration and as a result avoiding such phenomenon would be possible. This could also be tried using commercial CFD software packages, trying to simulate the wake bursting phenomenon for high lift devices.
- To conclude, as a last recommendation, more fundamental research and tests could be carried out on flow control devices which could prevent or postpone wake bursting. Nevertheless, this should be done based on wind-tunnel work or CFD simulations, otherwise this could lead to a trial and error effort, which would not give the appropriate insight into this research topic.

# Bibliography

- [1] L.H.J. Absil and D.M. Passchier. An experimental study of the trailing edge flow of an nlr 7702 airfoil, using laser-doppler anemometry. *Experimental thermal and fluid science*, 9(2):174–185, 1994.
- [2] D. Adair and W.C. Horne. Turbulent separated flow over and downstream of a two-element airfoil. *Experiments in Fluids*, 7(8):531–541, 1989.
- [3] U. Anand, Y. Sudhakar, R. Thileepanragu, V.T. Gopinathan, and R. Rajasekar. Passive flow control over naca 0012 aerofoil using vortex generators. In *Proceedings of the 37th National & 4th International Conference on Fluid Mechanics and Fluid Power*, Chennai, India, December 2010.
- [4] J.D. Anderson. *Fundamentals of aerodynamics*, volume 2. McGraw-Hill New York, 2001.
- [5] J.J. Bertin and M.L. Smith. *Aerodynamics for engineers*, volume 1. Prentice Hall, 1989.
- [6] P. Chang. *In Control of Flow Separation*. Hemisphere Publishing Corporation, 1976.
- [7] M. Drela. A users guide to mses 3.04. 2006.
- [8] D. Driver and G.M. Mateer. Wake flow in adverse pressure gradient. In *SAE/AIAA World Aviation Congress and Exposition, San Diego, CA, SAE Technical Paper*, pages 01–5511, 2000.
- [9] J. El Haddar. Flow separation control over a wing-flap model. Master’s thesis, Delft University of Technology, August 2012.
- [10] G.E. Elsinga, F. Scarano, B. Wieneke, and B.W. Van Oudheusden. Tomographic particle image velocimetry. *Experiments in Fluids*, 41(6):933–947, 2006.
- [11] Fugahumana Human Flight. Flow Separation. <http://fugahumana.com/2012/04/05/bio-mimetic-drag-reduction-part-3-morphing/flowseparation-2/>, 2012. [Online; accessed 15-August-2012].
- [12] M. Gad-el Hak. *Flow control: passive, active, and reactive flow management*. Cambridge University Press, 2007.
- [13] B. Günther, F. Thiele, R. Petz, W. Nitsche, J. Sahner, T. Weinkauff, and H.C. Hege. Control of separation on the flap of a three-element high-lift configuration. *AIAA paper*, 265:2007, 2007.
- [14] J. Hinze. 0. 1975 turbulence, 1972.

- [15] R. Hoffenberg, J. Sullivan, and SP Schneider. Wake measurements in a strong adverse pressure gradient. 1994.
- [16] W. Mason. *High Lift Aerodynamics*. McGraw-Hill, 2004.
- [17] T. Melin. Helix, innovative aerodynamics high-lift concepts. In *European Congress on Computational Methods in Applied Sciences and Engineering ECCOMAS2004, Jyväskylä, 24 to 28 July 2004*, 2004.
- [18] A. Melling. Tracer particles and seeding for particle image velocimetry. *Measurement Science and Technology*, 8(12):1406, 1999.
- [19] NASA. Green Aviation: A Better Way to Treat the Planet. <http://www.nasa.gov>, 2010. [Online; accessed 22-October-2012].
- [20] NPTEL. Laminar-Turbulent Transition. [http://nptel.iitm.ac.in/courses/Webcourse-contents/IIT-KANPUR/FLUID-MECHANICS/lecture-32/32-3\\_lami\\_turb\\_trans.htm](http://nptel.iitm.ac.in/courses/Webcourse-contents/IIT-KANPUR/FLUID-MECHANICS/lecture-32/32-3_lami_turb_trans.htm), 2012. [Online; accessed 15-October-2012].
- [21] University of Illinois at Urbana-Champaign. UIUC Airfoil Data Site. <http://www.ae.illinois.edu/m-selig/ads.html>, 1995. [Online; accessed 10-April-2012].
- [22] Delft University of Technology. M-tunnel. <http://www.lr.tudelft.nl/en/organisation/departments-and-chairs/aerodynamics-and-wind-energy/aerodynamics/contributor-area/scientific-staff/veldhuis-llm/facilities/low-speed-tunnels/m-tunnel/>, 2012. [Online; accessed 23-September-2012].
- [23] R.E. O'Malley Jr. Singular perturbation theory: A viscous flow out of göttingen. *Annual Review of Fluid Mechanics*, 42:1–17, 2010.
- [24] K.C. Pfingsten, R.D. Cecora, and R. Radespiel. An experimental investigation of a gapless high-lift system using circulation control. In *CEAS/KATnet II Conference on Key Aerodynamic Technologies, Bremen, Germany*, 2009.
- [25] M. Raffel, C.E. Willert, and J. Kompenhans. *Particle image velocimetry: a practical guide*. Springer Verlag, 1998.
- [26] D. Reckzeh. Flying community friendly - the role of high-lift aerodynamics. In *International Congress of The Aeronautical Sciences (ICAS) 2008*, Bremen, Germany, May 2009. Airbus.
- [27] J.C. Ross, B.L. Storms, and P.G. Carrannanto. Lift-enhancing tabs on multielement airfoils. *Journal of aircraft*, 32(3):649–655, 1995.
- [28] F. Scarano. *Experimental Techniques in Aerodynamics Lecture Notes*. Delft University of Technology, 2010.
- [29] A.M.O Smith. High-lift aerodynamics. *Journal of Aircraft*, 12(6):501–530, 1975.
- [30] A.R. Starke, R. Henkes, and M.J. Tummers. Effects of curvature and pressure gradient on a turbulent near wake. *Experimental thermal and fluid science*, 19(1):49–56, 1999.
- [31] T. Sutcliffe, Reckzeh D., and Fischer M. Hicon aerodynamics - high lift aerodynamic design for the future. In *International Congress of The Aeronautical Sciences ICAS 2006*, 2006.

- [32] Dassault Systems. Temperature Coefficient of convection. [http://help.solidworks.com/2012/Italian/SolidWorks/cworks/Convection\\_Heat\\_Coefficient.htm](http://help.solidworks.com/2012/Italian/SolidWorks/cworks/Convection_Heat_Coefficient.htm), 2012. [Online; accessed 15-October-2012].
- [33] M.J. Tummers, K. Hanjalić, D.M. Passchier, and R. Henkes. Computations of a turbulent wake in a strong adverse pressure gradient. *International journal of heat and fluid flow*, 28(3):418–428, 2007.
- [34] J.W. van der Burg, J.E.J. Maseland, and F.J. Brandsma. Low speed maximum lift and flow control. *Aerospace science and technology*, 8(5):389–400, 2004.
- [35] L.L.M Veldhuis. *Aircraft Aerodynamics Lecture Notes*. Delft University of Technology, 2010.
- [36] L.L.M. Veldhuis, D.P. Jansen, J. El Haddar, and G. Correale. Novel passive and active flow control for high lift. In *International Congress of The Aeronautical Sciences (ICAS) 2012*, Brisbane, Australia, September 2012. Delft University of Technology.
- [37] X. Wang, F. Wang, and Y. Li. Aerodynamic characteristics of high-lift devices with downward deflection of spoiler. *Journal of Aircraft*, 48(2):730–735, 2011.
- [38] Z.U.A. Warsi. *Fluid dynamics: theoretical and computational approaches*. CRC, 2005.
- [39] J. Westerweel. Fundamentals of digital particle image velocimetry. *Measurement Science and Technology*, 8(12):1379, 1999.
- [40] F.M. White. *Viscous fluid flow*, volume 66. McGraw-Hill New York, 1991.
- [41] Wikipedia. Flowfield formation. [http://en.wikipedia.org/wiki/Lift\\_\(force\)](http://en.wikipedia.org/wiki/Lift_(force)), 2012. [Online; accessed 19-July-2012].

# Appendix A

## Wind-Tunnel Campaign I

Appendix A, contains additional information based on experimental background theory, apparatus, set-up and further results of the first experimental campaign. Illustrations and schematics are presented to give further insight into several aspects. For more information, one is also referred to Chapter 3 of the report, where all the information of this appendix belongs to.

## A.1 X-400 wing-flap model and drooped spoiler panel (DSP)

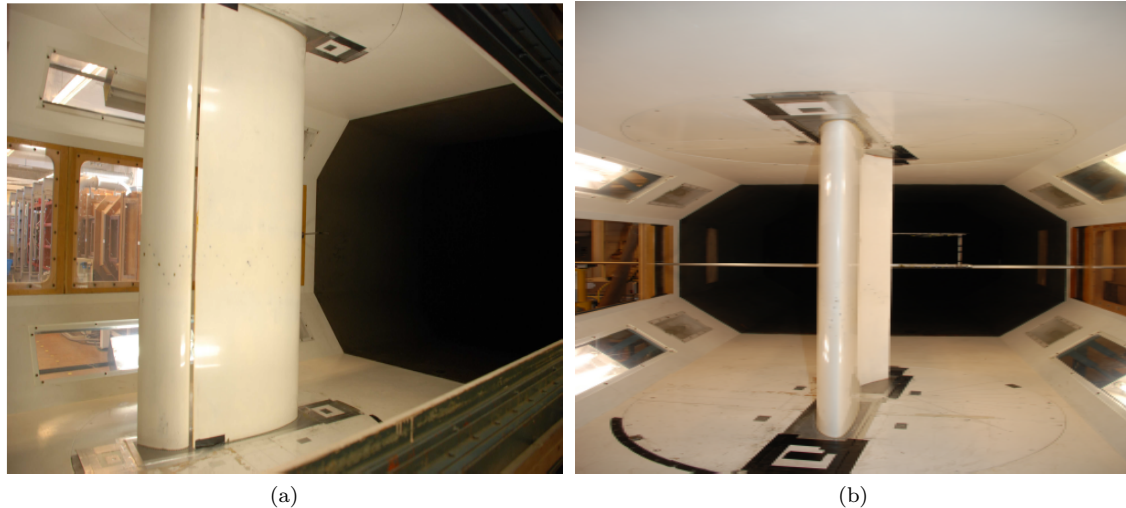


Figure A.1: The X-400 wing-flap configuration model positioned in the LTT. The model was set-up vertically to allow for angle of attack,  $\alpha$ , adjustments. On the left (a), the side view is shown which corresponds to the upper surface (suction side) of the airfoil i.e. the main element and the deflected flap. On the right (b), the front view of the airfoil is shown.

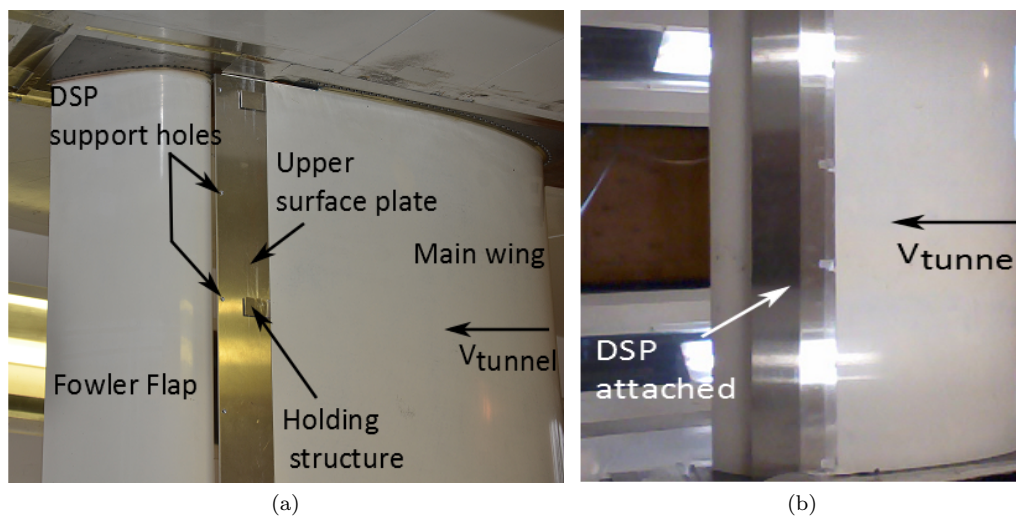


Figure A.2: The X-400 wing-flap configuration model positioned in the LTT with DSP attached. On the left (a), the upper surface plate is attached on the trailing edge of the X-400 main wing model. Geometrical details are explained in text. On the right (b), the drooped spoiler panel (DSP) device is attached on the wing-flap model configuration.

## A.2 Pressure measurements set-up

In order to change the flap angle, the aluminium tape was removed and then the bolts for the flap rotation were untightened. Then using a  $90^\circ$  ruler, aligned with the aluminium plate, the right angle was chosen using the already marked lines on the bottom wall disc, shown in Figure A.3. The final step was to tighten the bolts and replace the aluminium tape with new one. Following that, the whole configuration was set at an angle of attack of  $-6.79^\circ$ . Therefore, in order to have the flow facing the configuration at  $90^\circ$ , the flap had to be offset to  $6.79^\circ$ . Then, using a ruler, it was possible to see that the trailing edge of the main wing and the leading edge of the flap coincided at  $90^\circ$ . The reference line to check the trailing edge of the main wing and the leading edge of the flap were  $90^\circ$  perpendicular to the direction of the flow. Parallel to this line, a ruler was placed on the trailing edge of the main wing and leading edge of the Fowler flap and these two were aligned.

For the overlap setting, the procedure was fairly similar to the flap angle setting, by removing the aluminium tape and then untighten the x-direction bolts of the flap movement this time. Then, a template used. On this template, several lines were drawn. Hence, the thick line on the template had to coincide with the last line on the main wing. By doing so, the overlap was set at zero value. In order to further fix the overlap value, the distance from the start of the wind tunnel section to the trailing edge of the flap, was measured using a ruler.

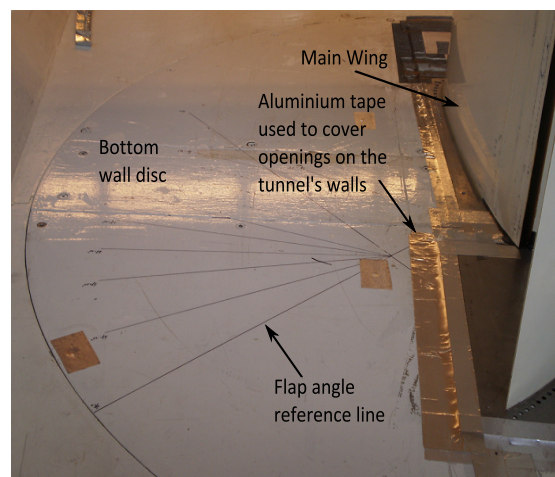


Figure A.3: Marked lines on the bottom wall disc of the LTT test section, used to set-up the Fowler flap angle,  $\delta_f$

Then, the angle of attack motor of the test section was connected to the computer. The computer gives a signal to the motor which rotates the upper and lower discs in the section. Finally, the pressure tubes connected first to the wing and then to the pressure scanner. Analytically, pressure tubes with numbers from 1-25 were connected to channel 1, tubes with numbers from 26-50 to channel 2, from 51-75 to channel 3 and finally tubes from 76-100 to channel 4. Then suction tubes were connected to a pressure pump in the basement. The tubes connected to the pressure scanner could be seen in Figure A.4. Finally, the author familiarised with the tunnel's operation.



Figure A.4: Pressure scanner connected with tubes from surface pressure taps on the X-400 wing-flap configuration model

## A.3 Particle Image Velocimetry (PIV)

### A.3.1 PIV Theoretical Background

Particle image velocimetry (PIV) is a successful measurement technique that over the past decades, due to advances in cameras, lasers and computer processing power, has developed from a qualitative to quantitative flow measurement technique. It is employed to acquire instantaneous measurements of the velocity and related properties of fluids in a two-dimensional plane with two-component PIV (2C-PIV) [25] or in three-dimensional space with tomographic PIV [10].

Particle image velocimetry measurement technique is based on the tracking of tracer particles within a fluid flow. A schematic overview of a 2C-PIV set-up is depicted in Figure A.5. A typical 2C-PIV system consists of a seeding system (not displayed), that intersperses small tracer particles into the flow, a laser system with laser optics to produce a laser-light sheet and a digital imaging and recording system consisting of at least one camera with imaging optics.

Tracer particles, which are often referred to as "seeding", are introduced into the flow. These particles have to be sufficiently small, in order to follow the fluid flow accurately and not alter the characteristics of the fluid. When moving through the region of interest, a pulsed light source will twice generate a thin light sheet, at a time-step  $\Delta t$  apart, thereby, illuminating the tracer particles. Simultaneously with the laser pulses, a camera, placed perpendicular to the measurement plane, will record the light scattered by the particles in two subsequent image frames. The two image frames,  $I(x,y,t)$  and  $I(x,y,t + \Delta t)$ , will contain the specific particle positions.

For evaluation, the image plane is commonly divided into small sub-domains, called "interrogation windows", as shown in Figure A.6. Then cross-correlation of the interrogation windows of two subsequent recordings yields the average particle displacement in pixels within such a window, as is indicated in Figure A.6. Evaluating the particle displacement with cross-correlation has the advantage that no explicit particle detection is required. By taking into account the magnification factor the displacement vector can be expressed in meters. Furthermore, by considering the time separation between the subsequent images,  $\Delta t$ , the velocity vector can be determined,

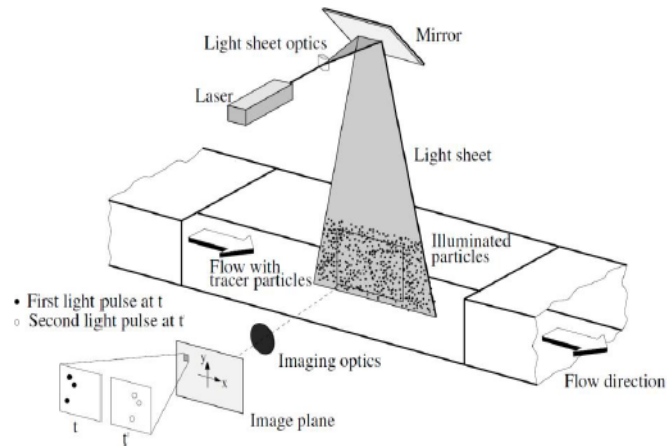


Figure A.5: Schematic overview of a 2C-PIV set-up [25]

and hence the velocity field can be reconstructed.

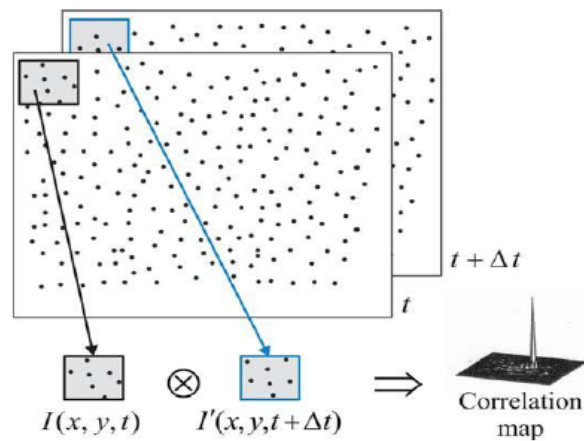


Figure A.6: Image windowing and discrete cross-correlation map [28]

PIV could be considered as non-intrusive as long as the tracer particles have no influence on the flow, following the flow accurately and not interacting with each other [39]. Also the optical equipment could be placed outside of the flow field, although the laser and camera do require optical access to area of interest. Furthermore, PIV measures instantaneous velocity fields with a high spatial resolution, while most other velocity measurement techniques can only measure the instantaneous velocity at a single point, as for example Hot Wire Anemometry (HWA) and Laser Doppler Velocimetry (LDV). Even though the temporal resolution of PIV is increasing, it is still limited by the acquisition frequency and laser repetition rate. Additionally, the storage of the camera puts restrictions on the recording time.

### Tracer particles

The tracer particles inserted into a fluid flow act as a tracking device and are typically employed with PIV or LDV. As described above, the particles are required to follow the flow accurately without altering the fluid flow characteristics. Consequently, the tracer particles characteristic response time has to be smaller than the smallest characteristic time scale of the fluid flow. Moreover, for the illuminated particles to be detectable by cameras, they should scatter enough light towards the camera.

### Mechanical properties

For accurate PIV measurements, the tracer particles need to faithfully follow the motions of the flow. This can be achieved, by ensuring the velocity difference between the particles and the fluid is very small. The velocity difference or slipping velocity, illustrated in Figure A.7, is  $U_s = U_p - U_f$ , where  $U_p$  is the particle velocity vector and  $U_f$  is the fluid velocity vector.

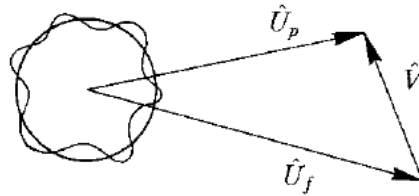


Figure A.7: Relative particle motion [18]

The entire motion of a small spherical particle immersed in a turbulent fluid flow is rather complex, but fortunately an acceptable approximation for the equation of motion is available from [14]. For very small tracer particles, as applied in PIV, the approximation of the equation of motion can be reduced to:

$$\frac{\pi}{6} d_p^3 \rho_p \frac{dU_p}{dt} = \overbrace{-3\pi\mu d_p U_s}^{\text{quasi-steady viscous force}} \quad (\text{A.1})$$

where  $d_p$  is the particle diameter,  $\rho_p$  the particle density and  $\mu$  the fluid dynamic viscosity [28]. The term on the left and right hand side represent, respectively, the force required to accelerate a particular particle in the flow field and the quasi steady viscous force in the form of Stokes' drag.

### Scattering properties

Besides mechanical requirements the tracer particles also have to scatter enough light towards the camera to allow for particle tracking. The light scattering depends on several factors, such as the ratio of the refractive index of the particles to that of the surrounding medium, their size, shape and orientation. However, there is little control over the last two factors, but the average size of the particles can be adapted, since that depends on the type of tracer particles. The larger the particle diameter, the more light is scattered, in fact the average intensity increases with the square of the particle diameter. Moreover, the relative angle between the illuminating light and the camera axis plays a significant role. For spherical particles with diameters  $d_p$  larger than the wavelength,  $\lambda$ , of the laser light, Mie's scattering theory could be applied to determine the

light scattering on a particle. The scattered light intensity distribution for an oil particle of  $1 \mu\text{m}$  in air with laser light having a wavelength,  $\lambda$ , of 532 nm according to Mie's theory is shown in Figure A.8.

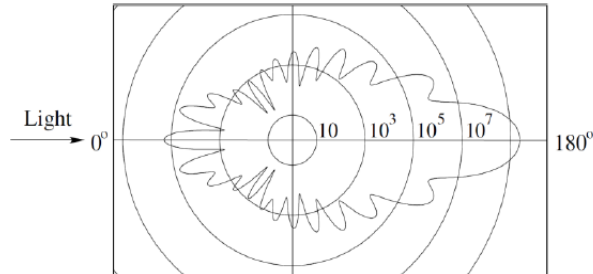


Figure A.8: Distribution of the light intensity scattered by a  $1 \mu\text{m}$  oil droplet particle in air [25]

As could be observed, the intensity of the light scattered towards the camera, can be improved by placing the camera in the so-called forward or backward scattering positions, as the intensity reaches a minimum near the  $90^\circ$  angles. It could be concluded, that a trade-off has to be made for the chosen particle diameter, since it needs to reduce enough to follow the flow accurately, but at the same time, the intensity of the light scattering towards the camera should be sufficient.

### Illumination

For illumination of the tracer particles, lasers are commonly used in Particle Image Velocimetry (PIV). This is because they emit monochromatic light with a high energy density, which can be easily bundled into thin light sheets. During the measurement, the tracer particles are illuminated twice by a laser sheet produced by two laser pulses. These pulses need to have a very short duration to avoid the appearance of particle streaks on the camera. As a laser pulse leaves the laser head, it passes through a set of lenses and is deflected by mirrors before a thin light sheet is eventually obtained at the measurement location. The light intensity of this sheet needs to be sufficient for the tracer particles to be detected by the camera. The typical arrangement of the lenses is a cylindrical lens, which expands the laser beam, followed by one or more spherical lenses that converge the laser beam, such that a thin laser sheet results.

### Particle imaging

The image of the tracer particles in the light sheet is focused on an image sensor of the camera, the imaging plane, by using a photographic lens. The imaging system, which is usually a Charge Couple Device (CCD) or a Complementary Metal Oxide Semiconductor (CMOS) camera, is characterized by its focal length,  $f$ , aperture number,  $f_\#$  and the image magnification,  $M$ . The aperture number,  $f_\#$  is defined as  $f/D$ , where  $D$ , is the aperture diameter. The image magnification is defined as:

$$M = \frac{d_i}{d_o} \quad (\text{A.2})$$

where  $d_i$ , is the image distance and  $d_o$ , the object distance. The magnification factor can also be expressed as the ratio between the sensor size and the field of view (FOV). The focal length, image and object distance are related through the lens equation.

$$\frac{1}{f} = \frac{1}{d_i} + \frac{1}{d_o} \quad (\text{A.3})$$

The applied aperture lenses are finite and therefore diffraction limited, which means that point sources will appear as Airy disks and rings on the image sensor. The size of such a disk  $d_{diff}$ , can be approximated by:

$$d_{diff} = 2.44 \cdot f_{\#} \cdot \lambda \cdot (M + 1) \quad (\text{A.4})$$

Then the minimal image particle diameter, as observed on the image sensor, is determined by:

$$d_{\tau} = \sqrt{(Md_p)^2 + (d_{diff})^2} \quad (\text{A.5})$$

For small particles of  $d_p \leq 1$ , this minimal image particle diameter is typically dominated by the diffraction limit,  $d_{diff}$ , although  $d_{diff}$  can be controlled to some extent with the aperture number,  $f_{\#}$ . Finally, the depth of the field,  $\delta_z$ , can be approximated by:

$$\delta_z = 2 \cdot f_{\#} \cdot d_{diff} \cdot (M + 1)/M^2 \quad (\text{A.6})$$

A significantly large aperture diameter is required to achieve sufficient light from all of the particles, and also to decrease the size of the diffraction pattern. However, a big aperture diameter decreases the depth of field, which is needed to have all the illuminated particles within the laser sheet in focus.

To accurately determine the velocity vectors from PIV measurements a proper choice of the seeding density and pulse separation is required. In order to achieve an error in the particle displacement of 1-2%, the pulse separation time has to be chosen, such that the particle displacement is approximately 10 pixels. Obtaining this pixel shift, will result in a high number of particle pairs, meaning the majority of the images particles are located in the same window during both exposures. Thereby the particle displacement can be determined accurately from the correlation peak. Considerably smaller displacements may be too small to correctly establish the velocity vectors and with larger displacements too many particles will have moved out of the window.

As far as the seeding is concerned, the distribution should be uniform. Furthermore, according to Scarano [28], there should be at least 10 tracer particles in an interrogation window. Lower seeding density would result in individual particle tracking, which would probably not be representative for the considered flow field. On the other hand, a very high seeding density would make it difficult to distinguish the individual particles.

### Image analysis

The image analysis yields particle displacement by applying cross-correlation between two subsequent images. However, the particle velocities are not uniform over the entire interrogation region. Hence the region is divided into smaller sub domains, called interrogation windows. The corresponding interrogation windows, at the first time instant  $t$  and second instant  $t + \Delta t$ , are then cross-correlated. After the cross-correlation procedure a cross-correlation map is obtained, where the correlation peak indicates the average particle displacement. This procedure is shown in Figure A.6.

For a distinct peak the signal-to-noise ratio should be high. Too large particle diameter images will increase the noise level, due to mutually overlap of the particle diameter images, thereby decreasing the image contrast, as is presented in Figure A.9(b). In the case the particle diameter image is smaller than one pixel, the particles will be pixel-locked and hence the determined displacement will be biased towards integer values (see Figure A.9(a)). According to [25] the optimal particle image size is around 2 to 2.5 pixels.

Furthermore, large interrogation windows are desired because of the large number of image pairs in each window. However, large windows result in poor spatial resolution. To solve this problem, while maintaining a high signal-to-noise ratio, a multi-pass iteration procedure can be applied, which repeats the correlation process for different window sizes. First the local average displacement is determined with a large window size, thereby providing an initial guess of the displacement vector, which can be used as an offset for the correlation windows in the second step. In this next iteration step smaller windows sizes can then be applied without losing the correlation peak.

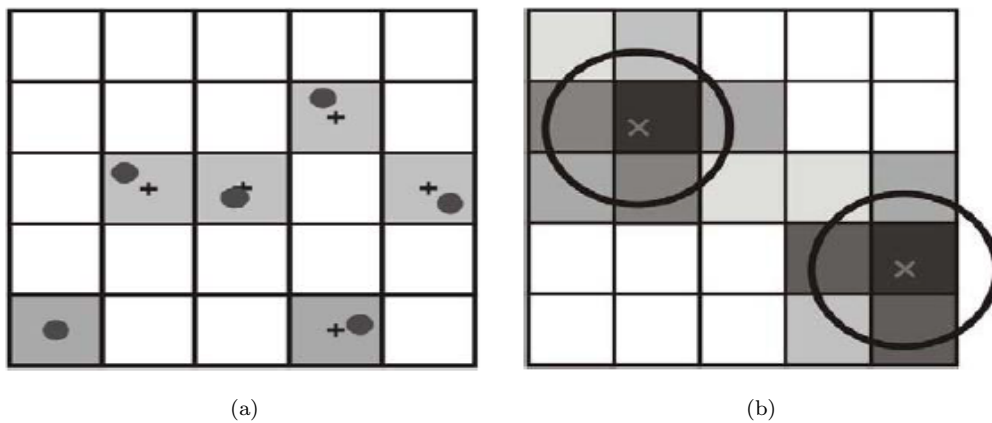


Figure A.9: Effect of particle image diameter for windowing. (a) Pixel locking and (b) too large particle diameter images [28]

The quality of the cross-correlation can be further improved by enhancing the image quality. This can be accomplished by applying pre-processing procedures to raw images. A commonly used pre-processing operation is subtraction of the minimum of each pixel to remove spurious light, due to for example reflections. Moreover, operations such as multiplying by a constant and division by the average, are applied for normalization. Also, many post-processing procedures can be applied to further enhance the vector field. For an overview of these operations the interested reader is referred to M.Raffel et.al. [25].

### A.3.2 PIV instrumentation

The PIV instrumentation used is discussed in four parts: laser, seeding production, CCD camera and the PIV acquisition system and software [28].

#### Seeding generator

The SAFEX fog generator produces a non-toxic water-glycol based fog from the SAFEX normal power mix fluid. The droplet size distribution in the fog is shown in Figure A.10. The mean diameter is 1  $\mu\text{m}$ . The fog machine is activated simply by switching it on, then it needs to warm up for about 5 minutes before it can produce smoke (until the green control lamp READY goes on and the control lamp HEATING goes off for the first time). The seeding production level is set from a remote control unit. In order to have stable seeding conditions the knob on the remote control unit should be set at the third tick with the lower button on 10%.

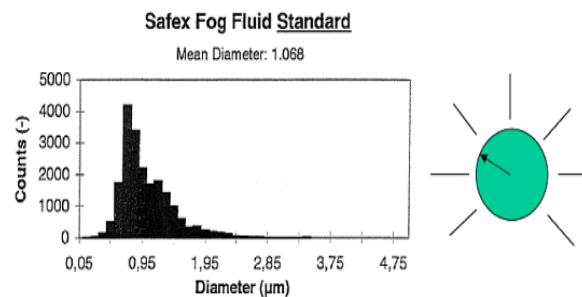


Figure A.10: Droplet size distribution (left) [taken from the SAFEX fog generator users guide]. Seeding knob position (right) [28]

The position of the seeding generator is shown in Figure A.11. This was decided to be behind the test-section, through a small opening of the tunnel, in order for the seeding particles to circulate around the wind-tunnel and "meet" the configuration, without any disturbance.

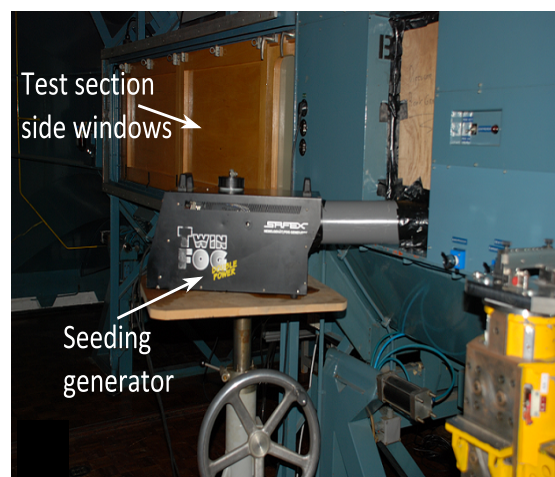


Figure A.11: Actual (3D) seeding generator image and its position with respect to wind-tunnel test section

## Laser

For the PIV experiments the Quantel Evergreen laser is used as light source, Figure A.12. The laser system is a double pulsed Nd:YAG laser consisting of two cavities producing infrared light of a wavelength at 1064 nm. A second harmonic generator halves the wavelength to 532 nm (visible green). At maximum power the energy in each laser pulse is 200 mJ. The laser light is hazardous at any power to eye and at high power ( $> 80\%$ ) to skin (class IV lasers).

Therefore some safety requirements for operating this system are needed, which are found in the appendix and are essential for you to read and understand them before coming to the Lab. The pulse energy is controlled by a PC through the LaVision software DAVIS. The pulse duration is 8 ns and the maximum repetition rate is 30 Hz for each pulse. At the laser exit the beam diameter is 7 mm. The flashing of the laser is controlled from Davis 7.2 software, where it is possible to set the repetition rate and the time separation between the two laser pulses. This information is sent from the computer to the digital delay control unit (PTU, programmable time unit), which produces the triggering signals for the laser and the CCD camera.

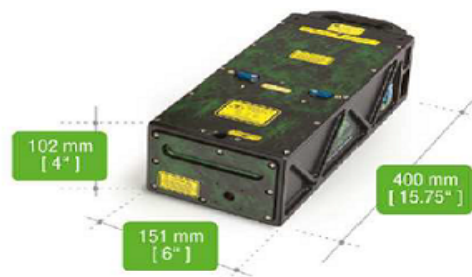


Figure A.12: Quantel Evergreen laser head [28]

## CCD Camera

The PIV images are recorded with a LaVision Imager Intense CCD camera (Figure A.13). The CCD consists of 1376 x 1040 pixel with 6.45 mm pixel pitch and can record 12-bit black and white images. In double shutter mode, which is used in double frame PIV, the maximum recording rate is 5.0 Hz (200 ms separation time between image pairs), so that only one out of three laser pulses can be used. In the presented set-up the CCD camera is limiting factor for the measurement frequency.

Like for the laser the camera is controlled by Davis 7.2 software. The camera exposure is such that the first exposure (frame A) has a duration of 10 ms and the second exposure (frame B) lasts about 100 ms. Therefore in double shutter mode frame A collects much less light from the ambient with respect to frame B. This effect causes more intense background light in frame B, which result in less accurate particle image recordings hence velocity measurement. A daylight filter is mounted on the objective, which only transmits light in a narrow band around the laser wavelength, which largely reduces the effect of background light due to ambient light. The camera settings are sent to the control box, which produces the triggering signals for the CCD camera and collects the recordings from the camera. For the imaging of particle onto the CCD sensor a Nikon  $f = 50$  mm lens is used. On the objective the  $f_{\#}$  can be set from 2.8 to 32.



Figure A.13: LaVision Imager Intense CCD camera [28]

### PIV software

For image acquisition and first analysis Davis 7.2 is used. This software exploits the following functions:

1. Illumination and acquisition control (laser and camera settings)
2. Image analysis (FOV analysis, region of interest, cross correlation)
3. Data post processing (velocity vector statistics, mean, rms, vector validation, calculate vorticity, streamlines)
4. Data display and output (plot velocity vectors, contours, tables, copy to clipboard)

The principle of the cross correlation algorithm implemented in the software is an iterative procedure: by cross-correlating corresponding windows of image A and image B, an initial guess of the particle displacement is computed. This is introduced as an offset for the window in frame B (window shifting). The new estimate of the displacement is used as the offset for the next iteration. In the process the interrogation window size is decreased also (multi-grid, which increases resolution while maintaining dynamic range, however the 1/4 rule still applies in the first iteration). Furthermore correlation window deformation is applied after the 1<sup>st</sup> iteration accounting for local deformation of the tracer particle pattern in the correlation window (i.e. inside shear layers) [28].

### A.3.3 PIV set-up

The calibration procedure was performed using a cardboard piece, shaped accordingly, in order to fit on the X-400's flap contour and with a piece of millimetre paper attached on it. Then through Davis, the calibration was carried out, as described step-by-step below:

1. Placing the calibration cardboard piece with the millimetre paper in the right position, on the surface of the Fowler flap's surface, by making sure that it is at the same level with the laser beam
2. Focus the camera and make sure that it is in straight position
3. After that, choose the calibration choice on Davis software and then define the wanted scale and select no image distortion

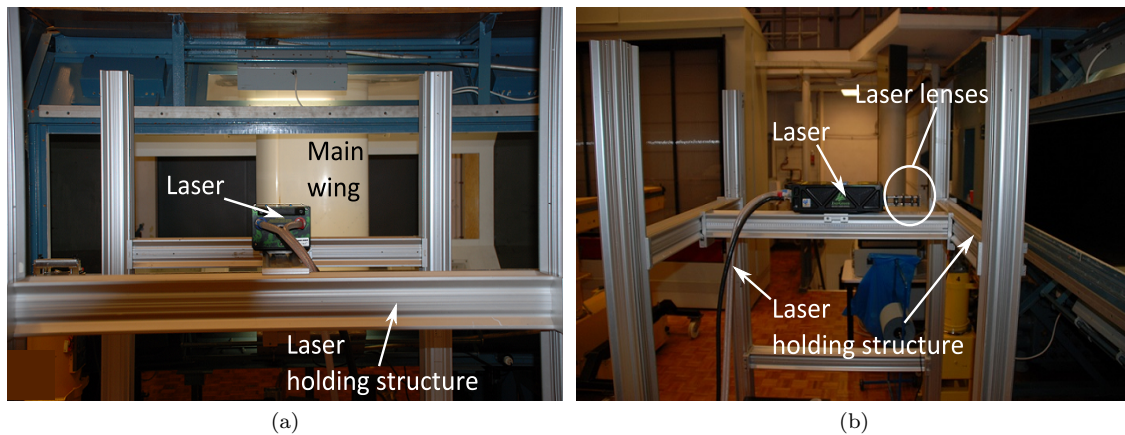


Figure A.14: Laser structure with laser attached on it (a) Back view and (b) Side view

4. Take a picture
5. Scale and put the right number of millimetres
6. End of Calibration procedure

From Figure A.15, the real calibration and the post-processed image from Davis are shown for CWC case. It is clear from both images, that a small part of the main wing's trailing edge and the Fowler flap are inside the FOV. The gap between these two, is the slot of the configuration. The cove area of the main wing is not captured and of course the flow there is not expected to be visible.

On the right image (b), showing the Davis post-processed picture, a thick black line around the flap and the trailing edge of the main wing is apparent. This line is the reflection caused by the laser beam. This reflection caused the loss of data very close to the surface. Hence, a small portion of the boundary layer, measured to be approximately 5 mm, is not captured due to this reflection. The red line around the wing-flap configuration represents the mask defined using the Davis software.

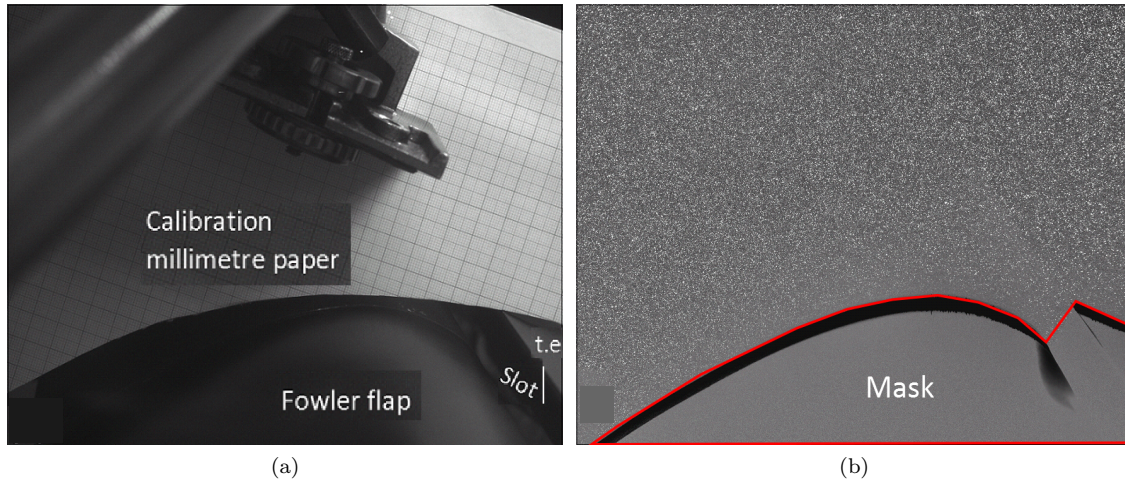


Figure A.15: Calibration image showing millimetre paper above Fowler flap (a) and Post-processed image from Davis software (b) for CWC

Test Case No.	PIV-Davis (Vers. 7.2) software acquisition settings based on test matrix				PIV-Davis (Vers. 8.1) software post-processing settings based on test matrix			
	V <sub>r</sub> Range [m/s]	dt [ $\mu$ s]	Laser Power [%]	Device offset [ $\mu$ s]	No. of Pictures	Windows size and Weight	Overlap [%]	Passes
TC.1	5-10-15-20-25-30-35-40	400-300-150-120-100-80-70-60	90	T <sub>1A</sub> : 0 - T <sub>1B</sub> : 50	500	96 x 96 & 24 x 24 [1:1]	75 & 75	2 & 2
TC.2	5-10-15-20-25-30-35-40	700-300-180-130-100-80-70-60	90	T <sub>1A</sub> : 0 - T <sub>1B</sub> : 50	500	96 x 96 & 24 x 24 [1:1]	75 & 75	2 & 2
TC.3	5-10-15-20-25-30-35-40	650-280-170-120-100-80-70-60	90	T <sub>1A</sub> : 0 - T <sub>1B</sub> : 50	500	96 x 96 & 24 x 24 [1:1]	75 & 75	2 & 2
TC.4	5-10-15-20-25-30-35-40	530-240-150-115-90-75-65-55	90	T <sub>1A</sub> : 0 - T <sub>1B</sub> : 50	500	96 x 96 & 24 x 24 [1:1]	75 & 75	2 & 2
TC.5	5-10-15-20-25-30-35-40	550-280-180-140-115-90-75-65	90	T <sub>1A</sub> : 0 - T <sub>1B</sub> : 50	500	96 x 96 & 24 x 24 [1:1]	75 & 75	2 & 2
TC.6	5-10-15-20-25-30-35-40	600-285-190-140-110-90-80-70	90	T <sub>1A</sub> : 0 - T <sub>1B</sub> : 50	500	96 x 96 & 24 x 24 [1:1]	75 & 75	2 & 2
TC.7	5-10-15-20-25-30-35-40	115-90-75-65-55	90	T <sub>1A</sub> : 0 - T <sub>1B</sub> : 50	500	96 x 96 & 24 x 24 [1:1]	75 & 75	2 & 2
TC.8	5-10-15-20-25-30-35-40	140-115-90-80-70	90	T <sub>1A</sub> : 0 - T <sub>1B</sub> : 50	500	96 x 96 & 24 x 24 [1:1]	75 & 75	2 & 2
TC.9	5-10-15-20-25-30-35-40	140-110-95-80-70	90	T <sub>1A</sub> : 0 - T <sub>1B</sub> : 50	500	96 x 96 & 24 x 24 [1:1]	75 & 75	2 & 2
TC.10	5-10-15-20-25-30-35-40	120-95-80-70-60	90	T <sub>1A</sub> : 0 - T <sub>1B</sub> : 50	500	96 x 96 & 24 x 24 [1:1]	75 & 75	2 & 2
TC.11	5-10-15-20-25-30-35-40	140-110-90-80-70	90	T <sub>1A</sub> : 0 - T <sub>1B</sub> : 50	500	96 x 96 & 24 x 24 [1:1]	75 & 75	2 & 2
TC.12	5-10-15-20-25-30-35-40	140-115-95-80-70	90	T <sub>1A</sub> : 0 - T <sub>1B</sub> : 50	500	96 x 96 & 24 x 24 [1:1]	75 & 75	2 & 2
TC.13	5-10-15-20-25-30-35-40	120-95-80-65-55	90	T <sub>1A</sub> : 0 - T <sub>1B</sub> : 50	500	96 x 96 & 24 x 24 [1:1]	75 & 75	2 & 2
TC.14	5-10-15-20-25-30-35-40	140-110-90-80-70	90	T <sub>1A</sub> : 0 - T <sub>1B</sub> : 50	500	96 x 96 & 24 x 24 [1:1]	75 & 75	2 & 2
TC.15	5-10-15-20-25-30-35-40	140-115-95-80-70	90	T <sub>1A</sub> : 0 - T <sub>1B</sub> : 50	500	96 x 96 & 24 x 24 [1:1]	75 & 75	2 & 2

Table A.1: PIV Davis settings used for acquisition and post-processing procedures

### A.3.4 Tufts and Oil-Flow Visualisation Pictures for DSP1

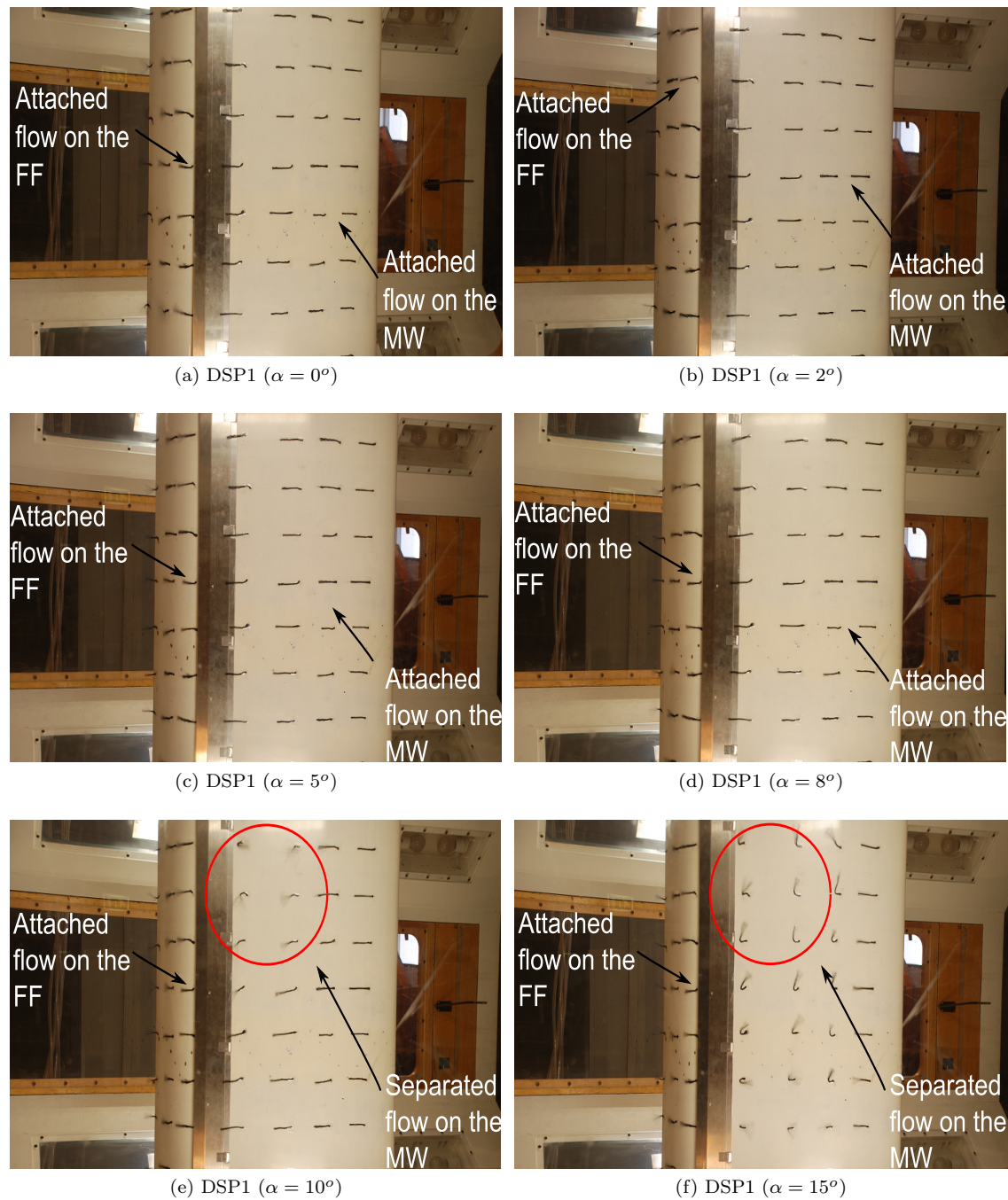


Figure A.16: Tufts flow visualisation with DSP1 at an angle of attack of (a)  $0^\circ$ , (b)  $2^\circ$ , (c)  $5^\circ$ , (d)  $8^\circ$ , (e)  $10^\circ$  and (f)  $15^\circ$  at  $Re = 1.6 \cdot 10^6$  with  $\delta_f = 50^\circ$ ,  $x_{overlap} = 0\%$  and  $y_{gap} = 3.7\%$

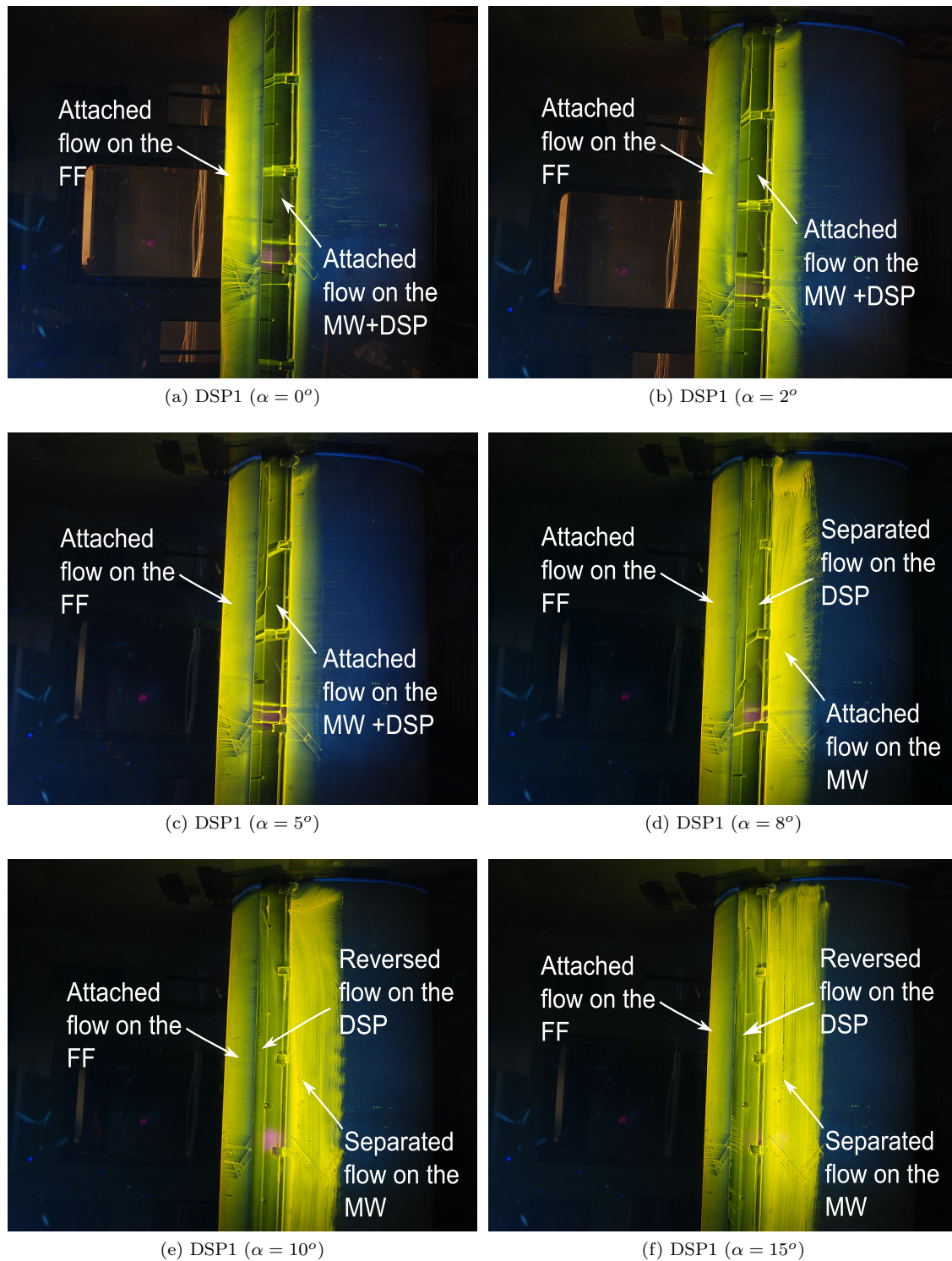


Figure A.17: Oil flow visualisation with DSP1 at an angle of attack of (a)  $0^\circ$ , (b)  $2^\circ$ , (c)  $5^\circ$ , (d)  $8^\circ$ , (e)  $10^\circ$  and (f)  $15^\circ$  at  $Re = 1.6 \cdot 10^6$  with  $\delta_f = 50^\circ$ ,  $x_{overlap} = 0\%$  and  $y_{gap} = 3.7\%$

### A.3.5 Proof for Total Pressure Loss in the Boundary Layer

In subsection 3.4.2, and from total pressure probe measurements, it was clear from the plots in Figures 3.34 and 3.35, that there was a small drop in total pressure from the wall of the wing's surface to the edge of the boundary layer measured. Initially, this looks unexpected and wrong, but using the equations and through a brief proof, it is shown that this small loss makes sense.

To begin with a small general proof will be presented and then this will be related to the first measurement at **point A** at  $\alpha = 0^\circ$ ,  $Re = 1.6 \cdot 10^6$  with  $\delta_f = 50^\circ$ ,  $x_{\text{overlap}} = 0\%$  and  $y_{\text{gap}} = 3.7\%$ . Firstly, a boundary layer formed on a flat plate is presented in Figure A.18, where point 1 is a point taken at the edge of the boundary layer and point 0 represents a point on the surface of the plate. Using these two points the small loss in total pressure across the boundary layer will be proved.

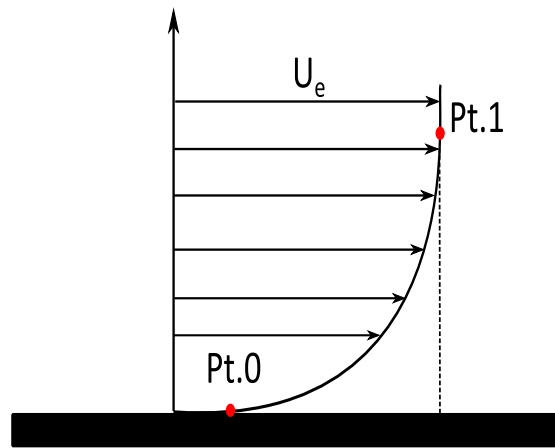


Figure A.18: Boundary layer formation across a flat plate, where **Point 0** is on the surface of the flat plate and **Point 1** on the edge of the boundary layer

Using the equation of total pressure at Point 1 (edge of the boundary layer), one gets:

$$P_{t_1} = P_{s_1} + q_1 \quad (\text{A.7})$$

Where,  $q_1$ , is the dynamic pressure at point 1 and is equal to:

$$q_1 = \frac{1}{2} \cdot \rho \cdot V_1^2 \quad (\text{A.8})$$

To make the total pressure non-dimensional, equation A.7, could be re-written and will be approximately equal to 1

$$R_{P_{t_1}} = \frac{P_{s_1} + q_1}{P_{t_e}} \approx 1 \quad (\text{A.9})$$

Now, using the equation of total pressure at Point (wall of the flat plate), one gets:

$$P_{t_0} = P_{s_0} + q_0 \quad (\text{A.10})$$

Where,  $q_0$ , is the dynamic pressure at point 0 and is equal to 0 as the velocity at the wall is known to be 0 :

$$q_0 = \frac{1}{2} \cdot \rho \cdot V_0^2 = 0 \quad (\text{A.11})$$

Hence, as the dynamic pressure at Point 0,  $q_0$  is 0, one gets:

$$P_{t_0} = P_{s_0} \quad (\text{A.12})$$

However, it is known that the static pressure on the vertical ( $y$ ) axis is equal along the boundary layer, thus:

$$P_{s_0} = P_{s_1} = P_{t_1} - q_1 \quad (\text{A.13})$$

As a result, the non-dimensional form of total pressure at Point 0, could be written as:

$$R_{P_{t_0}} = \frac{P_{t_1} - q_1}{P_{t_e}} = 1 - \frac{q_1}{P_{t_e}} \approx 0.03 - 0.04 \quad (\text{A.14})$$

As a result from this proof, it could be said that that the small loss it total pressure is justified. Moreover, by taking into account the data at Point A on the main wing of the wing-flap configuration, the velocity of the free stream could be found by taking the difference between the points on the surface of the wing to the edge of the boundary layer. The total pressure at the surface of the wing was measured to be  $P_{t_{wall}} = 100,223.24$  Pa. On the other hand, the total pressure on the edge of the boundary layer was measured to be  $P_{t_e} = 102,366.16$  Pa. As a result, using the equations A.7 and A.10 , it would be possible to calculate the velocity at the free stream and determine if it makes sense or not.

$$P_{t_1} - P_{t_0} = P_{s_1} - P_{s_0} + q_1 - q_0 \quad (\text{A.15})$$

$$P_T = q_1 - q_0 \Rightarrow 102,366.16 - 100,233.24 = \frac{1}{2} \cdot 1.225 \cdot (V_1^2 - V_0^2) \quad (\text{A.16})$$

$$2132.82 = \frac{1}{2} \cdot 1.225 \cdot (V_1^2 - V_0^2) \Rightarrow 3482.15 = V_{fs}^2 \quad (\text{A.17})$$

$$V_{fs} \approx 60 \text{ m/s} \quad (\text{A.18})$$

Concluding, this value of 60 m/s in the free stream makes sense as was also noticed from the PIV total velocity fields, which could be found in subsection 3.4.3 of Chapter 3 , where there was an increase in the free-stream velocity value due to the presence of the wind-tunnel walls.

### A.3.6 PIV Additional Results

Concluding, the PIV results for the same cases which presented in the report in subsection 3.4.3 of chapter 3 but at  $\alpha = 6^\circ$  and  $V_t = 40\text{m/s}$  are presented.

#### Test Case (3): Clean Wing Configuration (CWC) at $6^\circ$

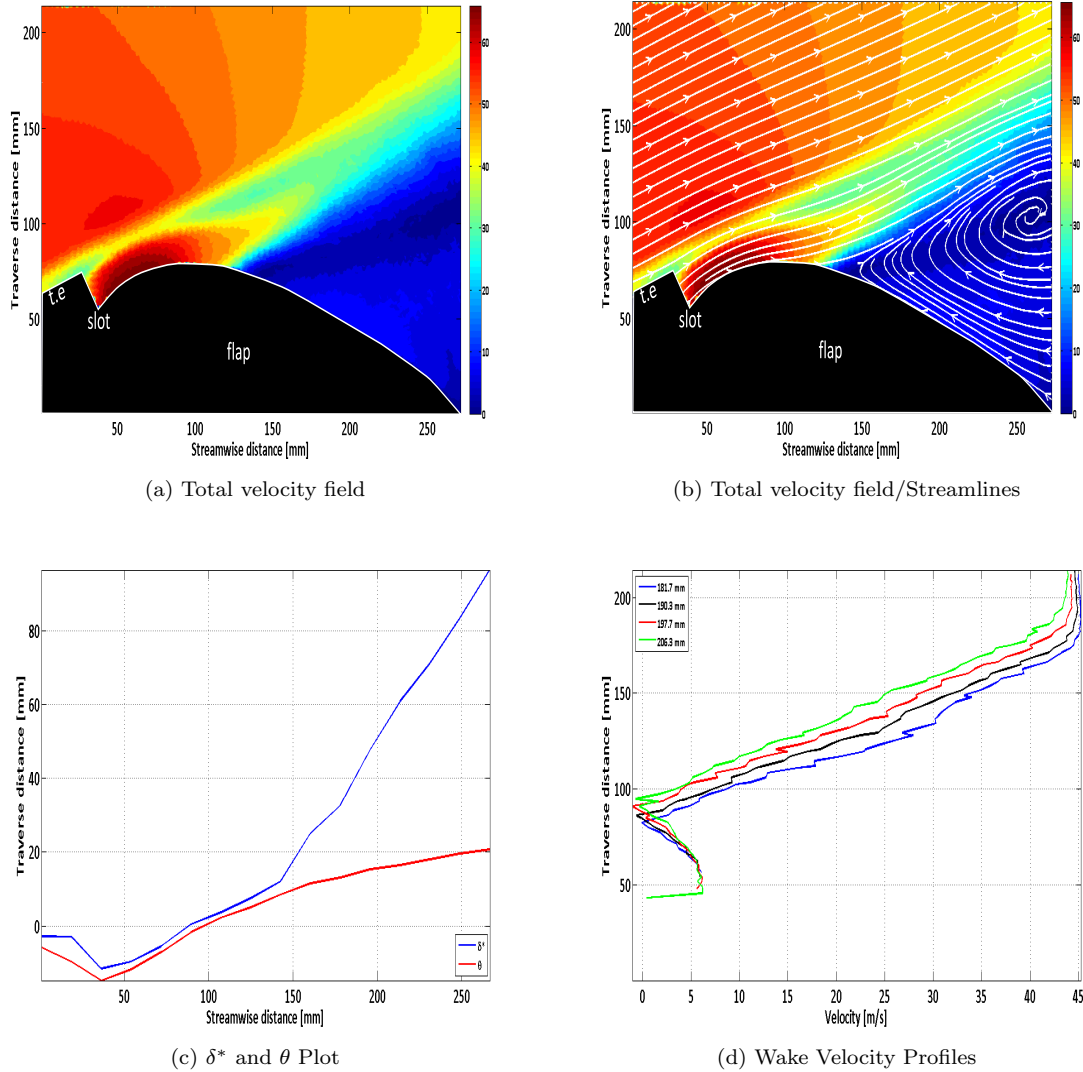


Figure A.19: (a) Total velocity field, (b) Total velocity field with streamlines, (c) Displacement,  $\delta^*$ , and momentum,  $\theta$ , thickness plot and (d) Wake velocity profiles at 4 different stations for CWC at  $\alpha = 6^\circ$  and  $V_t = 40\text{m/s}$

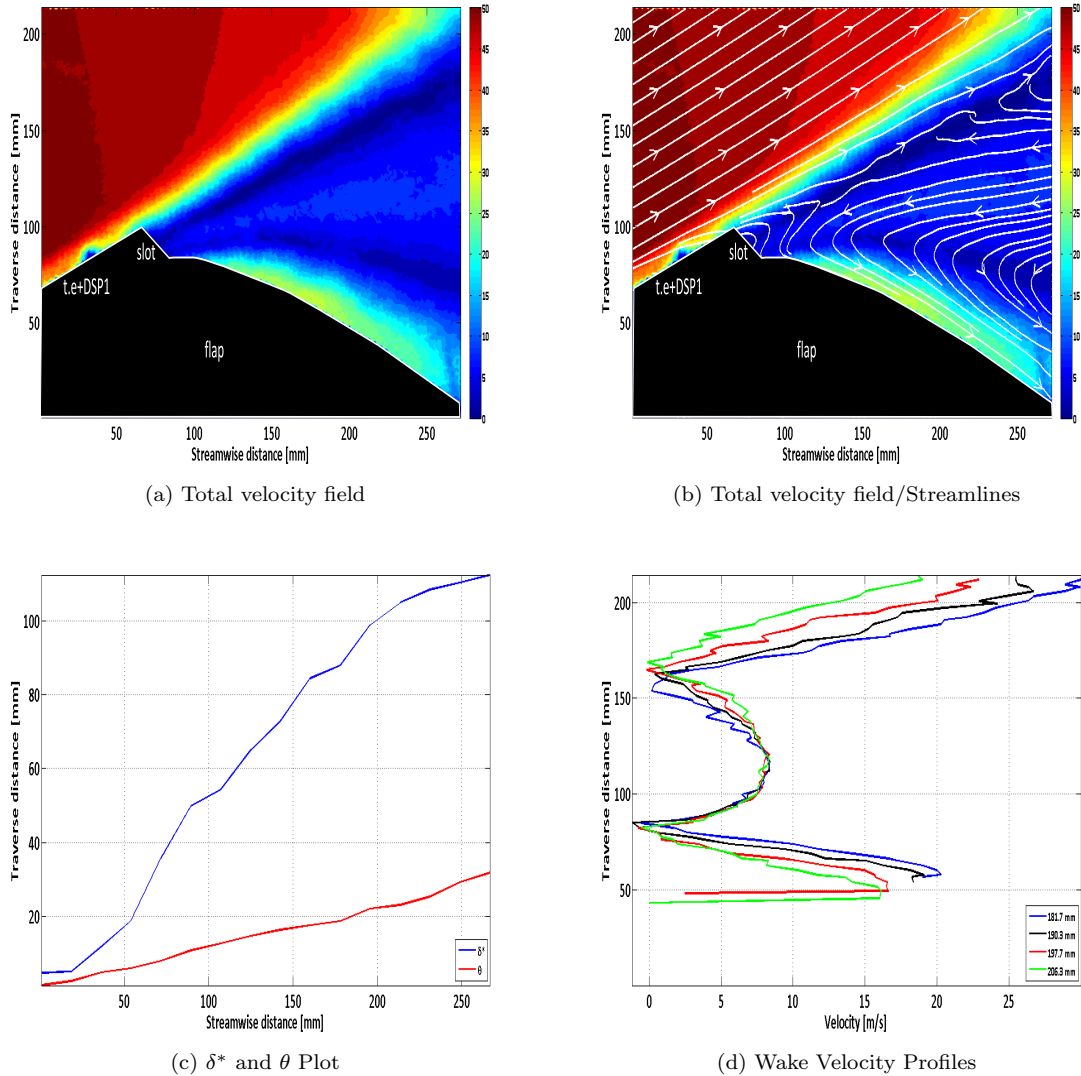
Test Case (5): Drooped Spoiler panel (DSP1) at  $6^\circ$ 

Figure A.20: (a) Total velocity field, (b) Total velocity field with streamlines, (c) Displacement,  $\delta^*$ , and momentum,  $\theta$ , thickness plot and (d) Wake velocity profiles at 4 different stations for DSP1 at  $\alpha = 6^\circ$  and  $V_t = 40\text{m/s}$

Test Case (7): Drooped Spoiler panel (DSP1) with (upper + lower) roughness at  $6^\circ$

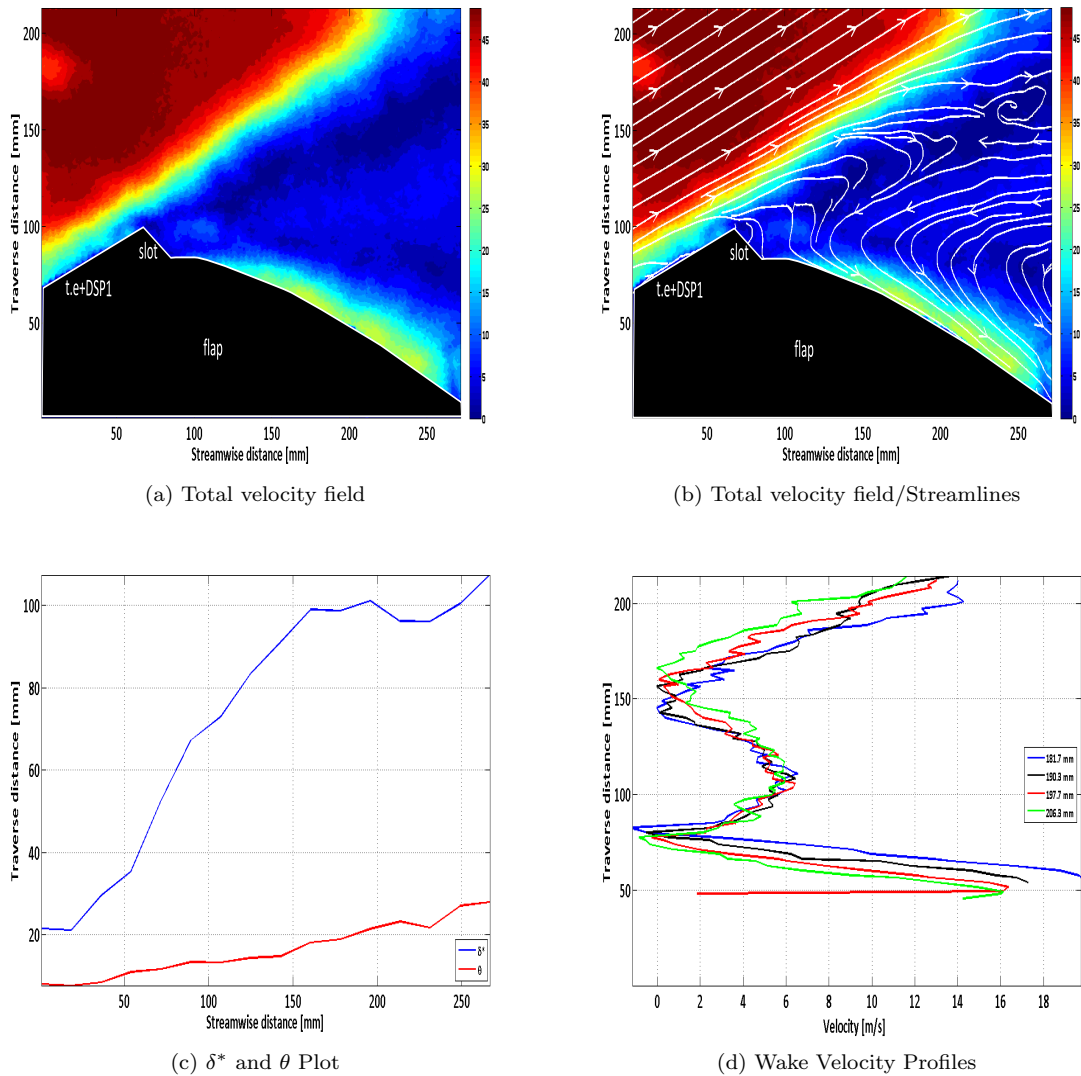


Figure A.21: (a) Total velocity field, (b) Total velocity field with streamlines, (c) Displacement,  $\delta^*$ , and momentum,  $\theta$ , thickness plot and (d) Wake velocity profiles at 4 different stations for DSP1 with upper and lower surface roughness on the main wing at  $\alpha = 6^\circ$  and  $V_c = 40\text{m/s}$

## Appendix B

# Wind-Tunnel Campaign II

Appendix B, contains additional information based on experimental apparatus, set-up, data and further results of the second experimental campaign. Illustrations and schematics are presented to give further insight into several aspects. For more information, one is also referred to Chapter 4 of the report, where all the information of this appendix belongs to.

## B.1 Experimental apparatus and final set-up

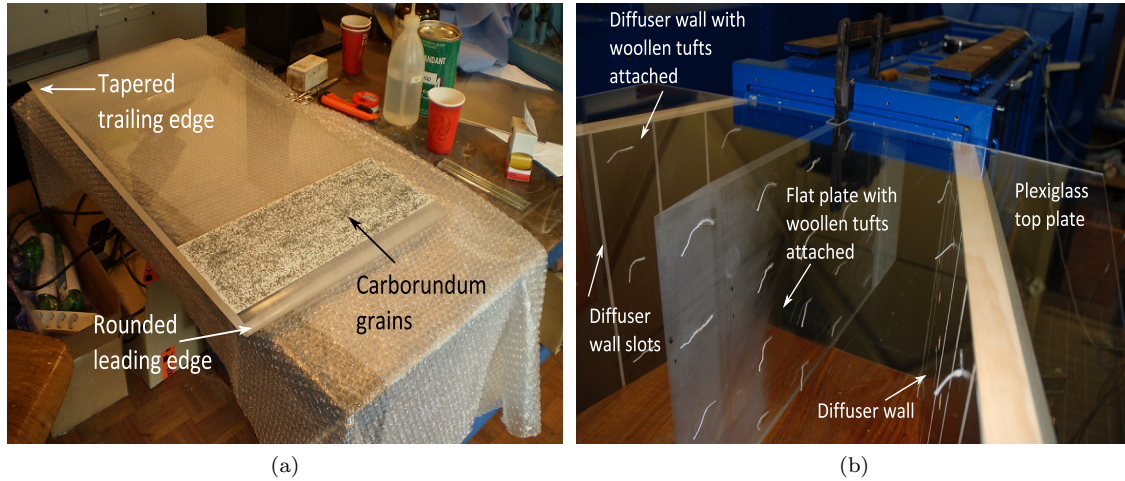


Figure B.1: Plexiglass flat plate (a) during manufacturing process and (b) Plexiglass flat plate's placement in the wind-tunnel-diffuser set-up, including explanations of key features

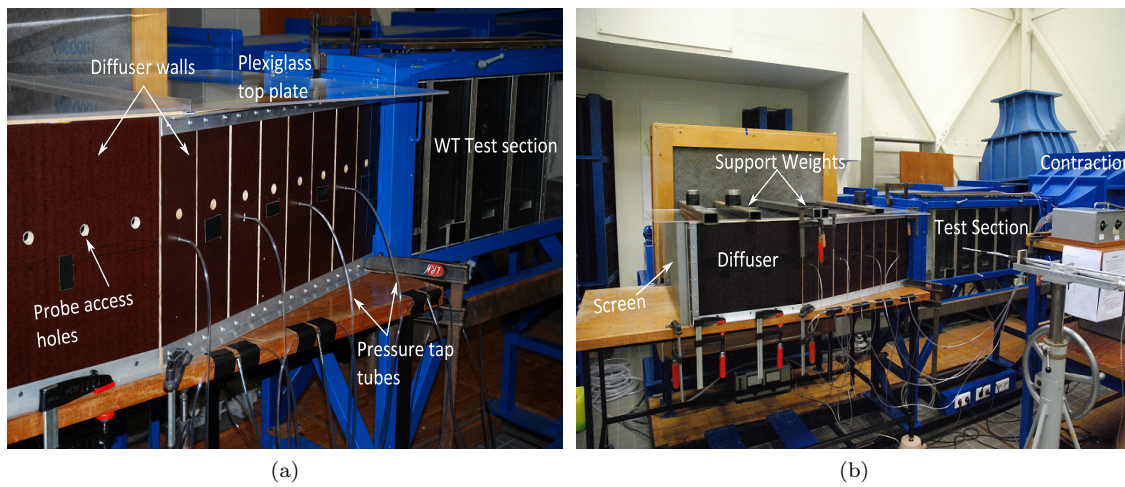


Figure B.2: Diffuser side-view (a) including explanations of various parts and (b) Final diffuser set-up prior to M-tunnel wind-tunnel testing

## B.2 Pressure measurements and PIV set-up

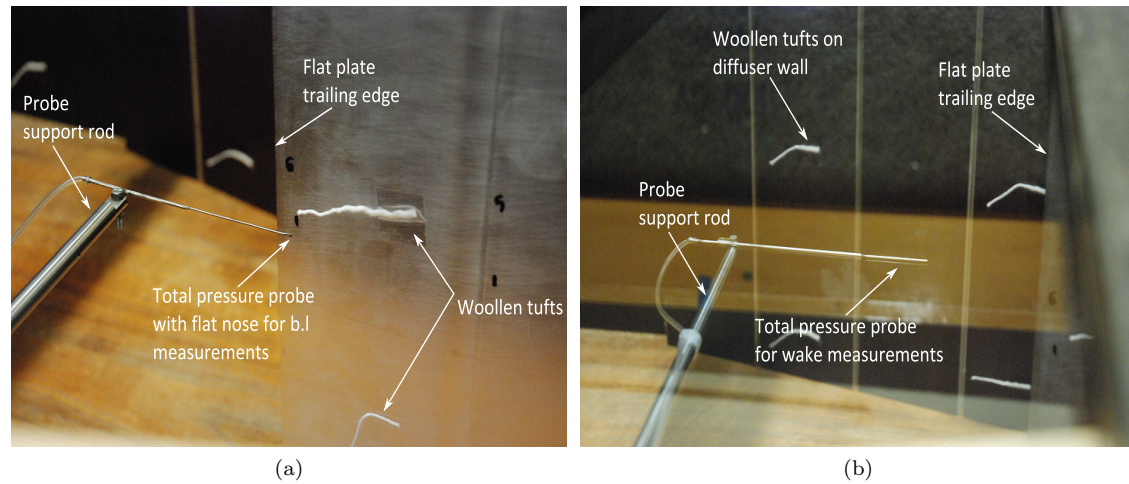


Figure B.3: Total pressure probe with flat nose (a) used for boundary layer measurements on the flat plate's surface and (b) Total pressure probe used for wake measurements behind the trailing edge of the flat plate

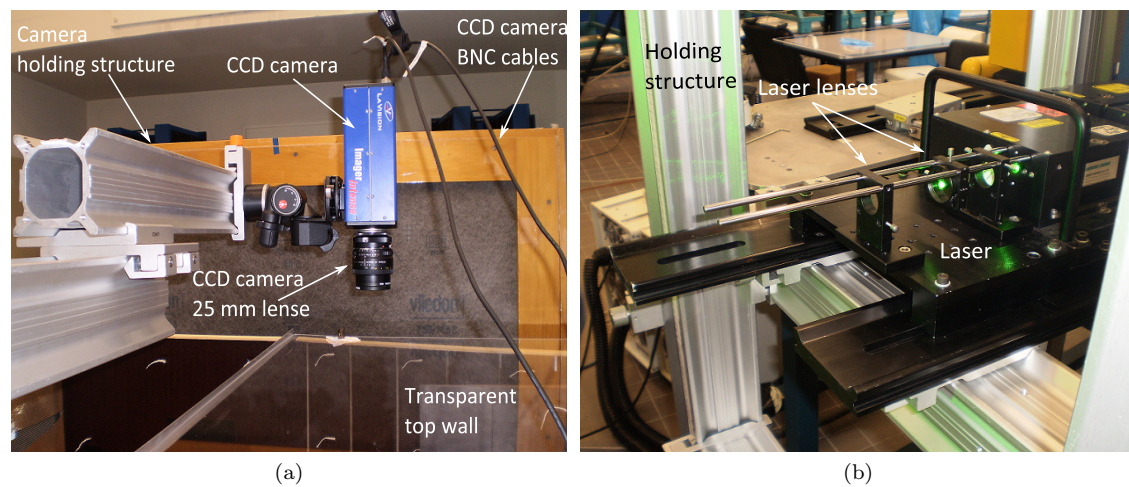


Figure B.4: CCD camera (a) position and holding structure and (b) Laser position with lenses placed in front of it's head as used during PIV experiments

## B.3 Pressure measurements additional information

### B.3.1 Boundary layer measurements

y [mm]	P1 [-495 mm]	P2 [-412 mm]	P3 [-297 mm]	P4 [-193 mm]	P5 [-102 mm]	P6 [-25 mm]
0	0.574	10.875	31.508	51.181	53.803	53.404
1	37.905	19.682	47.814	51.259	54.684	53.749
2	56.195	46.495	53.667	53.774	54.783	53.414
3	65.334	55.066	58.532	56.943	55.673	53.9
4	73.734	62.603	63.587	59.333	56.403	53.232
5	81.442	69.016	67.85	61.465	56.671	53.033
6	89.659	75.968	72.519	63.833	58.205	6 53.205
7	97.631	81.969	77.329	66.408	57.679	7 52.255
8	105.564	88.626	81.814	69.441	59.799	8 53.201
9	113.299	94.868	87.422	72.111	60.791	9 52.553
10	120.505	101.413	91.955	75.058	62.343	52.925
11	126.594	107.341	96.706	78.086	64.091	52.789
12	130.696	112.489	101.398	81.414	66.12	54.01
13	133.647	118.782	105.949	84.473	67.663	52.865
14	135.438	123.536	109.974	88.519	68.83	55.01
15	136.002	127.274	114.749	91.743	71.322	53.137
16	135.768	130.675	118.499	95.173	72.078	53.306
17	136.145	132.533	122.25	98.83	73.706	54.18
18	136.213	134.035	125.871	102.381	76.35	53.838
19	135.969	134.986	128.686	105.99	78.972	54.261
20	136.1	135.374	131.122	109.738	81.208	55.038
21	136.127	135.233	132.784	113.115	83.594	54.15
22	136.158	135.447	134.182	116.009	85.902	54.817
23	136.134	135.741	134.525	118.592	87.597	53.763
24	136.523	135.474	135.029	122.25	89.632	56.236
25	136.487	135.461	135.277	124.974	92.471	57.186
26	136.308	135.631	135.482	127.534	95.286	56.153
27	136.737	135.597	135.26	130.142	97.143	58.701
28	136.445	135.462	135.678	131.83	99.471	61.888
29	136.594	135.94	135.575	132.949	103.033	58.376
30	136.36	136.068	135.469	134.15	106.817	60.502
31	136.535	136.118	135.666	134.971	109.351	63.437
32	136.643	135.896	135.507	135.548	113.065	63.609
33	136.267	135.992	135.814	135.841	115.697	68.284
34	136.147	135.969	135.729	136.213	117.776	65.691
35	136.344	135.6	135.43	136.337	120.323	67.992
36	136.35	135.85	135.836	136.31	122.944	67.062
37	136.404	135.698	136.101	136.664	124.123	68.328
38	136.478	136.006	135.94	136.233	126.982	72.439
39	136.339	135.785	136.381	136.304	128.97	72.944
40	136.101	135.836	135.915	136.814	130.529	73.671
41	136.476	135.887	135.974	136.401	132.258	80.469
42	136.144	135.649	136.058	136.528	132.993	78.989
43	136.16	135.725	136.024	136.343	133.663	82.142
44	136.488	135.985	135.736	136.586 0	134.015	80.795
45	136.04	135.826	135.77	136.675	134.285	85.874
46	136.317	135.918	135.8	136.611	134.293	86.032
47	135.916	135.969	135.631	136.554	134.837	89.796
48	136.04	135.53	135.554	136.692	134.786	90.404
49	135.962	135.794	135.816	136.898	135.211	87.495
50	136.084	135.388	136.029	136.746	135.108	94.316
51	-	-	-	-	-	101.044
52	-	-	-	-	-	101.047
54	-	-	-	-	-	98.207
55	-	-	-	-	-	105.749
56	-	-	-	-	-	112.197
57	-	-	-	-	-	110.063
58	-	-	-	-	-	112.226
59	-	-	-	-	-	115.27
60	-	-	-	-	-	118.887
61	-	-	-	-	-	116.912
62	-	-	-	-	-	122.303
63	-	-	-	-	-	123.51
64	-	-	-	-	-	127.222
65	-	-	-	-	-	126.695
66	-	-	-	-	-	129.421
67	-	-	-	-	-	129.598
68	-	-	-	-	-	131.041
69	-	-	-	-	-	132.037
70	-	-	-	-	-	132.511

Table B.1: Boundary layer total pressure measurement data for all points

### B.3.2 Wake measurements

y [mm]	P0 [30 mm]	P1 [100 mm]	P2 [132 mm]	P3 [222 mm]	P4 [265 mm]	P5 [320 mm]	P6 [425 mm]	P7 [520 mm]	P8 [639 mm]
100	304.171	277.56	180.123	177.779	147.291	173.831	147.617	153.953	175.298
95	299.54	255.404	178.355	166.257	142.824	165.911	142.274	146.855	171.917
90	298.43	245.023	173.943	167.815	134.06	164.766	139.49	148.13	167.305
85	289.958	222.756	151.995	168.671	131.198	155.584	135.846	142.946	162.627
80	272.35	198.761	143.185	168.651	122.499	150.003	133.402	140.855	161.865
75	256.331	155.476	135.341	168.169	126.868	137.475	134.118	140.078	160.729
70	184.291	134.184	130.827	167.477	122.776	138.805	138.303	140.057	159.624
65	167.91	142.813	120.767	168.911	122.001	141.025	130.493	138.696	157.546
60	162.48	132.929	120.049	169.477	122.212	133.243	133.858	134.599	155.702
55	146.899	136.127	114.832	168.606	120.333	128.792	134.415	138.152	154.792
50	138.33	131.4	114.755	169.838	119.084	128.119	127.353	133.882	148.952
45	126.754	138.122	116.386	168.657	121.125	127.784	129.449	138.789	149.309
40	134.939	130.683	113.102	168.093	121.539	125.463	132.093	137.422	146.797
35	125.807	129.15	118.678	167.718	119.864	121.85	128.539	136	148.056
30	119.855	126.127	114.552	168.472	119.808	121.124	132.448	141.201	147.518
25	128.637	124.156	114.04	168.486	121.288	118.677	132.959	139.68	149.054
20	121.525	128.944	114.13	165.946	121.015	120.751	132.792	136.619	144.562
15	123.875	122.867	117.46	168.477	120.698	122.064	133.523	139.548	149.054
10	119.799	126.144	118.159	166.891	121.029	120.769	131.68	140.691	149.262
5	118.773	120.82	116.269	167.247	121.853	120.12	130.286	138.944	149.947
0	119.697	121.971	116.814	168.549	121.849	120.532	133.63	139.626	147.635
-5	121.076	123.076	117.235	166.928	120.412	119.957	128.819	139.225	147.84
-10	118.689	125.284	115.94	166.192	119.202	121.284	132.728	136.987	150.638
-15	120.085	121.195	115.114	165.674	121.87	119.597	130.611	136.446	148.49
-20	118.615	121.219	115.605	167.523	119.781	120.511	128.686	135.066	147.194
-25	120.177	121.88	115.021	168.509	120.555	121.178	129.846	136.846	146.742
-30	123.186	122.809	114.696	168.289	118.296	119.094	131.194	136.115	148.674
-35	121.297	125.174	114.337	167.396	118.994	122.791	131.885	134.767	150.446
-40	131.933	121.252	114.732	168.911	120.067	123.008	131.826	141.049	149.928
-45	136.722	126.829	117.632	169.061	121.545	121.734	129.035	139.214	143.977
-50	141.543	124.492	115.578	168.27	125.715	122.774	131.727	137.746	148.613
-55	148.855	131.013	114.383	169.416	122.965	123.052	129.662	136.173	153.126
-60	180.412	134.644	123.157	168.484	119.684	122.838	130.511	143.346	152.795
-65	218.909	144.295	122.004	169.263	121.928	123.51	131.441	146.48	153.442
-70	232.72	155.25	121.858	169.394	119.593	124.4	131.94	146.538	156.481
-75	241.118	153.598	129.638	167.606	122.123	126.771	135.961	146.084	161.826
-80	280.389	162.926	133.333	169.16	121.546	133.955	136.651	155.126	162.781
-85	289.572	186.188	140.868	168.615	127.049	139.513	137.618	157.889	163.675
-90	299.56	195.998	153.75	168.964	134.126	138.62	140.553	156.291	163.402
-95	298.76	206.33	177.659	169.42	141.42	137.82	140.678	162.065	167.898
-100	305.975	260.827	186.764	176.951	148.719	148.667	146.517	165.424	176.35

Table B.2: Wake total pressure measurement data for all points

### B.3.3 PIV measurements

Test Case No.	PIV-Davis (Vers. 7.2) software acquisition settings based on test matrix					PIV-Davis (Vers. 8.1) software post-processing settings based on test matrix			
	$V_i$ [m/s]	dt [ $\mu$ s]	Laser Power [%]	Device offset [ $\mu$ s]	No. of Pictures	Windows size and Weight	Overlap [%]	Passes	
TC.1	5.1	200	90	$T1_A : 0 - T1_B : 50$	400	$32 \times 32 \& 16 \times 16$ [1:1]	75 & 75	2 & 2	
TC.2	14.1	100	90	$T1_A : 0 - T1_B : 50$	400	$32 \times 32 \& 16 \times 16$ [1:1]	75 & 75	2 & 2	
TC.3	21.0	50	90	$T1_A : 0 - T1_B : 50$	400	$32 \times 32 \& 16 \times 16$ [1:1]	75 & 75	2 & 2	
TC.4	5.1	200	90	$T1_A : 0 - T1_B : 50$	400	$32 \times 32 \& 16 \times 16$ [1:1]	75 & 75	2 & 2	
TC.5	14.1	100	90	$T1_A : 0 - T1_B : 50$	400	$32 \times 32 \& 16 \times 16$ [1:1]	75 & 75	2 & 2	
TC.6	21.0	50	90	$T1_A : 0 - T1_B : 50$	400	$32 \times 32 \& 16 \times 16$ [1:1]	75 & 75	2 & 2	
TC.7	5.1	200	90	$T1_A : 0 - T1_B : 50$	400	$32 \times 32 \& 16 \times 16$ [1:1]	75 & 75	2 & 2	
TC.8	14.1	100	90	$T1_A : 0 - T1_B : 50$	400	$32 \times 32 \& 16 \times 16$ [1:1]	75 & 75	2 & 2	
TC.9	21.0	50	90	$T1_A : 0 - T1_B : 50$	400	$32 \times 32 \& 16 \times 16$ [1:1]	75 & 75	2 & 2	

Table B.3: PIV Davis settings used for acquisition and post-processing procedures

## B.4 PIV Additional Results

### B.4.1 Test Case 4: FOV 2- $V_t = 5.1\text{m/s}$

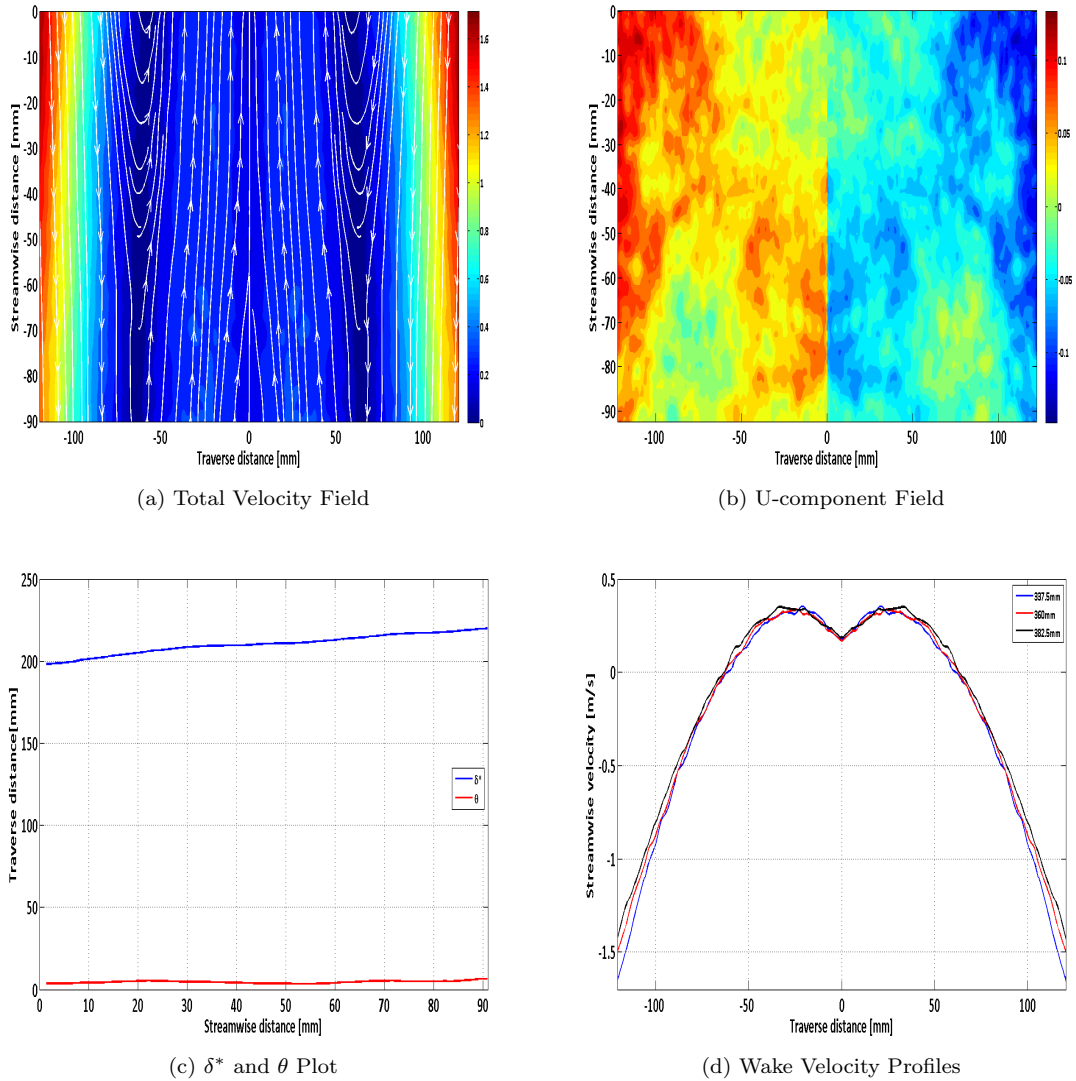


Figure B.5: (a) Total velocity field with streamlines, (b) U-component velocity field, (c) Displacement and momentum loss thickness and (d) Wake velocity profiles for FOV 2 and  $V_t = 5.1\text{m/s}$

### B.4.2 Test Case 5: FOV 2- $V_t = 14.1\text{m/s}$

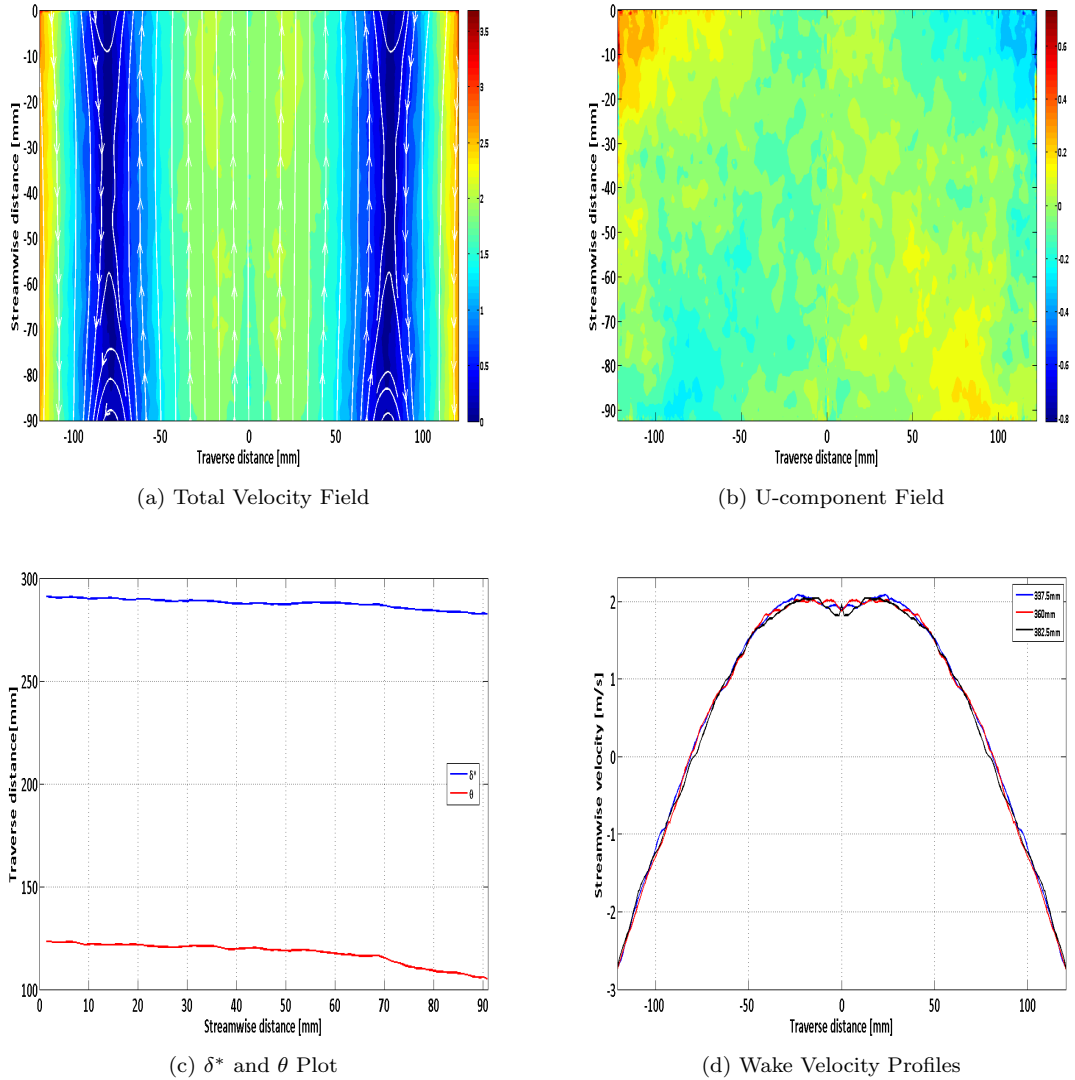


Figure B.6: (a) Total velocity field with streamlines, (b) U-component velocity field, (c) Displacement and Momentum loss thickness and (d) Wake velocity profiles for FOV 2 and  $V_t = 14.1\text{m/s}$

### B.4.3 Test Case 6: FOV 2- $V_t = 21.0\text{m/s}$

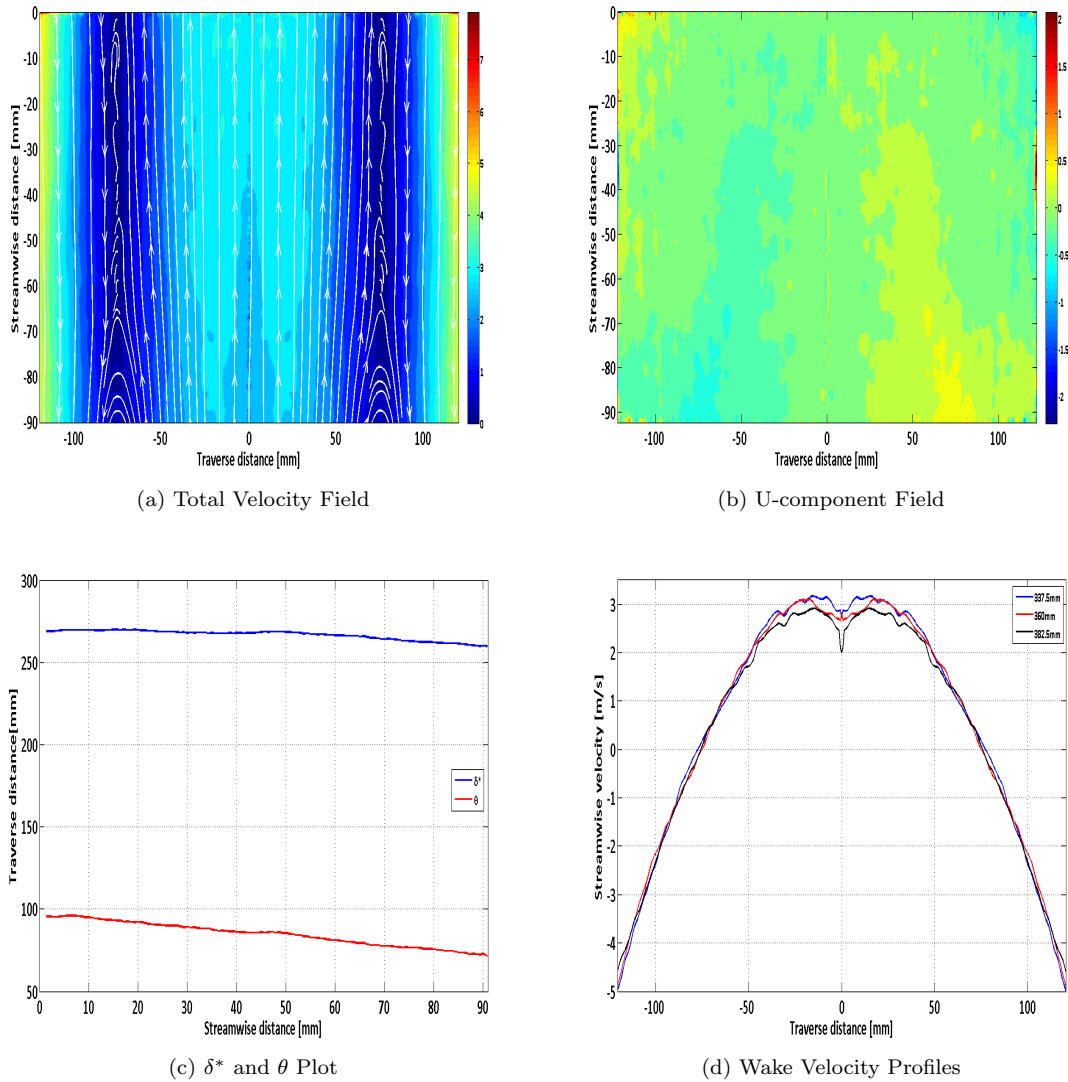


Figure B.7: (a) Total velocity field with streamlines, (b) U-component velocity field, (c) Displacement and Momentum loss thickness and (d) Wake velocity profiles for FOV 2 and  $V_t = 21.0\text{m/s}$

**B.4.4 Test Case 7: FOV 3- $V_t = 5.1\text{m/s}$**

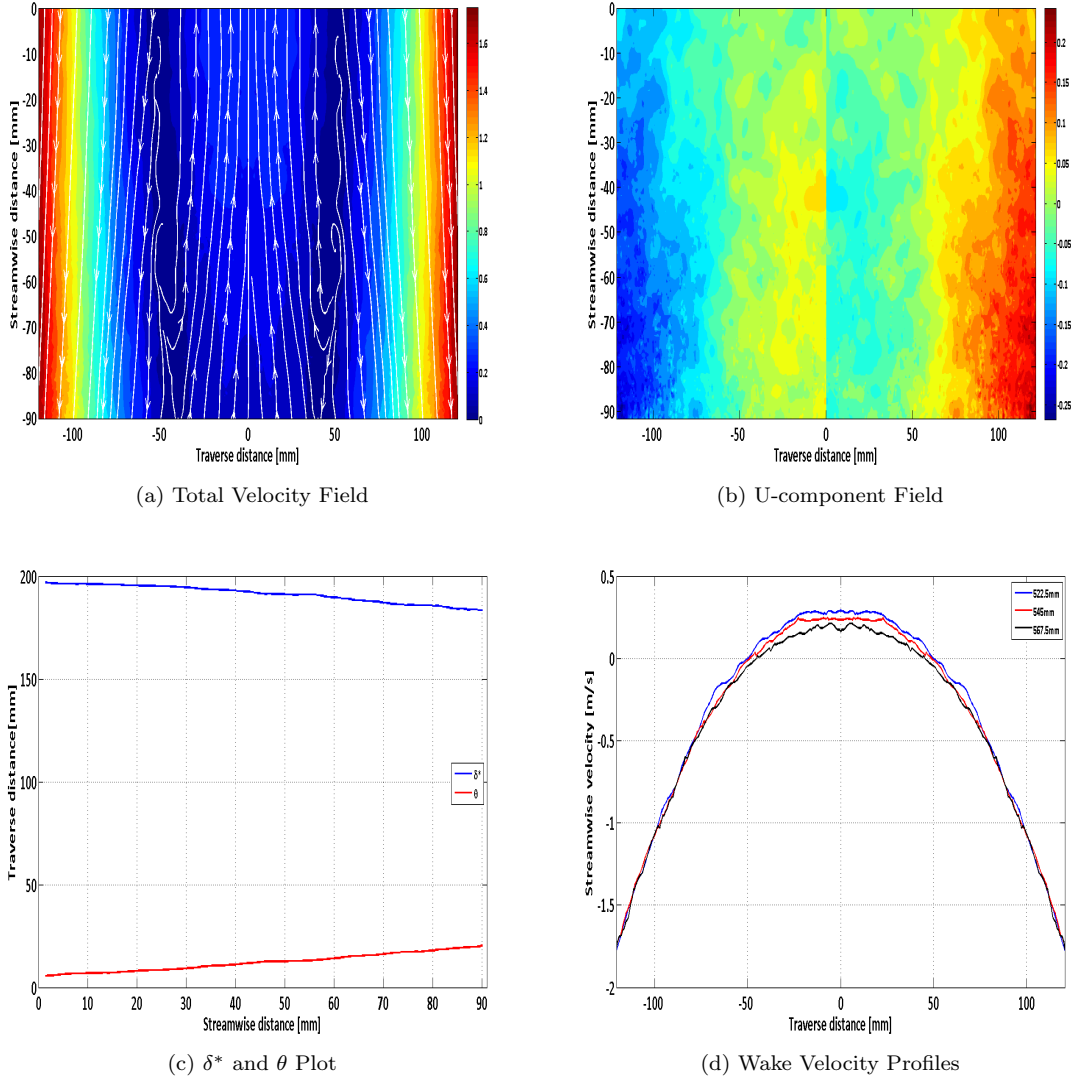


Figure B.8: (a) Total velocity field with streamlines, (b) U-component velocity field, (c) Displacement and Momentum loss thickness and (d) Wake velocity profiles for FOV 3 and  $V_t = 5.1\text{m/s}$

### B.4.5 Test Case 8: FOV 3- $V_t = 14.1\text{m/s}$

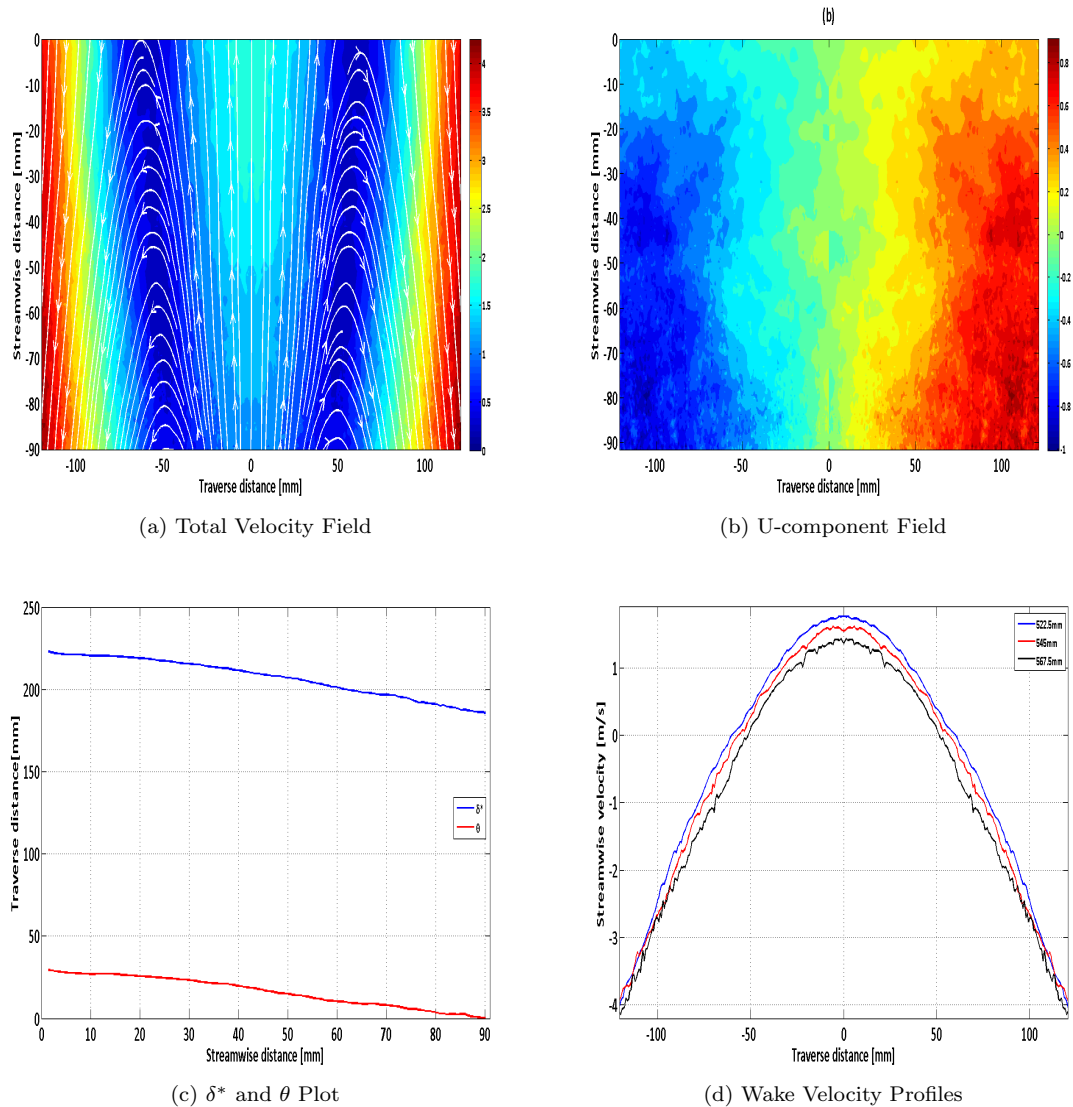


Figure B.9: (a) Total velocity field with streamlines, (b) U-component velocity field, (c) Displacement and Momentum loss thickness and (d) Wake velocity profiles for FOV 3 and  $V_t = 14.1\text{m/s}$

### B.4.6 Test Case 9: FOV 3- $V_t = 21.0\text{m/s}$

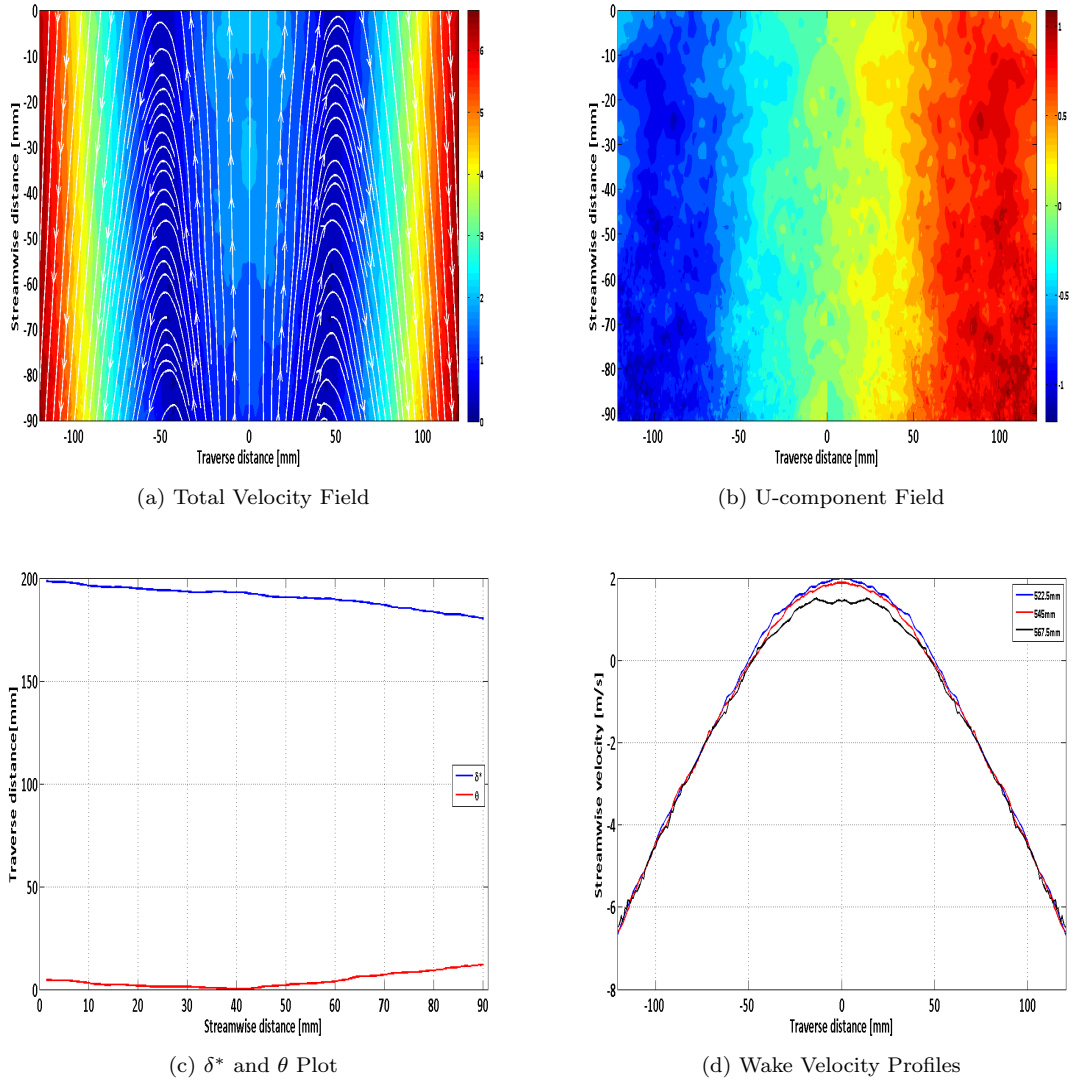


Figure B.10: (a) Total velocity field with streamlines, (b) U-component velocity field, (c) Displacement and Momentum loss thickness and (d) Wake velocity profiles for FOV 3 and  $V_t = 21.0\text{m/s}$

## Appendix C

# MSES Additional Information

Appendix C, contains additional information based on computational settings, format and further results of the MSES simulations. Data and figures are presented to give further insight into several aspects. For more information, one is also referred to Chapter 5 of the report, where all the information of this appendix belongs to.

## C.1 Standard input format

This section discusses and shows the format of the two input files required to run MSES i.e. **blade.xxx** and **msec.xxx**. The **blade.xxx** file is used by the initialization program **MSET** and by the airfoil manipulating program **AIRSET**.

```

NAME
XINL  XOUT  YBOT  YTOP
X(1,1) Y(1,1)
X(2,1) Y(2,1)
X(3,1) Y(3,1)
.      .
.      .
X(I,1) Y(I,1)
999.0  999.0
X(1,2) Y(1,2)
X(2,2) Y(2,2)
X(3,2) Y(3,2)
.      .
.      .
X(I,2) Y(I,2)
999.0  999.0
X(1,3) Y(1,3)
X(2,3) Y(2,3)
X(3,3) Y(3,3)
.      .
.      .

```

The **blade.xxx** file has the following structure:

where,

XINL is the X-location of the left grid inlet plane, in the same coordinate system as the airfoil coordinates.

XOUT is the X-location of the right grid outlet plane.

YBOT is the Y-location of the lowest grid streamline. It is also the location of the bottom wall in solid-wall cases.

YTOP is the Y-location of the topmost grid streamline. It is also the location of the top wall in solid-wall cases.

For a unit airfoil located between  $(x,y) = (0,0)$  and  $(1,0)$ , the recommended minimum values for the four grid-boundary locations are:

```
XINL  XOUT  YBOT  YTOP  :  -1.75  2.75  -2.0  2.5
```

X(1,1), Y(1,1) through to X(IL), Y(IL) are the coordinates of each airfoil element surface, starting at the trailing edge, going round the leading edge in either direction, then going back

to the trailing edge. The individual elements are separated by a "999.0 999.0" line as indicated above and are ordered from top to bottom e.g. for a three element airfoil the sequence is slat, main element and flap.

The format of the **mSES.xxx** file which serves as an input file for **MSES** and **MSIS** (not discussed in this work but also for **MPOLAR** and **MPOLIS**) is shown below. The meaning of the parameters can be found in the MSES User's Guide [7]. Parameters between brackets are optional.

```

GVAR(1)  GVAR(2)  ...          GVAR(N)
GCON(1)  GCON(2)  ...          GCON(N)
MACHIN   CLIFIN   ALFAIN
ISMOM    IFFBC    [DOUXIN   DOUYIN   SRCEIN]
REYIN    ACRIT    [KTRTYP]
XTRS1    XTRP1    XTRS2     XTRP2     XTRS3     XTRP3     ...
MCRIT    MUCON
[ISMOVE  ISPRES]
[NMODN   NPOSN]
[ISDELH  XCDELH  PTRHIN   ETAH]

```

## C.2 Input file mses.x400

The input file for the MSES calculations performed in Section 5.4 - **mSES.x400** - is shown here below. The format of the **mSES.xxx** file can be found in section C.1. For the exact meaning of the numbers used in the input file, one is referred to the MSES user's guide [7].

```

3      4      5      7
3      4      5      7
0.123  0.0    α
3      2
1.7 · E6  9.0
1.0     1.0   1.0   1.0
0.99    1.2
0       0

```

## C.3 Validation of MSES Linux version

The following  $C_p$ -distribution plots, are the results of the MSES Linux version validation study. For this study, numerous single element airfoils used in order to determine the accuracy and validity of the computational results. In this section, the data from simulations for Naca 0012, Naca 4412 and Naca 64210 are presented for various angles of attack simulated.

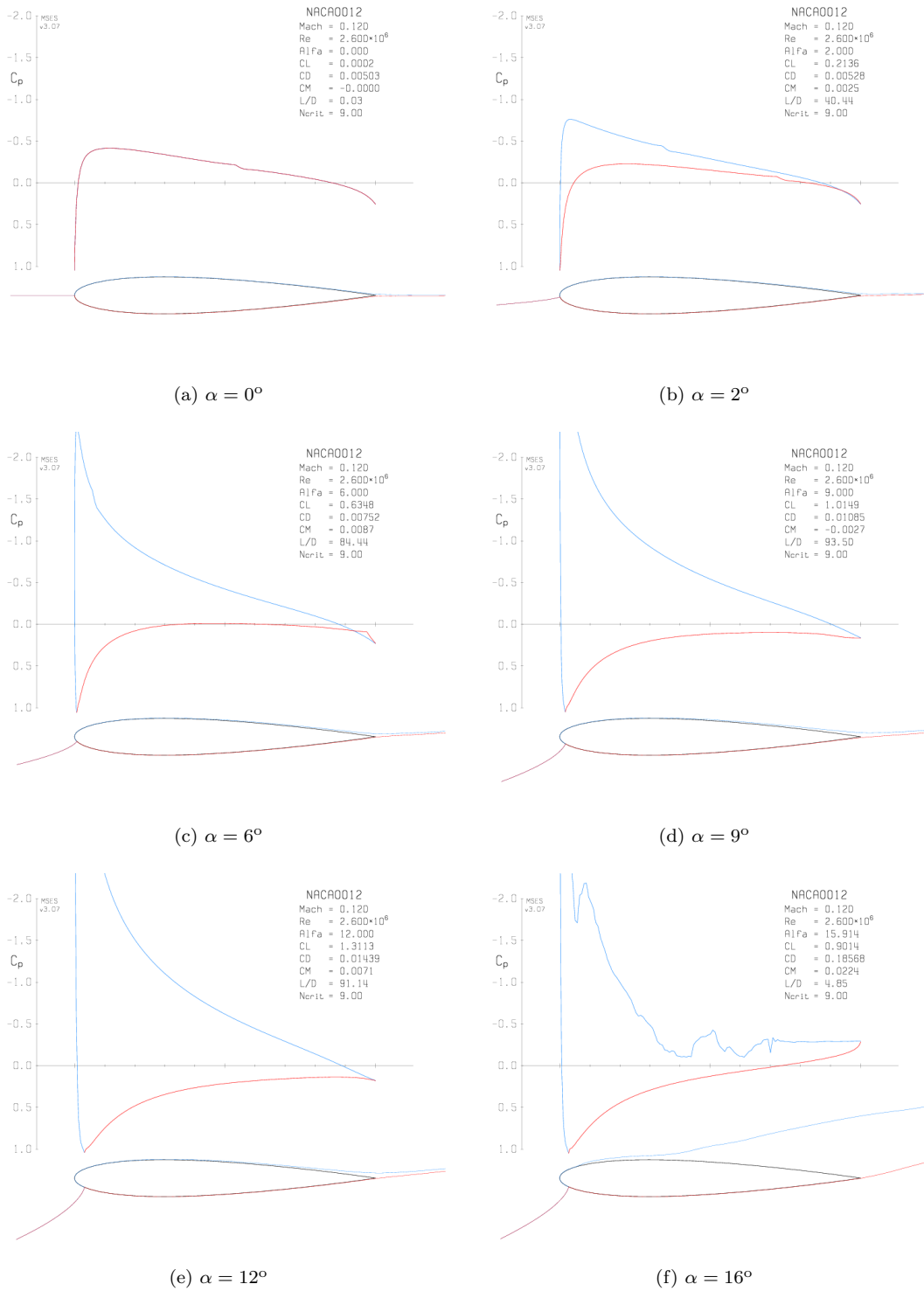


Figure C.1: NACA 0012  $C_p$ -distribution plots at (a)  $\alpha = 0^\circ$ , (b)  $\alpha = 2^\circ$ , (c)  $\alpha = 6^\circ$ , (d)  $\alpha = 9^\circ$ , (e)  $\alpha = 12^\circ$ , (f)  $\alpha = 16^\circ$

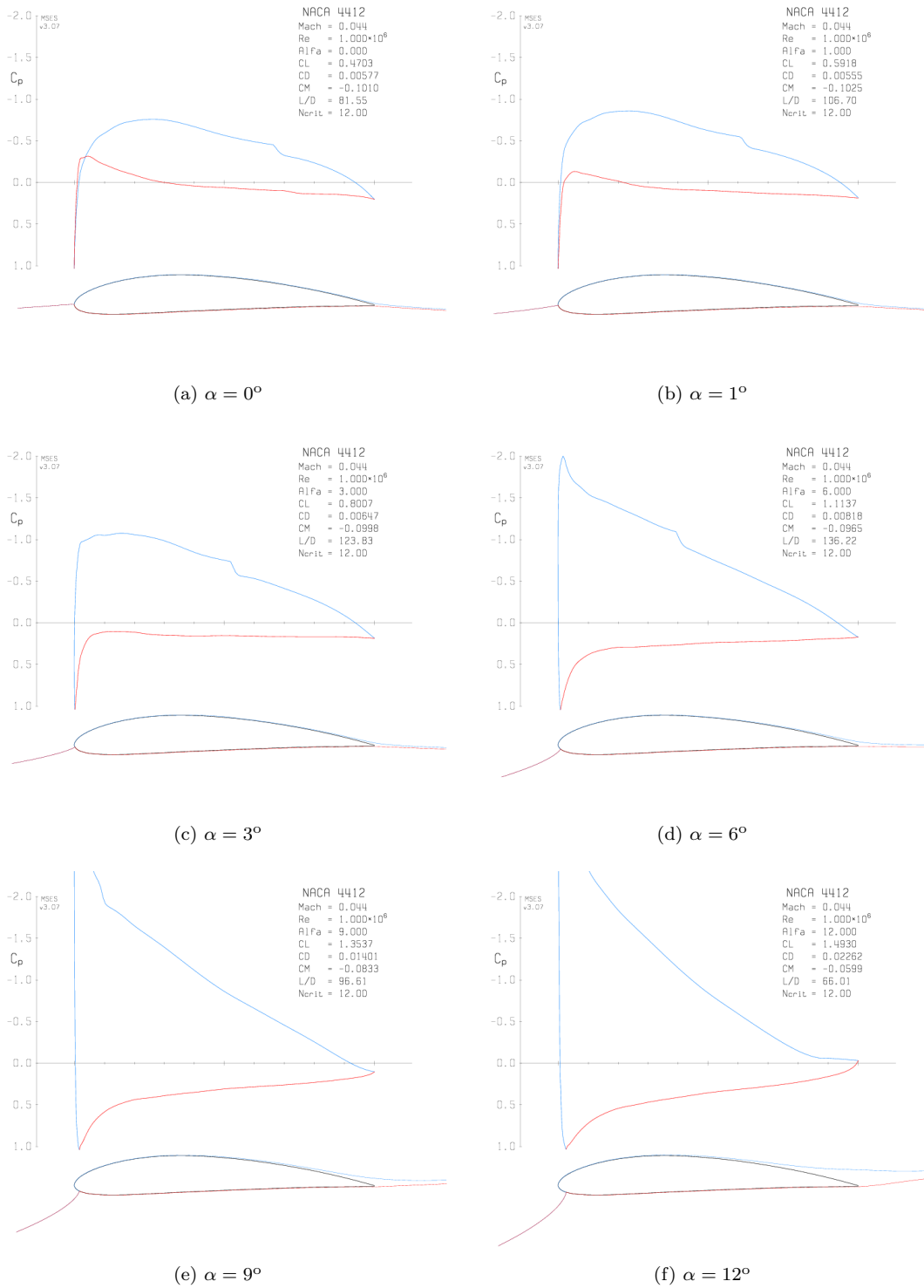


Figure C.2: NACA 4412  $C_p$ -distribution plots at (a)  $\alpha = 0^\circ$ , (b)  $\alpha = 1^\circ$ , (c)  $\alpha = 3^\circ$ , (d)  $\alpha = 6^\circ$ , (e)  $\alpha = 9^\circ$ , (f)  $\alpha = 12^\circ$

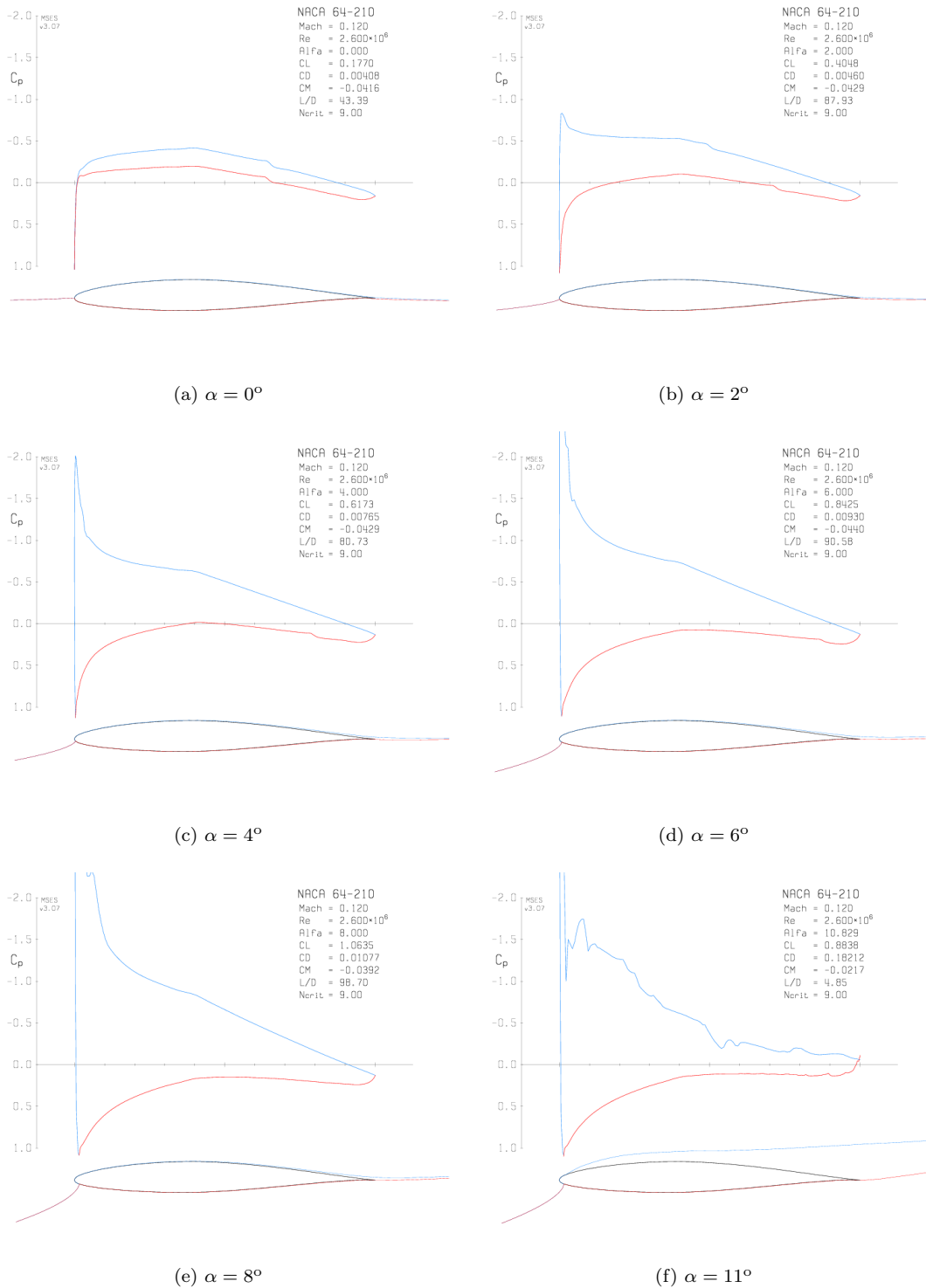


Figure C.3: NACA 64210  $C_p$ -distribution plots at (a)  $\alpha = 0^\circ$ , (b)  $\alpha = 2^\circ$ , (c)  $\alpha = 4^\circ$ , (d)  $\alpha = 6^\circ$ , (e)  $\alpha = 8^\circ$ , (f)  $\alpha = 11^\circ$

## C.4 Further results from X-400 model simulations

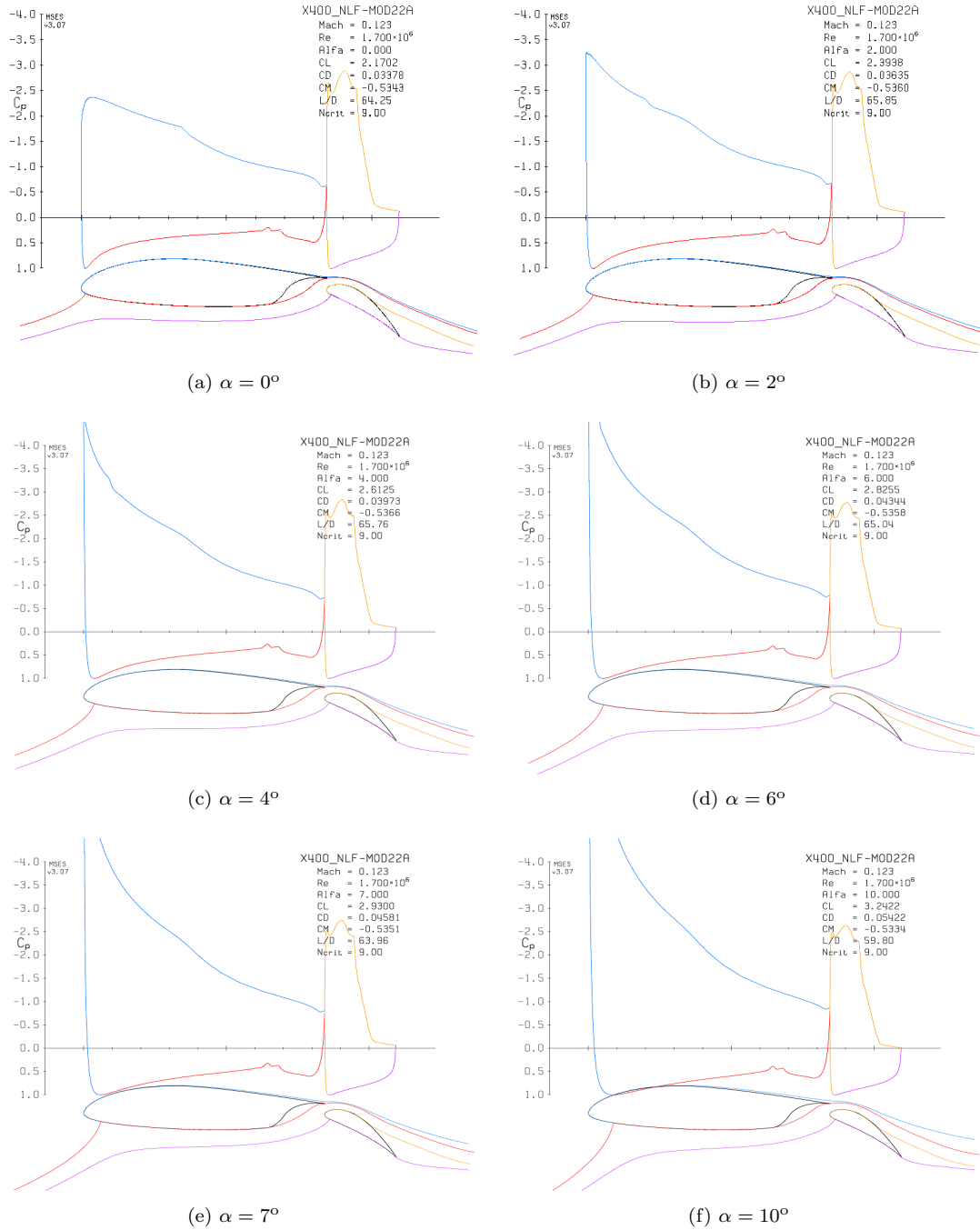


Figure C.4: X-400 wing-flap configuration at **Case 1**  $C_p$ -distribution plots at (a)  $\alpha = 0^\circ$ , (b)  $\alpha = 2^\circ$ , (c)  $\alpha = 4^\circ$ , (d)  $\alpha = 6^\circ$ , (e)  $\alpha = 7^\circ$ , (f)  $\alpha = 10^\circ$

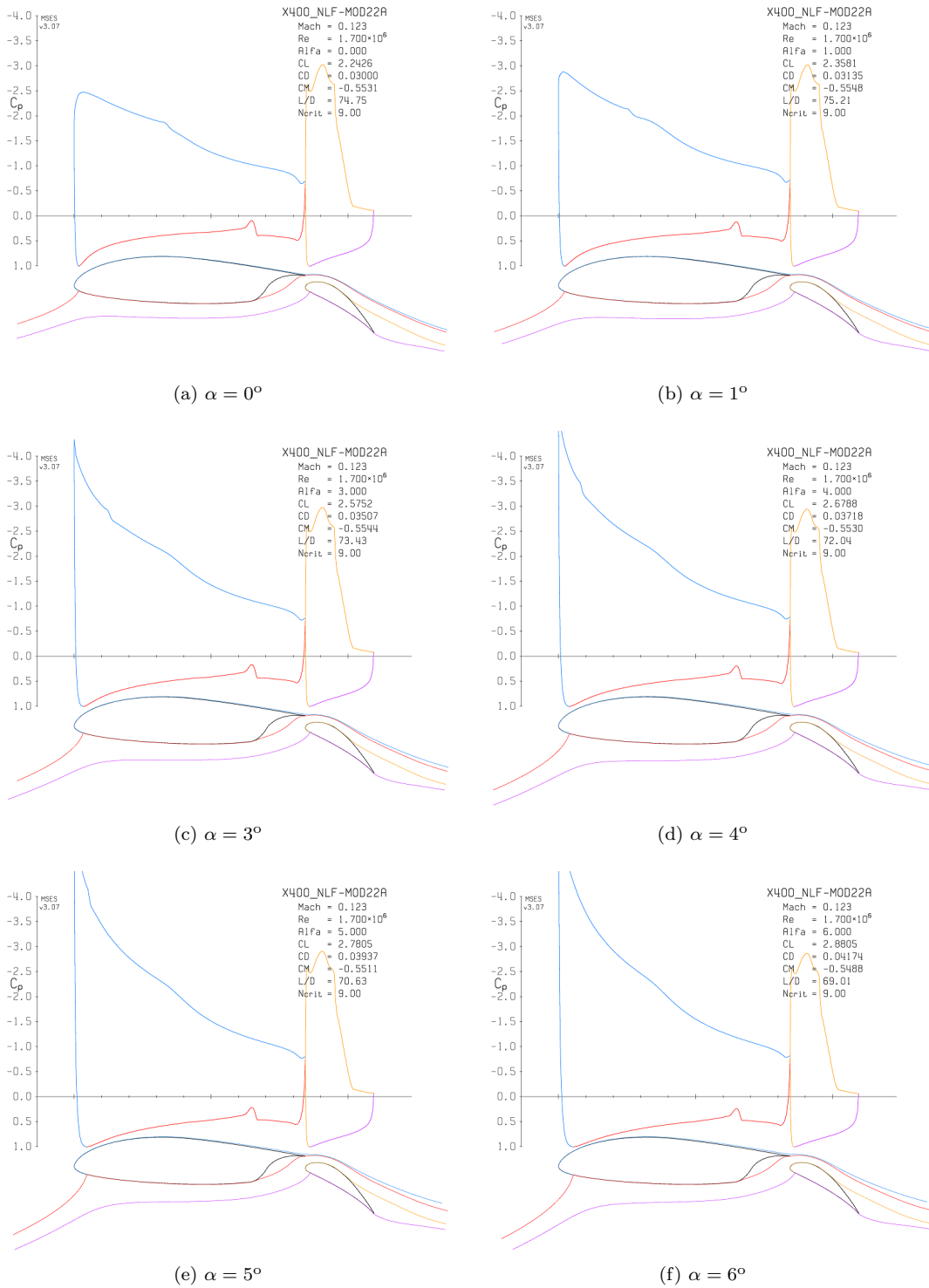


Figure C.5: X-400 wing-flap configuration at **Case 2**  $C_p$ -distribution plots at (a)  $\alpha = 0^\circ$ , (b)  $\alpha = 1^\circ$ , (c)  $\alpha = 3^\circ$ , (d)  $\alpha = 4^\circ$ , (e)  $\alpha = 5^\circ$ , (f)  $\alpha = 6^\circ$

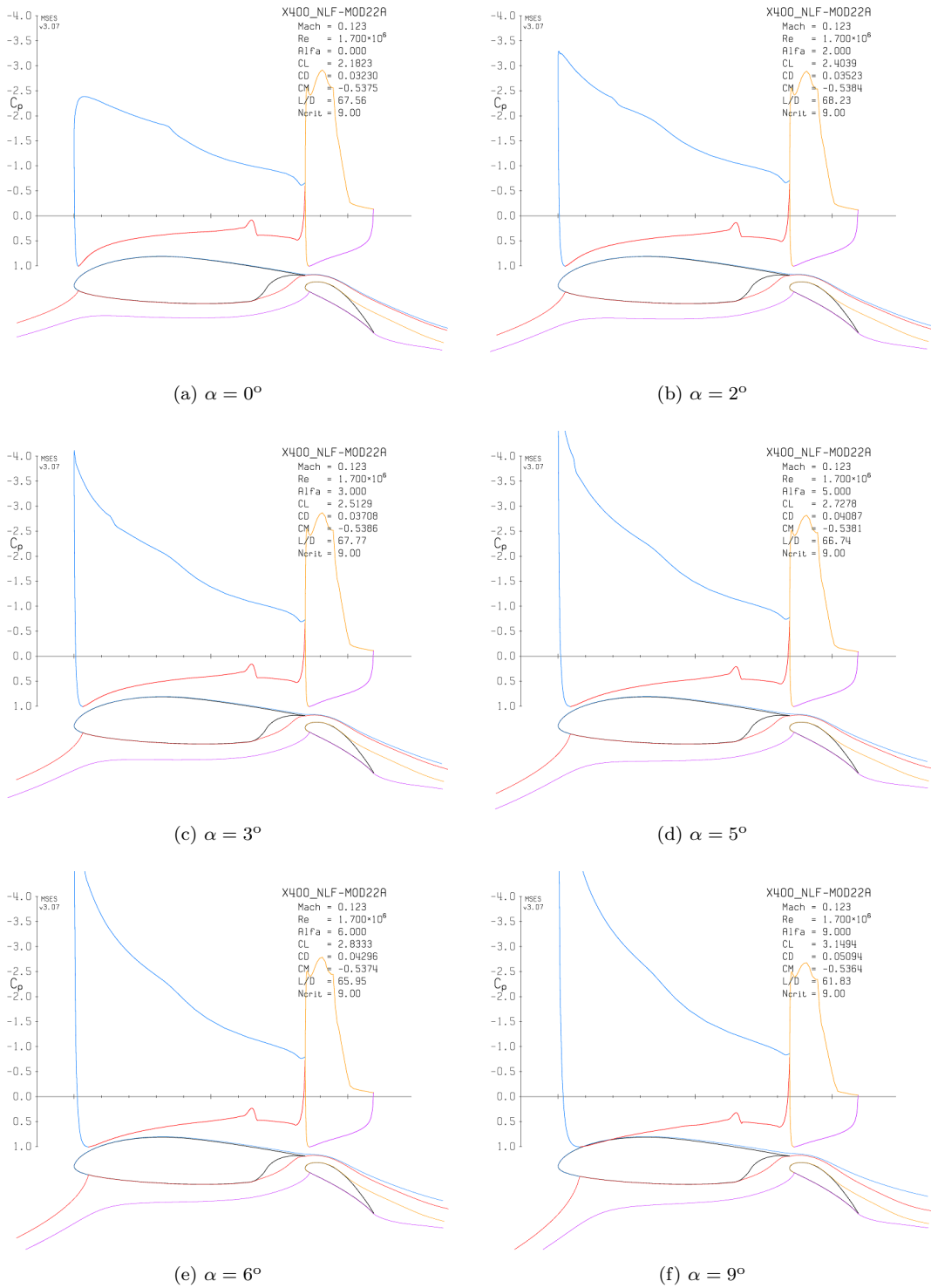


Figure C.6: X-400 wing-flap configuration at **Case 3**  $C_p$ -distribution plots at (a)  $\alpha = 0^\circ$ , (b)  $\alpha = 2^\circ$ , (c)  $\alpha = 3^\circ$ , (d)  $\alpha = 5^\circ$ , (e)  $\alpha = 6^\circ$ , (f)  $\alpha = 9^\circ$

